

# IoT Bio-Electronic Multi-Panel Device for On-line Monitoring of Anaesthesia Delivery

THÈSE N° 8800 (2018)

PRÉSENTÉE LE 7 SEPTEMBRE 2018

À LA FACULTÉ INFORMATIQUE ET COMMUNICATIONS  
LABORATOIRE DES SYSTÈMES INTÉGRÉS (IC/STI)  
PROGRAMME DOCTORAL EN GÉNIE ÉLECTRIQUE

ÉCOLE POLYTECHNIQUE FÉDÉRALE DE LAUSANNE

POUR L'OBTENTION DU GRADE DE DOCTEUR ÈS SCIENCES

PAR

**Francesca STRADOLINI**

acceptée sur proposition du jury:

Prof. J.-Ph. Thiran, président du jury  
Dr S. Carrara, Prof. G. De Micheli, directeurs de thèse  
Prof. D. Demarchi, rapporteur  
Prof. E. Alarcon, rapporteur  
Prof. M. Kayal, rapporteur



ÉCOLE POLYTECHNIQUE  
FÉDÉRALE DE LAUSANNE

Suisse  
2018



A traveler without observation  
is a bird without wings.  
— Moslih Eddin Saadi

To my beloved family...





# Acknowledgements

First of all, I would like to express my gratitude to my thesis director Dr. MER Sandro Carrara and co-director Prof. Giovanni De Micheli for the great opportunity they gave me in working in such a dynamic and friendly environment they have created in the lab. In particular, I would like to thank Sandro for having patiently taught me the “art of research”, giving me great independence and trust without ever forgetting to encourage me and to celebrate my achievements. In addition, I thank Nanni for having supported me throughout the PhD leaving me great freedom of action in his laboratory. Without their guidance and persistent help this thesis would not have been possible. Furthermore, I would like to thank each jury member for the interest and the involvement they have shown in the work I have realized during my PhD.

My heartfelt appreciation goes to Dr. Tugba Kilic for the passion she dedicated in guiding me in all the phases of my project, being always present to help and support me. Not only for her teachings I want to thank her, but also for her truly friendship.

I wish to acknowledge the help provided by Prof. Demarchi and his team in Polytechnic of Turin for the experience and assistance offered to the electronic development of my project. I am particularly grateful to Abduwaili Twoheti for his constant help, suggestions and encouragements. It was a real pleasure to work with such a good friend.

I want to express my gratitude also to the “CoMofA” team. To Dr. Chollet Madeleine, Prof. Thierry Buclin, Dr. Monia Guidi, Dr. Alena Simalatsar, and to Dr. Federico Angiolini for the stimulating discussions at CHUV about the research progresses of this thesis. In the context of my thesis, I would like to show my greatest appreciation for PrYv SA. It was really interesting and fruitful to work with all of them, especially with Ilia Krebs and Thèibaud Moudox.

From the “big-family LSI” there are some other very important people to thank. First of all, I would like to dedicate a huge thank to the “mum” Christina Govoni for her kindness, her constant help in PhD issues and, especially, for the private French lessons; I loved sharing with you all the joys during my staying in LSI. Now we are both ready to experience other life adventures! I want to thank Rodolphe Buret, for the technical support he has always provided in the field of computers and John Maxwell, who made enormous contribution in revising this work. I want to dedicate special thanks to some of my LSI mates. To Eleonora Testa, my friend and office mate, for her great courage that is an example for everyone of us. To Giovanni Resta, for always supporting us with his calm and his professionalism...obviously also with his precious culinary skills! To Francesca Criscuolo, for her sparkling way of being and for her immense energy that always share with us. To Giulia Meuli, for joining the zumba lessons on

## Acknowledgements

---

Friday afternoon that really helped to unload the tensions from the working week. To Ivan Ny Hanitra, for his gentleman way of being, always kind and helpful. To Aya Ibrahim and Younis, for their sweetness and strength that they have always shared with me. To Ioulia Tzouvadaki for the amazing trip we did together in Canada, making my first conference so special. To all the other LSers who shared with me the life of the lab, Nima, Winston, Bruno, Fereste, Ana, Matilda, Eda, Nadja, Mathias, Cunxi, Henz, Sattar and many others. Finally, to the more senior LSers, Dr. Irene Taurino, Dr. Camilla Baj Rossi and Dr. Cristina Boero, for the support they gave me as soon as I arrived in the laboratory and for the important advices on PhD life.

My PhD was such an enriching experience also thanks to the several wonderful people I have met. I want to thank Tamador Elboshra, Armando Biscontini, Sarah Tonello and Marius Schirmer for excellent collaborations we shared. To my lovely master students to whom I have always dedicated immense attention: Eleonora Lavallo, Diego Marino, Sofia Lydia Ntella, Nadia Tamburrano, Bruno Donato, Lucia Lobello and Sofia Milanese. I am grateful to have received such a great commitment from them and to have always felt their believe on me. A big thank goes to some other friends I have met here in Lausanne, Enrico, Alessandro, Alessandra, and many others. In particular, I would like to thank Flavia Basilotta, Francesco Bellando, Soumya Subhra Basu, Marta Franceschi, Maxime Thammasack, Maneesha Rupakula and Kunal Sharma for all the fun and carefree moments spent together. To Laura Ferlauto and her husband, Max, for their friendship and for being always willing to keep care of our beloved dogs while we go on holidays.

To our neighbors in Lausanne, Maria and Amato, with whom we shared pleasant evenings together and fantastic boat trips on the lake.

A special thanks to my Android teachers, Andrea De Gaetano and Grègoire Surrel, because despite I have bothered them so much they never gave up with me. In particular, I really thank Andrea for having always believed in me, so much as to push me up to present my work to the *droidcon* conference.

In Italy, I have some dear friends to thank for having been always present even when the distances have increased. To Alessia Borsari and Matteo Morando, because they are indispensable friends always present and careful to never miss an opportunity to spend some time together. To Giulia Migliaccio, for being always my energetic friend and for never having stopped supporting me. To Camilla De Regibus, because being grown together has made us feeling so close. To Stefania Tassara, because your madness and your enthusiasm have always fueled mine. Among the Italian friends, I would like also to dedicate a thank to Paolo, Charlotte, their daughters, and Annina.

My heartfelt thanks go to all my family. To my aunts, Carla and Silvia, to always treat us in such a special way. To the “Delle” family, because it is so fun to be part of such alive family. To my sister, Arianna, your determination and security always supported me. Several times you have made me feel like a “super sister”, giving me the strength to keep doing my best. To my parents, Paola e Lorenzo, for having been so wise as to be able to shoot their precious arrow so far away. You have never made me feel missing your support during these years and you have always believed in me. To Nonno Aldo, for having came here in Lausanne as a representative of my beloved grandparents. To Spike, because he came with me even at work, becoming the

## **Acknowledgements**

---

mascot of the lab, and to Diana for her sweetness.

Finally, but not least, my deepest gratitude goes to my husband, Enrico, for being extraordinarily tolerant and supportive. Thank you for making me live a joyful life rich of fantastic experiences in parallel with the PhD. We now continue our life's road by keeping holding our hands.

*Lausanne, 15 May 2018*

F. S.



# Abstract

After a failure of "One-Size-Fits-All" approach on traditional treatment of diseases, the age of multi-faceted personalized medicine came into being for tailoring therapy to get the best response in the highest safety margin. Personalized drug dosage is one of the promises of personalized medicine and is of great importance for critical medical treatments such as anesthesia. General anesthesia induces a reversible state of unconsciousness in the patient due to the synergetic action of a cocktail of drugs. A general anesthesia cocktail is made up of a hypnotic, such as propofol, an analgesic, such as opioid-based or paracetamol, and a myorelaxant drug, such as midazolam. The delivery rate of these individual drugs in the cocktail has to be continuously monitored and balanced to achieve and maintain the desired level of sedation in the patient to avoid severe psycho-physical complications of over-/under-doses. To this end, the common practice nowadays is to use *Target Control Infusion* (TCI) pumps, which regulate the delivery of anesthetic compounds according to their mathematical pharmaco-kinetic models that estimate the right dose for the injection on the basis of patients' health data. However, implementation of these models have been done considering a population that does not cover all individuals, hence, falling in the category of "One-Size-Fits-All" approach and fail to reproduce the inter-patient variability in metabolism. Therefore, one of the main challenges in general anesthesia practices is the monitoring of the *Depth Of Anesthesia* (DOA) in patients to be able to tune the drug dosage according to individual's responses.

One of the most widely used methods for DOA monitoring in Europe is the *BiSpectral Index* (BIS), a statistical predictor that is evaluated from *ElectroEncephaloGram* (EEG) signal. However, there exist several limitations regarding this technique such as being indirect measure of DOA and prone to be affected by artifacts and production of different signals in case of different anesthetics.

To overcome these limitations, there is a need for a *Therapeutic Drug Monitoring* (TDM) system capable of continuously measuring the actual concentration of each infused drug in the blood of patient during DOA for a safer, reliable and personalized anesthesia delivery. In this thesis, we present the design, the implementation and the validation of a complete TDM system for long-time and continuous monitoring of anesthetics' concentrations.

The complete TDM system consists of: (i) a custom-built *Raspberry-Pi* (RPi)-based electronic board to drive, (ii) the electrochemical sensors for propofol, paracetamol and midazolam detection, that are encapsulated into (iii) a fluidic device to drive the sample on the sensing sites, and (iv) an Android-based *Internet of Things* (IoT) network architecture to keep the anesthesiologist always connected with the sedated patient. Thanks to the IoT network,

## Acknowledgements

---

the developed system is capable of fast data visualization tools, as well as an alarm system activated in case serious physical conditions are detected in patient and remote monitoring through cloud-sharing.

This thesis describes in details the system and highlights the following results:

- Fouling-free propofol long-time monitoring by the use of *Pencil Graphite Electrode* (PGE) with a specific graphite/clay/wax composition.
- Successful assembly of electronics and sensors in a novel multi-panel system capable of monitoring several drugs in complex bio-fluids, such as undiluted human serum.
- Demonstration of simultaneous monitoring of several drugs concentrations trends over time.
- Powerful and innovative integration of an IoT network for providing a constant monitoring through Android app and for enabling telemedicine support.

**Keywords:** *anesthesia, electrochemical sensors, multi-sensing, long-term monitoring, anesthetic cocktail, propofol, custom-built electronics, fluidics, Internet of Things, Cloud support.*

# Résumé

Vu la carence de l'approche "One-Size-Fits-All" (une quantité égale pour tous) qui caractérise les traitements administrés par la médecine traditionnelle, la médecine personnalisée a été introduite dans le but d'administrer des thérapies individuelles dans le but d'obtenir le bénéfice maximum garantissant la plus haute marge de sécurité. Le dosage personnalisé du médicament est une des promesses essentielles de la médecine personnalisée et a une importance fondamentale au niveau des traitements médicaux aigus, comme par exemple l'anesthésie. En effet, l'anesthésie générale amène le patient dans un état réversible d'inconscience en exploitant l'action de synergie d'un cocktail pharmaceutique. En général, le cocktail anesthésique est composé de : un hypnotique comme le propofol, un analgésique soit à base d'opiacée ou de paracétamol ainsi qu'un myorelaxant comme le midazolam. La quantité administrée de ces médicaments doit être continuellement monitorée et réglée pour rejoindre et maintenir le niveau désiré d'anesthésiant afin d'éviter de graves complications psycho-physiques causées par un sur ou sous dosage. C'est la raison pour laquelle, de nos jours, la pompe à perfusion contrôlée est largement utilisée. Cette dernière repose sur l'administration des anesthésiants sur la base de modèles mathématiques pharmacocinétiques qui estiment (calcul) la dose correcte à administrer au patient, sur la base de données physiques. Cependant, l'implémentation de ces modèles est basée sur l'étude d'une population non exhaustive, retombant dans la catégorie "One-Size-Fits-All". En effet, ces modèles mathématiques ne sont pas en mesure de reproduire la diversité du métabolisme entre différents patients. Cependant, le défi principal dans les pratiques d'anesthésie générale est le monitoring du niveau d'anesthésie du patient dans le but de doser les anesthésiants sur la base de la réponse individuelle du sujet. En Europe, une des méthodes les plus utilisées dans le monitoring de l'anesthésie est l'indice *Bispectral* (BIS), un paramètre statistique évalué par le signal de l'électroencéphalogramme. Cependant cette technique a des limites, le BIS étant évalué de manière indirecte et pouvant être sujet à des erreurs de mesures et variabilité due à différents médicaments. Pour dépasser ces limites, il est nécessaire d'utiliser un système capable de mesurer la concentration effective de chaque médicament en continu, injecté dans le sang du patient durant l'anesthésie, ce qui garantit un dosage plus sûr, fiable et personnalisé. Dans cette thèse, nous présenterons la projection, l'implémentation et la validation d'un système complet concernant le monitoring continu de la concentration de différents anesthésiants dans la durée. Le système de monitoring est constitué de (i) un circuit imprimé piloté par *Raspberry-Pi* (RPi) qui contrôle (ii) les senseurs électrochimiques pour la détection de propofol, paracétamol et midazolam ; ces derniers sont encapsulés dans (iii) un dispositif fluide dans le but de guider l'échantillon sur les sites

## Acknowledgements

---

de détection, et (iv) un réseau IoT basé sur Android pour maintenir l'anesthésiste en contact permanent avec le patient anesthésié. Ce réseau offre des instruments pour une visualisation rapide des données, un système d'alarme activé dans le cas où une souffrance du patient serait détectée ainsi qu'un monitoring à distance au travers de Cloud. Cette thèse décrit dans le détail le système complet et met en évidence les résultats suivants :

- Monitoring à long terme du propofol sans mettre en évidence des signes de détérioration de l'électrode. Les mesures ont été effectuées en utilisant des électrodes avec une composition spécifique de graphite, d'argile et de cire.
- Assemblage optimisé de l'électronique et des senseurs dans un système capable de monitorer de manière continue et simultanée divers médicaments dans les fluides biologiques complexes, comme le sérum humain.
- Démonstration de l'efficacité du système dans le monitoring simultané des niveaux de concentration de différents anesthésiants dans la durée.
- Intégration innovatrice d'un réseau IoT pour fournir un monitoring constant au travers d'applications Android et activer le support à la télémédecine.

**Mots-clés:** *anesthésie, capteurs électrochimiques, multi-détection, surveillance à long terme, cocktail anesthésique, propofol, électronique sur mesure, fluide, Internet des Objets, support Cloud.*



## Sommario

Data l'inadeguatezza dell'approccio "One-Size-Fits-All" (una quantità uguale per tutti) che caratterizza i trattamenti somministrati dalla medicina tradizionale, la poliedrica medicina personalizzata è stata introdotta allo scopo di somministrare terapie individuali in grado di ottenerne il massimo beneficio nel più alto margine di sicurezza. Il dosaggio personalizzato del farmaco è una delle promesse fondamentali della medicina personalizzata ed è di importanza cruciale soprattutto in trattamenti medici critici, come ad esempio l'anestesia. Infatti, l'anestesia generale induce uno stato reversibile di incoscienza nel paziente sfruttando l'azione sinergica di un cocktail di farmaci. Normalmente, il cocktail anestetico è composto da: un ipnotico, come il propofol, un analgesico, solitamente a base oppiacea od il paracetamolo e un farmaco miorellassante, come il midazolam. Il tasso di somministrazione di ciascuno di questi farmaci deve essere continuamente monitorato e regolato per raggiungere e mantenere il livello desiderato di sedazione nel paziente per evitare gravi complicazioni psico-fisiche causate da sovra/sotto-dosaggi. A tal fine, la pratica più diffusa oggi è quella di utilizzare pompe ad infusione controllata (TCI, dall'inglese *Target Control Infusion*), che regolano la somministrazione degli anestetici secondo modelli matematici di farmacocinetica che stimano la giusta dose da iniettare sulla base dei dati fisici del paziente. Tuttavia, l'implementazione di questi modelli si è basata sullo studio di una popolazione non esaustiva, rientrando quindi nella categoria di "One-Size-Fits-All". Infatti, questi modelli matematici non sono in grado di riprodurre la variabilità del metabolismo tra diversi pazienti. Pertanto, una delle principali sfide nelle pratiche di anestesia generale è il monitoraggio del livello di anestesia del singolo paziente così da dosare gli anestetici in base alla risposta individuale del soggetto.

In Europa, uno dei metodi più utilizzati per il monitoraggio dell'anestesia è basato sull'indice *BiSpettrale* (BIS), un predittore statistico che viene valutato dal segnale dell'*Elettro-Encefalogramma* (EEG). Tuttavia, questa tecnica riscontra diverse limitazioni essendo il BIS misurato in maniera indiretta e perciò soggetto ad artefatti e variabilità in risposta a diversi farmaci. Per superare questi limiti, è necessario un sistema in grado di misurare continuamente la concentrazione effettiva di ciascun farmaco infuso nel sangue del paziente durante l'anestesia, così da garantire una somministrazione più sicura, affidabile e personalizzata.

In questa tesi, presenteremo la progettazione, l'implementazione e la validazione di un sistema completo per il monitoraggio continuo della concentrazione di diversi anestetici nel tempo. Il sistema di monitoraggio è costituito da: (i) una scheda elettronica guidata da *Raspberry-Pi* (RPi) che controlla, (ii) i sensori elettrochimici per il rilevamento di propofol, paracetamolo e midazolam; tali sensori sono incapsulati in (iii) un dispositivo fluidico per guidare il campione

## Acknowledgements

---

sui siti di rilevazione, ed (iv) un'architettura di rete IoT basata su Android per mantenere l'anestesista sempre collegato al paziente sedato. Questa rete IoT offre strumenti per una visualizzazione rapida dei dati misurati, un sistema di allarme attivato nel caso in cui si rilevino sofferenze nel monitoraggio del paziente e un monitoraggio anche da remoto tramite supporto cloud.

Questa tesi descrive nel dettaglio il sistema completo ed evidenzia i seguenti risultati:

- Monitoraggio a lungo termine del propofol senza evidenziare segni di deterioramento dell'elettrodo. Le misure sono state effettuate mediante l'uso di elettrodi con una specifica composizione di grafite, argilla e cera.
- Assemblaggio ottimizzato dell'elettronica e dei sensori in un sistema in grado di monitorare in maniera continue e simultanea diversi farmaci in bio-fluidi complessi, come il siero umano.
- Dimostrazione dell'efficienza del sistema nel monitoraggio simultaneo dei livelli di concentrazione di diversi anestetici nel tempo.
- Innovativa integrazione di una rete IoT per fornire un monitoraggio costante tramite applicazioni Android e per abilitare il supporto alla telemedicina.

**Parole chiave:** *anestesia, sensori elettrochimici, monitoraggio di diversi farmaci, monitoraggio a lungo termine, cocktail anestetico, propofol, elettronica dedicata, fluidica, Internet delle Cose, supporto Cloud.*

# Contents

<b>Acknowledgements</b>	<b>v</b>
<b>Abstract (English/Français/Italian)</b>	<b>ix</b>
<b>List of figures</b>	<b>xvii</b>
<b>List of tables</b>	<b>xxii</b>
<b>1 Introduction</b>	<b>1</b>
1.1 <i>General Anesthesia</i> (GA)	2
1.1.1 Cocktail of drugs	4
1.1.2 <i>PharmacoKinetics</i> (PK) and <i>PharmacoDinamics</i> (PD)	5
1.1.3 Three-compartment model	8
1.2 Current state-of-the-art of <i>Total Intra-Venous Anesthesia</i> (TIVA)	9
1.2.1 <i>Target Controlled Infusion</i> (TCI) pump: principles and limitations	9
1.2.2 <i>Bispectral Index</i> (BIS) monitoring: use and limitations	10
1.2.3 Anesthesia side effects and risks	12
1.3 Research contributions and thesis outline	12
<b>2 Background</b>	<b>17</b>
2.1 Drug monitoring with electrochemical sensors	17
2.1.1 Electrochemical sensing techniques: an overview	17
2.1.2 <i>ChronoAmperometry</i> (CA)	21
2.1.3 Sensor calibration	25
2.1.4 Enhancement of electrode performance	26
2.2 Electronics for electrochemical sensing	28
2.2.1 Potentiostat	28
2.2.2 Equivalent circuit for an electrochemical cell	32
2.3 IoT in medical applications	33
2.3.1 Cloud computing	36
2.3.2 Android operating system	38
2.4 Summary and main contributions	44

## Contents

---

<b>3 Propofol direct monitoring</b>	<b>45</b>
3.1 State-of-the-art	45
3.2 Polymeric membrane-coated carbon <i>Screen Printed Electrodes</i> (SPEs)	47
3.2.1 Materials and methods	48
3.2.2 Electrode preparation	49
3.2.3 Results and limitations	49
3.3 <i>Boron Doped Diamond</i> (BDD) and <i>Pencil Graphite Electrode</i> (PGE) electrodes	50
3.3.1 Materials and methods	51
3.3.2 Fouling characterization at PGE and BDD electrodes	52
3.3.3 Cleaning procedures	55
3.3.4 Results and discussion	56
3.3.5 Serum detection	61
3.4 Different compositions of PGEs	62
3.4.1 Materials and methods	62
3.4.2 Results and discussion	64
3.5 Summary and main original contributions	69
<b>4 Midazolam and Paracetamol direct monitoring</b>	<b>73</b>
4.1 State-of-the-art	74
4.2 Carbon-based nano-structured electrodes	75
4.2.1 Materials and methods	75
4.2.2 Results and discussion	77
4.3 Interference study	84
4.3.1 Interference at different PGEs	85
4.3.2 Interference at C- <i>Screen Printed Electrode</i> (SPE)	89
4.4 Summary and main original contributions	90
<b>5 Electronic platform</b>	<b>93</b>
5.0.1 System architecture of the electronic platform	94
5.1 Multi-channel potentiostat	95
5.1.1 Front-end design for drug monitoring	96
5.1.2 Front-end optimization process	98
5.1.3 Improved read-out signal by hardware filtering	105
5.2 Measure of pH and temperature for calibrations	107
5.2.1 System calibration and drug measuring processes	110
5.2.2 Preliminary calibration procedure	110
5.2.3 Validation of the pH-T module with propofol calibrations	110
5.3 <i>Graphical User Interface</i> on the RPi	112
5.4 System validation	114
5.4.1 Materials and methods	114
5.4.2 Results	117
5.5 Summary and main original contributions	122

<b>6 Overall IoT system architecture</b>	<b>125</b>
6.1 State-of-the-art . . . . .	126
6.2 IoT cloud-based network & Android development . . . . .	126
6.2.1 Smart-watch as paradigm-shifting player in medical IoT . . . . .	127
6.2.2 Cloud-based architecture for anesthesia monitoring . . . . .	133
6.3 Realization of the <i>sensing platform</i> with fluidics integration . . . . .	139
6.3.1 Fabrication of fluidic chambers in <i>Poly(di-methyl siloxane)</i> (PDMS) ( <i>Cham-</i> <i>bers nr.2 and nr.3</i> ) . . . . .	140
6.3.2 Characterization of the fluidic device . . . . .	144
6.4 Overall system validation . . . . .	145
6.4.1 Validation of the system in undiluted human serum . . . . .	147
6.5 Infusion pump integration: towards closed loop delivery . . . . .	149
6.5.1 Raspberry Pi-driven <i>Flow-Injection System</i> (FIS) . . . . .	150
6.5.2 FIS set-up . . . . .	150
6.5.3 Injection dose calculation . . . . .	152
6.5.4 <i>Flow-Injection System</i> (FIS) validation . . . . .	153
6.6 Summary and original contributions . . . . .	155
<b>7 Conclusions and future work</b>	<b>159</b>
<b>A Micro-controller firmware</b>	<b>163</b>
A.1 main.c . . . . .	164
A.2 Twi_protocol.h . . . . .	164
A.3 Setup_twi.c . . . . .	165
A.4 Setup_timer.c . . . . .	166
<b>Bibliography</b>	<b>188</b>
<b>Curriculum Vitae</b>	<b>189</b>



# List of Figures

1.1	Classification of drug administration errors in anesthesia . . . . .	1
1.2	Anesthetics sites of action . . . . .	3
1.3	Midazolam pH dependency . . . . .	5
1.4	PK/PD phases . . . . .	6
1.5	PK/PD curves . . . . .	7
1.6	Three-compartmental model . . . . .	8
1.7	Bispectral index . . . . .	10
1.8	Visual index of the thesis . . . . .	13
2.1	Electrochemical cell configurations . . . . .	18
2.2	Energy process of a RedOx . . . . .	19
2.3	Helmholtz planes theory . . . . .	20
2.4	Electrochemical cell as a "black box" . . . . .	21
2.5	ChronoAmperometry (CA) . . . . .	22
2.6	Cyclic Voltammetry (CV) . . . . .	23
2.7	Differential Pulse Voltammetry (DPV) . . . . .	24
2.8	Calibration line parameters . . . . .	25
2.9	Carbon-based nano-structures . . . . .	26
2.10	General scheme of a potentiostat . . . . .	28
2.11	Potential control unit: grounded CE . . . . .	29
2.12	Potential control unit: grounded WE . . . . .	29
2.13	SPI communication . . . . .	30
2.14	Readout circuit for a grounded WE configuration . . . . .	31
2.15	Equivalent circuit of an electrochemical cell . . . . .	32
2.16	IoT reference model . . . . .	33
2.17	IoT applications . . . . .	34
2.18	Economic impact of IoT . . . . .	35
2.19	Modular structure of data storage in PrYv middle-ware . . . . .	38
2.20	Android OS versions . . . . .	38
2.21	Android architecture stack . . . . .	39
2.22	Android activity life-cycle . . . . .	41
2.23	Project files in Android Studio . . . . .	43

## List of Figures

---

3.1	Propofol chemical structure . . . . .	45
3.2	Electrochemical CV characterization of propofol (from literature) . . . . .	47
3.3	Spin coating of the PVC membrane on the electrode . . . . .	48
3.4	Calibration curve for propofol detection in PBS at PVC-modified electrode and fouling effect evidence . . . . .	49
3.5	SEM image of the PVC membrane . . . . .	49
3.6	Pencil graphite electrode (PGE): the configuration . . . . .	51
3.7	SEM image of boron doped diamond (BDD) electrode . . . . .	52
3.8	SEM image of PGE . . . . .	52
3.9	pH and scan-rate studies for PGE . . . . .	53
3.10	Sensitivities without cleanings for propofol detection at PGE and BDD . . . . .	54
3.11	Propofol calibration lines affected by fouling . . . . .	55
3.12	Optimization process of the cleaning parameters . . . . .	56
3.13	Sensitivities with cleanings for propofol detection at PGE and BDD . . . . .	57
3.14	Propofol calibration lines with cleanings . . . . .	58
3.15	SEM imaging of PGE after cleanings . . . . .	58
3.16	Ferro(ferri)cyanide CV analysis at PGE . . . . .	58
3.17	Efficacy of PBS cleaning also in presence of propofol . . . . .	59
3.18	Long-term electrochemical propofol monitoring . . . . .	59
3.19	pH and scan-rate studies for PGE . . . . .	60
3.20	Propofol monitoring at PGE in human serum over time . . . . .	61
3.21	Lead composition scale . . . . .	62
3.22	Pencils set . . . . .	63
3.23	Sensitivity variations in propofol detection among different PGE leads . . . . .	64
3.24	CV calibration curves from different PGE leads . . . . .	65
3.25	<i>Intra</i> -electrode PGE sensitivity variations over 5 calibrations . . . . .	66
3.26	Fouling evaluation of different PGE leads . . . . .	67
3.27	Propofol in-time monitoring at different PGE leads . . . . .	67
3.28	SEM images of different PGE leads . . . . .	68
3.29	EIS analysis for <i>3H</i> and <i>3B</i> PGEs . . . . .	69
4.1	Paracetamol and midazolam chemical structures . . . . .	73
4.2	SEM images of C-SPE, MWCNTs and Fullerene surfaces . . . . .	77
4.3	Electrochemical characterization of midazolam (from literature) . . . . .	78
4.4	Midazolam CV calibration in PBS (10 mM, pH: 2.5) at bare C-SPE . . . . .	79
4.5	Electrochemical characterization of APAP (from literature) . . . . .	80
4.6	APAP CV calibration in PBS (10 mM, pH: 7.4) at bare C-SPE . . . . .	80
4.7	Typical voltammograms for APAP and MZ detection in PBS (10 mM, pH: 7.4) at bare, C <sub>60</sub> - and MWCNT-modified electrodes . . . . .	81
4.8	APAP and MZ CV calibrations in PBS at C <sub>60</sub> - and MWCNT-modified WEs . . . . .	82
4.9	APAP and MZ detection in human serum at MWCNT- and C <sub>60</sub> -modified WEs . . . . .	84
4.10	APAP interference study CV at PGE . . . . .	85



4.11 DPV PGE 3H PBS (10 mM, pH:7.4) . . . . .	86
4.12 DPV PGE 3H PBS (10 mM, pH:2.5) . . . . .	87
4.13 Interference study at different PBS pH conditions (7.4 and 2.5): DPV curves at PGE 3H in solutions containing APAP, propofol or a mix of the two drugs . . . . .	87
4.14 Interference study: CV comparison plots for midazolam detection in PBS (10 mM, pH: 2.5) at PGE 3H and C-SPE WEs . . . . .	88
4.15 CV interference analysis at C-SPE for midazolam detection in PBS pH 2.5 due to APAP and propofol drugs . . . . .	88
4.16 CV SPE midazolam calibration lines interference APAP and Propofol PBS (10 mM, pH: 2.5) . . . . .	89
5.1 Sketch of the <i>Raspberry Pi</i> (RPI)-based overall system . . . . .	94
5.2 Architecture of the RPi-based electronics . . . . .	94
5.3 Potentiostat interfaced with three SPE-based electrochemical cells . . . . .	96
5.4 Schematic of the electronic front-end for multi-panel drug monitoring . . . . .	97
5.5 First version PCB front-end for drug monitoring . . . . .	98
5.6 Different read-out transimpedance topologies being tested . . . . .	98
5.7 CV plots from first-version electronic platform . . . . .	99
5.8 Igor Pro low-pass FIR filter design window . . . . .	100
5.9 Signal noise comparison of the fixed gain and the programmable gain read-out circuits . . . . .	101
5.10 Noise evaluation and comparison at first and second stages of programmable gain read-out circuit at different DPOT gains . . . . .	101
5.11 Noise propagation schematic for mixed-signal design . . . . .	102
5.12 Grounding practice in mixed-signal on a single PCB . . . . .	103
5.13 Layout of the second version custom-built potentiostat in <i>star ground configuration</i> . . . . .	104
5.14 Screen-shot of the schematic details with the Atmel XMEGA micro-controller . . . . .	104
5.15 Final schematic of the custom-built potentiostat . . . . .	106
5.16 Sketch of the overall system including pH and T measurement module . . . . .	108
5.17 Schematic of the pH and T sensing module . . . . .	108
5.18 Process flows for pH-T calibration and drug monitoring . . . . .	109
5.19 Preliminary calibrations of the pH sensor at different T values . . . . .	111
5.20 Propofol calibrations at different pH and T conditions . . . . .	111
5.21 <i>Graphical User Interface</i> (GUI) implemented on RPi . . . . .	113
5.22 TCP/IP server on RPi . . . . .	113
5.23 System validation: CV, DPV and CA curves from custom-built potentiostat in comparison with commercial Autolab instrumentation . . . . .	118
5.24 System validation: CV, DPV and CA calibration curves from custom-built potentiostat in comparison with commercial Autolab instrumentation . . . . .	119
5.25 CV and DPV calibrations for propofol and APAP with custom-built potentiostat . . . . .	119

## List of Figures

---

5.26	Gaussian decomposition analysis on <i>Igor Pro 6.22</i> for propofol and APAP simultaneous detection . . . . .	120
5.27	Interference study for APAP and propofol . . . . .	121
5.28	Scan-rate analysis for propofol drug with CV and DPV techniques with custom-built potentiostat . . . . .	122
5.29	Scan-rate analysis for APAP drug with CV and DPV techniques with custom-built potentiostat . . . . .	122
6.1	Overall IoT bio-electronic system for on-line monitoring of anesthesia delivery	125
6.2	Smart-wearable unit sales prospective . . . . .	127
6.3	Smart-watch based IoT architecture . . . . .	129
6.4	Client Android app . . . . .	130
6.5	Server Android app and Smart-watch Android-Wear app . . . . .	131
6.6	Communication protocol between smart-watch app, intermediary server app and client app . . . . .	132
6.7	Cloud integration for anesthesia monitoring . . . . .	133
6.8	Different cloud-based tested architectures . . . . .	134
6.9	Data packet between RPi and Android app . . . . .	136
6.10	Main activities of the <i>AnControl</i> Android app for anesthesiologist . . . . .	137
6.11	WebApp cloud interfaces for patient and doctor . . . . .	137
6.12	Work-flows for patient-side and doctor-side to access the cloud . . . . .	138
6.13	Sketch of the <i>sensing platform</i> with the modular fluidic chambers . . . . .	140
6.14	Metrohm standard flow cell for SPEs . . . . .	141
6.15	Comsol fluidic chambers simulation results . . . . .	142
6.16	PDMS process flow . . . . .	143
6.17	Sandwich structure of the fluidic device . . . . .	143
6.18	Test of the fluidic chamber with dye . . . . .	143
6.19	CA measurements for fluidic characterization . . . . .	145
6.20	Propofol DPV calibrations in human serum under flow conditions . . . . .	147
6.21	Overall system validation: mixing test . . . . .	148
6.22	Overall system validation: in-time monitoring test . . . . .	149
6.23	Automatic flow-injection system set-up . . . . .	150
6.24	Communication protocols between RPi-syringe pump and RPi- <i>Matlab</i> . . . . .	151
6.25	Example of dose calculation and injection for the RPi-driven FIS . . . . .	152
6.26	FIS dye test . . . . .	153
6.27	FIS test in reproducing APAP time-trend . . . . .	154
7.1	Future work . . . . .	162
A.1	Micro-controller firmware work-flow . . . . .	163
A.2	Data packet adopted in the communication protocol from RPi to PCB . . . . .	164

# List of Tables

1.1	Table of correspondence: thesis chapters - publications . . . . .	15
3.1	PVC membrane composition . . . . .	48
3.2	CV and DPV procedures for BDD and PGE . . . . .	51
3.3	Comparison table for propofol sensing . . . . .	71
4.1	Sensitivity and LOD values for APAP and MZ detection in human serum at MWCNT- and C <sub>60</sub> -modified WEs . . . . .	83
4.2	Sensitivity values ( <i>S-interf-APAP</i> and <i>S-interf-Prop</i> ) from MZ calibration in solutions containing only midazolam and in presence of interferent compounds ( <i>interf1</i> is 50 $\mu$ M APAP and 19.6 $\mu$ M propofol, <i>interf2</i> is 100 $\mu$ M APAP and 80.5 $\mu$ M propofol). . . . .	90
4.3	Comparison table of MZ detection with literature . . . . .	91
4.4	Comparison table of APAP detection with literature . . . . .	92
5.1	LUT for propofol oxidation in human serum under different pH and T conditions	112
5.2	Electrochemical measurement parameters for APAP detection at C-SPE . . . . .	115
5.3	“Feasibility study” <i>Printed Circuit Board</i> (PCB) hardware parameters for APAP detection at C-SPE . . . . .	115
5.4	Electrochemical measurement parameters for propofol and APAP detection at PGE WE with the “feasibility study” PCB. . . . .	115
5.5	“Feasibility study” PCB hardware configuration for propofol and APAP detection at PGE WE. . . . .	116
5.6	Noise evaluation table for front-end PCB . . . . .	116
5.7	Comparison table for propofol detection using various electrochemical approaches . . . . .	123
6.1	Fluid parameters for <i>Comsol</i> simulations . . . . .	141
6.2	Fluidics flux velocities evaluation . . . . .	144
6.3	Electrochemical parameters for DPV, and CA measurements of APAP and Propofol	146
6.4	Comparison among different <i>Internet of Things</i> (IoT) solutions in health-care .	156
A.1	<i>Technique tag</i> table . . . . .	165
A.2	<i>Electrode index</i> table . . . . .	165



# 1 Introduction

In recent years, studies have been made of how personal variability in response to drugs is determined by genetic factors, and influenced by habits, age, health status, environmental exposures, and concomitant therapies [2]. These factors make highly challenging to the identification of an effective and personalized drug dosage for optimizing the outcome of a given therapy by limiting side-effects [3]. Therefore, the new paradigm in personalized drug therapy aims to administer “the right drug, with the right dose at the right time to the right patient” to avoid lack of response or toxicity effects [4]. This is extremely valuable especially in the practice of anesthesia, where several potent anesthetic compounds characterized by a fast action are delivered to the patient within a relatively short time-period. These drugs would lead to severe side effects if administered without paying maximum attention to dose balance, delivery time and administration order [1]. According to the *National Coordinating Council for Medication Error Reporting and Prevention* (NCCMERP) categorization, the higher incidences (%) of errors in anesthesia practices are due to a wrong choice of drug or an

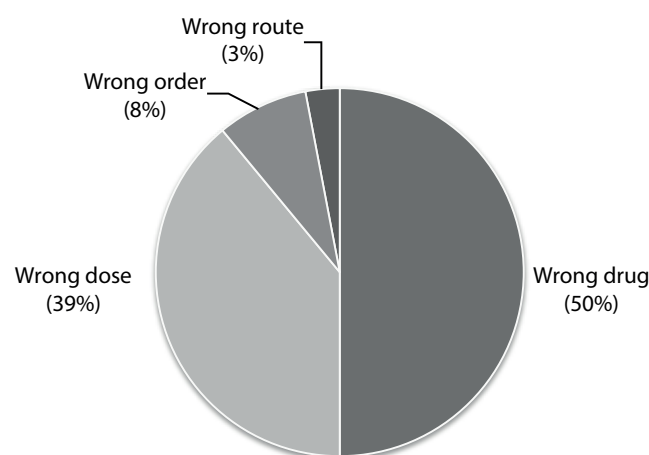


Figure 1.1 – Classification of drug administration errors in anesthesia malpractice cases according to the NCCMERP taxonomy (reprinted from [1]).

incorrect dosage, as shown in Fig. 1.1. To reduce these occurrences of malpractice, *Therapeutic Drug Monitoring* (TDM) systems are key concept that has to be introduced to tune the drugs delivery according to each patient's metabolic response [5]. The main function of a TDM system is to measure the actual concentration of each infused drug in a patient's veins, to provide the medical doctor with the real value of the individual metabolic response and treatment effect in real time. These TDM systems can be made even more effective if supported by the new paradigms of *Information and Communications Technologies* (ICT) [6]. In this context, the *Internet of Things* (IoT) concept, according to which **any device** able to access the Internet can be interconnected in a network for an easy exchange of data from **any place** and at **any time**, is gaining popularity also in medical applications [7]. Medical IoT solutions are paving the way towards the realization of "Smart Hospitals", where an optimized quality care of the patients with a more personalized approach, and a reduction of medical errors, are [8]. In the scenario of general anesthesia, medical IoT solutions would provide the anesthesiologist with a powerful tool to remain always connected with all the anesthetized patients under his/her supervision. Nowadays, in fact, the anesthesiologists oversee more than one operating room at once. Therefore, an IoT equipment for medical applications, which is able to make accessible the measured data of each patient from any hospital areas at any time, would guarantee a safer and reliable anesthesia. Moreover, the remote monitoring of data through cloud solutions, would also lead to the realization of telemedicine networks.

The next section will provide a broad introduction to general anesthesia medical practice and will describe the actual state-of-the-art of current technologies for DOA monitoring.

### 1.1 General Anesthesia (GA)

Nowadays, we refer to the term *anaesthesia* (from Greek "an"-, "not" and "aísthēsis", "sensation") as temporary and reversible state of unconsciousness characterized by loss of sensation, which is induced before undergoing some medical practices, such as surgery, to make the patient unresponsive to external stimuli [9]. This state is characterized by three periods: (i) induction, (ii) maintenance and (iii) emergence. During the anesthesia induction the patient is put to sleep, and he is maintained asleep for all the time of the surgery. At the end of the medical intervention, the patient is woken up, emerging from the sedation. Three different anesthesia categories are available [10]:

- *General Anesthesia* (GA) suppresses the activities of the *Central Nervous System* (CNS) leading to a totally unconscious state. The person can be induced to the anesthetized state by intravenous (IV) administration of by inhalation of gases.
- *Sedation* has a weaker suppression of the CNS activities, resulting in an inhibition of anxiety and of long-term reminiscences formation. The patient is put in an undisturbed and lethargic state.
- *Local or Regional Anesthesia* causes loss of sensation in a desired part of the body part

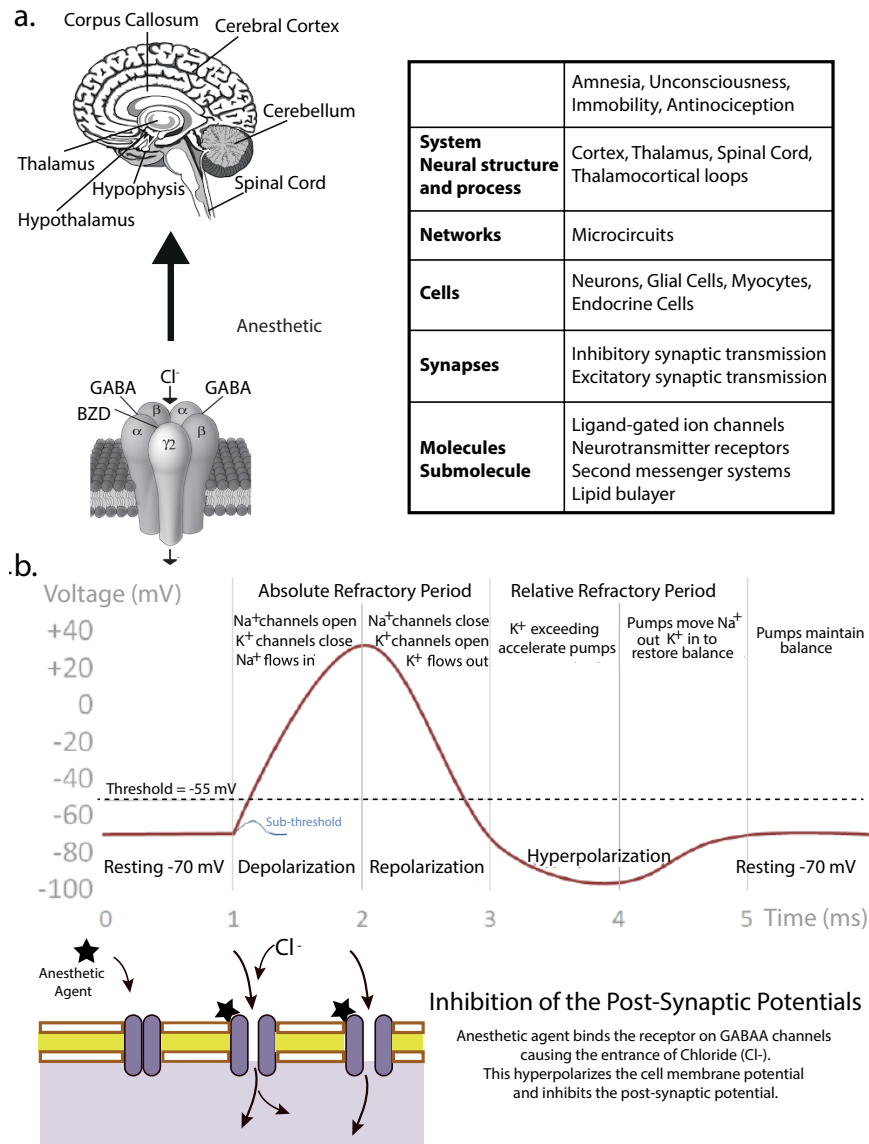


Figure 1.2 – a) Anesthetic sites of action at different levels of biological organization, b) hypnotic action on action potential due to inhibition of the Cl<sup>-</sup> channels (inspired by [11, 12, 13]).

by blocking the nerve impulses between the desired area and the spinal cord. It can block peripheral nerves, nerve plexus or central neuraxial areas (*e.g.* spinal or epidural). During this practice the patient remains fully conscious.

In this thesis only GA by IV administration will be considered. We will describe the design, realization and validation of a TDM system for the continuous monitoring of IV anesthetics over time.

### 1.1.1 Cocktail of drugs

During GA a cocktail of anesthetic compounds with different synergistic actions is administered [14]. It normally consists of a hypnotic, such as propofol, an analgesic, such as fentanyl (opioid) or paracetamol, and a muscle relaxant, such as midazolam. This cocktail of three agents is referred as the "triad of anesthesia" [9]. It is of vital importance to reach a correct balance of the "triad" to reach the desired levels of sedation with reduced side-effects. The choice of each component depends on the kind of surgical operation and on the characteristics of the patient. The anesthetic compounds have an action on the entire hierarchy of the biological organization, from cellular level where they alter the activity of neurons by interacting with ion channels, to an organism's behavior, as summarized in Fig. 1.2.a [13, 15].

Propofol (2,6-diisopropylphenol) is a highly lipophilic hypnotic agent normally administered to induce and maintain anesthesia [16]. It ensures a fast onset and a short predictable time of effect [17]. It produces its hypnotic action by an augmentation of the inhibitory function of the synaptic transmission binding with the receptors of the *gamma-amino-butyric acid type A* ( $GABA_A$ ) chloride channels. Fig. 1.2.b describes the process of this inhibition due to the activation of the  $Cl^-$  channels.  $GABA_A$  are involved in the regulation of anxiety, vigilance, memory, and muscle tension and are the most abundant fast inhibitory neurotransmitter receptors in the CNS [13]. Hence, they have an important role in the regulation of several neuronal structures, including the hippocampus, thalamus, spinal cord, and cortex [18, 19, 20].

Midazolam is an imidazobenzodiazepines highly preferred to other benzodiazepines because of its short-acting time and fast metabolic clearance. It is available as midazolam Hydrochloride (HCl) salt insoluble in water. Only its acid formulation is soluble in water and highly lipid soluble in vivo [21]. In acidic conditions midazolam is present as an equilibrium mixture Fig. 1.3.a of its closed-ring and open-ring structures due to acid-catalysis of the diazepine ring. The percentage of open-ring form depends on the pH of the solution, as shown in Fig. 1.3.b [22]. From the graph, the best pH range ranges from 2.5 to 4.

It acts as a depressant of the CNS by increasing the  $GABA$  neurotransmitters inhibitory activities. Therefore, midazolam produces a calming effect, relaxing skeletal muscles, and inducing sleep. Also in this case, benzodiazepines bind to the benzodiazepine site on  $GABA_A$  receptors facilitating the entrance of chloride [23].

Acetaminophen, also known as *Paracetamol* (APAP) (N-acetyl-p-amino-phenol), is a largely used analgesic and antipyretic drug. It primarily acts at the CNS level with an increase of the pain threshold due to an inhibition of all the cyclooxygenase isoforms (COX-1, COX-2, and COX-3) that are involved in the synthesis of the prostaglandins (PGs) [24]. It can be administered intravenously to treat mild and moderate postoperative pain in place of opioids to avoid their adverse effects [25]. It can be administered to reduce the pain associated with propofol injection, referred as *Pain On Propofol Injection* (POPI), that still induces pain or discomfort in large percentage of patients (28% - 90%) [26].

Analgesic opioids, such as fentanyl, are narcotic analgesics administered in combination in the



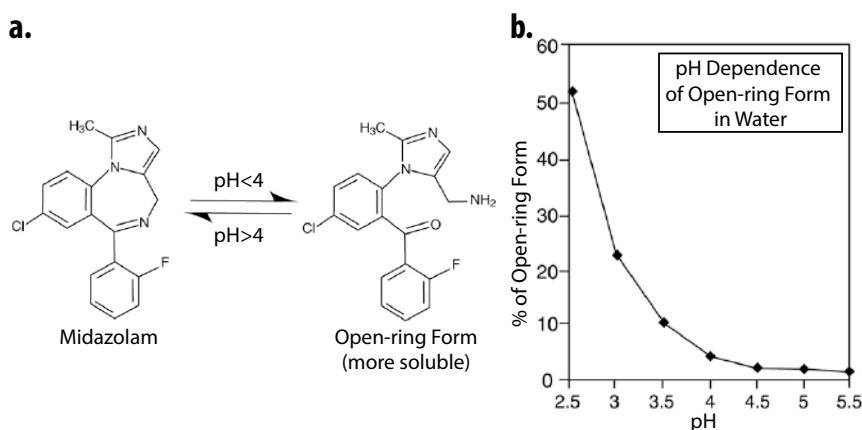


Figure 1.3 – a) Midazolam close- and open-ring structures equilibrium; b) Dependency graph between pH variations of the solution and % of open-ring form of midazolam structure (inspired by [22]).

anesthesia cocktail [27]. They combine with the opiate receptors on the G-protein modulating calcium and potassium ion channels on the G-protein complex. Following *guanosin-trifosfato* (GTP) to *guanosine diphosphate* (GDP) hydrolysis there is a channel deactivation of the inwardly rectifying potassium channel. Further, the intracellular *cyclic AMP* (cAMP) is reduced since adenylate cyclase is inhibited. Therefore, the membrane results hypopolarized and neuronal excitability is reduced. The opioids' coupling with the receptors affecting potassium and calcium channels has been demonstrated in different neural structures, as in the hippocampus, locus coeruleus, and ventral tegmental area to the dorsal root ganglia [28]. Fentanyl, an example of opioid, has an effect that is a hundred times stronger than a dose of morphine. Due to its potent action it may lead to serious side-effects and its therapeutic blood concentration has to remain very low (0.6 to 3 ng/ml) [29].

### 1.1.2 Pharmacokinetics (PK) and Pharmacodynamics (PD)

After the administration of a drug, metabolic processes occur before the drug reaches the target site. This drug-body interaction process is the object of study of the *Pharmacokinetics* (PK) and it can be sub-divided into four distinct phases, known as **ADME**: **A**bsorption, **D**istribution, **M**etabolism and **E**xcretion of the drug. The PK principles are fundamental to dosing the drug in an effective and safe manner enhancing its therapeutic effects and decreasing its toxicity. Once the drug has reached its target site, the attention goes to the *Pharmacodynamics* (PD) of the drugs that describes the relation between its concentration and the out-coming effects. The full PK/PD process is schematized in Fig. 1.4.

Fig. 1.5.a depicts a time trend of a typical plasma concentration of an administered drug. From the curve, some typical and crucial PK parameters can be extracted. As first, we can identify the *Minimum Effective Concentration* (MEC) and the *Maximum Tolerated Concentration*

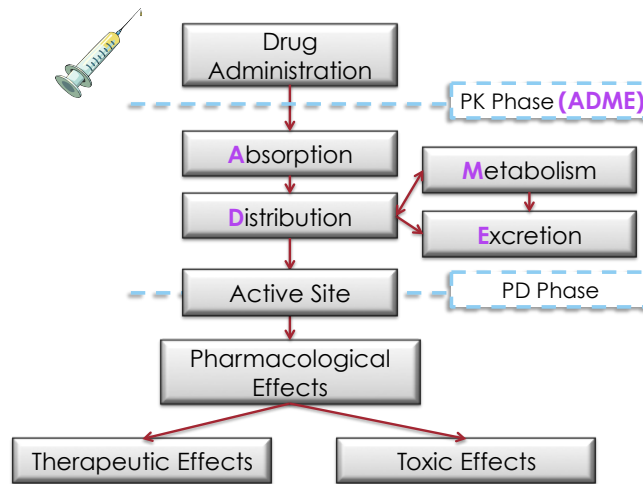


Figure 1.4 – *PharmacoKinetic/PharmacoDinamic* (PK/PD) metabolic pathway of an administered drug.

(MTC), which are very important in defining the therapeutic range of the drug [30]. If the drug concentration is maintained within its therapeutic range, its effects will be beneficial. Below the MEC threshold, the drug will probably not manifest its therapeutic benefits. On the contrary, if the drug concentration overcomes the MTC threshold, toxic effects may arise [31]. Following this, by intersecting the MEC threshold with the time-trend, we can identify the *onset time* when the drug action starts to be effective. The *duration of action* of the drugs corresponds to the time between the *onset time* and the time when the trend declines back to MEC.  $C_{max}$  is the highest obtained concentration obtained after a time  $t_{max}$ . It is strictly related to the rate of the drug absorption. Finally, the *Area Under the Curve* (AUC) depends on the drug absorption and indicates the overall action of the drug [30]. The PK model of a drug is extremely important in identifying the correct and personalized dosage administration to achieve a desired therapeutic effect.

As PD model the Hill equation [32], also known as " $E_{max}$  model", is recognized as the best adapted to describe the relationship between concentration and reversible drug effects. It is based on the assumption that the plasma drug concentration quickly reaches the equilibrium with respect to the effect site. It has been deduced by empirical observation of the dependency between the drug effect (E) and its concentration (C), and it follows this formula:

$$E = E_0 \pm \frac{E_{max} \cdot C}{EC_{50} + C} \quad (1.1)$$

Where  $E_{max}$  is the maximum effect obtained by the drug,  $EC_{50}$  is the drug concentration that results in half of the maximum effect and  $E_0$  is a baseline effect when applicable. These parameters are visible in Fig. 1.5.b where the drug effect is plotted versus the logarithm of the drug concentration.  $E_{max}$  is the plateau reached at high concentrations;  $EC_{50}$  is evaluated as  $0.5 \cdot E_{max}$  [33]. In PK context it is possible to define two important properties of the drug: the

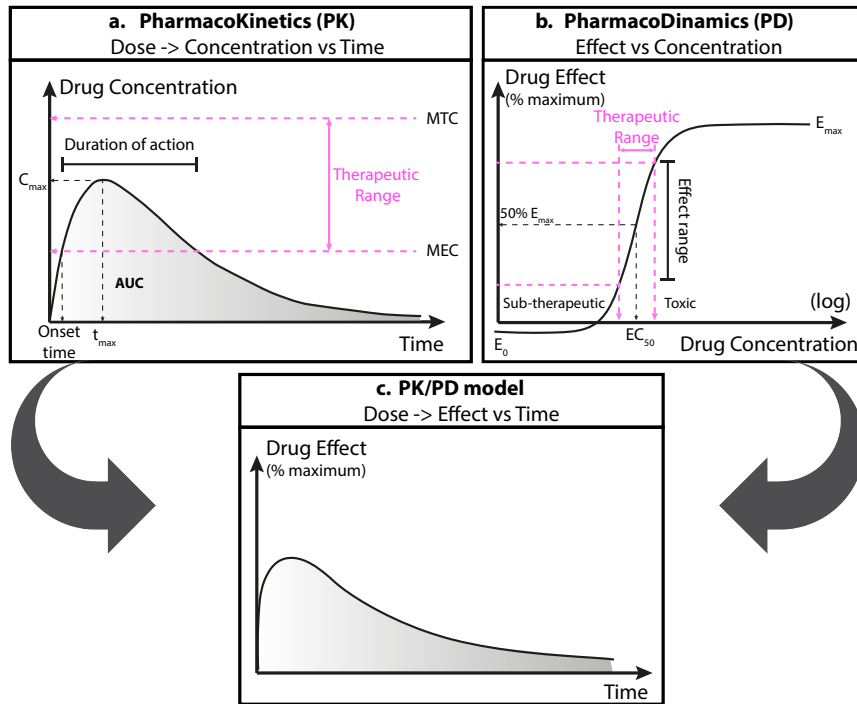


Figure 1.5 – PK/PD model (c.) combines the PK model (a.) describing "what the body does to the drug" (ADME) and the PD model (b.) defining "what the drug does to the body"; hence the effects.

*Volume of Distribution* (DL) and the *Clearance* (Cl) of a drug. The VD refers to the apparent volume into which the drug is distributed with respect to the administered dose and the plasma concentration subsequently observed [34]. The Cl is defined as the sum of the different drug elimination processes and it is calculated as the volume of plasma completely cleared from the drug per unit time (*i.e.* ml/min). Main eliminated pathways are through kidneys and liver (occasionally also lungs). By knowing these drug properties and the desired plasma concentration ( $C_p$  in mg/ml), it is possible to calculate the required dose ( $D_{required}$  in mg) as:

$$D_{required} = C_p \cdot I \cdot \frac{Cl}{f} \quad (1.2)$$

Where I is the interval between two subsequent doses (min) and f is the fraction of the dose that enters into the systemic circulation [35].

The PD model aims to define the drug- and system-specific properties that regulate the biological responses to drugs, meaning the therapeutic effects and not the toxic adverse reactions. Combined PK/PD models quantitatively describe the relationship between dose, exposure and response by integrating the PK time-trend of the concentration dosage regime with the PD observed response, occurring at variable drug plasma concentrations. Therefore, PK/PD models represent the time-course and the intensity of beneficial and/or non-beneficial

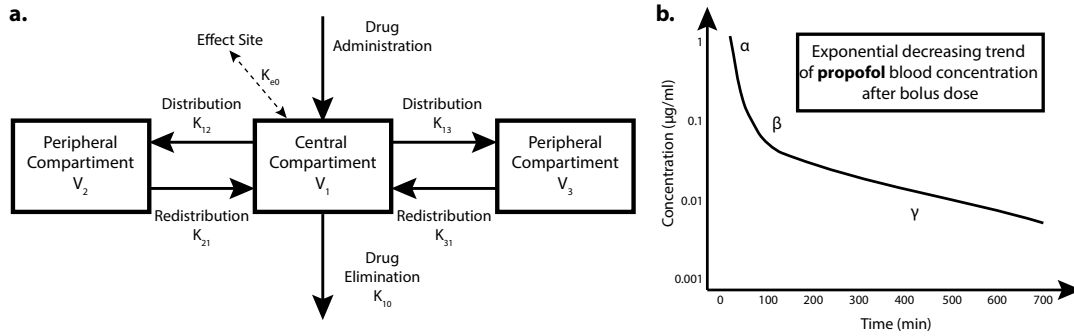


Figure 1.6 – a) Three-compartment model with the different compartments and their distribution, redistribution and elimination rate constants. b) Time trend of the blood concentration after bolus dose of propofol, considered as model drug.

effects resulting from a certain drug dose [33].

### 1.1.3 Three-compartment model

The PK observations after a drug dose administration can be theoretically described and simplified by modeling the in-vivo behavior of the drug through a compartmental model [36]. Three-compartment models, as in Fig. 1.6.a, are normally considered to describe anesthetic compounds [37].

In the case of anesthesia, the drug is intravenously administered in the central compartment (principally plasma) characterized by a volume  $V_1$  and it is then distributed into two compartments, with volumes  $V_2$  and  $V_3$ , respectively. One corresponds to well-perfused tissues, such as muscles, and the other to areas with slower perfusion, like fatty tissues [36].  $k_{12}$  and  $k_{13}$  are the distribution rate constants between compartment 1 and compartment 2 and between compartment 1 and compartment 3, respectively;  $k_{10}$  is the distribution rate from the central compartment [35]. The distribution volumes ( $V_i$  and  $V_j$ ) and the rate constants  $k_{ij}$  and  $k_{ji}$  are linked to each other according to this formula [38]:

$$V_i = \frac{k_{ij}}{k_{ji}} \times V_j \quad \text{with } i > j \quad (1.3)$$

The drug diffuses from plasma to brain (target site) following an exponential trend characterized by a first-order rate  $k_{e0}$ ; hence, there is a lag between the blood and effect site concentration [36]. The dimensions of the compartments and the inter-compartmental rates come from the properties of the administered drug (e.g. lipid solubility and patient factors) [37]. The typical decline time-trend of the plasma concentration obtained for an intravenous bolus administration is a descending exponential, as represented in Fig. 1.6.b. After the bolus administration, there is a first sharp reduction ( $\alpha$ ) of the concentration due to tissue with rapid redistribution, followed by a second concentration reduction ( $\beta$ ) due to the slower tissues and

---

## 1.2. Current state-of-the-art of *Total Intra-Venous Anesthesia* (TIVA)

then a third concentration reduction ( $\gamma$ ) mainly due to elimination. It is possible to deduce the actual concentration ( $C_p$ ) at the time  $t$  by this equation [35]:

$$C_p = G \cdot e^{-\gamma t} + A \cdot e^{-\alpha t} + B \cdot e^{-\beta t} \quad (1.4)$$

## 1.2 Current state-of-the-art of *Total Intra-Venous Anesthesia* (TIVA)

*Total Intra-Venous Anesthesia* (TIVA) is a method for inducing GA with a combination of anesthetic agents administered through an intravenous route. The first form of intravenous infusion was reported in the seventeenth century when Christopher Wren created a syringe from pig bladder fixed on a goose quill to inject opium into the veins of a dog (1650s). Afterwards, Johann Daniel Major from Kiel and Johann Sigismund Elsholtz from Berlin were the first to practice intravenous injections on people (1660s). Nevertheless, these experimental injections were not successful and only in the 1800s did this kind of drug administration begin to be popular. It has been continuously improved up until modern times [39].

### 1.2.1 TCI pump: principles and limitations

Nowadays, the increase in popularity of TIVA is related with two main factors: first, the improvement of PK/PD models for the most largely adopted IV drugs, such as propofol; secondly, the advances in new infusion pump technologies that implement mathematical algorithms to evaluate the dosage regime, such as TCI pumps [40]. The software of the TCI pump incorporates the PK model of the infused drug and drives the syringe pumps accordingly. By solving the complex equations coming from drug distribution in the compartments it allows dynamic drug-dosage adjustments to achieve and maintain a certain level of sedation in the patient [41]. The TCI follows the *Bolus - Elimination - Transfer* (BET) principle to approximate the plasma level of the drug. According to this principle, to achieve a desired drug concentration at the target site, a loading bolus dose is given to completely fill the central volume  $V_1$ . The subsequent infusion regime then compensates the rapid and the slow diffusions ( $k_{12}$  and  $k_{13}$ ) of drug into the peripheral compartments ( $V_2$  and  $V_3$ ) and the drug elimination rate ( $K_{10}$ ). The loading dose ( $D_{loading}$ ) is calculated as  $D_{loading} = C_p \cdot V_1$ ; where  $V_1$  is the initial volume of distribution (central compartment) and  $C_p$  is the desired concentration for clinical effect. The infusion rate after the bolus injection helps in maintaining a steady state plasma concentration of the drug [42]. The TCI system estimates the initial bolus dose and calculates the speed of subsequent infusion every 10 s to adjust the rate to reach and maintain the desired  $C_p$ . As soon as the target  $C_p$  decreases, the infusion is arrested until the plasma concentration reaches the indicated value and is then restarted with a lower rate [36].

The PK/PD model for propofol administration has been one of the most studied the implementation in the TCI pump. Two propofol models are implemented in the actual TCI systems: the Marsh and the Schnider. The Marsh model fixes all the rate constants, and evaluates the

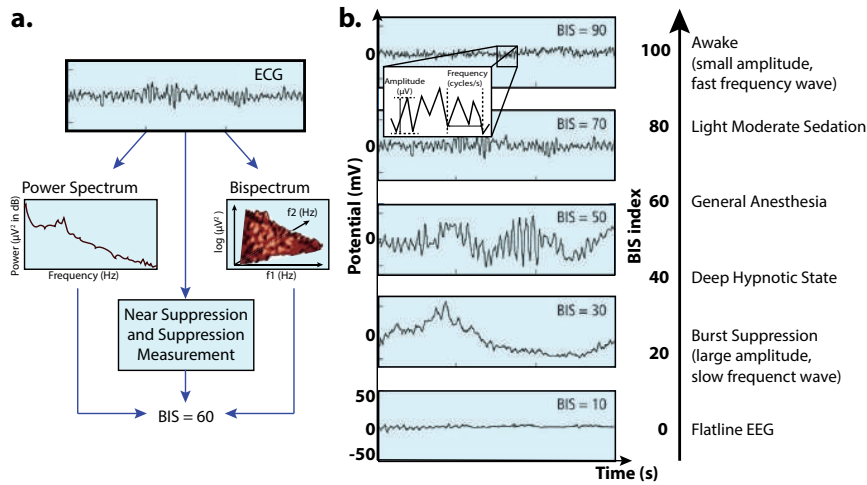


Figure 1.7 – The *bispectral index* is scaled to correlate with important clinical end points during the administration of an anesthetic agent (inspired by [45]).

compartment volumes and clearances depending on the patient's weight. The Schnider model fixes values for  $V_1$ ,  $V_3$ ,  $k_{13}$ , and  $k_{31}$ , while it adjusts the values of  $V_2$ ,  $k_{12}$ , and  $k_{21}$  according to the patient's age, and of  $k_{10}$  considering the patient's total weight, lean body mass (LBM), and height [43]. Up to now, no evidence has yet been provided to favour the use of one model over the other. The principal difference between the two methods concern the volume  $V_1$  that is set to 19.4 l and 4.27 l for Marsh and Schnider, respectively for a patient of 85 kg. Therefore, depending on the operation mode of the TCI pump one is more suitable than the other. In plasma targeting mode, where the user selects the target plasma drug concentration  $C_p$ , since the Schnider central volume is smaller than the Marsh one, lower doses of propofol are required to achieve the desired  $C_p$ . This bolus dose is often insufficient, leading to inadequate clinical effects. On the contrary, if the TCI works in effect-site targeting mode, where the user sets the desired drug concentration at the effect site, the Schnider model is recommended as larger bolus doses are infused compared to the Marsh model [36].

Even if these TCI system are now commercially available and widely used to administer anesthesia, there are still important limitations to keep into account. The PK/PD models implemented on the TCI pump have been developed starting from the observations of the drug effects on a population that did not cover all individuals. Therefore, they cannot reproduce the inter-patient variabilities in metabolism. Furthermore, no reliable technique for monitoring drug plasma concentration during TIVA has been presented yet [44].

### 1.2.2 Bispectral Index (BIS) monitoring: use and limitations

One of the main challenges in TIVA practices is the monitoring of the *Depth of Anesthesia* (DOA) in the patient. By providing an accurate evaluation of the DOA it would be possible to tune the drug administration according to the individual response. In this way, over- and under-dosing

## 1.2. Current state-of-the-art of *Total Intra-Venous Anesthesia* (TIVA)

---

would be avoided and side effects minimized. The need for monitoring anesthesia depth has led to the creation of a system based on *ElectroEncephaloGram* (EEG) or *Acoustic Evoked Potentials* (AEP) signals [46]. As stated above in *Section 1.1.1*, the large majority of anesthetics (e.g., propofol, paracetamol and midazolam) have an inhibitory effect on the  $GABA_A$  receptors in the brain, leading to a progressive diminution of the EEG activity with increasing drug concentrations [47].

AEP is evaluated by providing the patient with an auditory stimulus and by calculating the average of the EEG periods immediately after the stimulus, hence considering the evoked auditory potential. Normally, to measure the DOA, an intermediate latency AEP of 40 ms - 60 ms after stimulation is considered; it corresponds to the neural activity within the thalamus and primary auditory cortex [46]. Compared to the raw EEG, AEP is a less sensitive method [47].

Since the measured EEG waveforms are hard to be interpreted, some analyses have been introduced to reduce the data into a single number [48]. One of the most widely used indices for DOA monitoring in Europe is the *BiSpectral Index* (BIS), as introduced in 1992 by Aspect Medical Systems. It is statistically evaluated combining the contribution of key EEG signal features (bispectral analysis and others) recorded every 15-30 s [47]. The four EEG features that are taken into account for BIS extraction are: (i) the degree of high-frequency (14 to 30 Hz) activation, (ii) the amount of low-frequency synchronization, (iii) the presence of almost suppressed periods, and (iv) the presence of fully suppressed periods (*i.e.*, flat-line). The algorithm is represented in Fig. 1.7.a [45]. The BIS index ranges between 0 and 100, as shown in Fig. 1.7.b: if near 100 the patient is awake, while if 0 the EEG signal is iso-electric. To perform sedation, the BIS is maintained over the value 70 ( $> 70$ ) to noticeably decrease the memory functions, but with probable risk of consciousness [49].

To ensure efficient hypnosis during GA, the BIS values has to be kept between 45 and 60. Lower values than 40 show an high impact of the anesthetic on the EEG. If very low BIS values are reached, the risk for iso-electric EEG signals increases [45].

Even though BIS monitoring is a widely used DOA monitoring tool, which helps the anesthesiologist in regulation of the anesthesia dosage in induction, maintenance and emergence phases, there are some crucial limitations that have to be mentioned and considered.

First of all, the evaluation of the BIS value is not instantaneous with respect to the clinical status variations of the patient. The latency linked with the BIS value evaluation limits the efficacy of the monitoring.

In addition, also the placement and adherence of the EEG electrodes affect the BIS measure. Moreover, the BIS can be affected by artifacts due solely to interference from other electrical devices [50]. Finally, differences in a patient's age and administered anesthetics modify the range of BIS values [51].

According to recent studies [52, 53], EEG signal can be complemented by *Near-InfraRed Spectroscopy* (NIRS) hemodynamic signals that optically measure the variations in *Cerebral Blood Flow* (CBF), related with the DOA. Nevertheless, even if extremely promising, a combined monitoring of EEG and NIRS during anesthesia has been not reported yet. This is due to the

wide different dynamic ranges of the NIRS signal (10 pA - 10 nA), and because the variabilities due to diverse patients and/or to environmental conditions are not controllable [52].

As a conclusion of these drawbacks, the BIS has to be considered as additional datum to evaluate DOA and has to be interpreted in the context of other clinical data and monitors [45].

### 1.2.3 Anesthesia side effects and risks

One of the main advantages of performing TIVA/TCI practices is the reduction of *Post-Operative Nausea and Vomiting* (PONV) effects facilitating the GA recovery. To be able to provide these GA benefits, it is imperative to guarantee a dynamically balanced and personalized dosage of the administered "anesthetic triad". In fact, there is a large variability in the metabolism of a patient population: some have faster metabolisms, others slower. To achieve the same state of sedation, the former will need a larger dose of drugs, the latter a lower dose (Fig. 1.5).

However, there is still no mature monitoring system providing the doctor with the actual anesthetics concentrations in patient's plasma. As a consequence, a major concern is that the patient may suffer from undetected awareness [54]. The reported incidence of *Accidental Awareness under General Anesthesia* (AAGA) during TIVA varies between 0 and 1.1%—potentially a higher incidence than during volatile anesthesia [55]. AAGA consequences include psychological symptoms and *Post-Traumatic Stress Disorder* (PTSD) [56].

While AAGA is an undesired effect of the under-dosage of the anesthetic compounds, overdosing must also be prevented to avoid serious GA complications. These range from PONV common effects to critical ones like brain damage and death which are, luckily, extremely rare. The risk of death has been reported to be approximately 0.001% for the *American Society of Anesthesiologists* (ASA) evaluated for healthy or with moderate systemic disease patients. The risk increases with more critical patients' health status [57].

In the light of this, a continuous measurement of the anesthetic concentrations should be taken to prevent an incorrect GA dosage.

## 1.3 Research contributions and thesis outline

Nowadays, as described in Chapter 1, the anesthesia IV infusion is achieved by the use of TCI pumps. TCI software implements PK/PD mathematical models for each administered drug to predict and adjust the dose rate on the basis of some physical characteristics of the patient, such as age, gender *etc.*. However, these mathematical models are affected by inaccuracy due to inter- and intra-patients' variability [58] and due to the impossibility of predicting the direct relationship between kinetics and the clinical effects of the drug [59]. Therefore, monitoring tools are needed to keep the DOA of the patient under control. Among these monitoring tools, the BIS, evaluated from the EEG signal, is most frequently used in



### 1.3. Research contributions and thesis outline

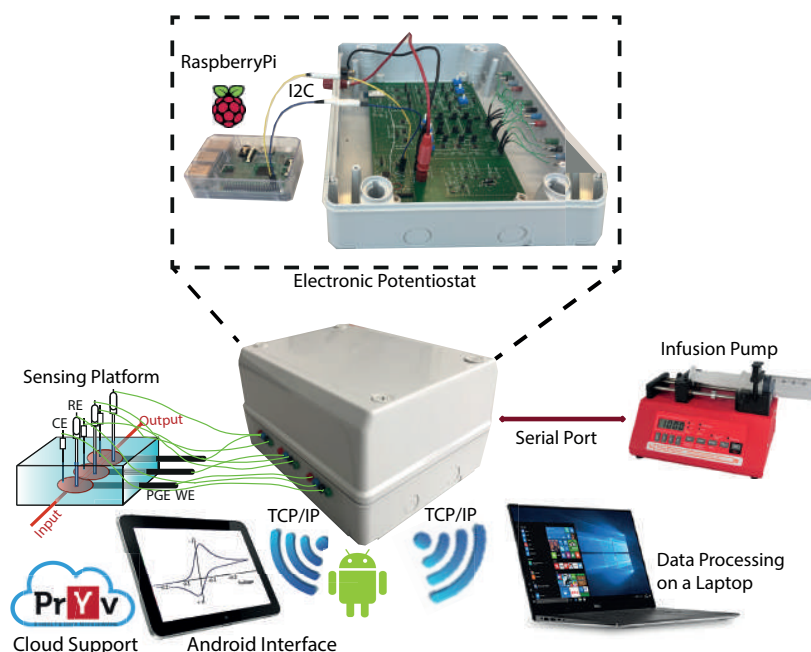


Figure 1.8 – Schematic representation of the system we want to perform for the monitoring of anesthesia. The figure can be seen as a sort of visual index of the thesis.

actual practices. Nevertheless, this index is evaluated in an indirect manner, hence, it can be affected by external factors and is influenced by a delay with respect to variations in drug concentration [60, 61]. The limitations of the actual technologies for anesthesia practices have been described in Section 1.2.1. The introduction of TDM systems being able to continuously provide a real measurement of the drug concentration in the patient would overcome the restrictions of the actual anesthesia delivery devices. The yield and efficiency of the infusion TCI pumps would be highly improved by the integration of such TDMs as are able to correct the mathematical models with real measurements, hence, guaranteeing a safer and more personalized infusion rate. The objective of this thesis is the design, the realization and the validation of a complete IoT system for the continuous monitoring of anesthetic compounds over time.

A sketch of the overall system is depicted in Fig. 1.8 and consists of: (1) a central low-noise, **custom-built electronic potentiostat driven by a RPi** that from one side interfaces with (2) an **electrochemical multi-sensing platform** integrated into (3) a **fluidic device** for directing the sample towards the sensing sites, while from the other side it drives (4) an **infusion pump** to withdraw the anesthetic drugs based on the output of (5) a *Matlab* software running on **laptop for data processing and drug concentration estimation**. Finally, the system is enriched by (6) an **IoT cloud-based network developed in Android** to keeping the doctor and the anesthetized subject constantly connected, offering a continuous on-line and remote sharing and visualization of the measured data.

The development of these systems has to keep in consideration several requirements. From

## Chapter 1. Introduction

---

one side, the sensing part must guarantee high sensitivity and selectivity for the detection of several different anesthetics at the same time, and it must be robust to resist deterioration over time. In fact, a normal anesthesia lasts for up to several hours. On the other side, the electronic part has to guarantee good performance in terms of easy integration with the sensors, and in terms of noise rejection.

Concerning the presented state-of-the-art, this thesis presents innovative contributions on:

- **Multiple drug detection over time** The long-time monitoring of several anesthetic compounds at the same time has been achieved by developing optimized electrochemical sensors from the point of view of high sensitivity and fouling resistance, and by using appropriate techniques of analysis. Ready-to-use electrochemical sensors have been proposed to facilitate the measurement procedure, while maintaining effective on-line monitoring performance.
- **Monitoring of different parameters** In addition to the sensors for monitoring anesthetic compounds, further sensors have been included in the developed system to measure pH and temperature parameters in parallel. Combining electrochemical sensors with pH and temperature measures is an advantageous strategy, optimizing performance in different physiological conditions, since these two parameters affect the electrochemical behavior of drugs.
- **Multi-channel portable potentiostat** We created a low-noise, powerful and portable custom-built potentiostat by exploiting the RPi computer. The RPi plays a central role in the system architecture being able to: (i) drive several electrochemical measurements in parallel for drugs detection, (ii) control the pH and T module, (iii) communicate with the Android-based IoT network and (iv) with the syringe pump. We proved the high quality performance of our portable multi-channel electronic system by referring to the bulky, commercially available Autolab potentiostat by Metrohm as control.
- **Medical IoT network** We realized “smart” solutions to provide a compelling tool to be adopted in hospital monitoring scenarios, such as in anesthesia. The data measured by our TDM system are sent by the RPi to an Android-based app running on smart-devices of the anesthesiologist, such as a tablet, a smart-phone or a smart-watch. Through the application we developed the medical doctor can require specific parameters or receive alerts of critical conditions registered by one or more of the sedated patients connected to the IoT network.
- **System integration and characterization** We integrated the different parts of the system and we proved that our system was able to successfully monitor multiple anesthetics' concentrations over time in complex biofluids, such as undiluted human serum.

Following the *Introduction*, this thesis is organized in the following way.

*Chapter 2* provides an overview of the theoretical background at the basis of this thesis. In particular, general anesthesia practices will be described in detail and limitations will be

### 1.3. Research contributions and thesis outline

---

highlighted. Afterwards, electro-chemistry and electronics notions will be provided together with important aspects of Android development for IoT.

*Chapter 3* presents the design, characterization and validation of the optimum electrochemical sensor for propofol detection in terms of sensitivity and resistance to undesired fouling, over time. We demonstrated the continuous long-time monitoring of the drug for more than 4 hours and, in human serum, in presence of its main interferent compound, *e.g.* APAP.

*Chapter 4* shows the implementation and the validation of the electrochemical sensors for the other two main anesthetic compounds of the cocktail, such as APAP and *Midazolam* (MZ). The performances of different carbon nano-allotropes have been compared with respect to the sensing properties of these two compounds in their pharmaceutical range.

*Chapter 5* describes the process for the realization and validation of a custom-built portable electronic platform for the simultaneous monitoring of several compounds at the same time, together with pH and temperature. To this aim, the platform has been designed with three independent channels and a pH-T module all driven by a RPi unit. The data are made available to external devices by exploiting Wi-Fi technology. The optimization process was focused on improving the board performances in terms of interfacing with electrochemical sensors and noise reduction.

*Chapter 6* reports on the integration of the different parts of the overall system, together with the realization of the IoT network and the fluidic device to drive the sample directly on the sensing sites. The complete system has been validated by proving the simultaneous monitoring of the concentration trends over time of two main anesthetics, *e.g.* APAP and propofol, in human serum.

Finally, *Chapter 7* sums up with the conclusions and presents possible future improvements of the system.

The work described in these chapters follows several publications obtained within this thesis. Therefore, the text and images in the chapters are often extracted from my published papers. The Table 1.1 makes a correspondence between the various parts of this thesis with the related citations.

Table 1.1 – Table of correspondence between the thesis chapters and my published works.

Chapter	Section	Ref.
3	3.1, 3.3	[62]
	3.4	[63]
4	-	[64]
5	5.1, 5.4	[65] and [66]
	5.2	[67]
	6.2	[68] and [69]
6	6.1, 6.3, 6.4	[70]
	6.5	[71]



## 2 Background

### 2.1 Drug monitoring with electrochemical sensors

Personalized drug dosage is crucial to optimizing benefits in patients' treatments. TDM is the clinical practice of measuring the drug concentration in patient's bloodstream at certain time-intervals and then correlating it to maintain the drug concentrations constant within a targeted therapeutic range, thereby optimizing individual dosage regimens [72]. TDM systems are of vital importance especially for drugs with narrow therapeutic ranges, drugs with marked PK variability, medications for which target concentrations are difficult to monitor, and drugs known to cause therapeutic and adverse effects [73]. This is the case of anesthesia practices where a cocktail of three difficult-to-handle drugs are infused in a patient's veins.

A reliable sensing platform is needed to develop a TDM system. To this end, electrochemical sensors are considered as ideal devices due to their high sensitivity and specificity, small dimensions and portability, low costs and simplicity, which allow an accurate, rapid and quantitative detection of drugs [74] and an easy integration within electronic platforms and read out circuits. The monitoring system we have designed and implemented integrates electrochemical sensors for simultaneously detecting the three main anesthetic compounds: the hypnotic, propofol; the analgesic, paracetamol and the muscle relaxant, midazolam. Hereafter, an overview of the adopted voltammetric techniques is provided.

#### 2.1.1 Electrochemical sensing techniques: an overview

Electrochemistry is the branch of chemistry which studies the interrelation between electrical and chemical effects. This includes chemical reactions caused by an exchange of electrons (current), and *vice-versa*, the production of electrical energy by chemical reactions [75]. These processes happen in an electrochemical cell which consists of an electronic conductor (an electrode) and an ionic conductor (an electrolyte) made by water-based or other solvents in which ions are solvated, *e.g.* human body fluids.

The typical electrochemical cell unit can be designed in two- or three-electrode configurations depending on the needs of the experiment. Fig.2.1 depicts the two different electrochemical

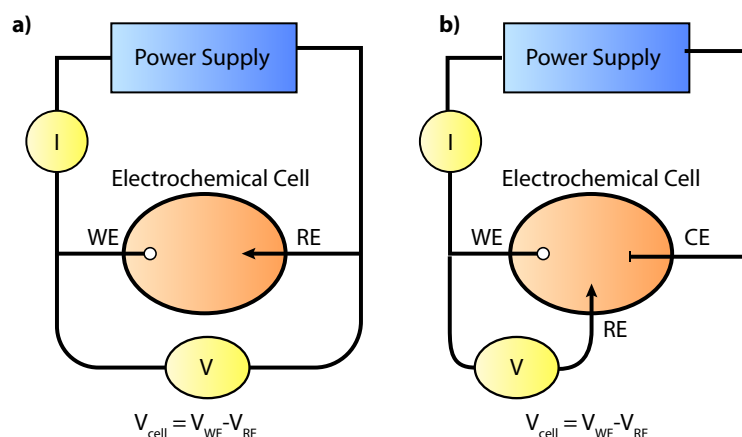


Figure 2.1 – Schematic representation of the a) two-electrode and b) three-electrode configurations (inspired by [76]).

architectures. The two-electrode configuration consists of a *Working Electrode* (WE) and a *Reference Electrode* (RE), while the three-electrode configuration also includes an additional auxiliary electrode, the *Counter Electrode* (CE).

The overall chemical reaction in the cell is based on two half-reactions happening at the two electrodes as a consequence of the potential difference at the interface (electrode/electrolyte). Normally, the interest is only in one of the two half-reactions, and the electrode at which it occurs is the WE. To standardize the other half of the cell, the RE is created by constant composition so that it is kept at a fixed and known potential. Hence, the potential of the WE can be read and controlled with respect to the RE. By driving the electrode to more negative potentials the electrons' energy increases up to a higher level where it will be transferred to the electrolyte. In this case, a *reduction current* from the electrode to the solution occurs, shown in Fig. 2.2.a. On the other hand, if the electrons' energy is decreased by imposing a more positive potential, the electrons of the electrolyte will be energetically facilitated to flow from the solution to the electrode creating an *oxidation current*, represented in Fig. 2.2.b. The potentials at which these electron transfers occur are related to the standard potential,  $E_0$ , which is characteristic for each chemical species. The internationally accepted primary reference is the *Standard Hydrogen Electrode* (SHE), which has a standard electrode potential ( $E_0$ ) of zero volts at all temperatures. A common-used RE is the silver-silver chloride electrode: Ag/AgCl/KCl (saturated in water), with a potential of 0.197 V vs. SHE. In the two-electrode configuration, the RE acts as electron supplier and as a reference for the potential at the same time; therefore, it is very difficult to maintain a constant potential to refer to [77]. For this reason, the three-electrode configuration is normally adopted. In this architecture, an additional CE is introduced to close the current circuit and is usually made of inert material (e.g. Pt) to not give contribution in the electrochemical reaction. The current flows between the WE and the CE; hence the CE must have a higher surface area with respect to the WE, not to limit the RedOx kinetics.

The potential difference is controlled between the WE and the CE and it is measured between

## 2.1. Drug monitoring with electrochemical sensors

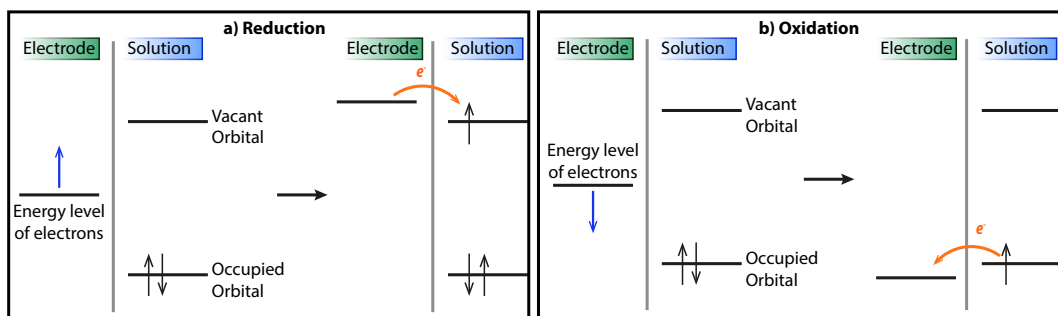


Figure 2.2 – Explanation of electron flow from electrode to solution, and vice-versa, in case of a) reduction and b) oxidation processes, respectively.

the RE and the WE. This configuration allows the potential across the electrochemical interface at the WE to be controlled with respect to the RE.

This configuration has been chosen for the design of the anesthesia monitoring system, the object of this work. The current from the cell is the result of two main contributions: *Faradaic* and *non-Faradaic* processes. The *Faradaic* reaction comprises the RedOx where electrons are transferred across the metal-solution interface. However, whenever an electrode is immersed in an electrolyte, adsorption and desorption of ions happens at the interface affecting the potential. More specifically, there will be a separation and re-distribution of charges on the metal electrode and in the solution, which has been shown experimentally to behave like a capacitor and is called *electrical double layer* ( $C_{dl}$ ). However,  $C_{dl}$  is often a function of potential across it, differently by the real capacitors. The formation of this  $C_{dl}$  at the electrode interface once in contact with the electrolyte solution is described by the Helmholtz theory. As shown in Fig. 2.3, at the electrode/electrolyte interface the ions in the solution tend to organize themselves in several "layers":

- *Inner Helmholtz Plane* (IHP), which contains solvent molecules and other species that are specifically adsorbed on the electrode's surface;
- *Outer Helmholtz Plane* (OHP), which contains solvated ions that are NON-specifically adsorbed on the electrode's surface;
- *diffuse layer* (DL), which extends from the OHP into the bulk of the solution.

Although the *Faradaic* processes are of primary interest to the investigation, the *non-Faradaic* contribution can not be neglected.

The potential of the cell, which corresponds to the potential difference between WE and RE ( $E$ ,  $V_{cell}$  in Fig. 2.1), can be expressed by the Nernst equation:

$$E = E_0 + \frac{RT}{nF} \cdot \ln\left(\frac{C_{ox}}{C_{red}}\right) \quad (2.1)$$

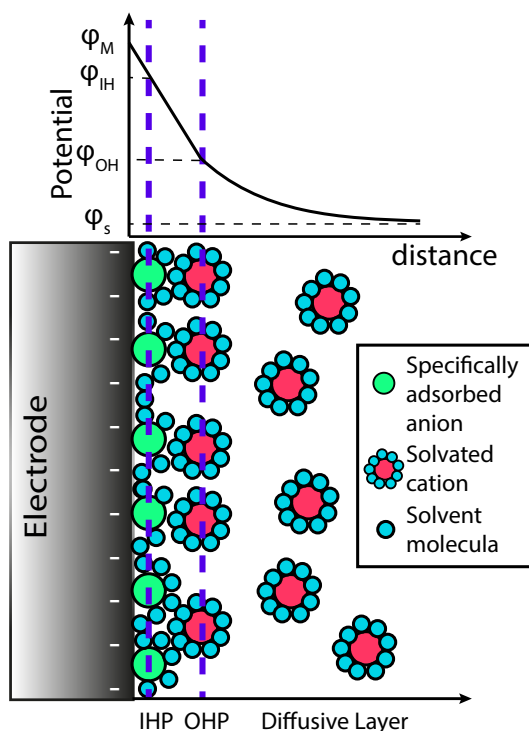


Figure 2.3 – Simplified illustration of the Helmholtz double layer planes where the potential is developed in the area of interface between negatively charged electrode and the electrolyte.

where  $E_0$  is the standard RedOx potential referred to the SHE,  $R$  is the gas constant ( $8.314472 \text{ J K}^{-1} \text{ mol}^{-1}$ ),  $T$  the absolute temperature,  $n$  the number of electrons exchanged in the RedOx reaction,  $F$  the Faraday constant ( $96485.33289 \text{ C mol}^{-1}$ ), and  $C_{ox}$  and  $C_{red}$  are the concentration of the oxidized and reduced species, respectively. The equilibrium potential is achieved when the RedOx reaches the equilibrium, which means that the concentration of oxidized species equalizes the concentration of reduced species.

The concentration of the species  $C_{ox}$  and  $C_{red}$  at the electrode's surface are not the same as those in the bulk solution. Therefore, a gradient is established and a driving diffusion force transports the analyte towards the electrode surface or the bulk solution. The current amplitude produced by the RedOx reaction of the analyte, once in contact with the electrode surface, is affected by this diffusive transport phenomena. The concentration gradient established between the solution near the electrode surface and the bulk solution depends on the applied potential, according to the Nernst equation (Eq. 2.1).

To have a complete understanding of the phenomenon at the electrode/electrolyte interface, we can combine Faraday's law (the observed current is related to the concentration of the analyte) with Fick's first law of diffusion (flux is proportional to the concentration gradient) as follows:

$$m = \frac{QM}{Fz} \tag{2.2}$$



## 2.1. Drug monitoring with electrochemical sensors

Where  $m$  is the mass,  $Q$  the charge (96485 coulombs),  $M$  the molar mass,  $F$  Faraday's constant and  $z$  the valence number.

$$J = -D \left( \frac{\partial \varphi}{\partial x} \right) \quad (2.3)$$

Which describes the diffusion process in terms of a flux ( $J$ ); hence as the amount of substance flowing through a given area in a determined period of time.

By combining Eq. 2.2 and Eq. 2.3 a fundamental general relationship to calculate the diffusion-limited current at the WE is obtained [78] :

$$i(t) = \frac{dQ}{dt} = -nF(Flux) = nFAD \left( \frac{\partial C}{\partial x} \right)_{x=0} \quad (2.4)$$

Where  $n$  is the number of electrons involved in the half-reaction,  $A$  is the electrode's area ( $\text{cm}^2$ ),  $D$  is the analyte's diffusion coefficient ( $\text{cm}^2/\text{s}$ ), and  $\left( \frac{\partial C}{\partial x} \right)_{x=0}$  is the concentration gradient at the surface of the electrode.

If we consider an electrochemical cell as a "black box", a particular excitation function (*e.g.* a potential waveform) can be applied as input, and a particular response function (*e.g.* the resulting variation of current with time) can be measured, as sketched in Fig. 2.4. To apply the desired potential waveform, the electrochemical cell is connected to a potentiostat instrument that controls the voltage across the WE and the CE adjusting it so that the desired potential is applied between the WE and the RE. The aim of the experiment is to obtain information about the electrolyte, with which the electrodes are in direct contact.

Several different electro-analytical techniques are available depending on the applied waveform, but the most common are potentiostatic and potentiodynamic methods.

In the next section the methods that were employed in this thesis will be described, in particular: *ChronoAmperometry* (CA), as potentiostatic method, and *Cyclic Voltammetry* (CV) and *Differential Pulse Voltammetry* (DPV), as potentiodynamic methods. The main objective of these investigative techniques is to measure the concentration of specific electro-active analytes; *e.g.* anesthetic compounds.

### 2.1.2 ChronoAmperometry (CA)

To perform a CA measurement, a fixed potential is applied at the time  $t_0$  to the electrochemical system and the current is measured as a function of time, as in Fig. 2.5.a. The applied potential



Figure 2.4 – Electrochemical cell SEEN as a "black box"

## Chapter 2. Background

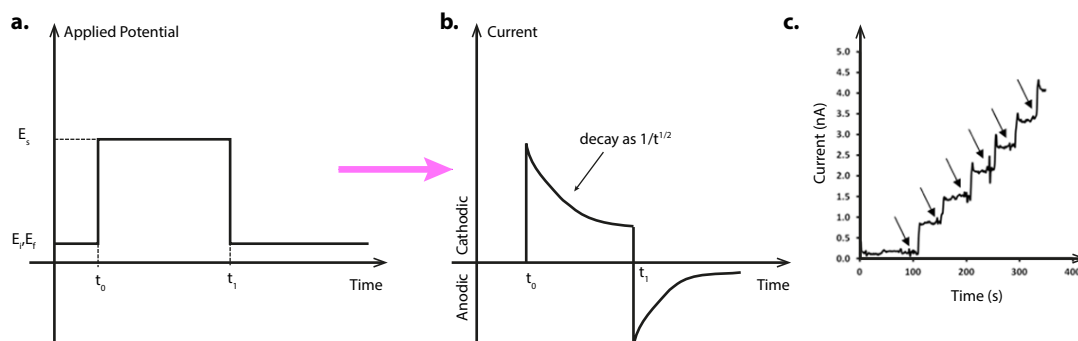


Figure 2.5 – Double potential step chronoamperometry (CA): a) exciting waveform and b) measured current. b) CA trend over time: current variations due to increased concentrations of the target analyte in the solution.

is chosen as the oxidation or the reduction potential of the target analyte, so that it is possible to monitor the variation of the current from the electrochemical cell in time, as in Fig. 2.5.b. The current ( $i$ ) flowing through the electrochemical cell is proportional to the analyte concentration and it is described by the Cottrell equation:

$$i = \frac{nFAc_j^O \sqrt{D_j}}{\sqrt{\pi t}} \quad (2.5)$$

Where  $n$  is the number of exchanged electrons,  $F$  is the Faraday's constant,  $A$  is the area of the electrode ( $\text{cm}^2$ ),  $c_j^O$  is the initial concentration of the reducible analyte  $j$  ( $\text{mol}/\text{cm}^3$ ),  $D_j$  is the diffusion coefficient for species  $j$  ( $\text{cm}^2/\text{s}$ ) and  $t$  is the time (s). This current also includes the contribution of the *double layer* phenomena at the interface, which generates a capacitive current  $i_C$ . This  $i_C$  decays as a function of  $1/t$ ; therefore, it is only visible during the initial instant (a few ms) of the application of the potential step, as shown in Fig. 2.5.a. It is normal practice to measure the current given by the solution without the analyte (blank solution) and then subtract this value from the measured  $i-t$  data [79].

### Cyclic Voltammetry (CV)

CV is a most popular electroanalytical tool for obtaining rapid quantitative information on a RedOx process: (i) electron-transfer kinetics, (ii) diffusion coefficients, (iii) thermodynamic and (iv) subsequent chemical reactions or adsorption processes. To perform a CV measurement a linear sweep-potential scan is applied as an input waveform to the electrochemical system, as shown in Fig. 2.6. The applied potentials are ranged in a determined interval of values ( $E_0$  and  $E_1$ ) so as to provide the RedOx potential at which the target analyte reacts. This technique is usually performed as a first investigation of the electrochemical system.

As soon as the applied potential reaches a sufficient negative or positive value, the target analyte in the solution may gain/transfer electrons from/to the electrode's surface; afterwards, the voltage is reversed towards its first value  $E_0$ . The measured current amplitude is propor-

## 2.1. Drug monitoring with electrochemical sensors

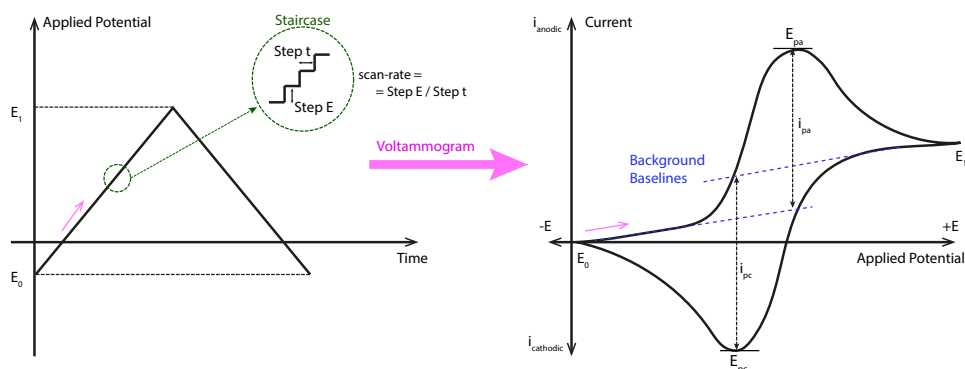


Figure 2.6 – A linear sweep potential scan is applied in real time to the electrochemical system; a voltammogram is obtained by plotting the measured current from the cell *vs.* the applied potential.

tional to the concentration of the analyte in the solution; therefore, it is possible to analytically evaluate it.

The measured current from the electrochemical cell can be plotted as a function of the applied potential obtaining a *voltammogram* (potential is plotted on the x-axis while current on the y-axis). The *voltammogram* may reveal several peaks; each of them denotes a particular electrolytic process in solution. It is possible to decide the initial direction of the first sweep, depending on the characteristic of the analyte: if the analyte is oxidable, the first sweep starts in the positive direction; whereas if the analyte is reducible, the first sweep begins in the negative direction.

Another information provided by the voltammogram refers to the electrochemical reversibility of the RedOx couple. If the reaction is reversible, two peak potentials from the anodic sweep (oxidation),  $E_{pa}$ , and from the cathodic peak (reduction),  $E_{pc}$ , can be read from the voltammogram, and their difference  $\Delta E_{peak}$  can be related, through the Nernst equation (Eq.2.1), with the number of electrons taking part in the RedOx ( $n$ ). The relationship is given by:

$$n\Delta E_{peak} = 59mV \quad (2.6)$$

To evaluate the reversibility of the process, it is possible to estimate the ratio of the peak currents  $\frac{i_{pc}}{i_{pa}}$ . If the ratio is equal to 1, it is an indication of reversibility. If the ratio is  $< 1$  but a return peak is present, then the electrochemical reaction is said to be *pseudo-reversible*. Finally, if only one peak is visible in the voltammogram, the process is *irreversible*. The peak current amplitudes are measured vertically from the peak down to a *background baseline*, which is extrapolated from the steady-states before the peaks area in the CV plot (as shown in Fig. 2.6).

The quantitative information regarding the analyte concentration is obtained by using the

## Chapter 2. Background

Randles-Sevcik equation:

$$i_{peak} = 0,4463 \cdot nFAC \sqrt{\frac{nFvD}{RT}} \quad (2.7)$$

Where  $n$  is the number of transferred electrons,  $v$  is the scan-rate for the potential sweep (V/s),  $F$  is Faraday's constant,  $A$  is the electrode area ( $\text{cm}^2$ ),  $R$  is the gas constant,  $T$  is the absolute temperature (K) and  $D$  is the diffusion coefficient of the analyte ( $\text{cm}^2/\text{s}$ ). Thanks to this equation it is possible to calculate the peak current,  $i_{peak}$  (either anodic or cathodic), in terms of the concentration  $C$  of the analyte. Moreover, if the analyte concentration is known, then this formula can be used to evaluate the diffusion coefficient of the analyte [78].

### Differential Pulse Voltammetry (DPV)

In the differential pulse techniques, two potential steps with similar short duration are superimposed on the potential waveform. The main advantage introduced by these techniques is that the *non-Faradic* current due to *double layer* effect is eliminated (or nearly); therefore higher sensitivity of the measurements is ensured. As a result of this advantage, these kinds of method are widely used in chemical analysis [80]. In the DPV, the potential waveform is generated by superimposing small pulses of constant amplitude upon a staircase waveform, as shown in Fig. 2.7. The measured current is evaluated as the difference between two currents sampled before and at the end of a pulse, respectively. That is why the *non-Faradic* current contribution is eliminated. Therefore, each pulse period will produce one point according to the equation  $i_{n2} - i_{n1} = \Delta i_{n,dp}$ ; where  $n$  corresponds to the pulse number and  $\Delta i_{n,dp}$  is the output current. The differential pulse voltammogram represents the  $\Delta i_{n,dp}$  as a function of the applied potential. In case of a reduction, as soon as the applied potential reaches a value near the RedOx potential, the differential current reaches a maximum, and decreases to zero as the current becomes diffusion-controlled; hence obtaining a symmetric peak [81].

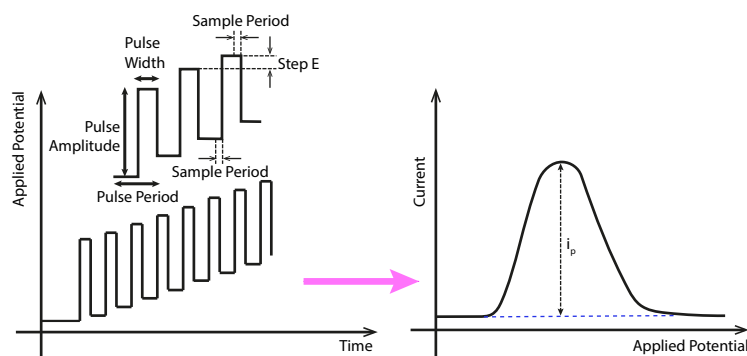


Figure 2.7 – DPV potential wave form and recorded voltammogram.

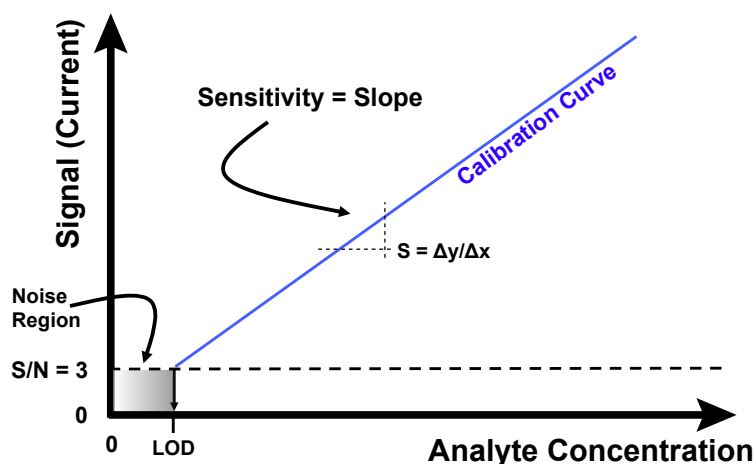


Figure 2.8 – Sensitivity and LOD evaluation from sensor' calibration line.

### 2.1.3 Sensor calibration

The design and the development of a sensor strongly depends on the requirements of the final application. Main sensor features that need to be evaluated are:

- Selectivity: the sensor must be selective toward the desired analyte;
- Sensitivity: ability to discriminate small variations of the analyte concentration;
- LOD: the minimum analyte concentration that can be detected by the sensor;
- Dynamic Linearity Range: ability to follow rapid changes in the input parameter (*e.g.* variations of the analyte concentration).

Therefore, before using a sensor, it is fundamental to calibrate it in order to characterize its performance. A calibration process provides a calibration curve which gives the relation between the sensor output and the analyte concentration. To build the calibration line, it is necessary to measure the sensor response (in voltammetric sensor it is a current), at increasing and known concentrations of the analyte. As shown in Fig. 2.8, the sensitivity can be evaluated as the slope of the calibration curve, while the LOD can be defined, according to *International Union of Pure and Applied Chemistry* (IUPAC) standard, as:

$$LOD = \frac{3 \cdot \sigma_b}{Sensitivity} \quad (2.8)$$

Where  $\sigma_b$  is the standard deviation from the signal obtained from the blank (a solution identical to that analyzed but without the analyte) and the factor 3 maintains the required confidence level of 99% between the observed signal and the blank response [82].

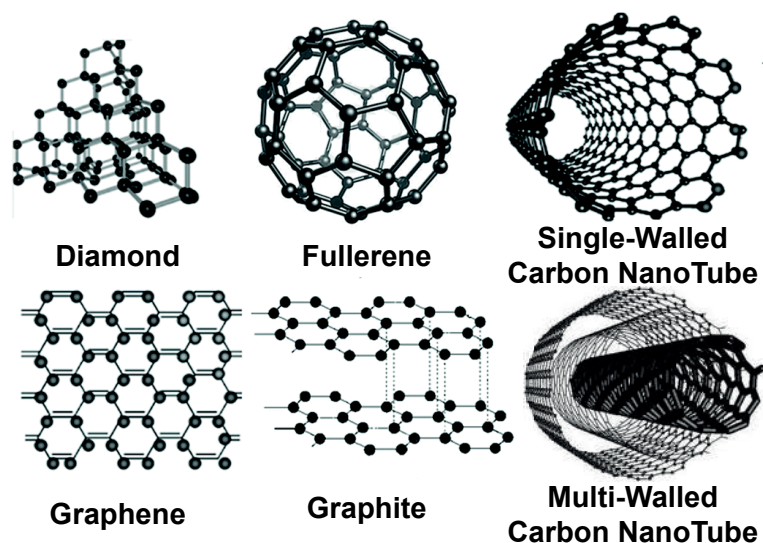


Figure 2.9 – Example of carbon nano-scale structures for enhancing the sensing performance (adapted from [84]).

Since this thesis is focusing on electrochemical sensors, the calibration has to consider pH and temperature variations of the analyzed solution. Indeed, according to the electrochemical theory, these two factors may vary the voltage at which the RedOx reaction is happening in the electrochemical cell and the amplitude of the measured current signal. These effects are visible if considering the full version of Nernst equation (Eq. 2.1):

$$E = E_0 + \frac{RT}{nF} \cdot \ln\left(\frac{C_{ox}}{C_{red}}\right) - \frac{RT}{nF} \cdot pH \quad (2.9)$$

It is evident that there is a dependence on pH and temperature (T) variations [83]. For this reason, monitoring pH and temperature is crucial to ensuring reliable electrochemical measurements. Moreover, by considering the final application where biological fluids represent the analyzed solution, if pH and temperature are also detected, additional information on the health-status of the patient can be revealed (*e.g.* fever, alkalosis, acidosis *etc.*).

#### 2.1.4 Enhancement of electrode performance

Electrochemical methods are promising technologies for clinical use. The main challenge in the fabrication of electrochemical devices resides in the improvement of their sensing performance. To that aim, nanomaterials can be employed to enhance their electron-transfer properties. Indeed, nanomaterials offer high electrical conductivity, improved surface-to-volume ratio, structural robustness, catalytic features and excellent stability characteristics [85].

Carbon nano-scale allotropes can be exploited for their outstanding chemical, mechanical and electrical properties, such as high stability at environmental conditions, strong covalent

## 2.1. Drug monitoring with electrochemical sensors

---

bond formation *etc.* [86]. Main carbon nano-scale allotropes are represented in Fig. 2.9 and listed hereafter [87].

- **Graphite** is a natural allotrope with an extended  $sp^2$ -hybridized carbon atoms network, organized in a hexagonal honeycomb structure. It is extremely conductive and with low dissipation power. It consists of countless layers of carbon atoms lying on top of each other, weakly bonded together. The material is extremely soft and it is employed for creation of graphite pencils [88].
- **Diamond** is a natural allotrope with a C- $sp^3$  hybridization and tetrahedral bonding atom network. It is extremely hard, chemically inert and with high electrical resistivity. To be used as electrode material, it has to be doped to become conductive. P-doping with boron is a common practice, and the obtained BDD conductive material is highly resistant to surface biofouling and chemical degradation [89, 90].
- **Fullerene C<sub>60</sub>** is a synthetic allotrope consisting of a spherical network of sixty structurally equivalent  $sp^2$ -hybridized carbon atoms in the shape of a sphere [87].
- **Graphene** is a single isolated layer of graphite in  $sp^2$ -hybridization form. It has extraordinary electrical, thermal, and physical properties [91].
- **Carbon NanoTube (CNT)** have properties similar to graphene since it is also in  $sp^2$  configuration. It can be created in *Single-Walled Carbon NanoTube* (SWCNT) or *Multi-Walled Carbon NanoTube* (MWCNT) structure. The former consists of a single graphene sheets wrapped into a cylindrical tube shape (diameter between 0.4 and 2.5 nm); the latter derives from more than one graphene sheets rolled in a cylindrical shape (diameters up to 100 nm) [88].

Carbon-based nano-materials have been widely adopted to modify electrodes in order to obtain improved sensing performance. For instance, ion selective sensors based on nano-structures as solid-contacts showed superior performance when compared to other conductive polymeric sensors [92]. In addition to this, since nano-structures provide a larger electrode's area, it was also proven that they enhance the electron-transfer properties as well, as they provide a more favorable adsorption of bio-functionalization structures, such as enzymes [93] and proteins [94].

In this thesis, diamond and graphite have been investigated for propofol detection to exploit their hardness and high conductivity properties, as described in *Chapter 3*, while fullerene-C<sub>60</sub> and MWCNTs have been used in modified carbon-based electrodes to enhance the sensitivity performance in midazolam detection, as reported in *Chapter 4*.

## 2.2 Electronics for electrochemical sensing

### 2.2.1 Potentiostat

Potentiostat instruments are fundamental tools for performing electrochemical measurements. The general structure of a potentiostat is illustrated in Fig. 2.10. The main functionalities of a potentiostat are:

- Driving the sensor electrodes by applying the desired excitation waveform to the cell ( $V_{CELL}$ ),
- Ensuring that the applied voltage remains stable in order to supply the current necessary for the electrochemical reaction to occur (*Potential Control* block in Fig. 2.10),
- Measuring a current as output signal from the electrochemical cell (*Current Readout* block in Fig. 2.10).

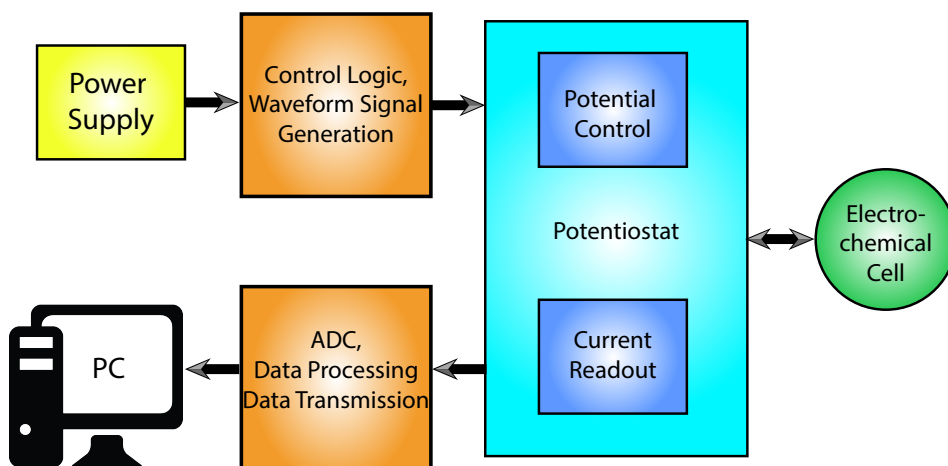


Figure 2.10 – Main blocks of a potentiostatic measurement.

#### Potential control configurations

To control the voltage applied between WE and RE two different configurations are feasible: the *grounded counter electrode* and the *grounded working electrode*. The former is depicted in Fig. 2.11, but the latter is normally preferred. As illustrated in Fig. 2.12.a, the basic implementation is obtained by keeping the WE at the ground (GND) while an operational amplifier (*Driving Amplifier*) controls the cell current  $I_{CELL}$ , so that the cell potential  $V_{CELL}$  corresponds to the desired excitation potential  $V_{IN}$ .

This architecture is extremely simple to implement; however, some limitations have to be considered. Indeed, the functionalities of the potentiostat depend on the *Driving Amplifier*



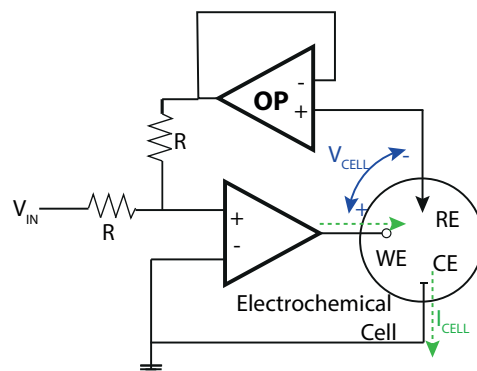


Figure 2.11 – General schematic of a grounded CE configuration.

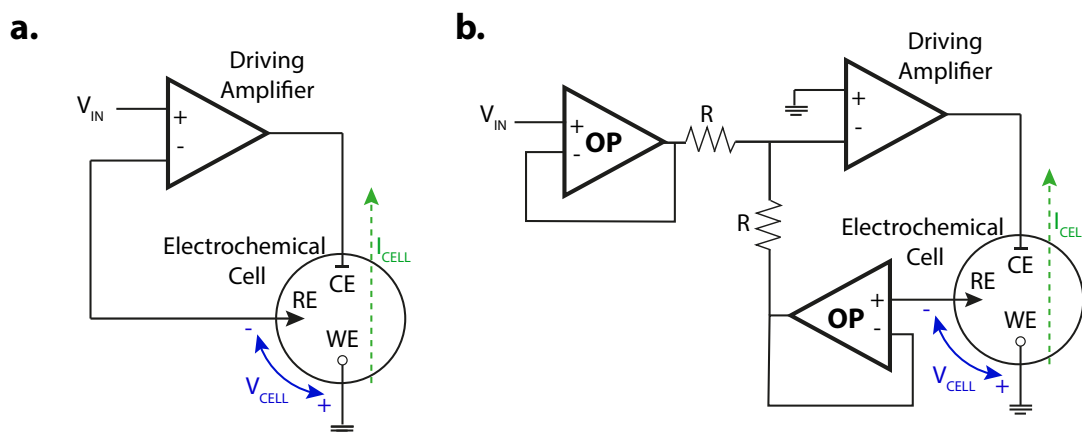


Figure 2.12 – a) General schematic of a grounded WE configuration and b) schematic with voltage buffers to isolate driving amplifier and RE.

characteristics. To ensure zero-current flowing in the RE to avoid polarization effects, the driving amplifier input bias current has to be small while the input resistance should be very large. Furthermore, since the electrochemical cell is the load and feedback network of the amplifier, it is possible to isolate the driving amplifier and the RE from whatever currents the load may produce by adding two buffer amplifiers in its input, as shown in Fig. 2.12.b. The voltage gain and the input offset voltage of the driving amplifier define the accuracy and the linearity of the potential control unit [95].

**Waveform generator** The various voltammetric techniques differ from one another according to the excitation waveform being applied to the electrochemical cell. Therefore, a waveform generator is a crucial block to be included in an electrochemical circuit instrumentation. A multi-mode waveform generator is desired to produce signals of various shapes, amplitudes and frequencies.

*Direct Digital Synthesizer* (DDS) architecture can be designed to generate all the needed

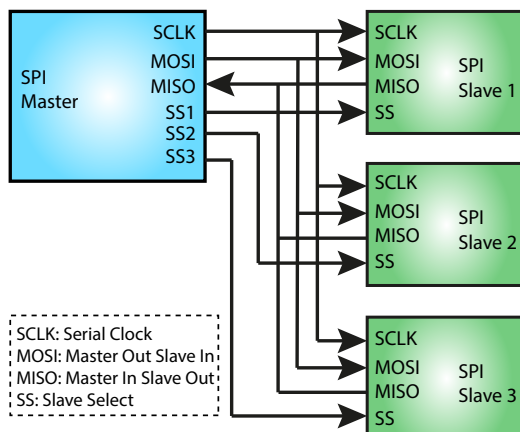


Figure 2.13 – Typical SPI bus: bidirectional communication between a *master* and three independent *slaves*.

excitation waveforms for different electrochemical measurements (*e.g.* CA, CV and DPV). DDS is a mixed-mode circuit consisting of a *Digital to Analog Converter* (DAC) digitally-controlled to implement all shapes and multiple frequencies from a reference frequency, which is provided [96].

In this thesis, the DDS has been developed by a micro-controller unit that sends, with a certain frequency, an increasing or decreasing digital value to the DAC, which converts it in an analog voltage to be applied to the electrochemical cell. The communication between the micro-controller and the DAC unit exploits the high speed *Serial Peripheral Interface* (SPI) interface, which only needs an external clock to generate the desired waves, as shown in Fig. 2.13. The micro-controller acts as the *master* while the DAC as the *slave*. Further, since the SPI bus can operate with a single master device and with one or more slave devices, it is possible to let the micro-controller control several DAC in parallel (three slaves architecture in Fig. 2.13). This is of high interest for the actual application since the system has to monitor up to three drugs (composing the anesthesia cocktail) at the same time. If more than one *slave* device is connected to the micro-controller, the *Slave Select* (SS) line is used to address the DAC of interest.

### Current read-out architecture

As soon as the driving signal is imposed on the electrochemical cell, RedOx reactions happen in the solution at the WE interface. Therefore, custom circuits for reading out the RedOx current have to be implemented. Also in this case, different approaches can be adopted. However, for the purposes of this thesis, only voltage-mode circuits will be described [95].

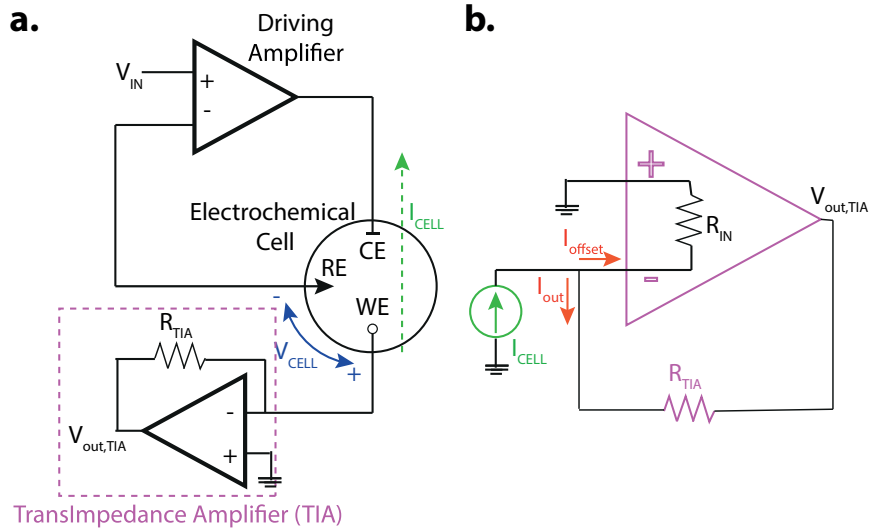


Figure 2.14 – General schematic with TIA.

**TransImpedance Amplifier (TIA)** In this configuration the measured current from the electrochemical cell is directly converted into a voltage signal by the use of a *TransImpedance Amplifier* (TIA), as shown in Fig. 2.14.a.

The *Faradic current*  $I_{CELL}$  from the RedOx reaction flows in the single resistor in the feedback  $R_{TIA}$  of the TIA and is converted into a voltage  $V_{out,TIA}$  according to the equation:

$$V_{out,TIA} = -I_{CELL} \cdot R_{TIA} \quad (2.10)$$

Therefore the output signal  $V_{out,TIA}$  is proportional to the *Faradic current*  $I_{CELL}$ . In addition to the TIA stage, it is possible to include in cascade further amplification stages to enhance the electrochemical signal. The final amplification would be provided by the product of the amplification stages. *Programmable Gain Amplifier* (PGA) can be used for this further amplification stage since it offers the possibility to test different gains, ensuring the flexibility of the circuit.

If we consider the equivalent circuit of the operational amplifier, as in Fig. 2.14.b, we can notice that the input impedance is equivalent to the impedance between the positive and the negative inputs. This impedance is affected by some leakage currents ( $I_{offset}$ ), which could cause problems both in  $I_{CELL}$  current readout and  $V_{CELL}$  tracking, especially if low *Faradic currents* are generated by the RedOx and a very high value of  $R_{TIA}$  is required. This error can be minimized by choosing an amplifier with low offset and bias current guaranteed by very high input impedance  $R_{IN}$ .

Furthermore, flicker and thermal noises of the TIA have to be considered for the design. These noises can manifest themselves as:

## Chapter 2. Background

- Output voltage ( $V_{noise}$ ):  $V_{OUT} = V_{out,TIA} + V_{noise}$
- Input current ( $I_{noise}$ ):  $I_{noise} = \frac{V_{noise}}{R_{TIA}}$  so that the minimum *Signal to Noise Ratio* (SNR) of the TIA is established as:

$$SNR = \frac{I_{CELL}}{I_{noise}} \quad (2.11)$$

### 2.2.2 Equivalent circuit for an electrochemical cell

A largely adopted approximation of the equivalent circuit for the three-electrode cell is shown in Fig. 2.15. Passive components of the circuit are  $R_{SW}$ ,  $R_{SR}$  and  $R_{SC}$  that take into account the distances from the electrodes and can be evaluated according to the Ohm's second Law as:

$$R = \rho \cdot \frac{d/2}{A} \quad (2.12)$$

Where  $A$  is the area of the electrode,  $d$  is the distance between the electrodes, and  $\rho$  is the resistivity of the solution.

A similar equation to Eq. 2.12 can be adopted for evaluating the charge transfer resistances for CE and WE branches; *e.g.*  $R_{CE}$  and  $R_{WE}$ , respectively. In this case, the  $d$  corresponds to the thickness of the electrode and  $\rho$  is the resistivity of the electrode's material. Normally, the area of the CE is designed to be very large, so as to observe a low resistance, which only depends on the material used for the fabrication. The resistance related to the RE branch  $R_{RE}$  is absent because both the resistance and the capacitance of the reference must be very large to ensure zero-current flow. Finally, the capacitances  $C_{WE}$  and  $C_{CE}$  model the double-layer capacitance effect at the WE-/CE-electrolyte interfaces, respectively [98]. In the circuit represented in Fig. 2.15 an active component is also present. This *Faradaic-current* generator  $i_W$  simulates the current deriving from the chemical reaction happening at the WE. According to electrochemical conventions, positive currents (oxidation) flow from the WE to the CE, and *vice-versa* for negative currents (reduction). This WE current  $i_W$  can be considered as the sum

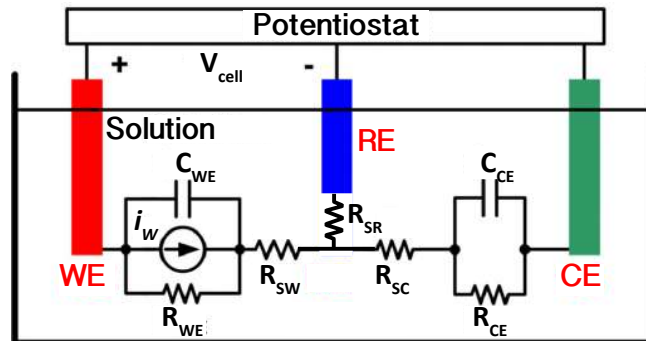


Figure 2.15 – Equivalent circuit for the three-electrode amperometric configuration, modified from [97].

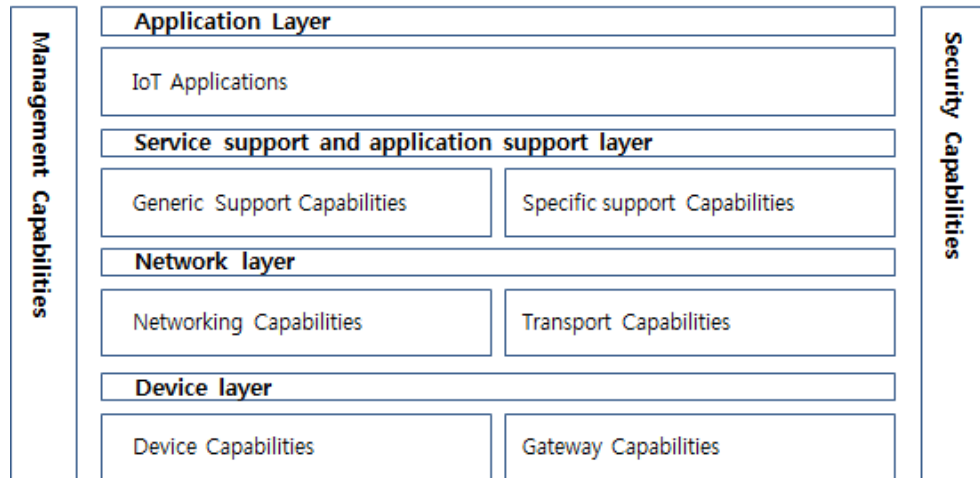


Figure 2.16 – Structure of the IoT reference model. (Reprinted from [101].)

of *Faradic* ( $i_F$ ), *non-Faradic* ( $i_{non-F}$ ) and noise ( $i_{noise}$ ) currents [83]:

$$i_W(t) = i_F(t) + i_{non-F}(t) + i_{noise}(t) \quad (2.13)$$

If a constant bias potential drives the electrochemical cell, as in CA measurements, then the current  $i_W$  does not depend on the bias, and it is possible to define  $I_W = I_F$  as the average value of the *Faradic* current obtained for a certain analyte concentration [98].

## 2.3 IoT in medical applications

IoT is a growing topic of common interest since it is having a great impact on several aspects of everyday-life and the behavior of users, in private and business contexts [99]. According to the definition provided by Recommendation ITU-T Y.2060 (06/2012), [100] IoT is a “global infrastructure for the information society, enabling advanced services by interconnecting (physical and virtual) things based on existing and evolving interoperable information and communication technologies”. “Any THING” that able to connect to the Internet is enabled to exchange data and interact with other devices within the network and access information at “any TIME” and from “any PLACE”. Therefore, an IoT network consists of a large number of heterogeneous devices that are dynamically interconnected so as to exchange data and services of different kinds. In this context, it is crucial to provide standard and flexible architectures able to handle and sustain this traffic. The IoT reference model, represented in Fig. 2.16, is based on four layers, including also management and security capabilities [100].

1. **Application layer** includes the IoT applications
2. **Service support and application support layer** consists of *generic* and *specific* capabilities. The former can be used by different applications; the latter are detailed capabilities



Figure 2.17 – Schematic representation of the IoT possible fields of application. (Reprinted from [102].)

to provide different support functions to specific target applications.

3. **Network layer** relies on *networking* and *transport* capabilities to provide control over network connectivity functions (*e.g.* access and authentication, *etc.*) and the transport of IoT service and data.
4. **Device layer** is categorized into *device* and *gateway* capabilities. The *device* capabilities include direct and indirect interaction (including "sleeping" and "waking-up" mechanisms to save energy) with the communication network even through *ad-hoc* networking in some specific scenarios. The *gateway* capabilities refer to the ability to interface different kinds of wired or wireless connectivity technologies (*e.g.* ZigBee, Bluetooth or Wi-Fi) and to communicate through various network technologies (*e.g.* 2G or 3G networks, digital subscriber lines (DSL), Ethernet or others). Furthermore, the *gateway* capabilities are also needed in protocol conversion when different device layer protocols are used (*e.g.* Wi-Fi and Bluetooth protocols), or when different protocols are used at the device and network layers (*e.g.* ZigBee protocol at the device layer and a 3G protocol at the network layer).
5. **Management capabilities** can be either *generic* or *specific*. The *generic* management capabilities include the general management of the device ((de)-activation, diagnostics, updating), and the management of the local network topology and of the traffic and congestion. The *specific* management capabilities are related with the specific requirements of the application.
6. **Security capabilities** are of two kinds: *generic* and *specific*. *Generic* security capabilities are independent of applications and are applicable to different IoT layers, such as

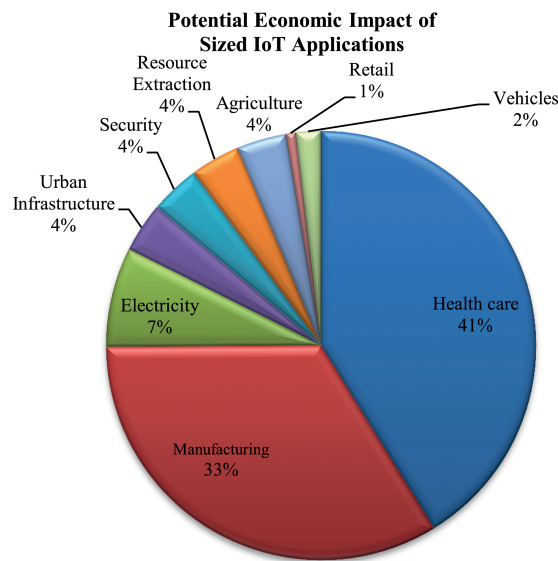


Figure 2.18 – Projected economic impact market of IoT applications by 2025. (Reprinted from [102].)

the application, the network and the device layers, handling the authorization, the authentication, the confidentiality and integrity protection. *Specific* security capabilities follow the application requirements.

There are several domains and environments in which IoT solutions can be adopted playing a remarkable role. These applications range from transportation and industrial automation to health-care and smart-environments [102], as in Figure 2.17. In particular, the adoption of IoT solutions in the medical field lead to the realization of powerful tools for medical staff and patients providing optimized monitoring even remotely, improved management of the health-care systems and advanced solutions to diffuse medical services with the respect to the specific policies and regulations.

If we have a look at the economic impact of IoT by 2025, shown in Figure 2.18, it is evident that health-care applications cover one of the largest markets (41% of impact). The whole annual economic impact caused by IoT is estimated to be in the range of \$2.7 trillion to \$6.2 trillion by 2025, of which \$1.1 – 2.5 trillion annual growth is from the health-care market [103]. Within this development of IoT, medical IoT applications are gaining increasing popularity paving the way towards the realization of *Smart-Hospitals*. Smart-Hospitals are supported by IoT technologies to provide advanced diagnosis, treatment, management and decision services by enabling device interoperability and fluent exchange of information [104]. Additionally, medical IoT solutions also include remote medical services, such as remote diagnosis and monitoring of patients, which are grouped under the concept of *Telemedicine* [105].

To guarantee high performance in an IoT network, some requirements has to be guaranteed [102, 106]:

## Chapter 2. Background

---

1. **Scalability** - The IoT network has to guarantee the possibility including new devices, services and functions without negatively affecting the quality of the existing services. To do that, a *ground-up* approach has to be followed. The challenges related to this requirement are due to the fact that diverse hardware platforms and communications protocols have to be interfaced. Furthermore, it is very difficult to create a testing set with such highly-scalable networks.
2. **Heterogeneity** - End-to-end interoperability challenges IoT networks since a large number of heterogeneous devices has to be connected together. This should be kept in consideration by both application developers and IoT device manufacturers in order to deliver services for all customers regardless of the specifications of the hardware platform that they use.
3. **Reliability** - The proper operation of the system should reflect the specification. Therefore, the availability of information and services has to be guaranteed over time. This is especially true in the case of medical applications. Reliability must be implemented throughout all the IoT layers.
4. **Mobility** - A key role of IoT is to provide services continuously to the connected users while on the move. Therefore, it is fundamental to handle such mobility and dynamism within IoT networks.
5. **Security and Privacy** - In IoT heterogeneous networks security and privacy represent two main challenges that have to be faced. Data must be protected from unauthorized access and has to be transmitted and received without any modifications, hence ensuring its integrity. In particular, for medical IoT networks, the main security challenges are related to: (i) confidentiality, (ii) authentication, (iii) access control, (iv) privacy, (v) trust and (vi) policy enforcement. The confidentiality ensures that the data is readable only by the target receiver. Authentication ensures the validity of an user and normally requires the generation of a session key. Access control algorithms provide new connections only after the verification of the quality of communication. These algorithms are a protection against “man in middle” attacks. Privacy is concerned with different aspects such as devices, communication, storage and processing. Trust management systems estimate the dynamic trust scores for all the cooperating nodes for handling misbehavior. Finally, policy enforcement governs the access rights of users for specific services [107].

### 2.3.1 Cloud computing

An IoT network connects a large number of physical objects through the Internet. Therefore, an enormous amount of data is exchanged among the devices in the network. We normally refer to this as “big data”. To handle and manage these loads of information correctly, efficient data storage and process mechanisms have to be provided. Due to the fact that “big data” normally exceeds the capability of commonly used hardware and software, emerging technologies like cloud computing and data analytics are spreading. Cloud services allow users to use software



remotely, as well as hardware components and services provided by third parties. According to Marston *et. al.* cloud computing features can be summarized by this definition: “It is an information technology service model where computing services (both hardware and software) are delivered on-demand to customers over a network in a self-service fashion, independent of device and location. The resources required to provide the requisite quality-of-service levels are shared, dynamically scalable, rapidly provisioned, virtualized and released with minimal service provider interaction.” [108]. Therefore, cloud solutions represent a powerful tool for the IoT “big data” handling. There are a lot of free and commercially-available cloud platforms and frameworks available to host IoT services. In this thesis, the PrYv middle-ware solution was used. It enables organizations to collect, store and use data to spark new and innovative projects, enhance existing services and improve consumers’ services [109]. The term “*middle-ware*” refers to a software layer placed between applications and objects. It is a “network-oriented” vision that aims to provide solutions to frequently encountered problems, such as heterogeneity, interoperability, security, *etc.*, and facilitates the interfacing of new services with previous technologies to produce novel and advanced services [110]. The main features offered by middle-ware are the transparency and the abstraction that offer a solution to architecture mismatch problems. In the following section PrYv middle-ware solution will be presented.

### PrYv e-health middle-ware

PrYv S.A. is a Swiss Company founded by Pierre-Mikael Legris in 2012 and located in the *École Polytechnique Fédérale de Lausanne* (EPFL) Innovation Park (Lausanne). It is a middle-ware solution that offers services and functionalities for the secure and private transmission and storage of sensible data on cloud platform. They adopt a privacy-by-design approach to meet the requirements established by regulations, such as *General Data Protection Regulation* (GDPR), *Health Insurance Portability and Accountability Act* (HIPAA) and *Software as a Medical Device* (SaMD). The decentralized design of the middle-ware ensures that the standards of other governmental or company-wide legislations and policies regarding sensitive data are met as well. This middle-ware was built to work with medical devices, and integrates easily with existing systems software. The highly sensible data are transmitted from the local browser to the cloud by exploiting *HyperText Transfer Protocol Secure* (HTTPS) which adopts an encrypted communication. Different kinds of data can be handled, stored, manipulated and visualized by the offered cloud-based tools. Stored data are private by default, the users can share the data by explicitly opening read-only or collaborative access to specific parts of their data. Data, which are called *events* in PrYv, are organized in a modular structure similar to files in computer folders, as shown in Fig. 2.21. Therefore, we can consider **events** as the primary units of content in PrYv. They can be defined as a timestamped piece of typed data belonging to a given context. Contexts are the circumstances in which events occur. The context of an event is the combination of a **stream** and *tags*. **Streams** are the fundamental contexts in which the events occur. They follow a hierarchical structure (*streams* and *sub-streams*). **Tags** provide further context to the event. Each event can be labeled by one or more tags [111].

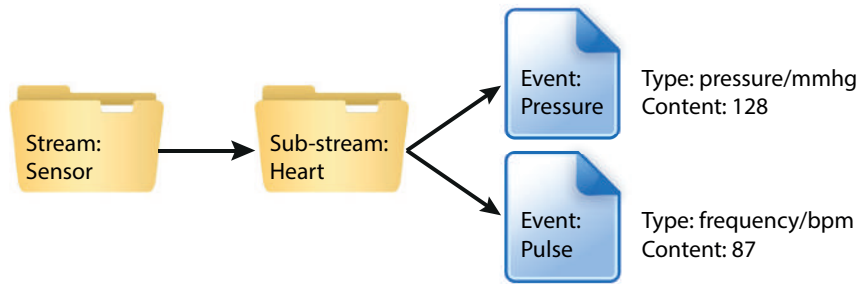


Figure 2.19 – Modular structure data organization in PrYv middle-ware solution.

Three different libraries are offered by the Company for interacting with PrYv middle-ware: (i) Java-script (browser & Node.js), (ii) Apple Cocoa (iOS & OSX) and (iii) Java (Android & desktop). In this thesis the PrYv Java library for developing a dedicated Android-based IoT solution was adopted. Indeed, Android is an open-source and widely diffused *Operating System* (OS), highly attractive for realizing custom solutions.

### 2.3.2 Android operating system

Android is a mobile *Operating System* (OS) developed by Google, based on a modified version of the Linux kernel. It offers the first complete and open-source platform for developing mobile applications. Starting in 2008, several versions and updates have been provided. The different versions, listed in Fig. 2.20, are indicated at the official level with a version number according to the computer standard accompanied by the most used "codename" inspired by traditional pastries and strictly in alphabetical order: Cupcake (Android 1.5), Donut (1.6), Eclair (2.0), Froyo (Frozen Yogurt i.e. 2.2), Gingerbread (2.3), Honeycomb (3.0), Ice Cream Sandwich (4.0), Jelly Bean (4.1), KitKat following an agreement with Nestlé (4.4), Lollipop (5.0), Marshmallow (6.0), Nougat (7.0) and the recent Oreo (8.0) [112]. The Android OS system

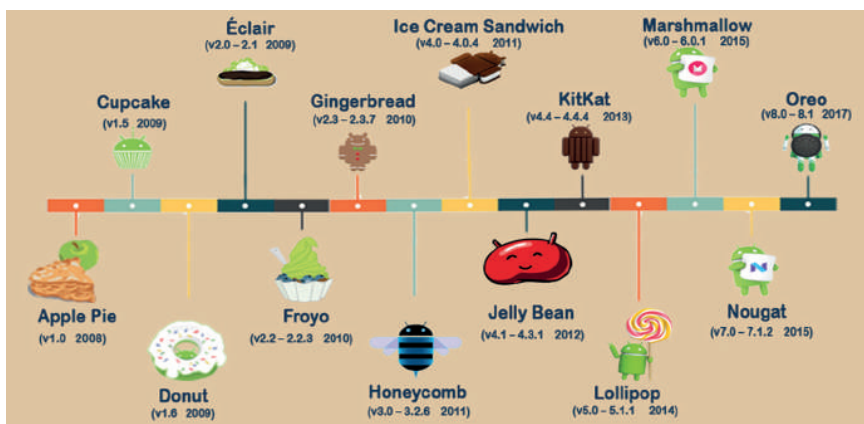


Figure 2.20 – Android OS versions (reprinted from [112]).

architecture is organized in the form of a software stack consisting of applications, operating system, run-time environment, middle-ware, services and libraries. It is typically divided into four layers [113, 114], as shown in Fig. 2.21.

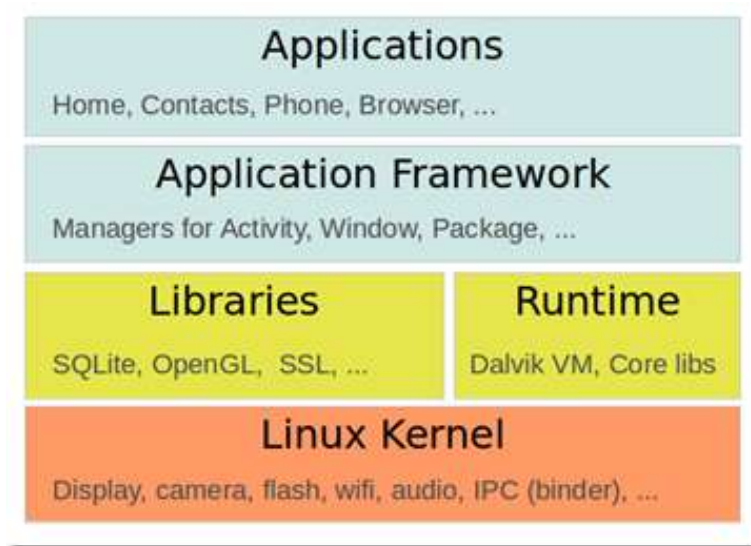


Figure 2.21 – Android OS system architecture (reprinted from [115]).

1. **Linux Kernel**, at the bottom of the stack, provides a level of abstraction between the device hardware and the upper layers. The kernel is based on Linux version 2.6, and it provides multitasking, low-level core system services (such as memory, process and power management), and device drivers to control the hardware components such as the device display, Wi-Fi and audio. Since Linux kernel provides multitasking execution, then multiple processes can be executed in parallel directly on the Linux kernel. This is possible because every Android application runs in its own process, with its own instance of the *Dalvik Virtual Machine* (DVM), which is a register-based VM included in the Android OS [116]. Running applications in VMs presents several advantages. First, applications cannot negatively interfere (intentionally or otherwise) with the operating system or other applications, nor can they directly access the device hardware. Secondly, this enforced level of abstraction makes applications platform neutral so that they are not tied to any specific hardware.
2. **Android Core Libraries**, also considered as *Dalvik Libraries*, can be divided into three main categories:
  - *Dalvik VM Specific Libraries* used for interacting directly with an instance of the DVM.
  - *Java Interoperability Libraries* are a subset of the Standard Java core libraries that have been adapted and transformed for use by applications running within a DVM.

## Chapter 2. Background

---

These libraries provide support for tasks such as string handling, networking and file manipulation.

3. **Application Framework** is a set of services that collectively form the environment for running and managing Android applications. It includes the following key services:
  - *Activity Manager* controls all the aspects of the application life-cycle and the activity stack.
  - *Content Providers* allows applications to publish and share data with other applications.
  - *Resource Manager* provides access to non-code embedded resources such as strings, color settings and user interface layouts.
  - *Notifications Manager* to display alerts and notifications.
  - *View System* used to create different kinds of views and layout for specific user interfaces.
  - *Package Manager* able to find out information about other applications currently installed on the device.
4. **Applications**, at the top of the stack, comprise both the *native applications* provided with the particular Android implementation (*e.g.* web browser and email applications) and the *developed applications* installed by the users.

### Application components

The application components are the essential building blocks for developing an Android application. There are four basic types of component with different roles within the application, own life-cycle and individual activation time. These components are:

- **Activity** is a single screen of the user interface through which the user can interact with the application to perform operations. Typically, an application consists of several *Activities* among which one is the *Main Activity* that is displayed as soon as the application is launched. An *Activity* can start another *Activity* by the use of the `startActivity(intent)` command in order to accomplish different tasks. Whenever an *Activity* is started it is inserted in the stack (Black Stack), while the previous one is suspended and maintained in a stack. Since the stack data adopts the *Last in - First Out* (LIFO) structure, if the button “Back” is pressed, the last suspended *Activity* is shown again.
- **Service** is an application component that performs operations in the background and does not provide any user interface. A service can take two basic forms: **started** and **bounded**. The *started service* is when the service is called by using the call `startService()`. Once it is started, it runs in the background until it is destroyed. It performs the requested operations and usually does not return anything to the caller. A *bounded service*

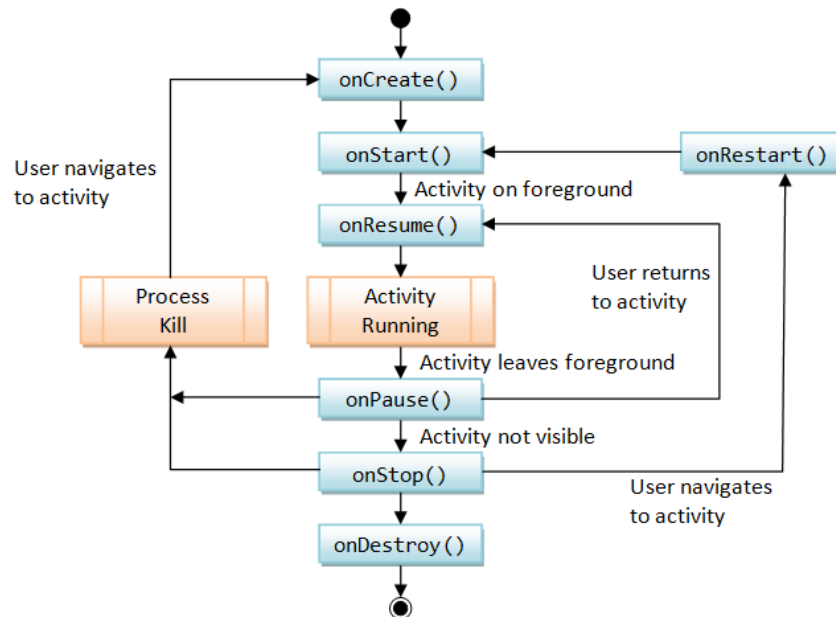


Figure 2.22 – Schematic of the life-cycle of an Android activity (reprinted from [118]).

takes this form when it is started by an application calling the `bindService()`. It offers a client-server interface to the components that want to interact with it and it lasts for as long the specific component runs.

- **Content Provider** manages access to a set of structured data. It offers data encapsulation and some mechanisms for defining the security. *Content Providers* are the standard interface for sharing secure information among different applications in read-only, read or write mode. An example of a *Content Provider* is the list of contacts on the phone. Applications, with the required permissions, can access the list of contacts for reading and writing information.
- **Broadcast Receiver** is a component that responds to the broadcast advertisement of the system. Most of the broadcasts are generated by the system, such as a warning when the charge level of the battery is low or when the screen has been turned off.

Three of the four application components - Activity, Service and Broadcast Receiver - are triggered by an asynchronous message called *Intent*. It associates the various components with each other in runtime either if they belong to the same application or to different applications. Thanks to the *Intent*, Android becomes an interconnected system composed of independent components that can communicate with each other [117].

### Activity life-cycle

The fundamental component of an Android interface is the *Activity*, which allows the user to interact with the application. The displayed window, through which the user interacts, is known as *View* and it is possible to place the different *User Interface* (UI) elements by using the command `setContentView(View)`. Activities in the system are managed in a stack: whenever a new activity is started it is placed on the top of the stack and becomes the running activity, while the previous activity is kept below in the stack, remaining in the foreground until the new activity exits.

An activity has essentially three states: if it is in the foreground of the screen (at the top of the stack), it is **active** (or running), if it has lost focus but it is still visible (when, for example, a new non-full-sized or transparent activity is placed on top of it), it is **paused** and if it is completely obscured by another activity, it is **stopped**. When an activity is paused or stopped, the system can drop the activity from the memory by either asking to finish it, or simply by killing its process. While, if it is displayed again to the user, it must be completely restarted and restored to its previous state. To enable these processes, three key life-cycle loops have to be considered:

1. The **entire lifetime** of an activity begins with the first call to `onCreate(Bundle)`, which contains all the setup "global" states, and ends with the final call to `onDestroy()`, that releases of all the remaining resources.
2. The **visible lifetime** of the activity happens between a call to `onStart()` until a corresponding call to `onStop()`. During this time the activity is visible on the screen, though it may not be in the foreground. The resources that are needed to show the activity to the user are maintained in memory.
3. The **foreground lifetime** of the activity starts with an `onResume()` call till the corresponding `onPause()` call. During this time the activity is in front of all the other activities and is interacting with the user.

Fig. 2.22 shows the entire Activity life-cycle with the important state paths. All the mentioned methods are hooks that it is possible to override in order to obtain personalized features when the activity changes the state. On the other hand, `onCreate(Bundle)` must be implemented by all the activities in order to ensure a proper initial setup. All these overridden methods always need to call up superclass in order to make effective their changes or initializations.

### Android Studio

Android Studio is the official *Integrated Development Environment* (IDE) for Android or Android Wear applications development. It offers advanced features to enhance the developer productivity when building Android apps, such as: flexible Gradle-based build system, extensive testing tools, smart editor suggestions *etc.*. Each project in Android Studio is organized

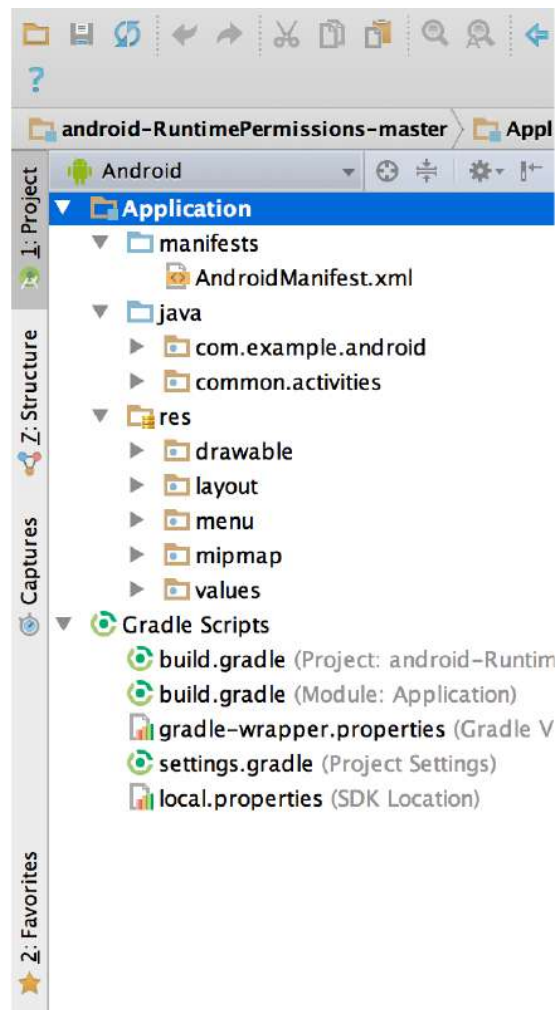


Figure 2.23 – The project files in Android Studio view (reprinted from [119]).

in modules containing code and resource files. These modules, visible in Fig. 2.23, are: (i) Android app modules, (ii) library modules and (iii) Google App Engine module. The Android app module consists of three folders:

- **manifests** that contains the `AndroidManifest.xml` file. This file declares all the components included in the Android application. The Android framework consults the Manifest to obtain the essential information about the developed interface in order to run any part of the code. It also contains also other details, such as descriptions of the *Application Programming Interface* (API) libraries, description of the intent filters and the permissions list, if any.
- **java** that contains the Java source code files.
- **res** that includes all the non-code resources, such as XML layouts, UI strings, and bitmap

images.

Android Studio uses Gradle build system to automate the process of program compilation. This build system is a plug-in that runs as an integrated tool from the Android Studio. The build files are named `build.gradle` [119].

### 2.4 Summary and main contributions

The creation of a complete IoT system for anesthesia monitoring requires the involvement and application of a range of different scientific disciplines, such as electro-chemistry, electronics and software development. This chapter contains important and fundamental notions for each of these fields. We can summarize the most crucial information of each part as follows:

- Electrochemical sensors are a valid option for accurate and reliable on-line drug sensing due to their advantageous characteristics, such as high sensitivity and specificity, small-dimensions and portability, low costs and the simplicity of their integration with electronics. The electrochemical set-up normally consists of a three-electrode cell (WE-RE-CE) in which RedOx reactions occur as a consequence of excitation potential waveforms. The excitation potentials vary depending on the electrochemical technique required. For instance, constant potential is applied for chronoamperometry, while a linear sweep potential ramp is imposed in case of voltammetric measurements. The chemical reaction is then converted in a measured current signal that contains the information about the presence and the amount of the target analyte in the solution.
- Potentiostats are fundamental tools for electrochemical measurements. They drive the electrochemical cell by applying the excitation potential waveform, ensure a stable applied voltage between WE and RE in order to provoke the electrochemical reaction to occur and read out the current signal generated by the RedOx reaction in the electrochemical cell. Different architectures can be implemented, such as grounded working and grounded counter electrodes.
- IoT solutions in medical applications are able to provide powerful tools to support the medical staff in their daily responsibilities. The great amount of data generated by IoT networks, named as “big data”, can be handled by cloud-supported structures that also make them accessible at any time and from any place. Any device that can connect to the Internet and wirelessly share data can be connected to these IoT networks.
- Android is a widely used mobile operating system that offers the first complete and open-source platform for developing mobile applications. It is therefore considered as a powerful tool for the creation of ad-hoc networks to be adopted in medical monitoring scenarios.



## 3 Propofol direct monitoring

2,6-diisopropylphenol (propofol), chemical structure in Fig. 3.1, is a well-known hypnotic agent used in many surgical and critical care settings. Its administration and correct dosage is of vital importance to prevent *Propofol Infusion Syndrome* (PRIS), due to high doses and prolonged administration [120]. PRIS is a sudden complication that, in the majority of the cases to the death of the patient. The main effects are: metabolic acidosis, rhabdomyolysis of skeletal and cardiac muscles, arrhythmias, myocardial failure, renal failure, hepatomegaly and death [121]. Only the early recognition and the immediate cessation of propofol infusion may prevent the fatal outcome of PRIS syndrome.

### 3.1 State-of-the-art

Various technologies have been already presented in the literature for propofol detection. For example chromatographic methods exploiting *High Performance Liquid Chromatography* (HPLC) [122] and *Chromatography-tandem Mass Spectrometer* (C-MS) [123] were used for accurate and efficient drug detection. However, despite the advantages of these techniques, the instrumentation is costly, requiring large quantities of expensive organics, not portable and requires experienced technicians [124, 125].

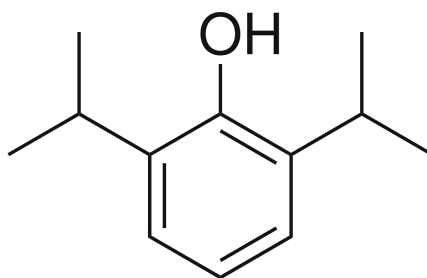


Figure 3.1 – 2,6-diisopropylphenol (propofol).

### Chapter 3. Propofol direct monitoring

---

Another widespread technique is based on the detection of propofol in human breath. In this case real-time monitoring is based on *Proton Transfer Reaction Mass Spectrometry* (PTR-MS) and *Solid-Phase Micro-Extraction coupled with Gas Chromatography Mass Spectrometry* (SPME-GC-MS) [126, 127, 128, 129]. However, by using the MS technique, the same disadvantages listed above are encountered, furthermore, there is still no evidence of strict correlation between propofol concentrations in blood and in breath. Therefore, serum samples are still preferred as background media for propofol monitoring [130].

To assess anesthesia delivery monitoring, including propofol hypnotic agent detection, an easy- and ready-to-use sensor able to guarantee reliable, on-line and accurate measurements over long periods of time has to be provided. This is because a common surgical operation, on average, lasts for up to several hours (~4 h). To meet this need, electrochemical sensors have been found to be exceptionally advantageous for the development of drug monitoring tools [131]; hence their use for propofol detection has already been investigated [132, 133, 134]. These studies have demonstrated that propofol can be easily oxidized; since it is a phenolic compound, and, therefore, it can be electrochemically sensed. However, phenolic oxidation produces free radicals that lead to electro-polymerization processes on the sensor's surface, decreasing the sensitivity over subsequent measurements. This phenomenon is referred to as "electrode fouling" [135, 136]. The electrochemical behavior of propofol and the consequent fouling effect happening at solid state *Glassy Carbon* (GC) electrodes have been investigated in [134]. Fig. 3.2.a shows the ten voltammograms obtained with GC electrodes ( $\varnothing$  3 mm) by consecutive scans (scan-rate = 0.1 V/s) at  $10^{-4}$  M propofol in  $10^{-2}$  H<sub>2</sub>SO<sub>4</sub>. After the first scan (red in Fig. 3.2.a) four peaks are evident; however, only the peak between 0.7 V and 0.9 V is related to the propofol direct oxidation. The other growing peaks (between 0.4 V and 0.6 V (oxidation) and between -0.1 V and 0.3 V (reduction) come from the electrochemically active layer which is deposited on the GC electrode surface with subsequent CV scans (fouling effect). After these 10 CV measurements, the GC working electrode was cleaned by running CV procedure 10 times in  $10^{-2}$  H<sub>2</sub>SO<sub>4</sub> without propofol. Fig. 3.2.b shows the obtained voltammograms from the cleaning procedure. The only two peaks that remained after the cleaning corresponded to the oxidation and reduction of the deposited layer, while the peak around 0.8 V disappeared after the third scan (green line). Even if the electrode passivating effect caused by propofol reaction was not overcome, the effect of this fouling phenomenon has been made clear by this study [134].

To overcome this unpleasant phenomenon, a recent study proposed the use of a polymeric membrane-coated electrochemical sensor [137, 133]. The polymeric membrane was realized by *PolyVinyl Chloride* (PVC) solution (PVC polymer, plasticizer, electrolyte, ion-exchange salt and solvent composition). They obtained a detection limit of  $0.012 \pm 0.004$   $\mu$ M for propofol sensing in serum-like media (containing physiologically relevant levels of albumin (5%) and *Ascorbic Acid* (AA) (3 mM) AA and paracetamol (1mM) as interfering agents). However, despite the promising results in terms of detection limit and resistance to fouling, the membrane deposition process on the electrode surface is very critical and not straightforward for standardization since proper thickness and uniformity of the polymeric layer has to be maintained.

### 3.2. Polymeric membrane-coated carbon *Screen Printed Electrodes* (SPEs)

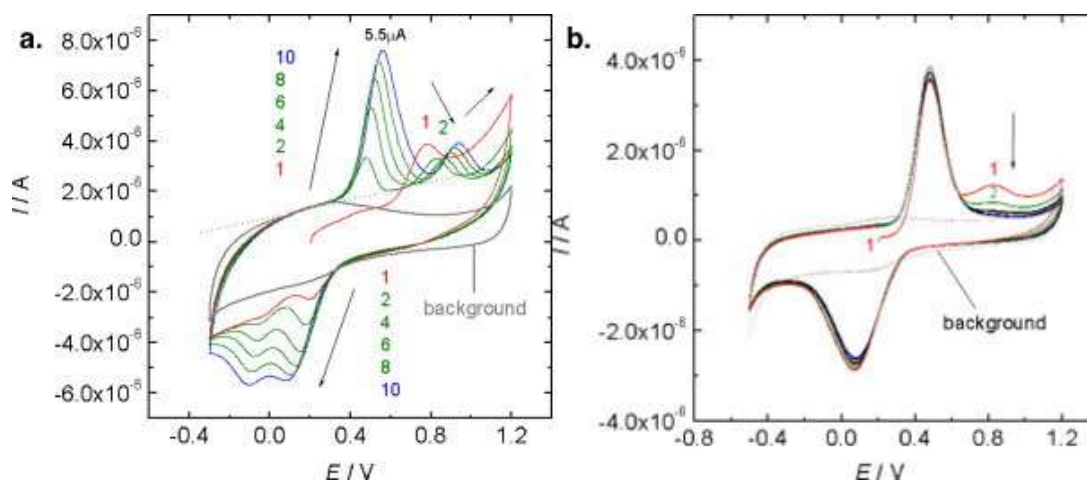


Figure 3.2 – Electrochemical CV characterization of propofol (reprinted from [134]).

Moreover, as an additional hurdle, PVC membrane-coated sensors are not able to ensure physical and mechanical stability for long-term use [138].

Recently, *Molecular Imprinted Polymer* (MIP) biosensors have been also investigated for propofol detection [139]. Promising results have been obtained from this study, but variability in the fabrication process can lead to heterogeneity in the of pore size and binding sites [140], resulting in sluggish mass transport - not adequate for drug monitoring over a long period of time [141]. Therefore, mature systems for the long-term continuous monitoring of propofol have yet not been developed.

In the following sections, the analysis to identify an optimal sensor for long-term propofol sensing will be described in all its investigative phases. The main objective of this research activity was to obtain and validate a ready-to-use and robust point-of-care sensor to be integrated in the overall system described in Section 1.3. The effects of different electrode materials on propofol electro-oxidation and the fouling phenomenon have been widely studied to fully understand the reaction mechanism.

### 3.2 Polymeric membrane-coated carbon *Screen Printed Electrodes* (SPEs)

As a first attempt for propofol detection while avoiding the fouling effect, we have implemented the approach presented in [133]. Therefore a PVC coated electrode has been constructed and tested.

Table 3.1 – PVC membrane composition.

PVC elements	Components	Quantities	%
polymer	PVC	25.5 mg	25
plasticized	DOS	49.5 mg	50
electrolyte	ETH500	21.5 mg	22
ion-exchange salt	NaTFPhB	3 mg	3
solvent	THF	2.5 ml	-

### 3.2.1 Materials and methods

Propofol was purchased by TCI Chemicals. Stock solution of 5.4 mM was obtained by diluting the 5 $\mu$ l of pure propofol in 5 ml of NaOH 0.1 M. Subsequent propofol dilutions have been done in *Phosphate Buffer Saline* (PBS) (10 mM, pH:7.4) to obtain the concentrations of: [9.9 - 19.6 - 38.5 - 56.6 - 80.5]  $\mu$ M for sensor calibration.

For membrane production, the chemicals are listed in Table 3.1, all the compounds are selectophore and were provided by Sigma Aldrich (Switzerland).

Two Carbon SPEs from DropSense (DS-110) have been used as electrochemical cells. One SPE was modified with the PVC membrane following the procedure described in Section 3.2.2 and used as WE (4 mm  $\varnothing$ ), the other SPE as carbon CE and silver RE. A Metrohm Autolab system (PGSTAT 302N) was used to run the CV experiments applying voltages in the range of [-0.3 - 1.4] V with 0.1 V/s scan-rate. *Scanning Electron Microscopy* (SEM) images have been performed with FEI XL30 (XLF-30) SFEG (*Interdisciplinary Center for Electron Microscopy* (CIME) at EPFL) in *Secondary Electrode* (SE) mode with accelerating voltage of 10 KV, magnitude 1200x and *Working Distance* (WD) of  $\sim$  10.

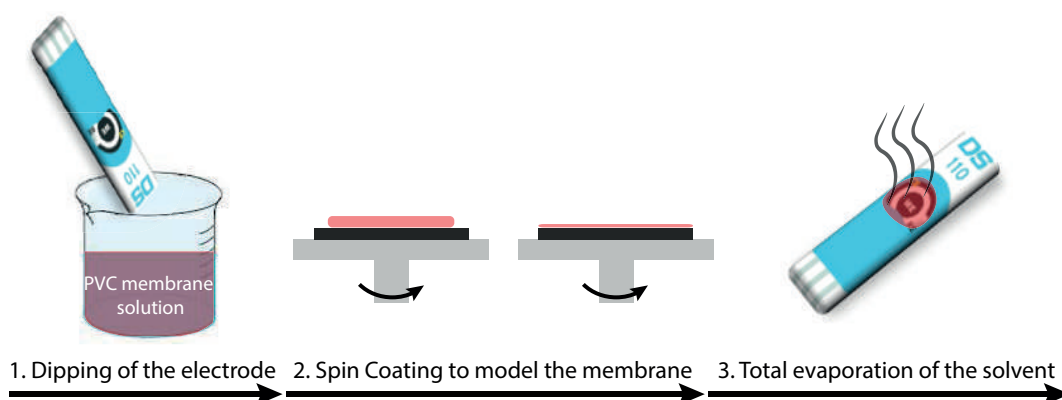


Figure 3.3 – Sketch of the process for PVC membrane deposition on C-SPE.

### 3.2. Polymeric membrane-coated carbon *Screen Printed Electrodes* (SPEs)

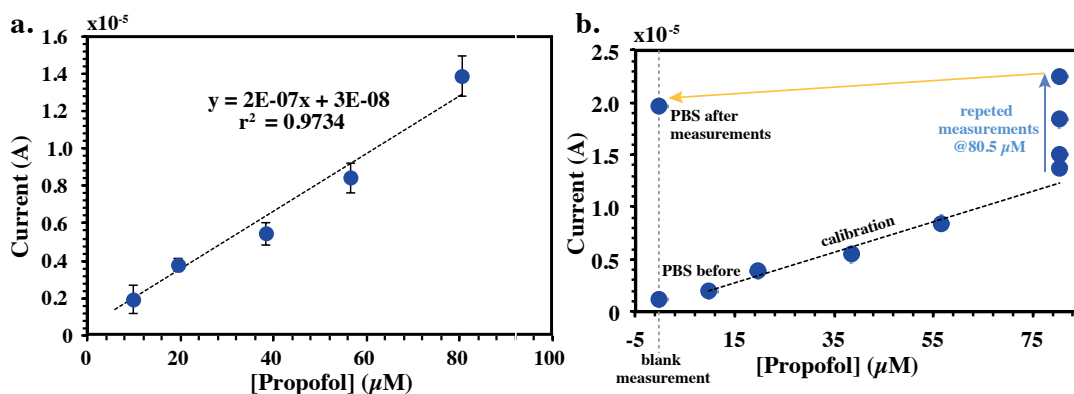


Figure 3.4 – a) Calibration line for propofol detection in PBS at PVC modified C-SPE surface, b) fouling effect visible after calibration procedure: the measured currents for *blank measurement* and the *PBS after measurements* are not corresponding.

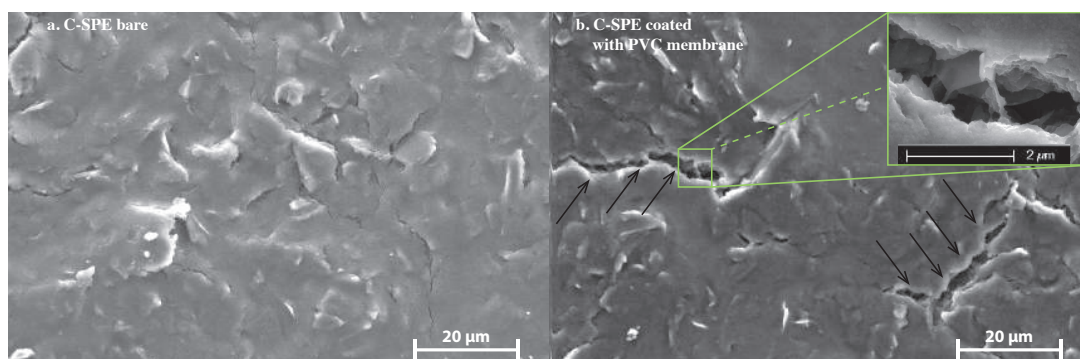


Figure 3.5 – SEM image of: a) bare carbon (C) SPE and b) PVC membrane coated C-SPE. In the zoom insertion, the detail of a PVC membrane fracture is shown.

#### 3.2.2 Electrode preparation

Carbon SPEs from DropSense (DS-110, C-WE of 4 mm  $\varnothing$ ) have been used as solid electrode substrate. To deposit the PVC membrane on the electrode the procedure depicted in Fig. 3.3 has been followed. The SPE was dipped in the PVC membrane solution (realized with the formulation in Table 3.1), then a spin coating action was performed to model the membrane in order to obtain a thin layer on the SPE surface. For this step a *spin coater model SCV* from LOT Quantum Design has been used. Finally the electrode was kept at room temperature until the total evaporation of the solvent. Before using the electrode for measuring propofol, it was dipped for 15 minutes in PBS solution as a conditioning step.

#### 3.2.3 Results and limitations

The PVC coated electrode has been characterized both for propofol electrochemical direct detection and with SEM analysis. Fig. 3.4.a shows the calibration line obtained by testing three

different electrodes with increasing propofol concentrations in PBS background solution. We have obtained a sensitivity of  $1.63 \times 10^{-02} \pm 1.58 \times 10^{-01} \mu\text{A}/\mu\text{M}$ , as the slope of the calibration line, and a LOD of  $6.38 \mu\text{M}$ . However, even if with the membrane coating on the electrode's surface, fouling effect was still visible after multiple measurements as shown in Fig. 3.4.b. Indeed, if performing multiple CV scans with  $80.5 \mu\text{M}$  propofol solution, the peak current was increasing and if a blank solution was measured immediately after (labeled as *PBS after measurements* in the figure), the current was not coming back to the initial value (*PBS before*). This effect derives from the formation of the electroactive passivation layer.

To understand the reason for this fouling effect, we have characterized the electrode surface through SEM analysis. Fig. 3.5 shows the C-SPE before and after the membrane deposition. As visible in Fig. 3.5.b, the membrane is not uniformly deposited with evident fractures, resulting in a non-effective protection against fouling. This is due to the fact that SPEs have not been left with a smooth surface after their fabrication process, and the spin coating process makes it extremely difficult to obtain a reproducible membrane that is thin enough. Furthermore, it is difficult to maintain the physical and mechanical properties of the PVC-coated sensors for ensuring its performance is long-term detection, as demonstrated by [138]. This is a crucial point in case of anesthesia monitoring.

For these reasons, alternative sensing platforms have been investigated to provide ready-to-use, low-cost and reliable propofol detection over long-time monitoring.

In the following section, the effect of BDD electrode and PGE materials on propofol electro-oxidation and fouling will be deeply analyzed to fully understand the chemical reaction mechanism and to compare their electrochemical performance in long-time monitoring.

### 3.3 BDD and PGE electrodes

The performance of BDD electrodes and PGEs were tested and compared in terms of sensitivity values and resistance to fouling over long-term propofol monitoring.

BDD was chosen for its low catalytic activity for hydrogen and oxygen that allows for a wider application of potential ranges [142] and because of the elevated mechanical strength and reduced chemical activity [143].

On the other hand, disposable PGE offers excellent electrochemical reactivity leading to high sensitivity, good mechanical rigidity, low cost, low background current, wide potential window, chemical inertness and easy miniaturization [144].

First, we characterized the fouling effect at the bare surface of the two electrodes by performing several propofol calibrations one after the other. Then we developed, tested and compared two surface cleaning methods to improve the electrode's performance over time by preventing the fouling. The two optimized cleaning procedures were carried out: 1) in *Phosphate Buffer Saline* (PBS) and 2) in *sodium hydroxide* (NaOH). By running one of the two cleaning procedures every six propofol measurements, we achieved a successful and reliable propofol detection of over 4 h.

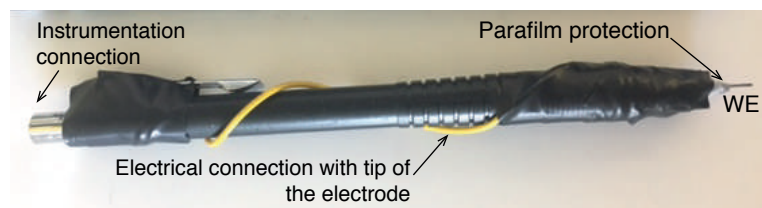


Figure 3.6 – PGE configuration: WE mine inside mechanical holder.

Table 3.2 – CV and DPV procedures for propofol detection at BDD electrode and PGE.

Technique		BDD	PGE
CV	potential range	[+0.75 - +1.4] V	[+0.2 - +1.4] V
	scan rate	0.1 V/s	0.1 V/s
DPV	potential range		[0.0 - +1.1] V
	interval time		0.2 s
	modulation amplitude	-	50 mV
	modulation time		50 ms
	scan rate		0.025 V/s

### 3.3.1 Materials and methods

Propofol stock solution and subsequent dilution concentrations were obtained as before (Section 3.2.1). NaOH and KNO<sub>3</sub> and heat inactivated human male serum (H3667-100ML) were purchased from Sigma Aldrich (Switzerland). 10 ml of Ferro(ferri)cyanide 5 mM solution for electrochemical area evaluation was obtained by mixing 0.0211 gr potassium hexacyanoferrate trihydrate II with 0.0165 gr potassium hexacyanoferrate III in PBS (10 mM pH: 7.4). All the chemicals were purchased by Sigma Aldrich.

Rotating disk BDD/*Silica substrate* (Si) WEs (electro active area of 12.4 mm<sup>2</sup>, 700 ppm) were purchased from NeoCoat SA. Before using BDD, a preliminary CA conditioning at +2.2 V for 900 s keeping the electrode in 0.1 M KNO<sub>3</sub> solution was recommended by the Supplier for proper activation of the electrode surface.

Pencil mines with diameter of 0.5 mm were used as PGE WE and a commercial mechanical holder was adopted and modified by soldering a copper wire to guarantee electrical contact between the WE tip and the instrumentation connection part, as shown in Fig. 3.6. The PGE was dipped for 8 mm into the solution to obtain an electro-active area comparable with the BDD electrode (considering the mine as cylindrical:  $A_{base} + A_{lateral}(\pi \times (0.5/2)^2) + (2 \times \pi \times (0.5/2) \times 8) = 12.7 \text{ mm}^2$ ). An Ag|AgCl|3.0 M KCl from Metrohm have been used RE and a Pt wire as CE. CVs and DPVs were performed with a Metrohm Autolab PGSTAT 302N potentiostat, and data analysis and plotting were performed in *Matlab* R2013a and *Excel* 2011. In particular, a *Matlab* script was implemented for the peak height evaluation with respect to a constant baseline. The constant baseline is selected and set for each calibration as the average value of the ordinates of the points in the area before the peak (steady state). CV and DPV procedures' parameters for BDD electrodes and PGEs are summarized in Table 3.2.



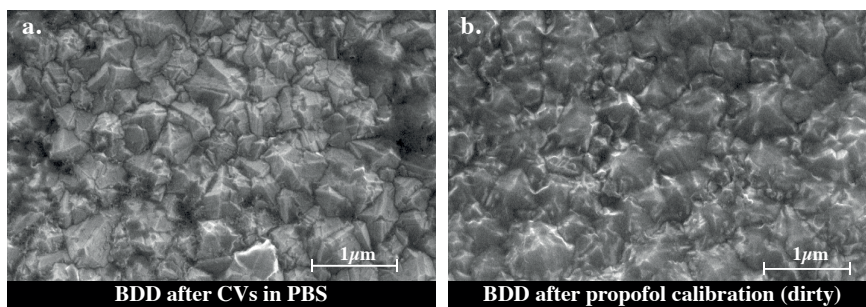


Figure 3.7 – SEM images of BDD electrode: a.) bare electrode after 5 cycles of CV in only PBS (background electrolyte), and b.) after one propofol calibration.

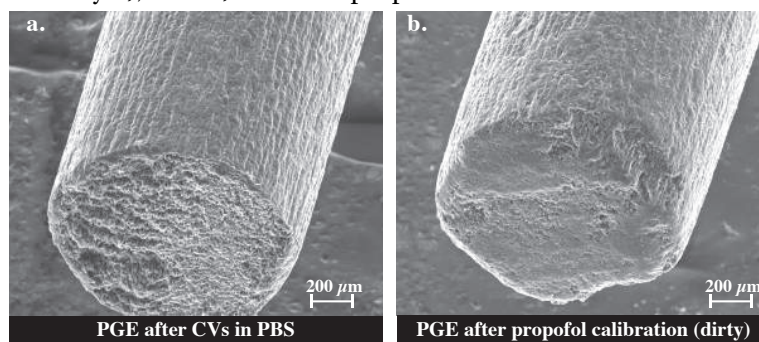


Figure 3.8 – SEM images of PGE: a.) bare electrode after 5 cycles of CV in only PBS (background electrolyte), b.) after one propofol calibration.

The sensitivity and the LOD values were evaluated for both the electrodes via CV technique by performing five subsequent sets of 5-point-calibrations. LOD was also experimentally determined in serum by performing DPV at null and at  $0.85 \mu\text{M}$  propofol concentration and by registering an increase of the blank signal when propofol was injected. An XLF30-FEG scanning electron microscope was used for SEM analysis. The *Secondary Electrons* (SE) images were taken by applying an accelerating voltage of 20 kV and at a WD of 9.9.

### 3.3.2 Fouling characterization at PGE and BDD electrodes

#### Surface characterization of the fouling layer

The electrode-fouling effect at BDD and PGE surfaces was investigated through SEM surface characterization.

Surface images of the BDD electrode have not shown any evidence of fouling, as visible in Fig. 3.7. On the contrary, the surface of the PGE shows traces of fouling from SEM analysis, as visible in Fig. 3.8.b. What is evident from this comparison is that, while in Fig. 3.8.a the bare PGE is characterized by graphite striae on the lateral surface and small pointed tips at the base, after a propofol calibration a deposited layer is clearly visible on both the lateral and the base surfaces of the electrode Fig. 3.8.b. This passivating layer of propofol fouling covers the



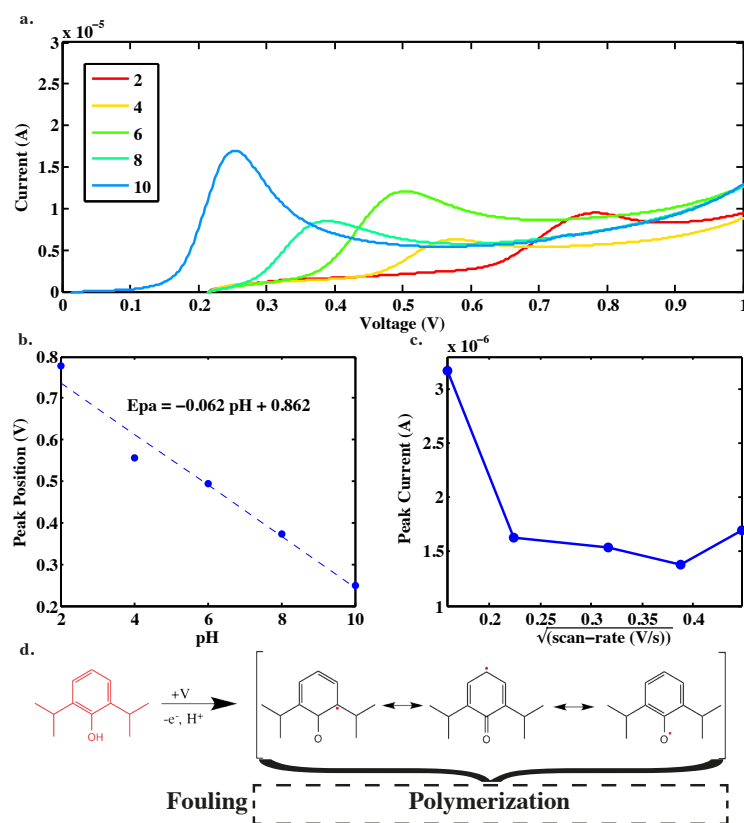


Figure 3.9 – pH and scan-rate studies with 30  $\mu\text{M}$  propofol electro-oxidation at PGE: a.) CVs in solutions at different pH [2 - 10], b.) linear dependency between peak position and pH variation, c.) peak current amplitude VS square root of scan-rate, and d.) suggested mechanism of propofol electro-oxidation reaction..

superficial structures of the electrode and causes the decrease of sensitivity registered by the electrochemical results.

### Electrochemical characterization of the fouling layer

To better characterize the mechanism of propofol electro-oxidation that leads to the formation of the fouling layer, pH and scan-rate effects were also investigated.

In fact, by studying the effect of pH on propofol electro-oxidation it is possible to deduce the number of electrons exchanged in the reaction. Two cycles of CV were performed in 30  $\mu\text{M}$  propofol solution at different pH values in the range between 2 and 10. As it is evident from Fig. 3.9.a, the CV peak current (height) and peak potential (position) are highly influenced by the pH of the solution. In particular, although there is not a trend for peak current, it is clear that the peak potential shifts to more negative values for higher pH values. A plot of the anodic peak ( $E_{pA}$ ) potential versus pH exhibits a slope value equal to 62 mV (Fig. 3.9.b) that is close

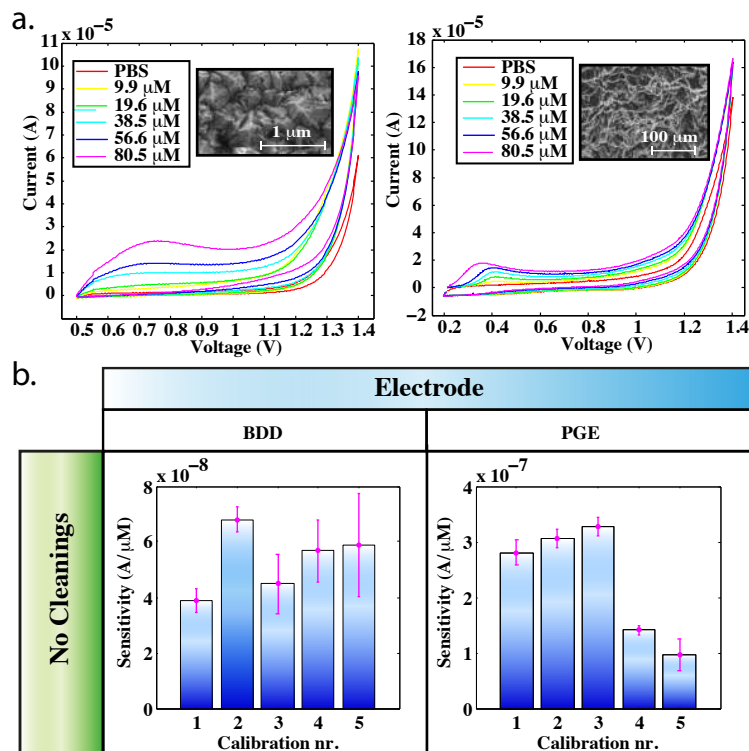


Figure 3.10 – a) Typical CV curves at increasing propofol concentrations ( $[9.9 - 80.5] \mu\text{M}$ ) at PGE and BDD surfaces; (b) change in sensitivity (S) values for BDD and PGE with respect to subsequent propofol calibrations performed in PBS (pH:7.4). Error bars represent the standard deviation from the linear regression analysis performed for S evaluation ( $n = 5$ , points in each calibration).

to the 59 mV predicted by the Nernst equation for the process involving an equal number of protons and electrons [145]. This result demonstrates that propofol electro-oxidation involves the exchange of one proton and one electron [146]. In addition to pH, the effect of different scan-rate values [0.025; 0.05; 0.1; 0.15; 0.2] V/s was also investigated by performing CVs in 30 μM propofol solution. In Fig. 3.9.c, the peak current is plotted versus the square root of scan-rate obtaining a non-linear trend. This proves that the reaction is not a diffusion-controlled process, since it is characterized by a combination of adsorption and fouling phenomena at the electrode's surface, in agreement with the previous characterization results.

Therefore, considering the results obtained from electrochemical and surface characterizations of the electrodes, and congruently with previous works [147], the chemical oxidation of propofol is illustrated in Fig. 3.9.c. When the positive potential is applied, propofol is oxidized by one electron and one proton removal; three types of intermediate phenoxy radicals would possibly form and initiate the polymerization process that results in electrode fouling (in the dashed frame).

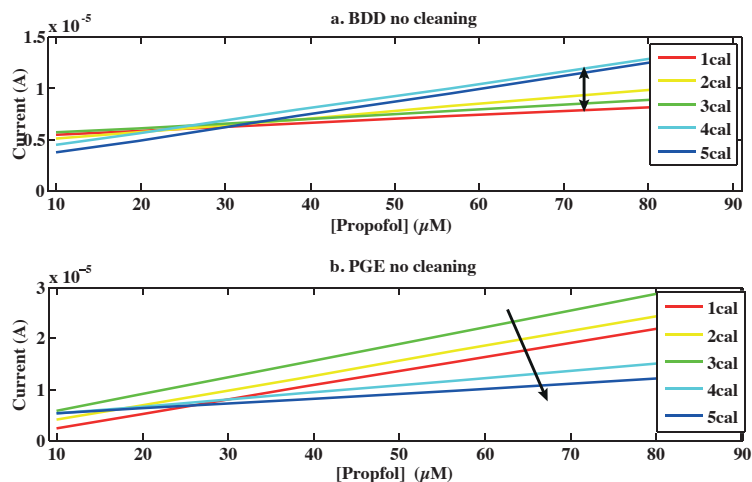


Figure 3.11 – The effect of fouling on calibration lines for a) BDD and b) PGE without intermediate cleanings. The lines were drawn for five concentrations [9.9 - 19.6 - 38.5 - 56.6 - 80.5]  $\mu\text{M}$ .

After having characterized electrochemical and surface properties of the fouling effect at both PGE and BDD electrodes, we wanted to estimate the fouling resistance and the sensitivity of these two different C-based materials.

Electrochemical behavior of the two electrodes have been studied by performing five CV propofol calibrations (five points each) one after the other. Typical voltammograms are depicted in Fig. 3.10.a, while the sensitivity values obtained over the five calibrations are reported in Fig. 3.10.b. A higher sensitivity of  $(2.3 \pm 1.0) \times 10^{-07} \text{ A}/\mu\text{M}$  is obtained by the PGE compared to the one of  $(5.3 \pm 1.2) \times 10^{-08} \text{ A}/\mu$  evaluated for the BDD electrode. Nevertheless, both the electrodes appear to be affected by the fouling effect due to propofol oxidation reaction. The undesired phenomenon is more evident in PGE measurements where a sharp reduction of the sensitivity is visible after the third calibration. However, the BDD sensitivity, even if it obtains similar values in all the consecutive calibrations, is affected by a high variability limiting the reproducibility. To further underline this phenomenon, the obtained calibration lines are also reported in Fig. 3.11.

### 3.3.3 Cleaning procedures

Two cleaning procedures have been implemented and tested for eliminating the effects of fouling caused by propofol oxidation at BDD and PGE electrodes. The electrochemical cleaning was performed after every six CV measurements.

- **NaOH cleaning:** ten CV cycles in 10 ml of 0.1 M NaOH solution. The applied potential range is the same as the one for drug sensing ([+0.75 - +1.4] V for BDD and [+0.2 - +1.4] V for PGE).
- **PBS cleaning:** CA in 10 ml of 10 mM PBS (pH: 7.4) performed by applying +1.4 V for 30 s

### Chapter 3. Propofol direct monitoring

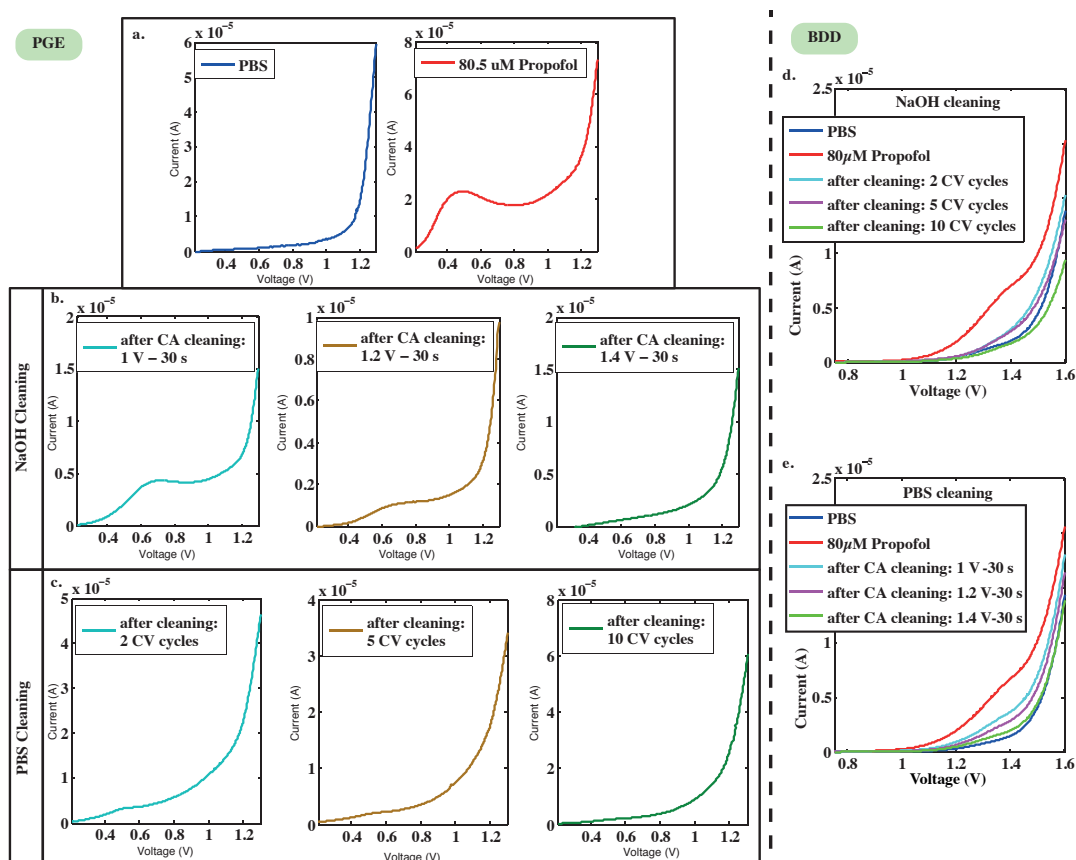


Figure 3.12 – Cleaning optimization process for PGE (left) and BDD electrode (right). PGE cleaning tests: a.) anodic CV scan without (blue) and with (red) propofol in solution; b.) NaOH cleaning procedure by increasing the number of CV scans; c.) PBS cleaning by increasing the applied voltage and keeping constant the CA time. BDD cleaning analysis: a) effect of number of CV cycles for NaOH cleaning, b) effect of applied potential for CA based PBS cleaning.

without stirring.

The cleaning criteria were obtained from an optimization process in which the effect of different combinations of parameters was investigated. As concerns the NaOH cleaning procedure, the effect of number of scans (2, 5 and 10) has been tested; while for the PBS cleaning procedure different fixed potentials have been applied (+1, +1.2 and +1.4 V) for a constant duration (30 s). Results from the optimization study for PGE and BDD electrode are reported in Fig. 3.12.

#### 3.3.4 Results and discussion

To avoid the formation of the passivating layer at BDD and PGE surfaces (Fig. 3.10 and Fig. 3.11), and to stabilize the sensitivity values over time, two kinds of electrochemical cleaning procedures have been introduced between one calibration and the subsequent one.

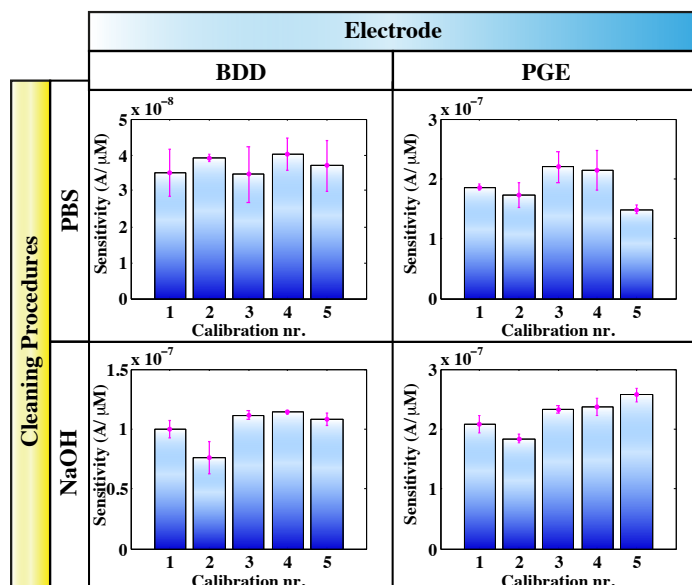


Figure 3.13 – Sensitivity (S) values evaluated for PGE and BDD with respect to calibration number (nr) and type of intermediate cleaning (PBS and NaOH). Error bars are the standard deviation from the linear regression analysis for S evaluation ( $n = 5$ , points per calibration).

Fig. 3.13 shows the results of sensitivity for BDD and PGE electrodes over each calibration curve (up to five) with cleaning procedures; *i.e.* PBS or NaOH cleaning, applied in between two subsequent calibration curves. It is clear that, even if both PBS and NaOH cleanings have an improvement against the fouling effect, NaOH guarantees the best maintenance of the electrode over time. In particular, the sensitivity values after NaOH cleaning are higher and characterized by the lowest variability compared to use without cleaning or after cleaning in PBS. To underline further the success of the intermediate cleaning procedures, calibration lines for PGE and BDD electrodes are shown in Fig. 3.14.

We have also studied the cleaning effects by performing SEM analysis at PGE, since for BDD the fouling was not evident. After performing NaOH or PBS intermediate cleanings the passivating layer that was covering all the PGE surface in Fig. 3.8.b is removed and the morphology of the PGE is recovered back to its original bare structure, as visible in Fig. 3.15.

As support of SEM imaging observations, variations in PGE *Electro-Active Surface Area* (EASA) were evaluated by performing CVs in 5 mM ferro(ferri)cyanide ( $K_3[Fe(CN)_6]/K_4[Fe(CN)_6]$ ) [148] before and after the cleanings. Fig. 3.16 shows the voltammograms acquired during this analysis. The EASA of the electrode has been evaluated from Randles-Sevick equation as follow:

$$A = \frac{i_p}{286.6 \times n^{3/2} \times D^{1/2} \times C \times \nu^{1/2}} \quad (3.1)$$

Where  $i_p$  is the anodic peak currents from CV plot,  $D$  is the diffusion coefficient ( $cm^2/s$ ),  $C$  is

### Chapter 3. Propofol direct monitoring

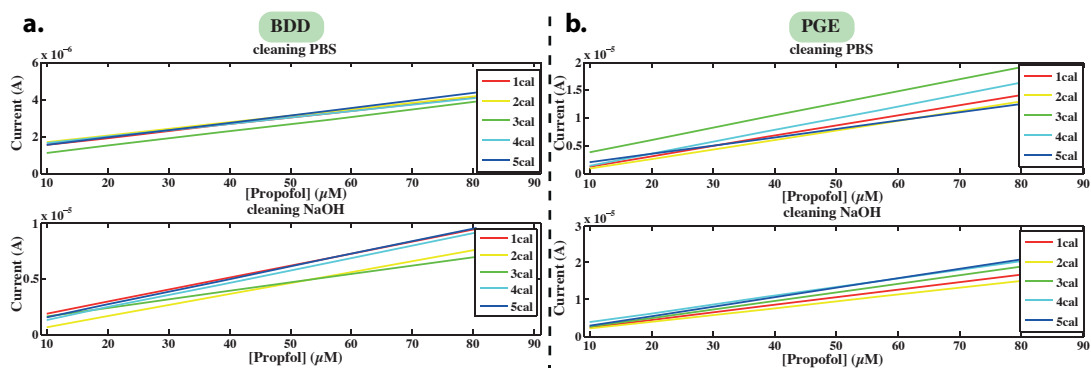


Figure 3.14 – Effect of intermediate cleanings (PBS and NaOH) in calibration lines for: a) BDD electrode and b) PGE. The lines were drawn for five concentrations [9.9 - 19.6 - 38.5 - 56.6 - 80.5]  $\mu\text{M}$ .

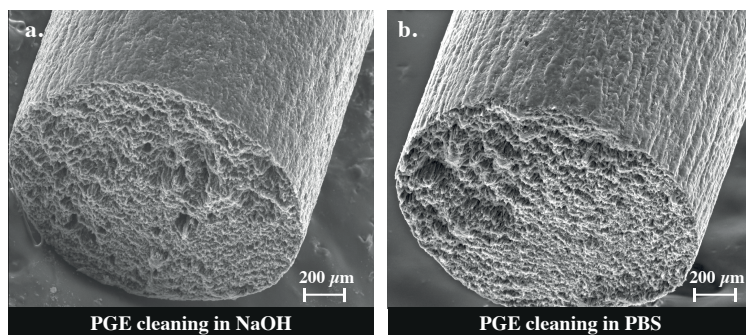


Figure 3.15 – SEM images of PGE: a) after NaOH and d) after PBS cleanings.

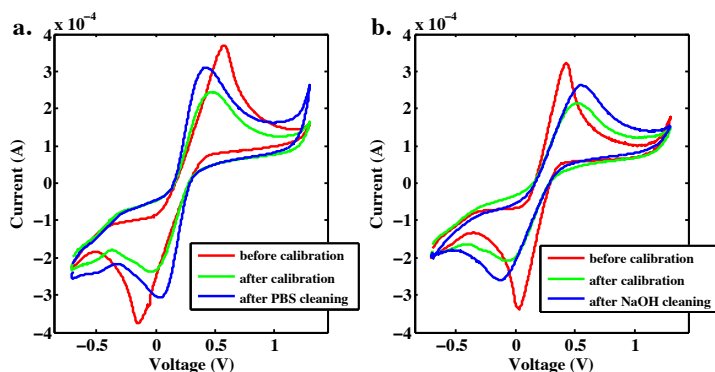


Figure 3.16 – Electrochemical characterization in ferro(ferri)cyanide (5 mM each) of PGE surface after a) PBS and b) NaOH cleanings.

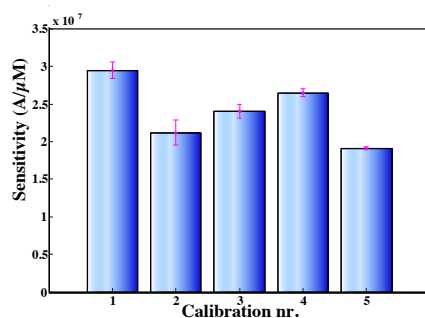


Figure 3.17 – PGE S values with respect to calibration nr where each time an intermediate CA-cleaning step is performed in PBS solution with 80  $\mu\text{M}$  propofol. Error bars are the standard deviation from the linear regression analysis performed for S evaluation ( $n = 5$ , points per calibration).

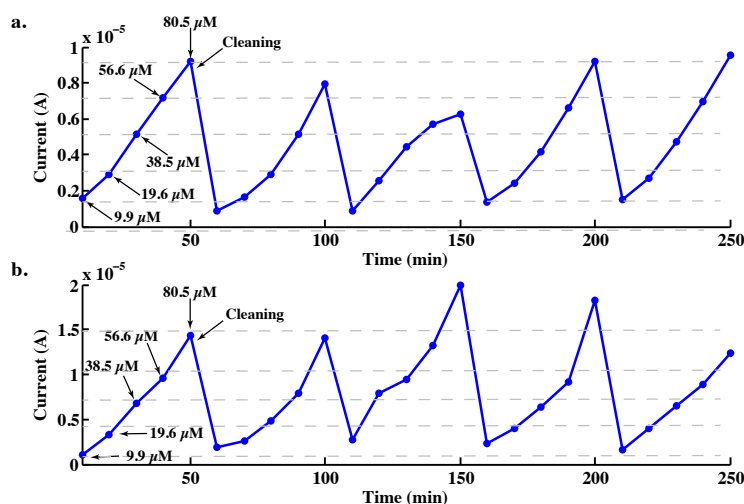


Figure 3.18 – Long-term electrochemical propofol monitoring with best electrode-cleaning combinations: a) BDD electrode with NaOH cleaning and b) PGE with PBS cleaning. The arrows indicates the points where the propofol concentration was changed and where cleaning procedure was implemented. Successive cycles have the same trend in concentration as the one in first cycle, then demonstrating the success of the intermediary cleanings being used.

the concentration of the electro-active species in the bulk solution ( $\text{mol}/\text{cm}^3$ ), and  $v$  is the scan-rate ( $\text{V}/\text{s}$ ). As visible in Fig. 3.16 the ferro(ferri)cyanide peaks decrease after propofol calibration with 5 concentrations. That shows the effect of propofol polymerization on the active area of the electrode. After PBS and NaOH cleaning the peaks are recovered again. This is because the cleaning procedures are effectively regenerating the surface of the electrode. According to the results before and after cleanings, it is concluded that the EASA is recovered of 99.6% and 71.2% for PBS and NaOH cleanings, respectively. From this analysis, we concluded that BDD electrode sensitivity values were more stable, especially if applying NaOH cleaning step, while PGE is more sensitive to propofol (shown in Fig. 3.13) and, therefore, by adopting a

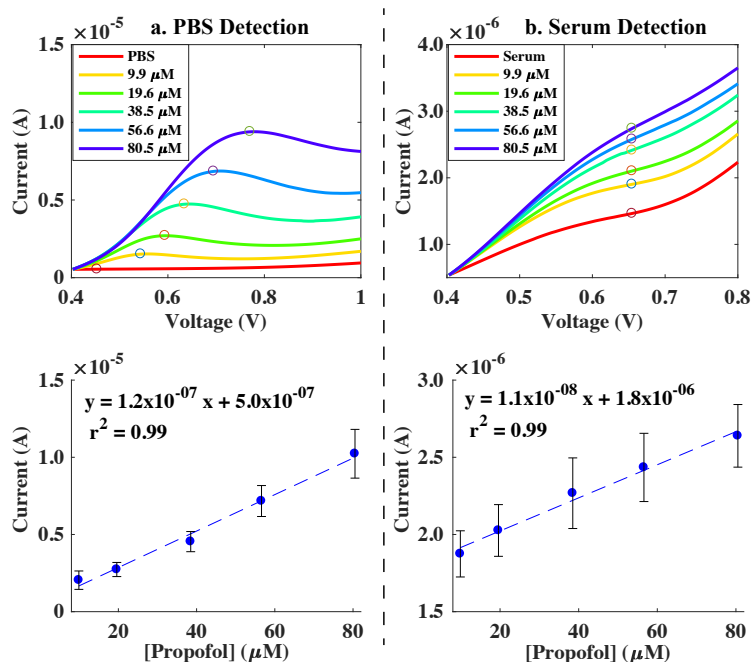


Figure 3.19 – pH and scan-rate studies with 30 μM propofol electro-oxidation for PGE: a.) CVs in solutions at different pH [2 - 10], b.) linear dependency between peak position and pH variation, c.) peak current amplitude VS square root of scan-rate, and d.) suggested mechanism of propofol electro-oxidation reaction..

proper cleaning procedure, it is favorable for performing direct propofol detection in human serum. Moreover, since it could be more convenient to avoid extra chemicals, such as NaOH, so as not to complicate the system design and reduce the measurement time, the use of PBS cleaning is preferable for the final application. To that aim, we also tested the cleaning in PBS with 80 μM propofol concentration inside and comparable results with only PBS solution are obtained, as in Fig. 3.17. We proved that the cleaning is successful also in presence of the analyte itself. Therefore the two best electrode-cleaning combinations are: i) PGE with PBS cleaning, identified as the most suitable in view of the final application, and ii) BDD with NaOH cleaning, which was providing the best performance.

We finally demonstrated the long-term monitoring properties for both these two selected combinations by performing five calibrations (5-concentrations each) resulting in 25 subsequent measurements adding up to 4 h of total measurement time. According to the diagnostic definition in [42], we have achieved a continuous monitoring system by measuring one sample every 10 minutes (6 measurements for one hour). However, if we estimate the time required by combining cleaning and measuring procedures, the system provides a sample every minute that is even better in the case of drugs with fast clearance, such as propofol. In Fig. 3.18 we have reported the measurements in time both for PGE with PBS cleaning and for BDD with NaOH cleaning. Therefore, we demonstrated the success of the used cleaning processes.



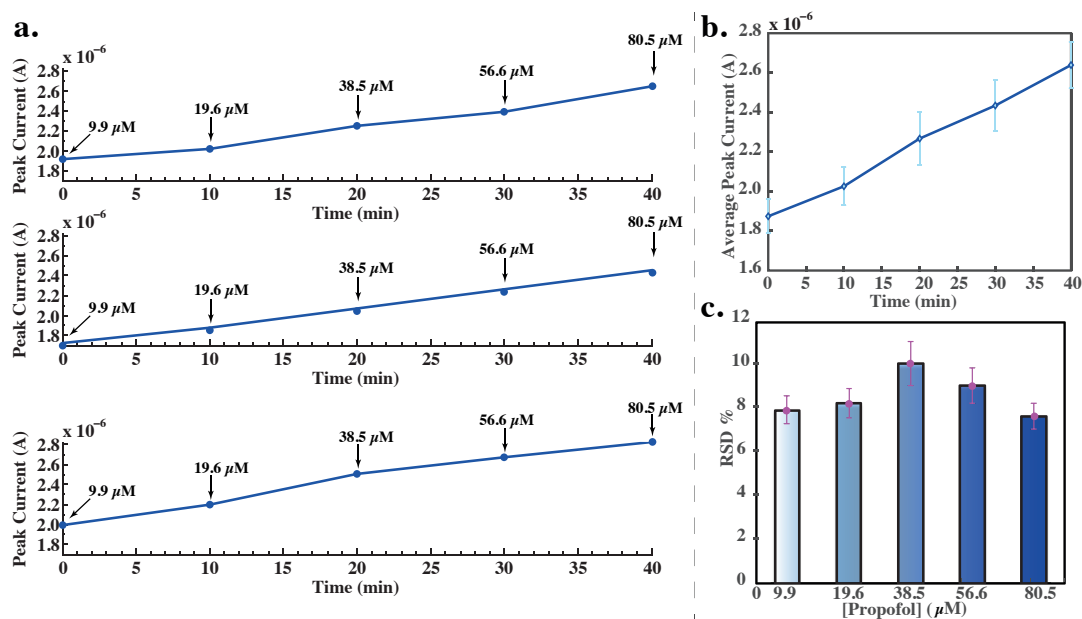


Figure 3.20 – Reproducibility of propofol measurements in serum with PGE: a) propofol oxidation peak trend in time of three different PGE sensors running DPV procedure at various concentrations (9.9 - 19.6 - 38.5 - 56.6 - 80.5)  $\mu\text{M}$ , b) change in oxidation peak current by time and c) bar graph of RSD% (<15%).

### 3.3.5 Serum detection

After the optimization of the cleaning parameters, the analysis of pH and scan-rate effects and the identification of the best electrode-cleaning combination (considering the final application, PGE with PBS cleaning was preferred for the highest propofol sensitivity), it was possible to verify the detection of propofol inside human serum. PGEs and DPV electrochemical technique have been used for this aim. In particular, DPV was preferred to CV since it is a more sensitive technique [149]; hence, more suitable for serum measurements. The same PBS cleaning procedure was run every 6 measurements as for CVs. As preliminary step, propofol calibration was carried out in PBS to identify the oxidation peak position and the best potential range, as shown in Fig. 3.19.a. The same set of calibrations was then carried out in undiluted human serum. Fig. 3.19.b reports a visible oxidation peak in the same potential range within PBS. The peak current values are linearly related with the increase of the propofol concentrations. Therefore, a linear calibration equation with an  $R^2$  of 0.99 was evaluated by the regression analysis ( $n = 3$ ). The slope of the calibration lines corresponds to the electrode's sensitivity:  $1.2 \times 10^{-1} \mu\text{A}/\mu\text{M}$  and  $1.1 \times 10^{-2} \mu\text{A}/\mu\text{M}$  for PBS and serum detection, respectively. Evidently, there is a drop (one order of magnitude) in sensitivity in serum solution compared to the one in PBS. This is due to the fact that propofol is highly lipophilic drug and binds to human serum components more than 95%, in particular to albumin [150]. Therefore, only a small fraction (called "free drug concentration") is electrochemically detectable. Furthermore, serum is a complex solution rich in components that also affect the electrode's performance by

### Chapter 3. Propofol direct monitoring

reducing the sensitivity. However, from the obtained calibration curve, the LOD was calculated to be  $0.82 \mu\text{M}$  with 9.3 (%) *Relative Standard Deviation* (RSD) and this concentration is in the physiological range ( $[1 - 60] \mu\text{M}$ ).

Fig. 3.20 compares the performance over time of three different PGEs. It is evident that the three trends are very similar proving the reliability and the stability of the monitoring. Measurement reproducibility was evaluated by estimating the RSD(%) values for every step of the calibration considering the three tested PGEs, reported in Fig. 3.20.c. An average value of 8.6 (%) RSD was obtained, which is considered acceptable for medical applications [151]. This reflects the precision across the three different electrodes that were tested.

### 3.4 Different compositions of PGEs

As a consequence of the results obtained in the previous Section 3.3, it emerged that PGE is the most suitable electrode for propofol detection since it ensures reliable monitoring over long time periods. Since the pencil graphite is a composition of graphite, clay and a binder (typically wax, resins or high polymer) in various percentages, we decided to investigate which composition guarantees the best performance in terms of sensitivity and fouling resistance, considered as the ability to remain unaffected by fouling agents that gradually cause the formation of the passivating layer on the electrode's surface [152]. In fact, the lead composition influences both the chemical (*e.g.*, ion exchange) and structural properties (*e.g.*, the degree of disorder and surface morphology) of the pencil graphite mine used as WE. According to the *European Letter Scale*, graphite pencils are marked with letters H (hardness) and B (blackness) and numbers indicating the degree of hardness or blackness. B type leads contain more graphite and are softer, and the harder H type leads have more clay. Therefore, we could test 20 different leads spanning from 9H (the hardest) to 8B (the softest), as in Fig. 3.21.

#### 3.4.1 Materials and methods

The 3-electrode electrochemical cell consisted of a PGE, with different lead compositions, as WE, a K0265 Ag/AgCl electrode from Ametek Scientific Instruments as RE and a Pt wire as

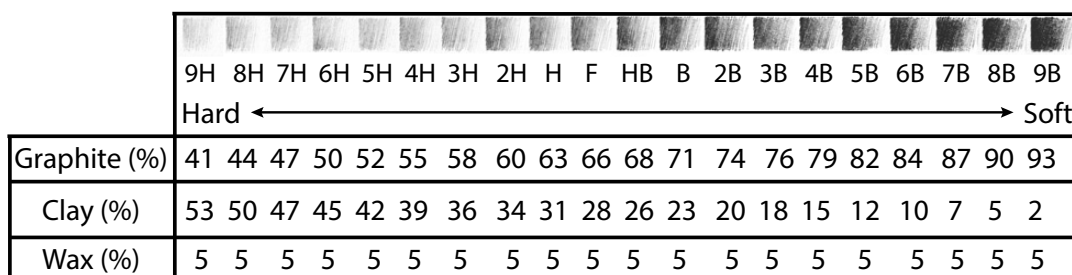


Figure 3.21 – WE lead compositions in wt% of: wax, clay and graphite.

### 3.4. Different compositions of PGEs



Figure 3.22 – Staedtler Mars Lumograph Wood Pencil Set of 20.

CE. A Staedtler Mars Lumograph Wood Pencil Set of 20 (Fig. 3.22) was purchased from Cult Pens (United Kingdom) and used as WEs with different graphite-clay compositions, with wax as binder. The electrode was made by peeling the two ends of the pencil in order to expose the internal lead. One pencil extremity has been used to provide electrical contact with the potentiostat. The other has been cut so as to guarantee a flat surface before being immersed in the analyzed solution. Carbon (C)-SPE (DS-110) from Metrohm has been used as a control electrode to highlight the PGE performance.

CV measurements with applied potentials in the range [+0.2 - +1.4] V and scan-rate of 0.1 V/s were carried out with the PGSTAT 302N Metrohm Autolab. Data analysis and plotting were carried out in *Matlab R2013a*. The propofol oxidation current peak was identified as the maximum current value recorded in the voltage range [+0.7 - +0.8] V.

Two main tests were performed in order to compare the performance in propofol monitoring of different PGE compositions as WE:

- three calibrations with three different WEs with the same composition to verify *inter-electrode* variability.
- five subsequent calibrations with the same WE to test *intra-electrode* variability with time, and fouling resistance;

Since the lead diameter varies according to the pencil graphite compositions, the immersed height of the PGE inside the solution has to be regulated to guarantee a constant EASA of  $\sim 12.6 \text{ mm}^2$ . To further characterize the surface properties of the tested electrodes, also *Electrochemical Impedance Spectroscopy* (EIS) and SEM analysis were carried out. EIS was performed in 5 mM ferro(ferri)cyanide solution by using the Autolab *Frequency Response Analyzer* (FRA), with a frequency range of 0.1 Hz to 100 KHz and AC amplitude of 5 mV. The measured impedance spectra were analyzed in Nova 1.11 software with the Electrochemical circle fit tool. SEM was done with both the XLF30-FEG and the Zeiss Gemini microscopes, with accelerating voltages of 10 kV and 3 kV, respectively.

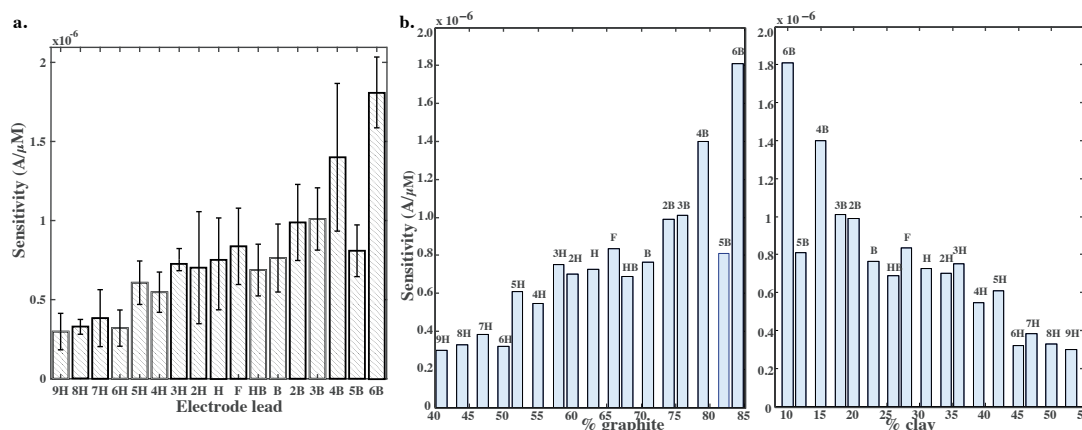


Figure 3.23 – Different representation of electrode sensitivity. a) Diagram of the inter-electrode sensitivity for different PGE compositions and C-SPE. b) Comparison in sensitivity for different wt% of graphite and clay in lead compositions

### 3.4.2 Results and discussion

To investigate the *inter*-electrode variation we have repeated a 5-points CV propofol calibration three times, for all the twenty types of PGEs. From this investigation we found out that no signal was obtained from 7B, 8B, 9B PGEs because they present an immediate fouling effect due to their very soft lead compositions.

Fig. 3.23.a summarizes the resulting sensitivity values estimated for all the other PGE compositions. There is an evident growing trend of sensitivity values with an increase of the graphite content (wt%) in the lead composition. We can notice that the sensitivity values evaluated for 5B and 6B PGEs are affected by high standard deviation that can be justified with their soft composition. Indeed, due to the high graphite content, these leads are extremely soft and fragile so that it is very challenging to obtain the same EASA as the others.

Looking at the sensitivity values, it is possible to identify a range where the  $S \pm \sigma$  is approximately constant. This range is between 3B and 5H PGE leads.

Another representation of the sensitivity variance upon percentage of clay or graphite content is depicted in Fig. 3.23.b. The sensitivity clearly increases with higher wt% of conductive material (graphite), while it decreases with higher wt% of insulating material (clay) in the composition. Therefore, while the graphite-content of the electrode is the key for the electrochemical activity, the clay within it could provide a sort of protective shield against fouling.

To confirm these results, we have evaluated the fouling-resistant properties of the electrodes by performing five subsequent calibrations ( $n = 5$ ) with the same WE. Typical CV calibration curves are reported in Fig. 3.24 for the PGE lead compositions 9H (hardest), F, 3H (intermediate) and 6B (softest). From Fig. 3.24.a and Fig. 3.24.c it is possible to notice that the oxidation propofol peak height current decreases by half the magnitude due to an increase in clay content. Indeed, the clay has an insulation effect on the PGE lead. Conversely, the oxidation

### 3.4. Different compositions of PGEs

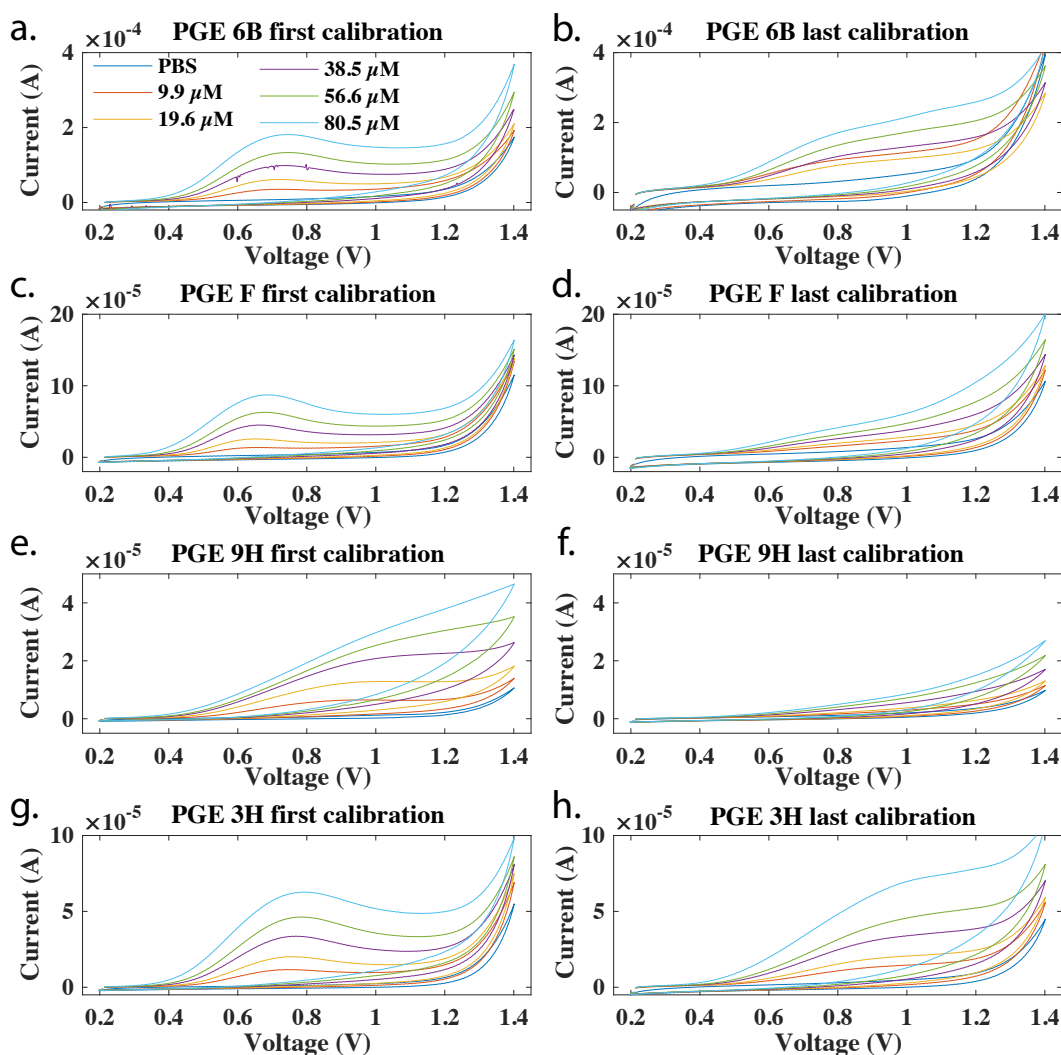


Figure 3.24 – CV curves for the 1<sup>st</sup> and the 5<sup>th</sup> propofol calibrations at PGE: a.) and b.) 6B, c.) and d.) F, e.) and f.) 9H, g.) and h.) 3H lead compositions.

peak becomes more well-defined at higher graphite contents. Furthermore, from Fig. 3.24.b, Fig. 3.24.d and Fig. 3.24.f we can see that all 9H, F and 6B PGEs lose their sensitivity in time. Unlike these, the intermediate 3H lead provides more stable and reproducible results, so that it stands out as a suitable compromise between sensitivity and fouling resistance. Indeed, even if the shape of the oxidative peak varies during successive calibrations, due to modification of the capacitive current after hours immersed in the solution, the peak amplitude, which correlates to the drug concentration, does not change significantly, as shown in Fig. 3.24.g and Fig. 3.24.h. By plotting the change in sensitivity upon five calibrations for various PGE leads, as in Fig. 3.25, the first observation is that when the graphite (wt%) is reduced and the clay (wt%) is increased in PGE lead, it is possible to identify a *switch-point* in clay to graphite ratio for which the fouling effect is less evident in the electrochemical analyses. As a consequence of

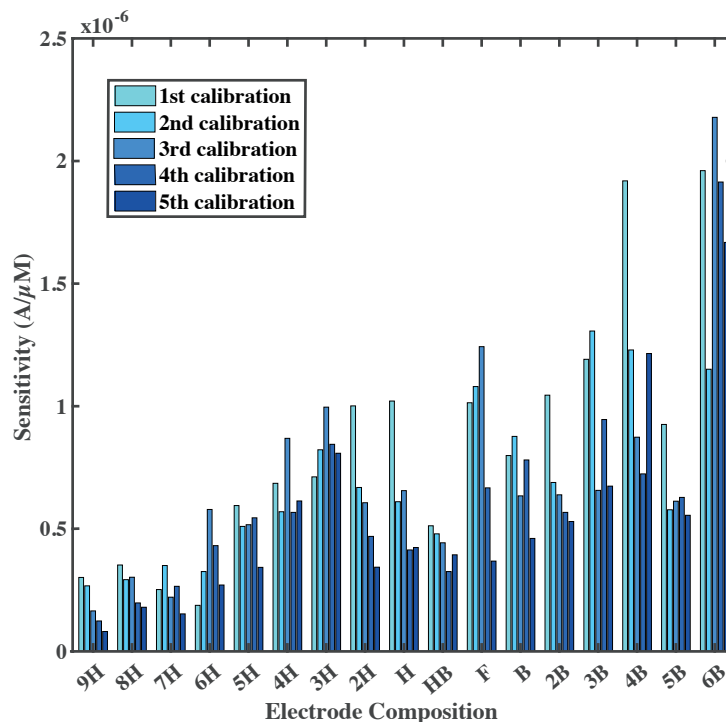


Figure 3.25 – *Intra*-electrode sensitivities obtained by 5 subsequent propofol calibrations performed on each PGE. Trend for all the different lead compositions are reported.

this, it can be said that, with a certain clay content, pre-treatment or regeneration of electrodes are not needed due to the fact that fouling does not occur - thanks to the properties of the lead. Therefore, these PGEs can be selected as the best substrate for a direct electrochemical detection of propofol. The identified optimum point of clay/graphite ratio is set for a value of 0.4, which corresponds to the lead composition having 66% w/w in graphite and 28% w/w in clay (assuming a fixed amount of wax at around 5% w/w). In other words, for achieving the reliable long-term propofol monitoring, the clay/graphite ratio has to be between 0.4 and 1.5. This range corresponds to the PGE leads between *F* and *9H*. Among the lead compositions in the selected range, we wanted to identify the optimum candidate in terms of fouling prevention and stability properties over time. Hence, two principal analyses have been conducted. First, we drew the bar graph with the normalized standard deviations from the *inter*-electrode sensitivity analysis (Fig. 3.23.a) with respect to sensitivity (Standard deviation/S), as shown in Fig. 3.26.a. Secondly, the bar graph was drawn with the normalized fouling standard deviation with respect to the *intra*-electrode sensitivity (Fouling standard deviation/*intra*-electrode S), in Fig. 3.26.b, based on the analysis of subsequently run calibration curves in Fig. 3.25. Both figures, Fig. 3.26.a and Fig. 3.26.b show the trends of PGEs for resistance to fouling effect and stability. It can be deduced from these figures that, *3H* PGE composition (58% graphite, 36% clay and 5% wax, with clay-graphite ratio of 0.62, calculated as  $\frac{36\%}{58\%}$ , and indicated by the green arrow in the figures) has the best performance by providing the minimum normalized standard deviation values in both the analyses.

### 3.4. Different compositions of PGEs

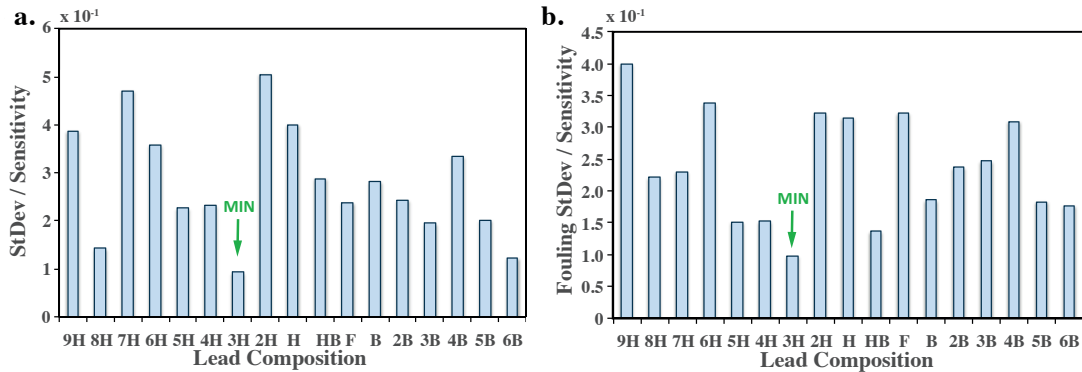


Figure 3.26 – Comparison: a.) ratio Standard Deviation (StDev)/Sensitivity (S) for the analyzed PGEs to identify the best lead composition in terms of high S and small *inter*-electrode variation; b.) variability in S for subsequent propofol calibrations on the same electrode respect to the average S of the electrode itself (Fouling StDev/S).

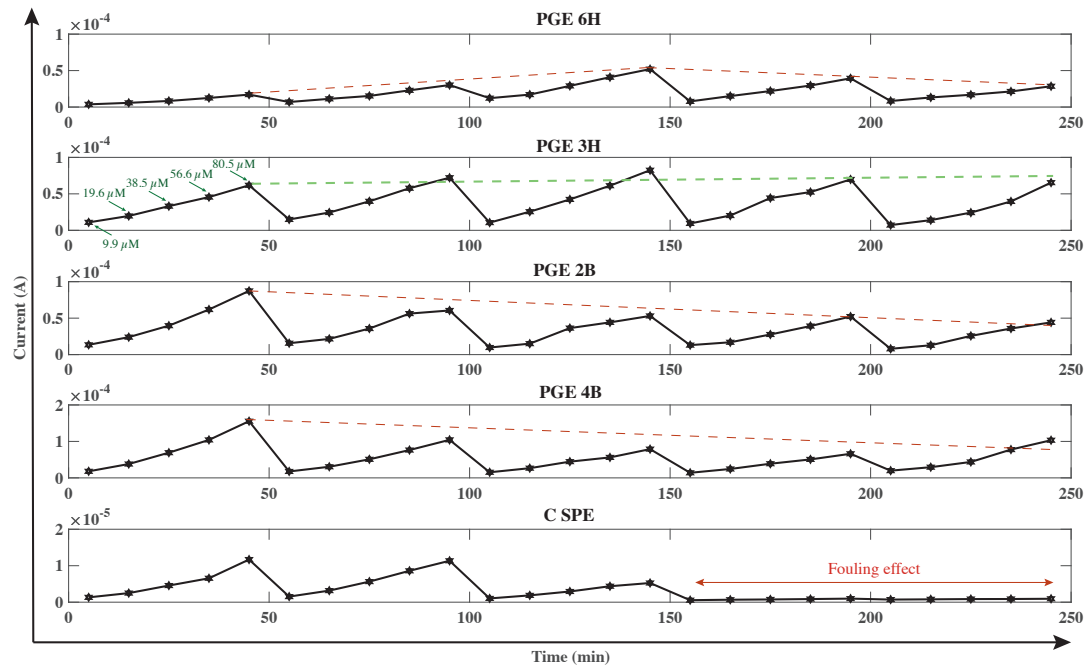


Figure 3.27 – Continuous monitoring experiments with four different kinds of PGE (6H, 3H, 2B and 4B) with respect to a carbon-SPE. Five calibrations (with five rising propofol concentrations each) were carried out resulting in 25 subsequent measurements, for a total of 4 hours, without any intermediate cleaning.

The best performance of 3H PGE in terms of stability and current amplitudes is also evidenced by Fig. 3.27 where different PGEs were compared for long-term (up to 4 h) propofol monitoring, repeating the same experiment as in the previous section but without intermediate electrochemical cleanings. A carbon (C) SPE has been used as control electrode in the comparison. C-SPE was affected by fouling already from the third calibration (*Fouling effect zone*



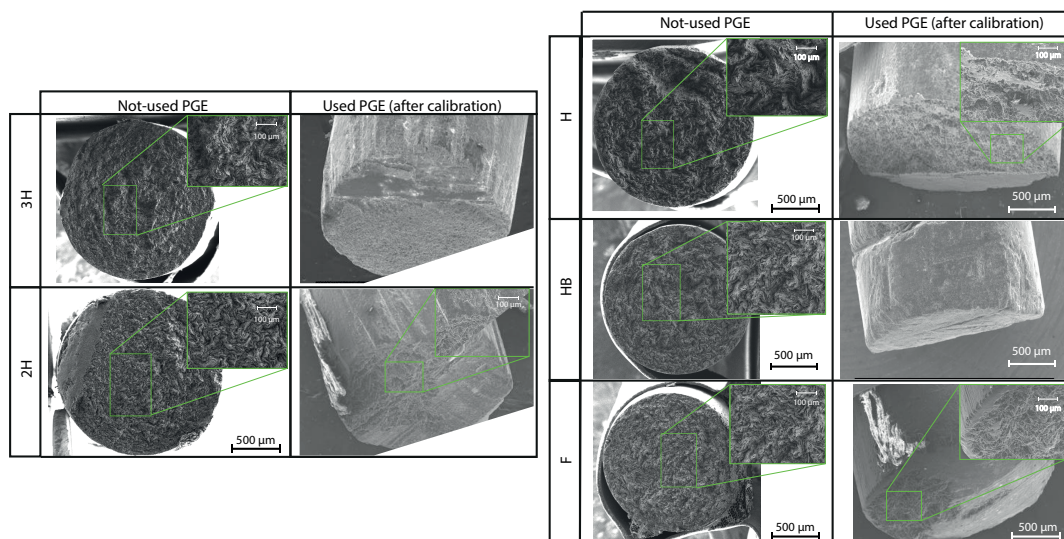


Figure 3.28 – SEM images of 3H, 2H, H, HB, F PGEs before (*Not-used*) and after 5-points propofol calibration measurement (*Used*).

in Fig. 3.27) and no further detection was possible afterwards. This limited performance was overcome by all the PGEs. Considering the PGEs' time trends, it is visible that 4B PGE lead, despite its higher current amplitude values, had a strong fouling that made it unsuitable for long-term monitoring. The same is also visible for the 2B PGE, even if it seemed to have better performance than 4B PGE. Regarding 6H PGE, although the fouling effect is not evident due to its higher clay content, it has the lowest current values and less reproducibility, making it unattractive for the final application. Therefore 3H composition turned out to be the best trade-off between sensitivity and fouling resistance properties. Moreover, the LOD of the optimum PGE was evaluated to be  $7.79 \pm 2.17 \times 10^{-07} \mu\text{M}$ , which is lower than lowest concentration in the physiological range of propofol (1 - 60  $\mu\text{M}$ ).

### Surface characterization

To support the electrochemical investigation of the different lead compositions, SEM and EIS analyses were performed to compare the electrodes' surfaces properties before and after propofol detection. SEM images were taken for all types of electrodes; Fig. 3.28 compares the clean PGE surface before performing propofol sensing (*Not-used* PGE) with the used one after the measurement (*Used* PGE (after calibration)) for PGE leads from F to 3H. F PGE has been identified as the critical point for fouling and sensitivity, while 3H was the optimum lead composition for propofol monitoring.

From Fig. 3.28, a fouling layer is visible on the surface of HB and F PGE leads after their usage. This layer seems to be reduced by increased clay content. Indeed, lead compositions of H, 2H and 3H do not present evidence of this undesirable effect. Moreover, since the hardness of the PGE lead increases, the surface is cut in an easier and more efficient way, ensuring flatter



### 3.5. Summary and main original contributions

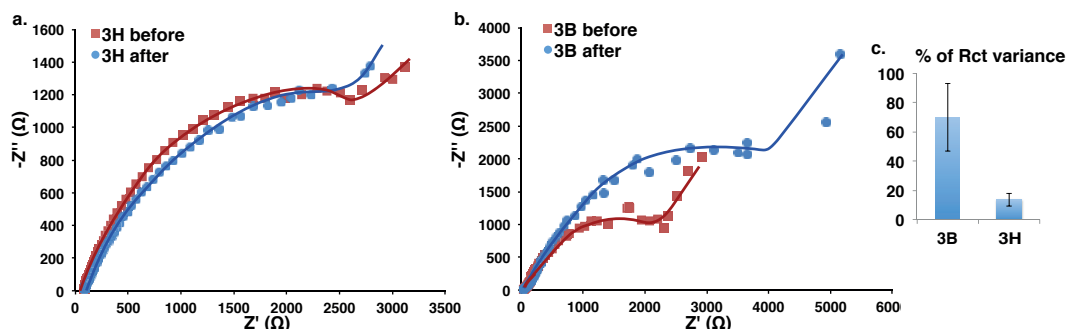


Figure 3.29 – EIS analysis comparison between *Not-used* and *Used* PGEs: Nyquist plots of a) *3H* and b) *3B*, c) bar graph with error bars representing standard error (n = 3) for  $R_{ct}$ (%) variance.

and more homogeneous surfaces. We further analyzed the electrodes surface by performing EIS. Charge-transfer resistance ( $R_{ct}$ ) values of *3H* and *3B* PGEs were compared before and after propofol monitoring. Looking at Fig.3.29.a and Fig.3.29.b, the  $R_{ct}$  value of the unused *3B* PGE is lower than the *3H* one since it contains less clay. It is also evident that, propofol sensing resulted in fouling and hence increased  $R_{ct}$  value for *3B*, while the surface for *3H* seems almost not affected. Bar graph in Fig. 3.29.c shows normalized changes in  $R_{ct}$  values (%), evaluated by the formula:

$$R_{ct\%} = 100 \times \frac{R_{ctUsed} - R_{ctNotUsed}}{R_{ctNotUsed}} \quad (3.2)$$

This value is extremely high for *3B* PGE compared to the one of *3H*.

### 3.5 Summary and main original contributions

In this chapter we have exposed the steps of the development process of an electrochemical sensor for propofol detection during anesthesia practices. Propofol is a widely-used hypnotic agent, which is intravenously administered during anesthesia induction and maintenance phases. The correct and balanced dosing of this compound is crucial to avoid over- or under-dosing that might lead to serious health damages/syndromes or to experiences of awareness, respectively. Only a continuous monitoring of its concentration in patient's veins would enable a personalized and dynamic adjustment of the infusion rate.

Bare carbon-based materials were identified as suitable and ready-to-use substrates to make propofol RedOx to happen. However, the fouling effect due to free radicals produced by propofol oxidation reaction results in an electro-active polymeric layer on the electrode's surface, preventing continuous detection. We selected boron-doped diamond and pencil graphite working electrodes for their properties: from one side BDD for its low catalytic activity and elevated mechanical strength and reduced chemical activity, from the other side PGE for its excellent electrochemical reactivity and sensitivity, good mechanical rigidity, low cost, low background current, wide potential window, chemical inertness and easy at miniaturization.

### Chapter 3. Propofol direct monitoring

---

The main steps and contributions of our research process in propofol detection can be summarized as follows:

- Characterization of the fouling phenomenon at both BDD and PGE. They appear to be both affected by the fouling effect due to propofol oxidation reaction, even if the undesired phenomenon was more evident in PGE measurements after the third 5-point calibrations performed in rows. However, the PGE sensitivity for propofol detection was evaluated to be one order of magnitude higher than the one from BDD.
- We defined and validated two electrochemical cleaning procedures (in PBS and NaOH solutions) to be run alternately with propofol measures as an intermediate step between one 5-point calibration and the subsequent one. We identified two best electrode-cleaning combinations: (i) PGE with PBS cleaning, the most suitable in view of the final application since PGE has higher sensitivity, and (ii) BDD with NaOH cleaning, providing the best performance but requiring an external compound, *e.g.* NaOH, to be flushed. Therefore, we demonstrated the success of both of these combinations in propofol long-term monitoring (up to 4h).
- Table 3.3 summarizes and compares the obtained results with the literature. We can conclude that both our sensors are suitable for reliable propofol detection. This is true also for propofol monitoring in undiluted human serum where we obtained a LOD in human serum by performing DPV technique with PGE, obtaining the lowest sensitivity of  $0.011 \mu\text{A}/\mu\text{M}$ . The main advantage of our technology is that it can be adopted as propofol sensors in an extremely easy- and ready-to-use procedure.
- PGE and PBS cleaning were selected as the most suitable electrode/cleaning combination in view of the final application in detecting the concentration of propofol in human serum. Indeed, PGE electrodes registered a higher sensitivity to propofol and PBS cleaning does not add any non-physiological chemical to the measurement. The DPV propofol detection in undiluted human serum resulted in a LOD of  $0.82 \mu\text{M}$  with 9.3 (%) RSD, which is below the propofol physiological range ([1 - 60]  $\mu\text{M}$ ).
- PGE composition is made of graphite, clay and wax (binder) in different percentages. We investigated and compared the performance in propofol long-term detection of different lead compositions in terms of: (i) propofol sensitivity and (ii) fouling resistance properties. The electrodes were characterized by electrochemical analysis, EIS measurements and SEM imaging. By electrochemical analysis, we demonstrated that the higher the graphite content (wt%), the higher the sensitivity, whereas the higher the clay content (wt%), the smaller the fouling effect. This is also reflected by EIS results where higher charge-transfer resistance ( $R_{ct}$ ) values characterize the PGE with the higher clay content.

We identified a significant value of clay-to-graphite ratio, as equal to 0.4, for which the fouling effect is not significant in the time-series of measurements. This value corresponds to the *F* lead composition (66% w/w in graphite, 28% w/w in clay and

### 3.5. Summary and main original contributions

5% w/w in clay). Therefore, we identified a range of clay/graphite ratios suitable for reliable long-term propofol monitoring, such as from 0.4 to 1.5 (from *F* to *9H*). Within this selected suitable range, we discovered that the *3H* lead (58% graphite, 36% clay and 5% wax, with clay-graphite ratio of 0.62) was providing the optimum material substrate in terms of preventing the fouling effect, electrode stability, and detection sensitivity, for measurements of propofol over a period of time of 4 hours in continuous monitoring. The higher performances of this PGE composition have been confirmed and validated further by SEM and EIS analysis.

Table 3.3 – Comparison of the performance of the sensors for propofol sensing presented in the literature: ready to use (*RtU*), electrochemical technique (*T*), LOD (error limits are evaluated as standard deviation of the dataset  $n = 5$ ), Long-Term Monitoring (*LTM*), possibility to detect in human serum background electrolyte (*HS*) and on-line electrochemical cleaning procedures implemented (*CPI*) in which solution (*CS*) are taken in consideration.

Ref.	WE	RtU	T	LOD ( $\mu\text{M}$ )	LTM	HS	CPI	CS
[134]	GC SPE	×	CV	$3.2 \pm 0.1$	–	–	×	–
[132]	PVC WE	×	CV	$0.08 \pm 0.05$	3 h	–	×	–
	PVC WE	×	CA	$0.012 \pm 0.004$	–	✓	×	–
This Thesis	BDD	✓	CV	$2.38 \pm 0.5$	> 4 h	–	✓	PBS
	BDD	✓	CV	$2.4 \pm 0.9$	> 4 h	–	✓	NaOH
	PGE	✓	CV	$8.1 \pm 5.6$	> 4 h	–	✓	PBS
	PGE	✓	CV	$3.1 \pm 1.1$	> 4 h	–	✓	NaOH
	PGE	✓	DPV	$0.82 \pm 0.08$	–	✓	–	–



## 4 Midazolam and Paracetamol direct monitoring

In *Chapter 3* the complete analysis to identify the best electrochemical sensor for direct long-term propofol detection, the hypnotic agent of anesthesia cocktail, has been explored. In this chapter, to complete the array of electrochemical sensors required for full monitoring of the anesthesia cocktail, two other drugs, the analgesic (APAP) and the muscle relaxant (midazolam), have to be investigated. As mentioned in *Section 1.1.1*, both midazolam and APAP, whose chemical structures are reported in Fig. 4.1, are common drugs extensively used in sedation procedures. On the one side, APAP treats mild to moderate pain and reduces fever. It is often administered in place of opioids to alleviate pain resulting from POPI that still affects between 28% and 90% of patients [26]. Therefore, it is still considered as one of the most critical problems in the current anesthesia practices [153]. Since, APAP is metabolized primary by the liver, overdose may lead to hepatotoxicity. After 1 h of ingestion, the drug concentration in plasma ranges from 2 to 20 mg/L, whereas levels of 30 - 300 mg/L are often observed in overdosed patients [154, 155].

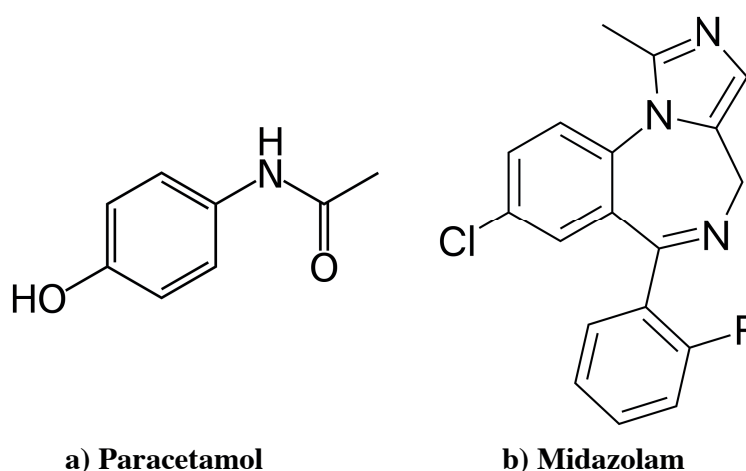


Figure 4.1 – Chemical structures of: a) paracetamol and b) midazolam.

On the other side, MZ is a water-soluble benzodiazepine in its acid formulation with a rapid onset of action and high metabolic clearance. It is largely adopted in anesthesia induction and maintenance, as well as in sedation [21]. Since it affects CNS activity, serious breathing problems may be encountered if a dose of 0.15 mg/kg is administered [22].

Finally, we will conclude the chapter with the results obtained in an electrochemical interference analysis among propofol, midazolam and paracetamol drugs.

### 4.1 State-of-the-art

Different approaches have been used for APAP and MZ detection in human fluids, such as titrimetry [156], spectrophotometry [157], flow-injection spectrophotometry [158] and chromatographic methods [159], liquid chromatography with mass spectrometric [160], electron-capture gas chromatographic [161, 162], *RadioImmunoAssay* (RIA) [163], and potentiometric electrodes [138]. However, alternative methods of detection still need to be investigated in order to develop reliable point-of-care to avoid any over dosage of such invasive compounds. As stated above, electrochemical sensors are suitable candidates since they offer high sensitivity, low cost, easy manufacturability and fabrication reproducibility, as well as the possibility to be miniaturized and easily integrated in electronic circuits and read-outs [164]. Moreover, the electron transport performance of electrochemical sensors, in terms of sensitivity and specificity, can be highly improved with the integration of nano-materials [165, 85]. This enhancement of detection sensitivity is extremely beneficial in case of drugs with a narrow therapeutic range, and with small differences between therapeutic effects and toxic doses of the administered concentrations [166].

As far as the electrochemical detection of APAP and MZ is concerned, direct sensing with carbon electrodes has been already extensively verified in the literature [167, 168, 169].

Faced with the vast literature about nano-structured electrochemical sensors, we have investigated and compared the performances obtained by different nano-allotropes of carbon materials, namely fullerene ( $C_{60}$ ) and MWCNTs, with respect to bare C-SPE, in order to estimate the enhancement in MZ and APAP sensing due to C-nanostructures deposition. The objective of this analysis is to identify the best nano-composite substrate for APAP and MZ monitoring in human serum.

In order to guarantee a proper and reliable comparison among tested electrodes, we used the approach (developed by our group) described in [170] for sensor functionalization to obtain equal EASA among different nano-structured electrodes. It is based on an *a-priori* evaluation of the EASA for each material that is used to know the amount of nano-material to drop-cast on the WE surface. In this way, it is possible to exclude the EASA effect on sensing enhancement and, therefore, to highlight the contribution only related to the electron-transfer and electro-catalytic properties of the nano-materials, by excluding the increased effect that is purely related to the catalytic area of the surface.

## 4.2 Carbon-based nano-structured electrodes

### 4.2.1 Materials and methods

APAP has been purchased in powder from Sigma-Aldrich (Switzerland), as well as the human serum heat inactivated (H3667-100ML). APAP 30 mM stock solution has been obtained by dissolving 5 mg of powder in 1 mL PBS (10 mM, pH: 7.4). Subsequent concentrations of [50 - 100 - 150 - 200 - 250 - 300]  $\mu\text{M}$  were obtained by injecting 16.6  $\mu\text{L}$  of stock solution in 10 mL PBS or human serum background electrolytes. The range of concentration was chosen in agreement with the pharmaceutical formulation of the drug [169].

*Midazolam Hydrochloride* (MZ HCl) was provided in powder from Lipomed AG. A 15 mM stock solution was prepared by diluting 10 mg of powder in 2 mL distilled water to reach the desired solution. Sample aliquots of 1 mL were prepared by diluting the stock solution in acidic PBS (10 mM, pH: 2.5) and undiluted human serum to desired concentrations of [0.45 - 1.35 - 2.25 - 3 - 4.5] mM. The range of concentration was chosen in agreement with the pharmaceutical formulation of the drug [171]. The acid formulation was used to increase the solubility of midazolam as described in *Section 1.1.1*.

10 ml of ferro(ferri)cyanide 1 mM solution for experimental EASA evaluation was obtained by mixing 0.0042 gr potassium hexa-cyanoferrate trihydrate II with 0.0033 gr potassium hexa-cyanoferrate III in PBS (10 mM pH:7.4). All the chemicals were purchased by Sigma Aldrich.

Commercial C-SPEs (WE, 4 mm  $\varnothing$ ) were purchased from Metrohm (DRP-110). Powder of MWCNTs (90% purity; 0.05% functionalized with  $\text{NH}_2$ ) with diameter of 10 nm and length of 1 to 2  $\mu\text{m}$  was purchased from DropSens (Spain) and was dispersed in chloroform to a final concentration of 2  $\text{mg mL}^{-1}$ , and was sonicated for 1 hour to achieve a homogenous solution. Fullerene,  $\text{C}_{60}$  powder (average diameter: 60-80 nm) was provided by Nanoshel Company (India) and was dispersed in methanol to the final concentration of 1  $\text{mg mL}^{-1}$ , and was sonicated for 1 hour to achieve a homogenous solution.

Autolab potentiostat (PGSTAT128N) by Metrohm was used to carry out experiments. The data analysis was performed in Excel and Matlab, where a dedicated script for peaks height evaluation was implemented.

Surface characterization has been carried out using a Zeiss Merlin scanning electron microscope with accelerating voltages in the range of 1.2 kV to 3 kV. The nanostructure solutions were deposited on Copper (Cu) foils by standard drop casting.

### Nano-structured electrode preparation and theoretical EASA calculation

For electrode functionalization the amount of nanomaterials to drop-cast on the electrode's surface was evaluated *a-priori* by using *Specific Surface Area* (SSA) calculation, as in [170], in order to obtain an equal additional EASA by different nanomaterials. The SSA ( $\text{m}^2/\text{g}$ ) of a

## Chapter 4. Midazolam and Paracetamol direct monitoring

---

sample can be evaluated as [172]:

$$SSA_{nanoparticle} = \frac{area}{mass} \quad (4.1)$$

For MWCNT, assumed to have cylindrical shape, the SSA has been evaluated in [170] as 215.7  $m^2/g$ , according to this calculation:

$$SSA_{MWCNT} = \frac{SSA_{GS} \times d_e}{n \times d_e - 2 \times d_{s-s} \sum_{i=1}^{n-1} i} \quad (4.2)$$

Where  $d_e$  is the MWCNTs diameter (10 nm),  $d_{s-s}$  is the inter-shell distance (0.34 nm),  $SSA_{GS}$  is the SSA of one side of the graphene sheet (1315  $m^2/g$ ), and  $n$  is the number of shells (calculated to be 8).

The SSA of  $C_{60}$  sample, assumed as spheres, was calculated as equal to 29.0  $m^2/g$ .

$$SSA_{C60} = \frac{3}{r \times \rho} \quad (4.3)$$

Where  $r$  is the radius of a fullerene spherical nanoparticle (60 nm) and  $\rho$  is the density (1.72  $g\ cm^{-3}$ ).

According to [173], the optimum additional-EASA of MWCNT is 4314  $mm^2$ . Therefore, to guarantee an appropriate comparison between the electrochemical properties of the two different carbon nano-scale allotropes, the gain in terms of EASA has to be the same. The required amount of MWCNTs and  $C_{60}$  in  $\mu g$  to achieve the same optimum additional-EASA can be evaluated from Equations 4.4 and 4.5, respectively:

$$4314\ mm^2 = 215.7 \frac{m^2}{g} \times X_{MWCNT} \Rightarrow X_{MWCNT} \approx 20\ \mu g \quad (4.4)$$

$$4314\ mm^2 = 29 \frac{m^2}{g} \times X_{C60} \Rightarrow X_{C60} \approx 149\ \mu g \quad (4.5)$$

### Surface characterization

We have performed SEM analyses of bare C-SPE, MWCNTs and  $C_{60}$  samples to observe and compare the morphological characteristics of the nano-structures also with respect to a bare electrode, in Fig. 4.2. As visible from Fig. 4.2.b, MWCNTs present high homogeneity in morphology and a dense 3D coverage of the surface. The diameter of the nano-structures is estimated and confirmed to be about  $10 \pm 2$  nm.

On the other hand, the  $C_{60}$  sample turned out to be assembled in globular aggregates, as shown in Fig. 4.2.c. The dimensions of the structures vary and are not perfectly homogeneous, as due to the fabrication method. The average size of these nanostructures is estimated to



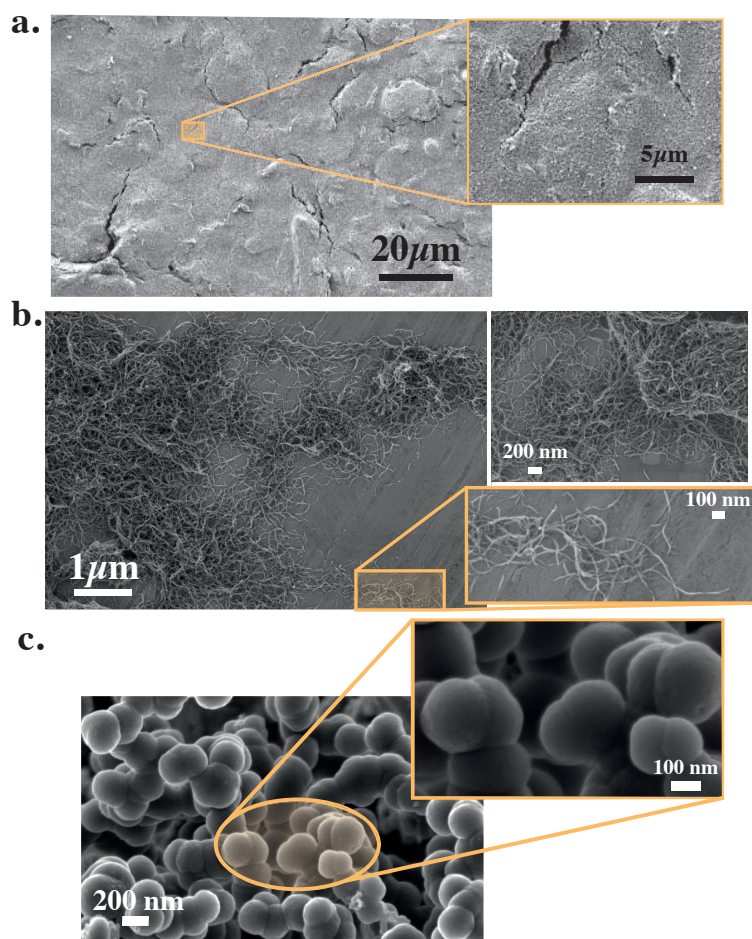


Figure 4.2 – SEM characterization of a) bare C-SPE, b) MWCNT- and c) fullerene-modified surfaces.

be around 120 nm, indicating a quite high standard deviation of 40 nm, as previewed from repeated SEM imaging obtained on different areas of the modified surface. In some cases, even larger structures are found with a diameter up to 200 nm, mainly due to an intense clustering occurring between neighboring smaller structures.

#### 4.2.2 Results and discussion

##### APAP and MZ characterization at bare C-SPE

The electrochemical behavior of MZ have been investigated with glassy carbon electrode by [169] in *Britton–Robinson* (BR) buffer containing 0.1% cationic surfactant. Typical voltammogram (900 μg/mL midazolam) exhibited four well defined peaks, as shown in Fig. 4.3.a. However, they found that *peak 0* was not registering any signal enhancement after increasing the analyte's concentration in the solution unlike the other peaks (*peak 1, 2 and 3*). Therefore,

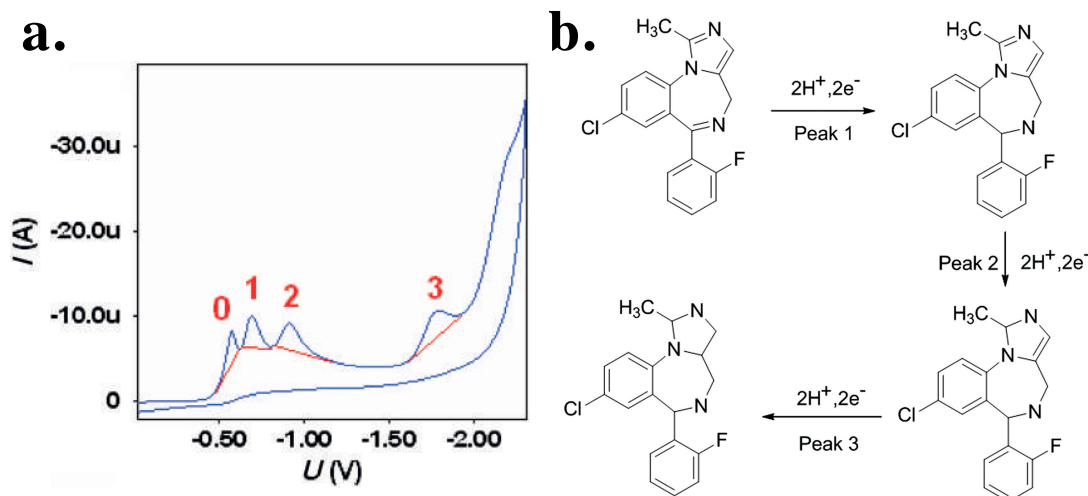


Figure 4.3 – a) Cyclic voltammogram of midazolam (900  $\mu\text{g/mL}$ ) shows peak 0, 1, 2 and 3 in presence of 0.1% cationic surfactant indicating the irreversibility of electrode process. b) Sketch of the reaction mechanism for midazolam reduction (*reprinted from [169]*).

they supposed that *peak 0* might correspond to a pre-adsorption step not affected by the analyte concentration. Concerning the other peaks, they assigned the *peak 1* to the 2-electron reduction of the  $-\text{C}=\text{N}-$  bond of the seven membered ring, *peak 2* to the 2-electron reduction of  $-\text{C}=\text{N}-$  bond of the five membered ring and *peak 3* to the 2-electron reduction of  $-\text{C}=\text{C}-$  of the five membered ring of midazolam structure. Since no peak is observed in the reversed CV scan, these reactions are irreversible processes. On the basis of these results, they postulated a reduction mechanism for midazolam as in Fig. 4.3.b.

We started from these findings and we characterized the electrochemical response of midazolam at C-SPE by performing CV in the range of potentials between -1 V and 0 V with 0.1 V/s scan-rate. Typical CV plots obtained for increasing midazolam concentrations are shown in Fig. 4.4.a. Three reductive peaks are visible from the plots, corresponding to the first three peaks detected by [169]. Also in this case, *peak 0* seems to be unaffected by variations of the drug concentration. For the calibration analysis, the CV area with the peaks has been isolated and rendered in absolute value, as seen in the Fig. 4.4.b (to have a more easy intuition of the relationship between increase in concentration and corresponding augmentation of the peak current). Both *peak 1* and *peak 2* have been considered for the analysis (blue and orange areas in the figure, respectively). Fig. 4.4.c shows the calibration lines obtained from three C-SPEs for both the considered peaks. For *peak 1* a sensitivity of  $1.60^{-05} \pm 1.7^{-06}$  mA/mM and an LOD of 0.29 mM were evaluated, while for *Peak 2* the sensitivity was of  $1.94 \times 10^{-02} \pm 2.16 \times 10^{-03}$  mA/mM and the LOD 0.20 mM. We can notice that both the peaks gives very similar responses in midazolam calibration procedure.

As far APAP direct detection is concerned, [174] reported its electrochemical characterization

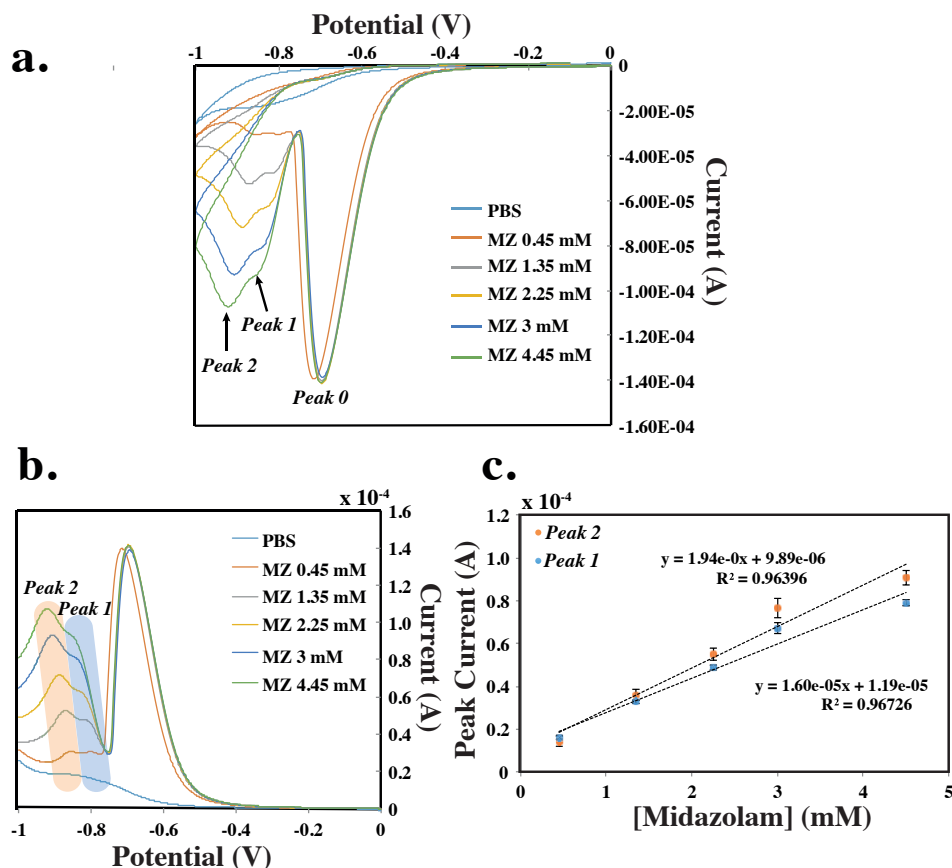


Figure 4.4 – Midazolam calibration at bare C-SPE in acid PBS solution (pH: 2.5): a) typical CVs for increasing concentrations of midazolam; all show three peaks 0, 1, 2. b) Module of the peak area for *peak 1* (blue area) and *peak 2* (orange area) height evaluation and relative c) calibration line plots obtained from *peak 1* and *peak 2* at three different C-SPEs, errors bar represents the standard deviation.

with bare *Glassy Carbon* (GC) electrode. It has been found that in the pH range between 3 and 11 (containing the physiological pH: 7.4) the chemical reaction is characterized by a reversible process since both an oxidation and a reduction peaks are visible in the voltammogram at +0.1 V and +0.5 V (vs. Ag/AgCl), respectively. The typical CV plot and the reversible reaction mechanism for APAP have been reported in Fig. 4.5. Starting from this study, we characterized the detection of paracetamol at C-SPEs by running a CV procedure between -0.1 V and +1.1 V with a scan-rate of 0.1 V/s. Typical CVs for increasing concentrations of APAP are reported in Fig. 4.6.a. Both oxidative and reductive peaks are visible confirming the reversibility of the RedOx process, as predicted by [174]. From the calibration line in Fig. 4.6.b, which was evaluated for the oxidation peak (green area in the figure), we have found that the sensor sensitivity was of  $6.02 \times 10^{-02} \pm 6.38 \times 10^{-4} \mu\text{A}/\mu\text{M}$  and the LOD of  $0.58 \mu\text{M}$ .

After having characterized the electrochemical behavior of MZ and APAP at C-SPE, we investi-

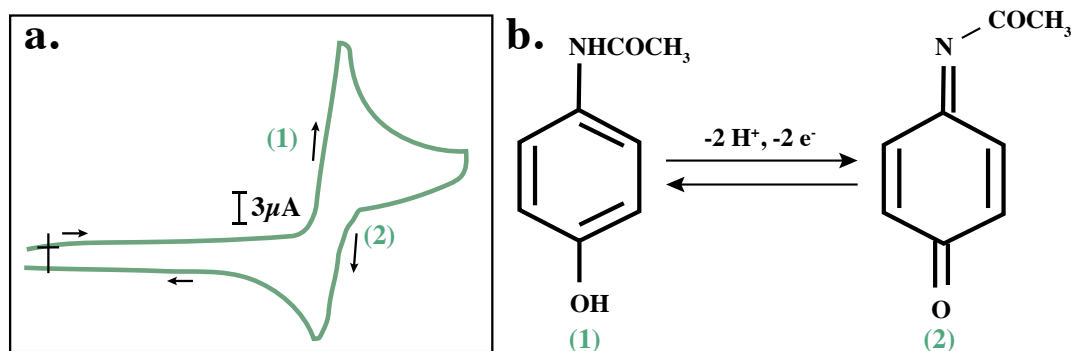


Figure 4.5 – a) CVs of  $1 \times 10^{-3}$  M APAP at bare GC electrode in aqueous solutions at pH 3. Reprinted from [174]. b) Reversible reaction mechanism for APAP at pH 3.

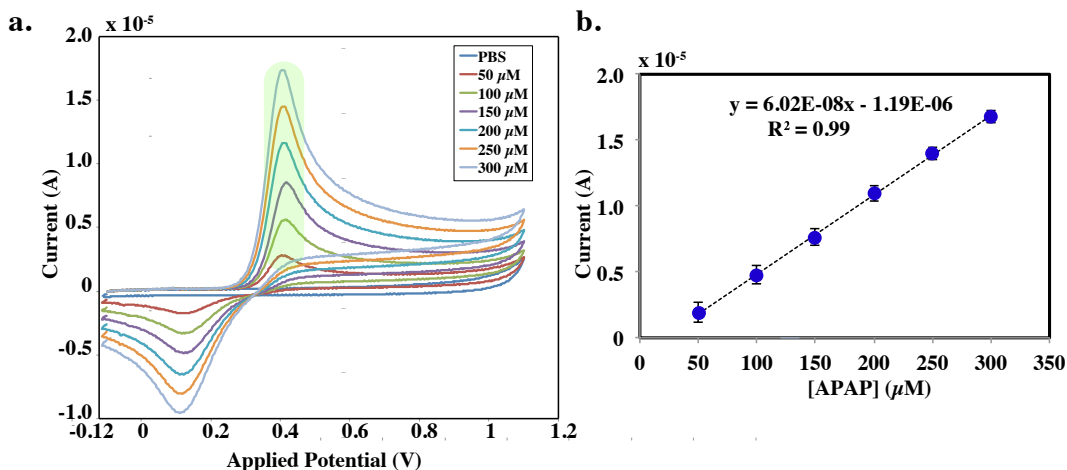


Figure 4.6 – APAP calibration at bare C-SPE in PBS solution at pH 7.4: a) typical CVs for increasing concentrations of APAP; all show the oxidation and reductive peaks. b) Calibration line plot obtained from APAP oxidation at three different C-SPEs, errors bar represents the standard deviation.

gated and compared the performances obtained from the functionalization of the electrode with two carbon nano-allotropes, *i.e.* fullerene ( $\text{C}_{60}$ ) and MWCNTs.

#### APAP and MZ characterization at carbon nanoscale allotropes modified electrodes

**Experimental Determination of EASA** We have experimentally evaluated the EASA of bare, MWCNTs- and fullerene-modified WEs to validate the efficacy of the EASA theoretical calculation for obtaining optimum and comparable surface nano-structuring, as presented in Section 4.2.1. To this aim, CV procedure between -0.5 V and 1 V and scan-rate 0.1 V/s was carried out in ferro(ferri)cyanide 1 mM solution. Since the RedOx process for the electrochemical couple  $\text{Fe}^{2+}/\text{Fe}^{3+}$  is well-known, it is possible to evaluate the total EASA (A in the following equation) from Randles-Sevcik equation as in Eq. 3.1, knowing that  $n = 1$  is the

## 4.2. Carbon-based nano-structured electrodes

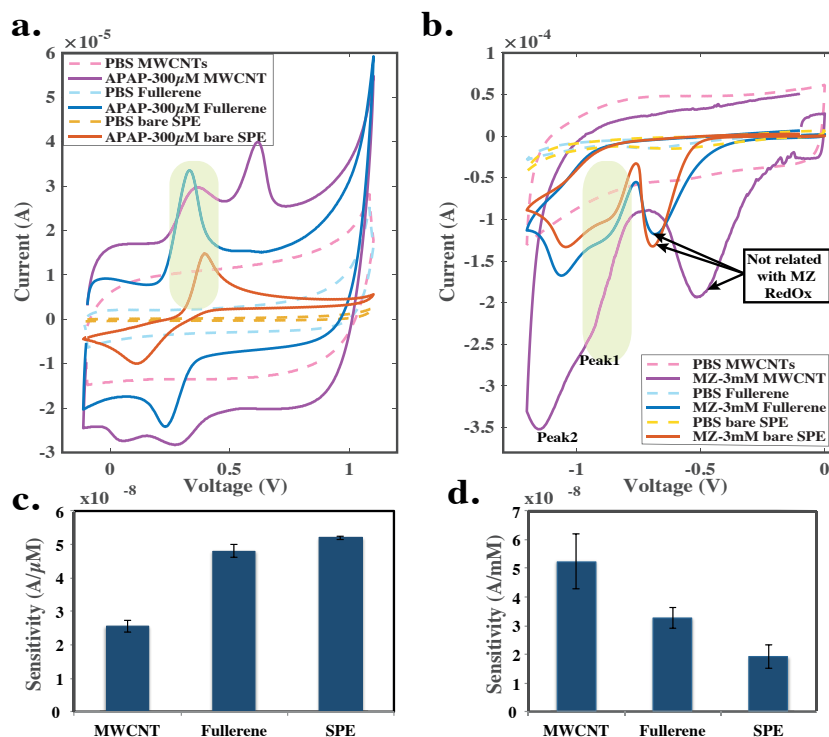


Figure 4.7 – Comparison of voltammograms obtained for: a) APAP 300  $\mu\text{M}$  and b) MZ 3 mM at bare, MWCNTs- and fullerene-modified electrodes (PBS blank measurements have been reported for all the electrodes as control). It is visible how nano-structures improve the EASA and electron-transfer properties respect to the bare electrode; c) and d) compares the sensitivity values obtained for the three tested electrodes (calibration performed considering the peaks in the yellow areas).

number of electrons exchanged in this reaction,  $D = 6.20 \times 10^{-6} \text{ cm}^2$  is the diffusion coefficient of ferro-cyanide [175],  $C = 1 \text{ mM}$  is the concentration and  $\nu = 0.1 \text{ V/s}$  is the scan-rate adopted in the CV procedure.

We found that the EASA of MWCNT- and  $\text{C}_{60}$ -modified electrodes were respectively increased by  $43.9 \text{ cm}^2$  and  $47.8 \text{ cm}^2$  (26.5% and 24.3%), respectively, in comparison with the bare C-SPE. Hence, confirming the efficacy of the theory for EASA calculation (theoretical assumption for equal to  $43.14 \text{ cm}^2$ ).

**Electrochemical characterization** We have carried out CV procedures to electrochemically characterize the performance of MWCNTs and fullerene nanostructured electrodes in determining APAP and MZ concentrations. Typical voltammograms for 300  $\mu\text{M}$  APAP and for 3 mM MZ obtained by bare C-SPE, MWCNT- and  $\text{C}_{60}$ -nanostructured electrodes are reported in Fig. 4.7.a and Fig. 4.7.b, respectively. In dashed lines there are the blank measurements (baseline currents) measured for every tested electrode, as *per* control. These measurements were obtained at a scan-rate of 0.1 V/s in PBS (10 mM, pH:7.4 and 2.5 for APAP and MZ, respectively).

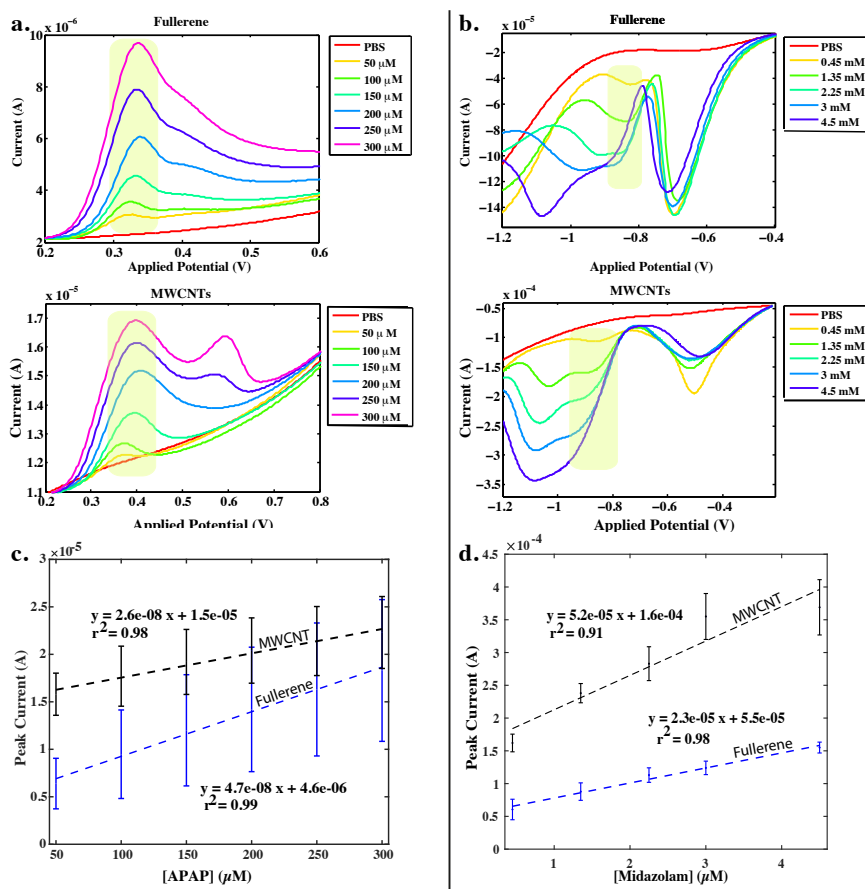


Figure 4.8 – APAP and MZ CV calibrations at C<sub>60</sub>- and MWCNT-modified WEs in PBS (10 mM, pH: 7.4): extraction of the peaks area from CVs for increasing concentrations of a) APAP (oxidation) and b) MZ (reduction); c) and d) are the calibration lines obtained from APAP and MZ detection considering three different WEs, errors bar represents the standard deviation.

It is clear that a higher capacitive current is measured from MWCNT-modified electrodes. In agreement with what we have already discussed in *Section 4.2.2*, the electrochemical response of all the tested electrodes for APAP detection presented well-defined oxidation and reduction peaks, while, for MZ detection three reductive peaks are registered (the first one, indicated by arrows in the figure, is not related to MZ concentration). A preliminary significant observation on Fig. 4.7 can be done on interference action of the two target drugs, that will be further discussed in *Section 4.3*. The two drugs were found not to be interfering each other since MZ shows only reductive peaks at negative applied voltages, while APAP manifests oxidative and reductive peaks at positive potentials.

What is more, there is an evident shift of the peaks-position toward smaller potentials when the RedOx occurs on modified electrodes as explained by the Nernst effect [176]. Fig. 4.7.c and Fig. 4.7.d. reports the error bar graph with the sensitivity values obtained for all the tested electrodes (error bars represents the standard deviations, n = 3) considering the peaks highlighted in yellow (oxidative peak for APAP and *peak 1* for MZ). Even if for APAP detection

## 4.2. Carbon-based nano-structured electrodes

in PBS there is no an evident enhancement of the sensitivity with nano-allotropes with regards to the bare C-SPE, for midazolam both are notably increasing the sensitivity with respect to the bare electrode. In particular, MWCNTs are almost doubling the sensitivity obtained for bare SPE.

We then performed CV measurements at different APAP and MZ concentrations, ranging between [50 - 300]  $\mu\text{M}$  and [0.45 - 4.5] mM, respectively, to calibrate the sensors. The peaks area extracted by the measured voltammograms with MWCNT and fullerene- $\text{C}_{60}$  modified electrodes are shown in Fig. 4.8.a and Fig. 4.8.b. As concerning APAP detection (Fig. 4.8.a), we can notice that MWCNTs-modified electrode revealed a second oxidative peak beyond 250  $\mu\text{M}$  APAP concentration. Also in this case, the calibration analysis was carried out considering the oxidation peak for APAP and *peak 1* for MZ, since it is also visible also with the lowest MZ concentration at MWCNT (yellow areas in the figure). Calibration lines for APAP and MZ on both modified electrodes are reported in Fig. 4.8.c and Fig. 4.8.d, respectively. The sensitivities for APAP detection at the two kinds of modified electrodes are close ( $(2.6 \pm 0.2) \times 10^{-2} \mu\text{A}/\mu\text{M}$  MWCNTs and  $(4.7 \pm 0.2) \times 10^{-2} \mu\text{A}/\mu\text{M}$  fullerene). However, the fullerene electrodes are affected by lower reproducibility, as measured by the larger estimated standard error ( $\sigma_d/\sqrt{n}$ ) where  $\sigma_d$  is the standard deviation and  $n$  is the number of evaluated points,  $n = 3$ ). Indeed, the average estimated standard error was found to be 3.2 and 5.7 for MWCNTs and fullerene- $\text{C}_{60}$  modified electrodes, respectively.

For MZ detection, the sensitivities of the two kinds of modified electrodes are also comparable:  $52.4 \pm 9.6 \mu\text{A}/\text{mM}$  for MWCNTs and  $32.8 \pm 3.7 \mu\text{A}/\text{mM}$  for fullerene.

**APAP and MZ detection in Human Serum** After having characterized the electrochemical behavior of the two differently nano-structured electrodes in PBS solution, we have then performed CV measurements in undiluted *Human Serum* (HS). This allowed us to validate the sensor's efficacy in MZ and APAP detection within the scope of the final application for anesthesia monitoring. The voltammograms and calibration lines obtained from this analysis are presented in Fig. 4.9. The first observation we can make is that we were not able to measure MZ in human serum with  $\text{C}_{60}$ -modified electrodes. As we have seen in both surface and electrochemical characterizations, in fact, these electrodes were affected by inhomogeneous deposition leading to instability. Therefore, we have confirmed their inefficiency in MZ detection in human serum.

As for the calibration lines we obtained, the current amplitude of the peaks is increasing

Table 4.1 – Sensitivity and LOD values for APAP and MZ detection at MWCNT and fullerene- $\text{C}_{60}$  modified electrodes in human serum.

		Sensitivity	LOD
APAP	MWCNT	$0.052 \pm 0.001 (\mu\text{A}/\mu\text{M})$	$0.352 \pm 0.023 \mu\text{M}$
	$\text{C}_{60}$	$0.046 \pm 0.001 (\mu\text{A}/\mu\text{M})$	$1.179 \pm 0.105 \mu\text{M}$
MZ	MWCNT	$10.1 \pm 0.4 (\mu\text{A}/\text{mM})$	$0.319 \pm 0.038 \text{mM}$



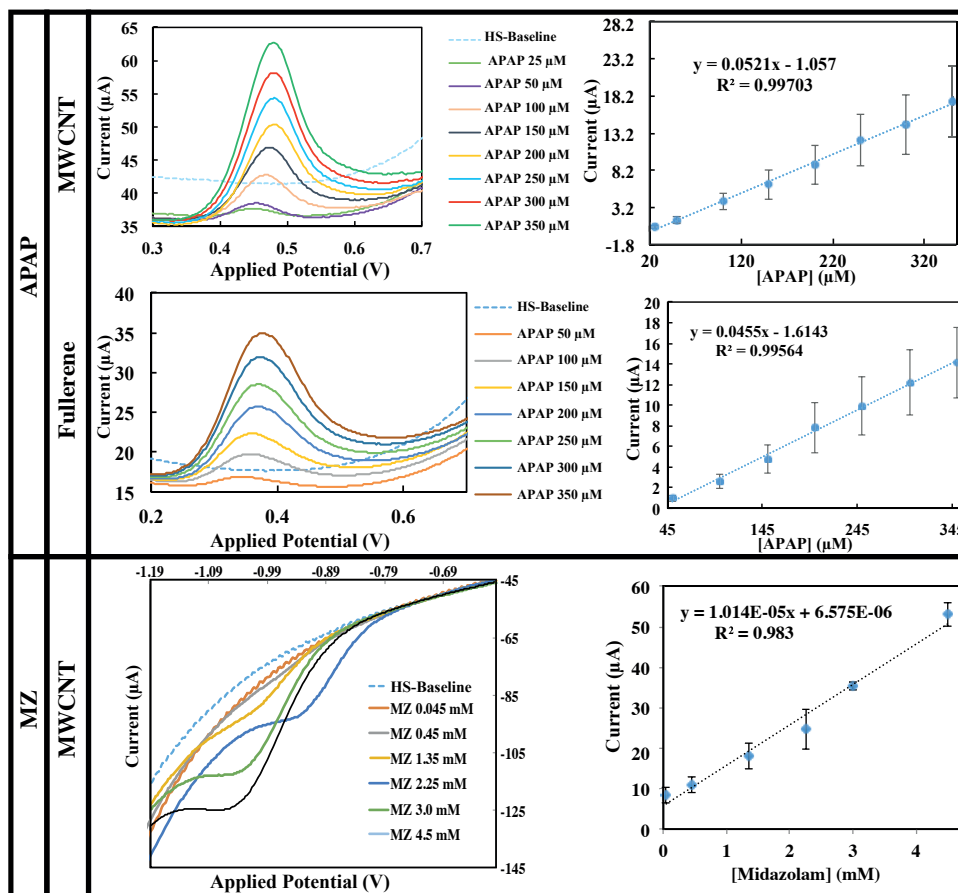


Figure 4.9 – APAP and MZ detection in undiluted HS at MWCNT and fullerene-C<sub>60</sub> modified electrodes. Peak areas extracted by the voltammograms and calibration lines (n = 3) are reported for increasing concentrations of APAP and MZ.

in linear fashion with the APAP and MZ subsequent concentrations. The sensitivity and LOD values for all the calibrations were evaluated as summarized in Table 4.1. From this comparison table, MWCNT-modified electrodes are also shown to be best option for APAP detection in undiluted human serum.

### 4.3 Interference study

To sum up the findings in *Chapter 3* and previous *Section 4.2*, we concluded that the sensors should include:

- For propofol detection: Ag/AgCl RE, Pt wire CE and wood PGE 3H WE;
- For APAP and MZ detection: Ag RE, carbon-based WE and CE.



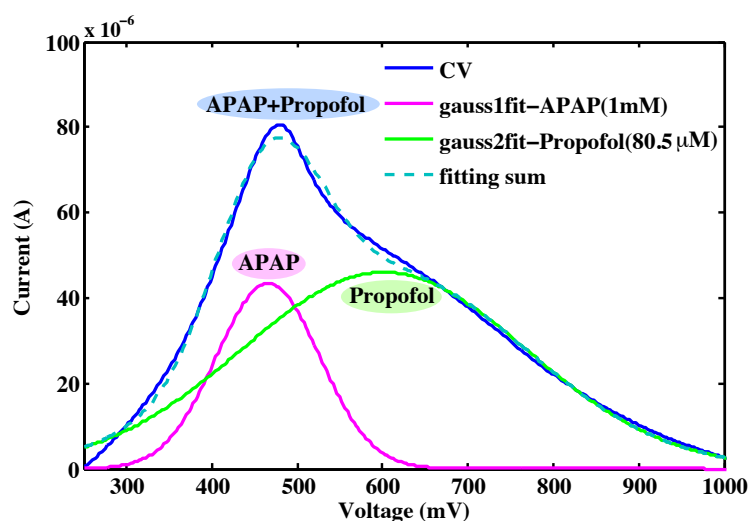


Figure 4.10 – APAP interference study: Gaussian decomposition of the CV procedure ([+0.2 - +1.4] V, scan-rate 0.1 V/s at PGE) belongs to the mixture of APAP (1 mM) and propofol (80.5  $\mu\text{M}$ ).

Therefore, the analysis has to be completed by an interference study. Interference will be considered mainly among the monitored drugs, but also with respect to the main interfering components, *e.g.* *Ascorbic Acid* (AA), *Uridic Acid* (UA) and cysteine.

#### 4.3.1 Interference at different PGEs

Interferences between APAP and Propofol oxidation processes have been evaluated with PGE in PBS background electrolyte. Indeed, APAP can be administered to alleviate pain due to POPI to avoid opioids. Therefore, it can be present in patient's blood when propofol is infused. Furthermore, APAP is an electro-active phenol compound as propofol and its oxidation CV peak appears at around [+0.3 - +0.5] V, which is very close to that of propofol at PGE ([+0.4 - +0.9] V). Fig. 4.10 shows the oxidation peak resulting from CV procedure applying potentials between +0.2 V and +1.4 V at 0.1 V/s scan-rate in a solution containing 1 mM APAP and 80.5  $\mu\text{M}$  propofol with background correction. This isolated current peak region was fitted with two Gaussian functions centered at +0.47 V and +0.60 V. Since the two Gaussian components are well discriminated, it is possible to identify and separate the contribution due to paracetamol (*gaussian1fit* at +0.47 V) from the propofol current peak in the voltammogram (*gaussian2fit* at +0.60 V).

Since we confirmed the interference action between APAP and propofol, we further investigated the optimal conditions (in terms of pH and post-processing analysis) to be able to monitor both the drugs simultaneously. DPV procedure (potential range between +0 V and +1.1 V, interval time 0.2 s modulation amplitude 50 mV modulation time 50 ms and scan

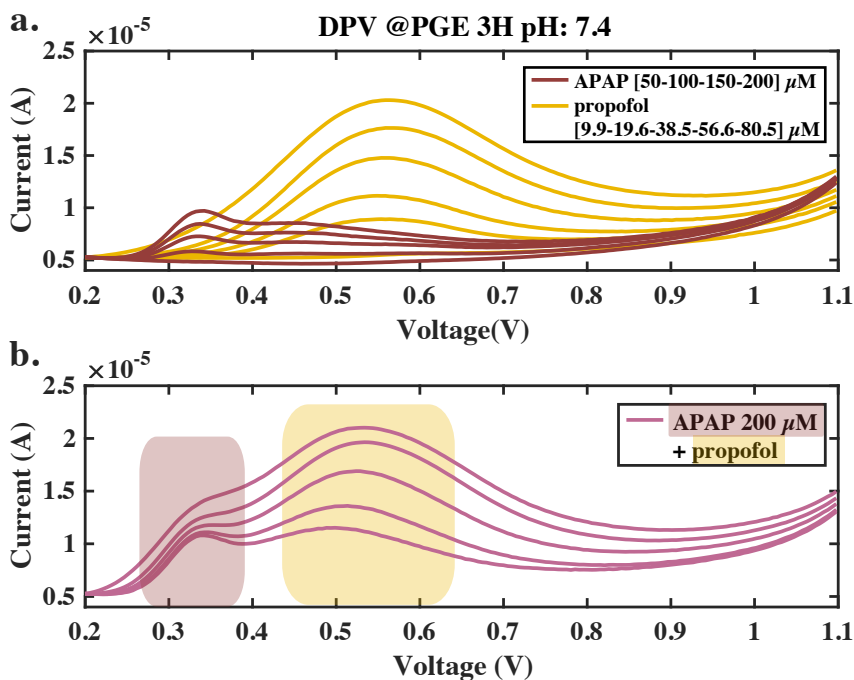


Figure 4.11 – DPV plots from APAP and propofol interference study at PGE 3H in neutral PBS (10 mM, pH:7.4) background solution.

rate 0.025 V/s) has been performed keeping the concentration of APAP fixed at 200 μM and increasing the propofol concentration during subsequent measurements. We have considered the influence of pH since, as discussed in the *Chapter 2*, it affects the potential at which the drug reacts (peak position).

Fig. 4.11 and Fig. 4.12 show DPV results at physiological and acid background solutions (PBS, 10 mM pH: 7.4 and 2.5), respectively. Both the figures report: a) overlapped typical DPV plots obtained for increasing concentrations of propofol ([9.9 - 80.5] μM) and APAP ([50 - 300] μM) if separately present in the buffer solution; b) typical DPV plots registered at fixed APAP concentration (200 μM and 300 μM) and increasing concentrations of propofol (range [9.9 - 80.5] μM).

Regarding Fig. 4.11.a, we can predict an interference action between APAP and propofol oxidation peaks between +0.4 V and +0.7 V. Indeed, Fig. 4.11.b shows only two peaks, one at ~ +0.35 V (pink area), deriving from APAP and the other from the double contribution of APAP and propofol oxidations (yellow area).

Conversely, Fig. 4.11.a shows a peak for APAP at ~ +0.6 V well separated from the two propofol oxidation peaks at ~ +0.39 V and at ~ +0.75 V. This result in three separated peaks (yellow areas for propofol and pink area for APAP contributions) also in the DPV measurement in the presence of both the drugs in the solution. The different contributions from the two drugs are more easily seen in Fig. 4.13 where single DPV plots resulting from solutions containing only APAP, only propofol and a mix of the two drugs are overlapped.

As a conclusion of this analysis, the acid pH condition is preferred, in general for sensing

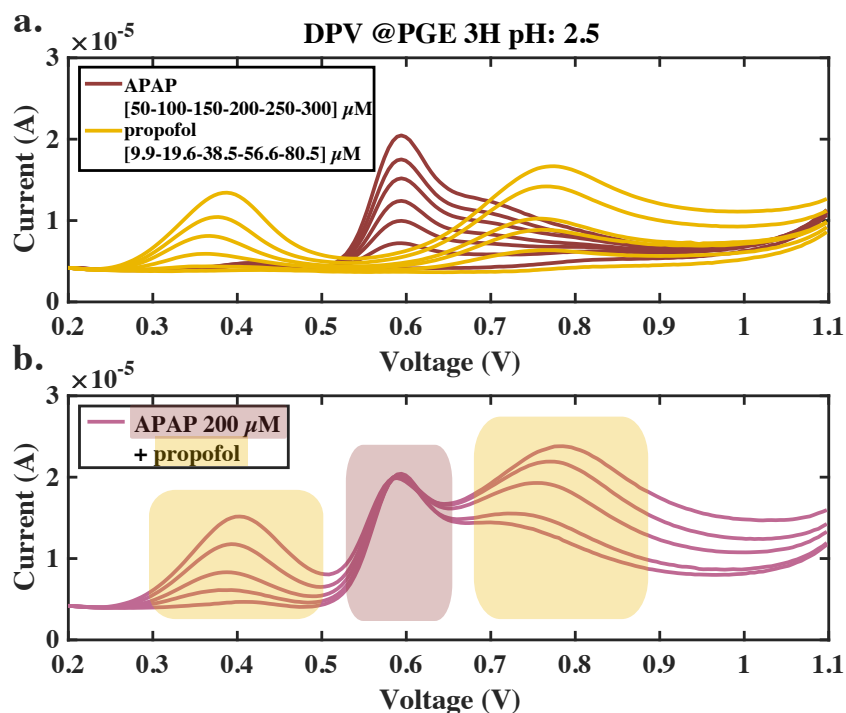


Figure 4.12 – DPV plots from APAP and propofol interference study at PGE 3H in acid PBS (10 mM, pH:2.5) background solution.

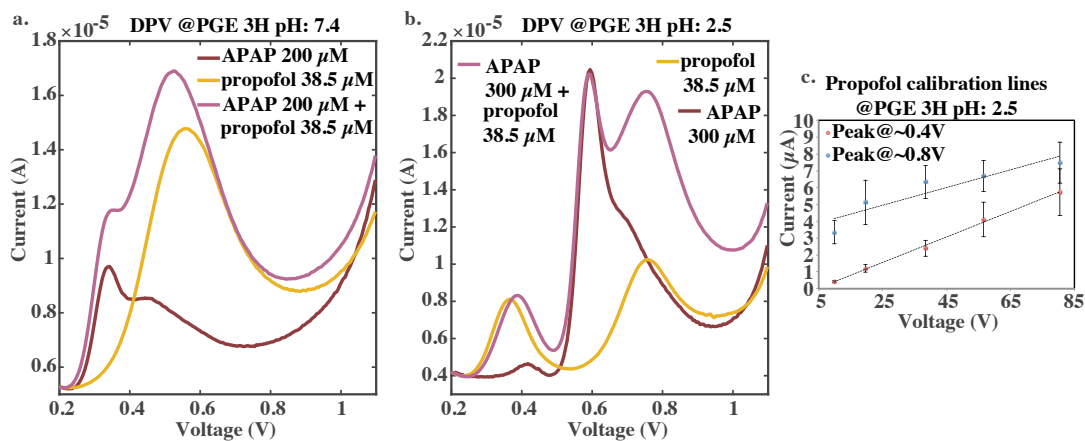


Figure 4.13 – Interference study at different PBS pH conditions: overlap of DPV curves at PGE 3H in solutions containing 200  $\mu\text{M}$  APAP, 38.5  $\mu\text{M}$  propofol or a mix of the two drugs at a) neutral and b) acid PBS. c) Propofol calibration lines from oxidation peaks at  $\sim +0.4$  V and  $\sim +0.8$  V in the presence of 200  $\mu\text{M}$  APAP interferent compound in acid PBS background solution. Variation bars correspond to standard errors (n = 3).

## Chapter 4. Midazolam and Paracetamol direct monitoring

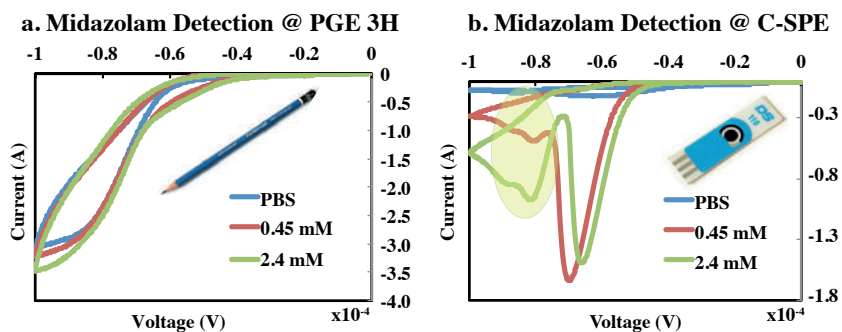


Figure 4.14 – Interference study: midazolam detection (0.45 mM and 2.4 mM) in PBS (10 mM, pH: 2.5) at a) PGE 3H and b) C-SPE WEs. No visible reductive peak is visible at PGE 3H.

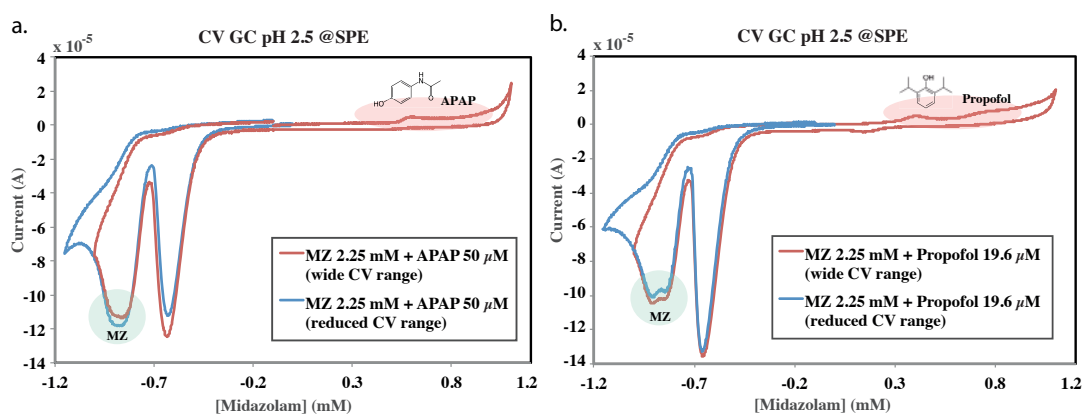


Figure 4.15 – Interference study: CV plots at C-SPE for midazolam detection in PBS pH 2.5 in the presence of APAP and propofol drugs.

aims. Fig. 4.13.c reports the calibration lines for the two oxidation peaks of propofol at +0.4 V (red) and +0.8 V (blue) in the presence of 300  $\mu\text{M}$  of its interferent APAP. Sensitivity values have been evaluated as  $0.053 \pm 0.012 \mu\text{A}/\mu\text{M}$  and  $0.076 \pm 0.002 \mu\text{A}/\mu\text{M}$  for propofol peaks at +0.4 V and + 0.8 V, respectively. As far midazolam is concerned, we have performed CV measurements between -1 V and 0 V at PGE WE for midazolam concentrations 0.45 mM and 2.4 mM. However, as visible in Fig. 4.14.a, midazolam is not reacting at this electrode's substrate. Fig. 4.14.b reports the voltammogram obtained by running the same CV procedure in the same midazolam solutions to demonstrate the presence and the correct electro-activity of MZ drug in the analyzed solution. Therefore, we could conclude that no interference action would derive from MZ for propofol and APAP detection at PGE.

Finally, other interfering compounds, *i.e.* AA, UA and cysteine were not investigated further at PGE since their oxidative peaks are not in the same potential window of propofol. Indeed, AA and UA oxidation peaks are recorded at +0.1 V and +0.5 V, respectively (at graphite-based WE and saturated calomel electrode as RE) [177]. Moreover, cysteine had an oxidation peak at 0 V on modified graphite electrodes (saturated calomel electrode as RE) since the sensitivity of

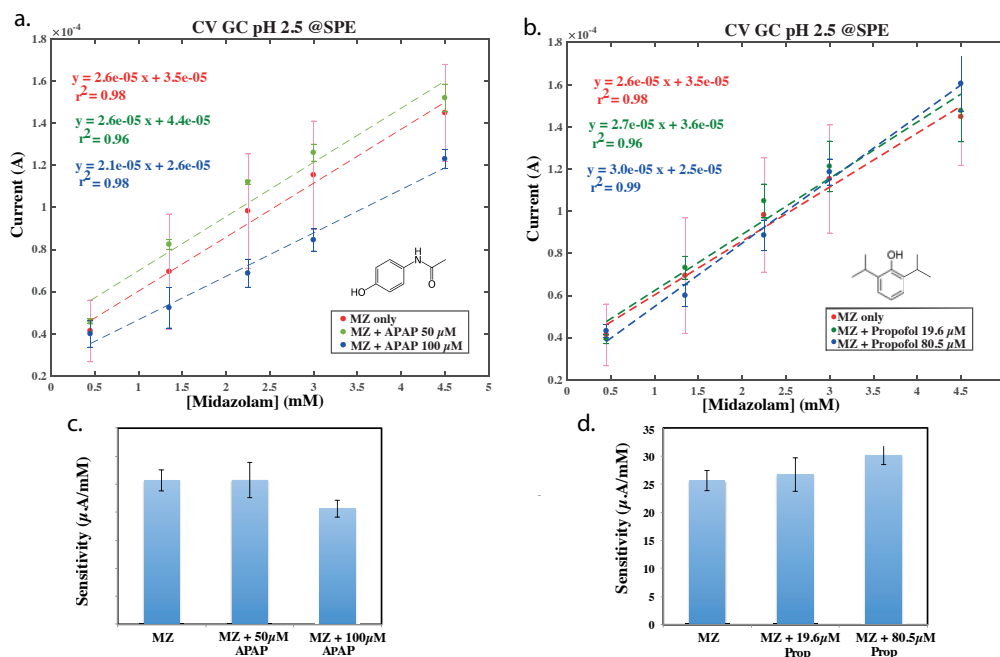


Figure 4.16 – Calibration lines for MZ detection in PBS pH 2.5 in the presence of: a) APAP and b) propofol interference compounds. Error bars represent the standard deviation from the three tested WEs.

bare electrodes were very low [178].

#### 4.3.2 Interference at C-SPE

Midazolam detection was demonstrated at C-SPE (Metrohm) as WE. In this section the interference action of APAP and propofol, the other two electro-active drugs administered in the anesthesia cocktail, will be analyzed. The interference action on the midazolam electrochemical response has been evaluated in acid PBS (pH: 2.5) background electrolyte in presence of 50  $\mu$ M APAP and 19.6  $\mu$ M propofol, separately. Fig. 4.15.a and Fig. 4.15.b show the CV plots obtained for a reduced applied potential range ( $[-1.1 - 0]$  V, blue lines) and for a wider potential range ( $[-1.1 - +1.1]$  V, red lines) in the presence of APAP and propofol, respectively. As we can observe, in the CV with reduced potential range, only typical MZ reduction peaks are visible (blue areas in the figures), while, once the potential range is enlarged, the oxidation peaks from APAP and propofol oxidation reactions at positive potentials also appear (red areas in the figures). Fig. 4.16.a and Fig. 4.16.b report the calibration lines for MZ detection in the presence of increasing concentrations of interferent compounds. In particular, Fig. 4.16.a shows the calibration lines for MZ in the presence of 50  $\mu$ M and 100  $\mu$ M APAP, while Fig. 4.16.b reports the calibration lines for MZ detection in the presence of 19.6  $\mu$ M and 80.5  $\mu$ M propofol. The sensitivity values from the calibration lines are summarized in Table 4.2 and graphically reported in Fig. 4.16.c and Fig. 4.16.d. The sensitivity values are slightly changing in the presence

## Chapter 4. Midazolam and Paracetamol direct monitoring

of increasing concentrations of interferent compounds in the solution. In case of APAP, the S from MZ calibration is decreasing of 0.4% and 19.6% in the presence of 50  $\mu\text{M}$  and 100  $\mu\text{M}$  of APAP, respectively. On the other hand, S from MZ calibration increases of 4.1% and 17.4% if 19.6  $\mu\text{M}$  and 80.5  $\mu\text{M}$ , respectively, of propofol are added into the solution. Therefore, we

Table 4.2 – Sensitivity values (*S-interf-APAP* and *S-interf-Prop*) from MZ calibration in solutions containing only midazolam and in presence of interferent compounds (*interf1* is 50  $\mu\text{M}$  APAP and 19.6  $\mu\text{M}$  propofol, *interf2* is 100  $\mu\text{M}$  APAP and 80.5  $\mu\text{M}$  propofol).

	S-interf-APAP ( $\mu\text{A}/\text{mM}$ )	S-interf-Prop ( $\mu\text{A}/\text{mM}$ )
only MZ	$25.75 \pm 3.18$	$25.64 \pm 1.86$
interf1	$25.64 \pm 1.86$	$26.69 \pm 2.95$
interf2	$20.62 \pm 1.51$	$30.09 \pm 1.67$

could conclude that midazolam detection can be performed on a C-SPE electrode by running the CV procedure between the reduced range of potentials [-1.1 - 0] V without any interference action even in presence of propofol and APAP in the analyzed solution.

### 4.4 Summary and main original contributions

In this chapter the design and the manufacture of the sensors for detecting midazolam and paracetamol anesthetics in human serum have been reported. In the previous chapter, we identified the PGE 3H substrate as the optimum for propofol direct monitoring in terms of sensitivity and fouling resistance. Therefore, in this chapter, we have finally identified the best sensors for all the anesthesia triad (hypnotic, analgesic and myorelaxant). The main contributions reported in this chapter can be summarized as follows:

- We have realized and compared the performance of different carbon nano-scale allotropes for APAP and MZ detection. In particular, MWCNTs fullerene- $\text{C}_{60}$  were considered as nano-materials. By comparing our results for APAP and MZ with the literature, as summarized in Tables 4.4 and 4.3, respectively, we can notice that, to the best of our knowledge, we have reported for the first time on a complete measure of MZ in undiluted HS with MWCNTs-modified SPE. We also obtained excellent LODs for APAP detection with respect to the only previous works [179] and [180], in relation to its detection in highly diluted human serum. Hence, we confirmed the superior efficacy of MWCNT-SPE in MZ and APAP detection in HS. This is also confirmed by the fact that the reported LOD for the sensor is lower than the minimum concentration of the therapeutic range of these drugs.
- The two differently nano-structured electrodes, *e.g.* modified with MWCNTs and fullerene- $\text{C}_{60}$ , were prepared according to theoretical EASA calculation. Indeed, by performing an *a-priori* evaluation of the EASA for each material, it is then possible to know the amount of nano-material to drop-cast on the WE surface in order to have a

#### 4.4. Summary and main original contributions

proper and reliable comparison among the tested electrodes. In this way, it is possible to exclude the catalytic effect due to area enhancement and, therefore, to highlight the contribution related only to the electron-transfer and electro-catalytic properties of the nano-materials.

- MWCNT-modified SPE have given satisfactory results for both midazolam and APAP sensing in undiluted human serum compared with literature. The excellent performance of MWCNTs nano-structures were also confirmed by SEM imaging analysis.
- We conducted an interference study among propofol, midazolam and APAP compounds. Main results from the investigation are: (i) APAP and propofol can be detected by the same PGE WE and (ii) Gaussian decomposition can be used to discriminate the current contributions of the two drugs, (iii) midazolam neither undergoes nor causes any interference with the other two drugs since it is characterized by reduction reaction at negative potentials, whereas APAP and propofol react by oxidation at positive potentials.
- Acid pH solutions may facilitate the process of discrimination for APAP and propofol detection since more separated current peaks from the two drugs are recorded. Hence, Gaussian decomposition turns out to be more straightforward.

Table 4.3 – Comparison of electrochemical performance of previously reported sensors for MZ detection.

Electrode	Detection Method	LOD ( $\mu\text{M}$ )	Stock	Biosample	Ref.
PVC membrane	potentiometry	5	MZ tetraphenyle borate solution	×	[138]
CPE (Carbon Paste Electrode)	potentiometry	60	MZ tetraphenyle borate solution	Highly diluted HS	[181]
GC	DPV	-	Organic solvents and surfactants	BR buffer	[169]
MWCNT-SPE	CV	536	PBS	Undiluted HS*	This Thesis

\*To the best of our knowledge,  
this is the only MZ detection in undiluted human serum with a reported LOD.

## Chapter 4. Midazolam and Paracetamol direct monitoring

Table 4.4 – Comparison of electrochemical performance of previously reported sensors for APAP detection.

Electrode	Detection Method	LOD ( $\mu\text{M}$ )	Stock	Biosample	Ref.
Fullerene GC	DPV	50	PBS	Urine	[182]
CPE	SquareWave voltammetry (SWV)	1.6	PBS	×	[183]
MWCNT	DPV	0.6	PBS	Highly diluted HS	[179]
SWCNT– Graphene NanoSheet (GNS)/GC	voltammetry	0.038	PBS	Highly diluted HS	[180]
SWCNT - pyrolytic electrode (EPPGE)	voltammetry	0.003	PBS	Urine	[184]
C <sub>60</sub> -SPE	CV	1.18	PBS	Undiluted HS*	This Thesis
MWCNT-SPE	CV	0.35	PBS	Undiluted HS*	This Thesis



## 5 Electronic platform

The creation of a complete electrochemical sensor requires the integration of two main building blocks: (i) the sensing platform to detect and measure the target compounds, and (ii) the front-end electronics to control and readout the sensors. In *Chapter 3* and *Chapter 4* we examined the investigation process to obtain the best electrochemical sensors for anesthetics monitoring. In this chapter, the design, development and validation of a portable *Point of Care* (PoC) electronic system to be integrated with the electrochemical sensors will be presented and described. This hardware platform will not only be interfaced with the sensors for drug detection, but also with two other commercial sensors for pH and temperature monitoring for sensors calibration.

The development of the hardware and the sensing systems was running in parallel, therefore the final electronic board has been produced through a progression of improved hardware versions. Two main features were considered for the advancement of the circuitry: (i) optimizing the interfacing with the sensors that were gradually selected for anesthetics' detection, and (ii) improving the performance by reducing the noise and increasing the signal to noise ratio. The optimization process for obtaining the final electronic system made with *Components Off-The-Shelf* (COTS) will be presented in detail throughout the following sections.

A sketch of the custom-built portable potentiostat system is represented in Fig. 5.1. The main control unit of the system consists of a powerful and low-cost RPi platform (version 3 model B [185]) that interfaces with a potentiostatic front-end PCB realized with COTS components. A dedicated *Graphical User Interface* (GUI), developed using the C++ programming language in *QT Creator 3.2* software<sup>1</sup>, allows the user to interact with the RPi and, through it, directly with the PCB circuit. The communication between RPi and PCB exploits the I<sup>2</sup>C serial protocol. As it can be seen in the schema, we have interfaced the system with both SPE and PGE-based electrochemical cells. The rest of the system includes a TCI pump<sup>2</sup> connected to the RPi *via* serial port communication, to infuse the anesthetic drugs and a laptop for data processing

<sup>1</sup>The code for RPi system was developed by Abuduwaili Tuoheti, Politecnico di Torino, Italy.

<sup>2</sup>The *Matlab* code implemented for driving the pump injections has been developed under my supervision by Bruno Donato, internship master student at *Laboratory of Integrated System*, EPFL, Switzerland.

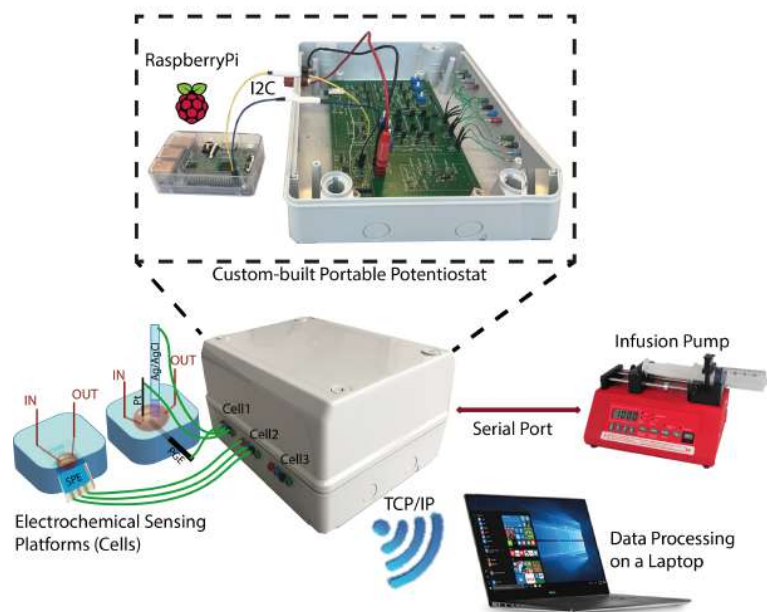


Figure 5.1 – Sketch of the RPi-based portable system for anesthesia monitoring.

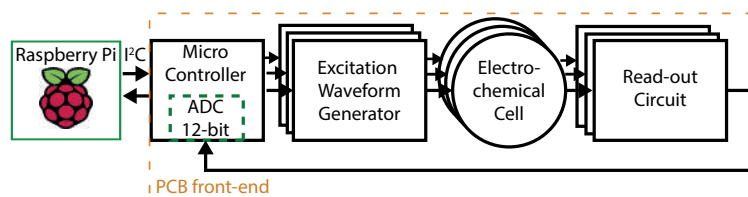


Figure 5.2 – Architecture of the RPi-driven electronic circuit for monitoring up to three anesthetics at the same time.

and for actual drug concentration evaluation.<sup>3</sup>

In this chapter we will focus on the development and validation of the electronic platform. All the schematics and layouts of the PCBs were realized in *Altium Design Software*, while the fabrication process of the hardware was provided by *Eurocircuits Online PCB Prototype* and by *Atelier de fabrication de circuits imprimés (ACI)* at EPFL.

### 5.0.1 System architecture of the electronic platform

The schematic representation of the RPi-based electronic architecture is depicted in Fig. 5.2.

RPi has been chosen and integrated in the circuit to exploit its high performance and excellent hardware and software features. It is in fact based on Quad-Core Broadcom BCM2837 chip

<sup>3</sup>The algorithms for automatic estimation of the drug concentration were implemented by Alena Simalatsar and Monia Guidi, our partners in *Centre Hospitalier Universitaire Vaudois (CHUV)*, Switzerland.

with 1.2 GHz CPUs. It also has 40 GPIO pins that can be configured as I<sup>2</sup>C, SPI ports and/or UART ports and some of them can also provide stable 3.3 V and 5 V supply. Hence, the PCB is powered from the 5 V pins of the RPi. Thanks to the I<sup>2</sup>C module library, the specific pins have been configured to be connected with the micro-controller's *Two Wire Interface* (TWI) port on the PCB to enable the exchange of the data packets. A dedicated GUI, that will be describe afterwards in *Section 5.3*, has been developed to let the user interact with the electronic system.

The PCB front-end potentiostat offers three independently programmable parallel channels to guarantee the flexibility of the platform in detecting different target compounds at the same time. Each channel implements actuation and sensing blocks consisting of: (i) **generation of excitation waveform** according to the electrochemical technique to run and (ii) **read-out** circuit to collect the response signal from the electrochemical cell. The *ATxmega32E5 micro-controller* Atmel AVR XMEGA family<sup>4</sup> plays a pivotal role in the front-end circuit since it receives the setup parameters chosen by the user through the GUI from the RPi. It controls the voltage generator circuit to apply a stable potential between the WE and the RE to make the RedOx reaction happen, and it digitalizes, through its internal 12-bit *Analog to Digital Converter* (ADC) (bandwidth up to 1 MHz), the measured analog signal from the electrochemical cell to send it back to the RPi unit. The main details on the micro-controller firmware are reported in *Appendix A*.

The portability of the system was guaranteed by limiting the dimensions of the electronic platform (10 × 8 cm), which was included in a containing box (27 × 21 × 13 cm) together with the RPi to ensure an easy system portability.

In the following sections more details will be provided about the development and optimization processes that have contributed to the manufacture of this optimized multi-channel potentiostat. Finally, the chapter will conclude with the validation of the system.

## 5.1 Multi-channel potentiostat

The main advantage of a custom-built electronic system resides in the fact that several commercially available potentiostats are bulky and expensive [186], therefore not fully suitable for providing services in everyday medical practices, where costs are required to be kept as low as possible [187]. Furthermore, the majority of potentiostatic circuits developed up to now provide only restricted electrochemical techniques [188, 189, 190] and only few of them are used for drug monitoring scopes [191, 192].

To overcome these limitations, we focused on the realization of a multi-channel potentiostat for the simultaneous detection of up to three drugs at the same time to be used for monitoring the concentrations of the anesthesia triad (*e.g.* propofol, midazolam and paracetamol) over time. In addition to the drug monitoring front-end, pH and temperature measurements will also be included in the electronic platform since they affect the electro-active drug behavior.

---

<sup>4</sup>Micro-controller programmed by Abuduwaili Tuoheti, Polytechnic of Turin, Italy

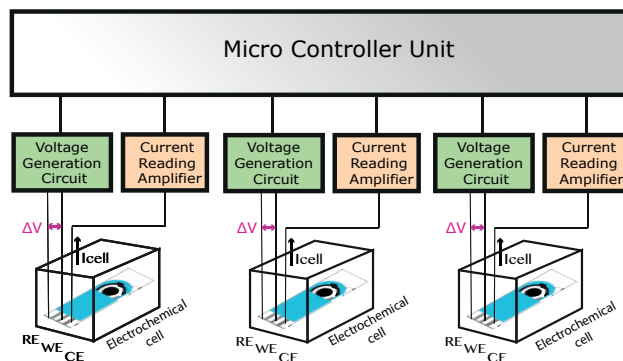


Figure 5.3 – Sketch of electrochemical cells interfaced with the multi-channel potentiostat system blocks: the micro-controller unit drives the voltage generation circuits and receives amperometric signals from the readout circuits.

### 5.1.1 Front-end design for drug monitoring

First of all, a front-end PCB was realized as a “feasibility study” in order to identify the required constraints to the final prototype of a custom-built potentiostat. The front-end architecture was designed to enable the simultaneous monitoring of three different compounds with the aim of avoiding multiplexing techniques by providing independent channels for each cell. An ATxmega32E5 micro-controller was used to drive the three independent actuation and sensing blocks for interfacing with three separated electrochemical cells, as shown in Fig. 5.3.

To provide three independent amperometric sensing channels three voltage generators and three readout circuits were implemented in the PCB. This is also visible in the schematic of the multi-channel potentiostat in a grounded-WE configuration, as shown in Fig. 5.4. The building blocks are: (i) the **micro-controller unit** (*ATxmega32E5* by Atmel), a key component of the circuit since it controls both the (ii) **voltage generator circuit** for applying a stable potential between WE and RE to make the RedOx happen and (iii) the **read-out circuit** based on a TIA to collect the current signal from the electrochemical cell.

It is also important to notice, in the schematic in Fig. 5.4, that the circuit is virtually grounded at half the value of the power supply ( $V_{cc}/2$ ) at the non-inverting input of the TIA to allow positive and negative signals.

The voltage generator circuit was built by implementing a DDS architecture for each channel. Every DDS consists of the micro-controller and a 10-bit DAC (*MCP4911* by Microchip Technology Inc.). The shape of the excitation signal waveform is first digitally defined inside the micro-controller and then converted to the correspondent voltage levels through the DAC. The communication between the micro-controller and the DAC is based on SPI interface. The analog value, the output of the DAC, is applied to the sensing cell through a control amplifier that offers high input resistance and zero current suitable for connecting the RE.

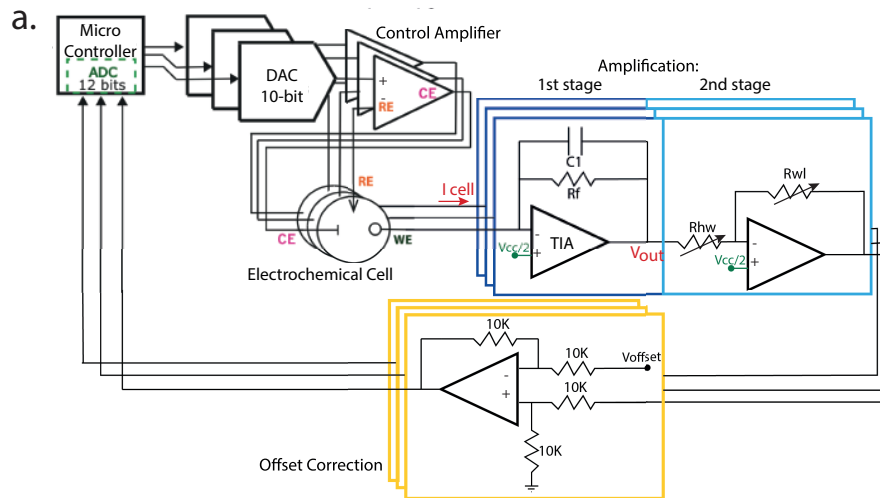


Figure 5.4 – Schematic of the multi-channel front-end for monitoring up to three anesthetics at the same time.

The RedOx current signal from the electrochemical cell passes through a **3-stage readout circuit** before reaching the 12-bit ADC internal the micro-controller. The first two stages of the readout are based on: (i) a TIA and (ii) a PGA in cascade. The TIA converts the value of the RedOx current from the electrochemical cell ( $I_{cell}$ ) into a voltage by the very well-known relation  $V_{out} = V_0 - R_f \times I_{cell}$ , where  $V_0$  is  $\frac{V_{cc}}{2}$  since the circuit is grounded at half the value of the power supply,  $R_f$  is the feedback resistance of the TIA (10 K $\Omega$ ). Furthermore, a capacitor  $C_1$  (1nF) is placed in parallel to the resistor to obtain a low-pass filtering effect (1<sup>st</sup>-order hardware *Low Pass Filter* (LPF)) since the electrochemical signal is contained at low frequencies. The cut-off frequency (16 KHz) was selected as experimental threshold.

The PGA stage is implemented by a programmable digital potentiometer (DPOT, *TPL0102* by Texas Instruments) with 256 wiper positions and an end-to-end resistance of 100 K $\Omega$ . The resulting gain is given by the ratio  $R_H/R_L$ . Therefore, the total gain of these two cascade stages is given by:  $Gain = R_f \times R_H/R_L$ . Operational amplifiers LMC6482 by Texas Instruments were used in the circuit since they provide ultra-low input current and excellent *Common-Mode Rejection Ratio* (CMRR) and *Power Supply Rejection Ratio* (PSRR). The configuration of the readout circuit is set by the user before starting the measurements through the GUI provided in the RPi. Thanks to the separate channels for each electrochemical cell, it is possible to set the suitable gain differently for each of them, hence guaranteeing the flexibility of the system. The final stage of the read-out consists of an offset correction block driven by a trimmer. It has been introduced to regulate the offset of the amplified signal in order to exploit the full dynamic of the internal ADC of the micro-controller for the conversion (bandwidth up to 1 MHz).

Once the measured analog voltage has been converted by the micro-controller ADC, the digital value is sent back to the RPi. The bi-directional communication between RPi and micro-controller relies on I<sup>2</sup>C serial protocol.

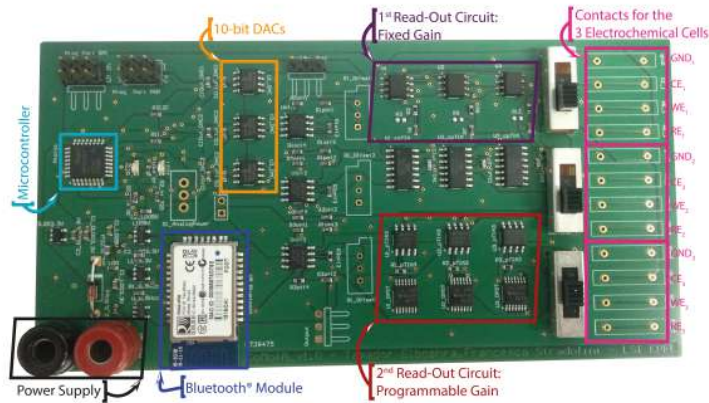


Figure 5.5 – First version PCB developed for CV and CA measurements with three independent electrochemical cells.

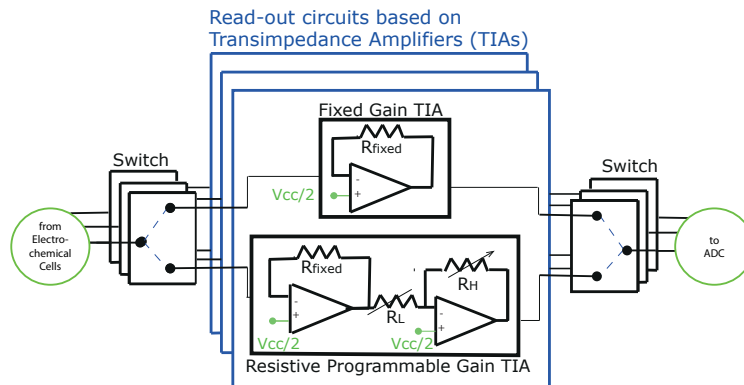


Figure 5.6 – Schematic of the different read-out trans-impedance topologies selectable by a switch.

In the following sections we will provide a detailed description of the optimization process being followed, to obtain the final multi-channel potentiostat as “prototype” that will be used for serum detection in *Chapter 6*.

### 5.1.2 Front-end optimization process

The first version of the front-end PCB realized as “feasibility study” is shown in Fig. 5.5 (16 × 6 cm dimensions). This first version did not include the interfacing with the RPi and the microcontroller autonomously managed the measures<sup>5</sup>. The read-out circuit was assembled

<sup>5</sup>Micro-controller programmed by Tamador Elboshra, Khalifa University, Abu Dhabi, KU.

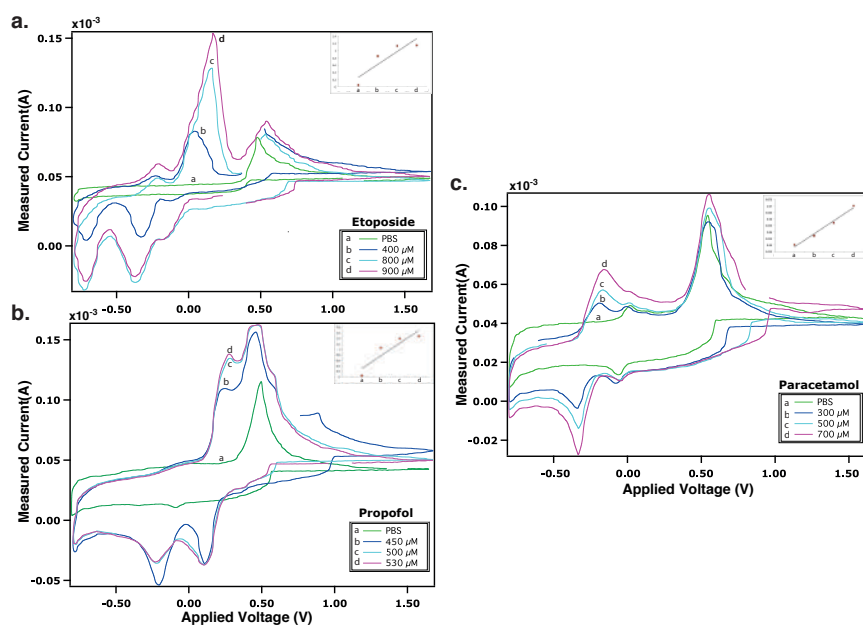


Figure 5.7 – Cyclic Voltammograms obtained for: a) etoposide, b) propofol and c) paracetamol.

with two trans-impedance topologies selectable *via* a switch, as shown in Fig. 5.6. The first topology was based on a fixed-gain TIA (10 K $\Omega$ ), while the other topology was implemented with two-stage amplification, *e.g.* a TIA and a PGA in cascade. Any offset correction stage was provided in this read-out. The configuration of the readout circuit is set before starting the measurements so that, during the experiment, the characteristics of the switches are negligible. To record the signals at different components' output pins, we have used the *Wave Surfer 3000* oscilloscope by *Teledyne Lecroy*.

The fixed-resistor readout of each on-board electrochemical channel was tested and validated by performing CV measurements of three different drugs: propofol, APAP and etoposide. It was considered the case that the patient under anesthesia is also subjected to other therapeutic treatments, which is very often the case. Carbon SPEs from Metrohm have been made to interface with the electronic board through dedicated connectors. Stock solutions for the three target compounds were obtained as follows: 5 mM propofol in 0.1 M NaOH, 30 mM APAP by dissolving 5 mg of powder in 1 ml PBS (10 mM, pH: 7.4) and 30 mM etoposide by dissolving 15 mg of powder in 1 ml Dimetil Sulfoxide (C<sub>2</sub>H<sub>6</sub>OS). All chemicals were provided by TCI (propofol) and by Sigma Aldrich (others).

Voltammograms acquired in PBS background solution (10 mM, pH:7.4) by applying the potential range between  $-0.8$  V and  $+1.7$  V with 0.1 V/s scan-rate are shown in Fig. 5.7. All the measured data have been post-processed in *Igor Pro 6.03A2* software by applying a *Finite Impulse Response* (FIR) LPF, characterized in Fig. 5.8 to eliminate the high frequency noise. A three-point calibration procedure was carried out for each tested compound: (i) etoposide was measured at 400 mM, 800 mM and 900 mM, (ii) propofol at 450 mM, 500 mM and 530

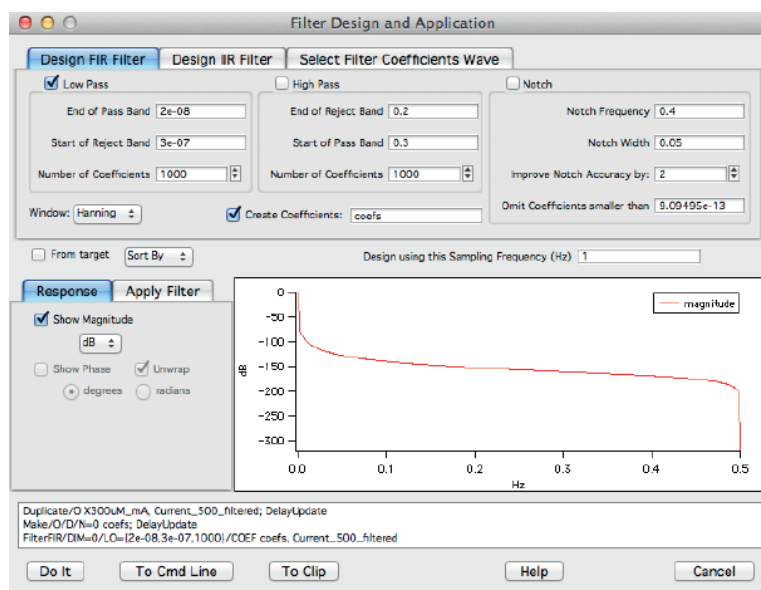


Figure 5.8 – Screen-shot of the filter design widows of Igor Pro software with the parameters for the low-pass FIR filter used in data post-processing.

mM, and (iii) APAP at 300 mM, 500 mM and 700 mM. From these preliminary results, we could identify the characteristic peaks of each target analyte and demonstrate an increase of the traces due to subsequent increasing drug concentrations. Furthermore, we could also observe the propofol fouling phenomenon between 500 mM and 530 mM concentrations (slight increase of the output traces) due to the use of a C-SPE. This problem was afterwards solved by using a PGE 3H WE as described in *Chapter 3*. However, a considerable limitation of this circuit implementation lay in the design of its layout. In fact, as visible in Fig. 5.5, there was not a clear division between the analog and the digital parts of the circuit so that a large noise component from the electronics was affecting the electrochemical measured signal, especially the variable-resistor read-out channel. Fig. 5.9 demonstrates the overlapped signals recorded at the output pins of: the DAC and of the readout circuit. It is evident that, when comparing the two readout circuit configurations, the fixed gain TIA results in better *signal-to-noise ratio* (SNR) with respect to the PGA-based read-out. Indeed, by evaluating the SNR as the maximum signal variance over the maximum deviation of the signal from the mean value, we obtain a value of 12 (21.58 dB) for the fixed-resistor TIA while only of 1.8 (5.10 dB) for the variable one. This is due to the fact that the digital potentiometer (DPOT) introduces noise that, added to the noise on the input signal from the sensing cell, is amplified by the second stage. To investigate this aspect further, we have compared the output signals of the first and second amplification stages of the variable-resistor TIA read-out at different DPOT gains, in Fig. 5.10. Clearly, a big part of the noise component at the output comes from the second amplification stage due to the digital component (DPOT). This noise increases when the DPOT gain decreases, in fact the calculated SNR values are: 2.56, 1.9, 1.8, 1.4 (8.16 dB, 5.57 dB, 5.10 dB, 2.92 dB) for 4.12, 1, 0.71 and 0.28 DPOT gains, respectively.



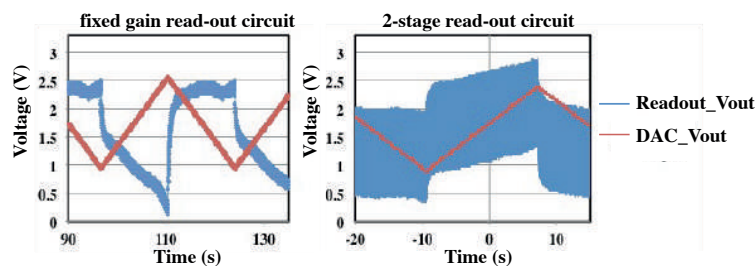


Figure 5.9 – Signal noise comparison of the fixed gain and the programmable gain read-out circuits. The output signal from the DAC and the output signal from the read-out circuit of interest are reported in each plot.

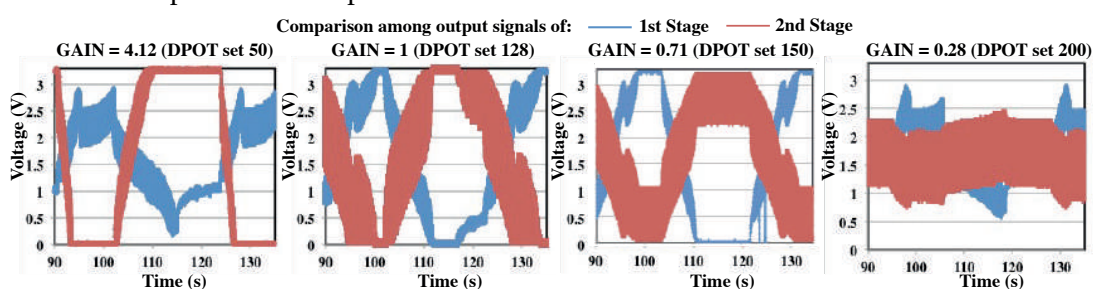


Figure 5.10 – Programmable gain read-out architecture: noise evaluation and comparison of output signals at different gain values set in the digital potentiometer (DPOT).

From this analysis, on the one side we demonstrated that the proposed front-end schematic was able to detect three different compounds, such as propofol, paracetamol and etoposide with the same circuitry, but on the other side it was clear that we had to focus on improving the layout of the PCB front-end to obtain optimized performances and reduce the circuit noise. Based on these considerations, an improved architecture was implemented with the aim to provide an optimized system in terms of noise and performance. Hence, the second-version front-end potentiostat was able to interface with any type of electrochemical cell and to apply different exciting potentials between RE and WE, to provide all the principal electrochemical techniques, *e.g.* CV, DPV and CA. Concerning the noise reduction, we followed some good-practices in mixed-signal circuit design as reported in the following *subsection*.

### Considerations on practical aspects in mixed-signal circuit design

In order to improve the performance and reducing the noise of the circuit much attention was paid to the co-design of the mixed signal circuit layout. Indeed, mixed-signal circuits require very careful consideration of the floor-plan to protect the more noise-sensitive analog part from the noise propagation of the more noisy digital part, as represented by the schematic in Fig. 5.11. To confine this noise propagation, appropriate circuit design techniques should be followed; *e.g.* careful placement of components and input/output blocks, taking into account the layout routing, powering, grounding and decoupling. In particular, two basic principles of

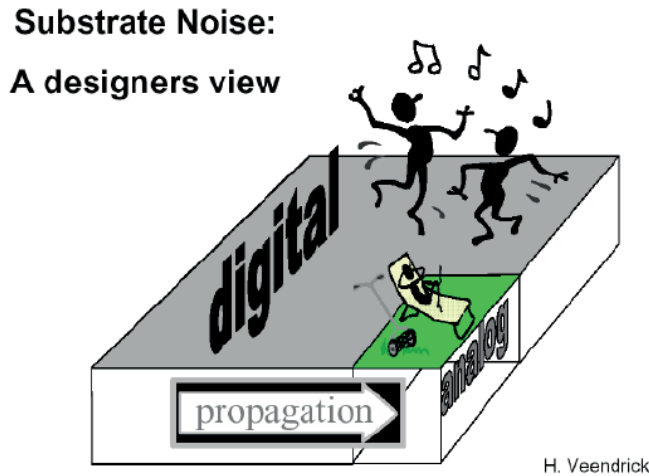


Figure 5.11 – Schematic of mixed signal circuit design: the concept of noise propagation from digital to analog parts.

*ElectroMagnetic Compatibility* (EMC) should be taken into account [193]:

1. Currents should be returned to their sources locally. Otherwise, an antenna loop is created.
2. A system should have only one reference plane, as two references create a dipole antenna.

As a consequence of these two principles, grounding is one of the most frequently discussed subjects. The general recommendation is to split the PCB ground plane into an analog plane (AGND) and a digital plane (DGND), not overlapping each other in order to minimize capacitive coupling between the two. Further, the ground plane could be connected to a single point, which is generally the power supply. This results in a mixed-signal device with a so called "*star*" *ground configuration* [194], as shown in Fig. 5.12. In this way, all noisy digital currents flow through the digital power supply to the digital ground plane and back to the digital supply remaining isolated from the sensitive analog portion. In addition, to guarantee signal isolation, the physical distance between the signal traces should be respected by following some good practices [195]:

- Minimizing long parallel lines and close proximity of signal traces on the same board to reduce inductive coupling.
- Minimizing long traces on adjacent layers to prevent capacitive coupling.
- Signal traces requiring high isolation should be routed on separate layers and, if not possible, they should run orthogonally to one another with ground plane in between to minimize capacitive coupling. In this case the ground will form an electrical shield.

Concerning the circuit decoupling, performance degradation may be derived from ripple and/or noise on the power supply pins. Traditionally, the sensitivity of an analog circuit to

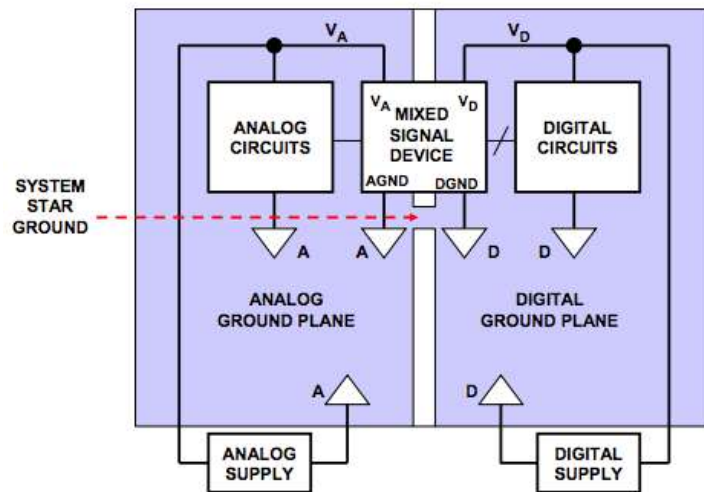


Figure 5.12 – Grounding practice in mixed-signal on a single PCB: "star" ground (GND) configuration (reprinted from [194]).

power supply variations is specified as *Power Supply Rejection Ratio* (PSRR). Normally, in the applications section of data-sheets for practically all mixed-signal components there are recommended power supply decoupling circuits that should always be used to ensure proper operation of the device. Some of the main rules can be summarized as follows [196]:

- A large electrolytic capacitor (typically 10 - 100  $\mu\text{F}$ ) should be placed close to the chip. The capacitor acts as a reservoir of charge to supply the instantaneous charge requirements of the circuit locally.
- A smaller capacitor (typically 0.01 - 0.1  $\mu\text{F}$ ) should be placed as physically close to the power pins of the chip as possible. The purpose of this capacitor is to short the high frequency noise away from the chip.
- All decoupling capacitors should be connected to a large-area low-impedance ground plane through a VIA or short trace to minimize inductance.
- Optionally, one can also place a small ferrite bead in series with the supply pin to obtain the follow benefits: (i) localize the noise in the system, (ii) keep external high frequency noise from the circuit and (iii) keep internally generated noise from propagating to the rest of the system.

Of course, for each application it is important to deeply examine the constraints, noise sources and signal amplitudes to develop *ad-hoc* solutions capable of guaranteeing successful circuit performance. This is especially true in the context of Bio/CMOS co-design, where designing a high performance circuit does not guarantee correct results from the biological information, if not properly integrated with the correct sensing transducer. Taking into account the practices

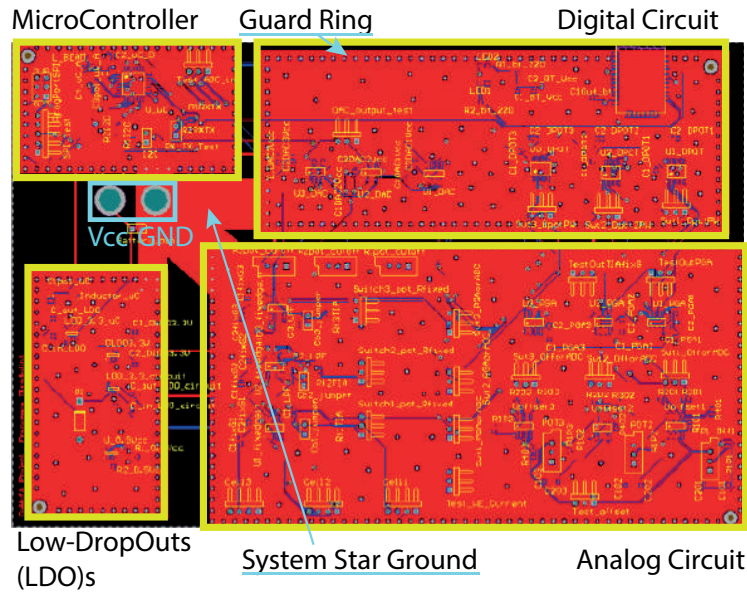


Figure 5.13 – Layout of the custom-built potentiostat in *star ground configuration*.

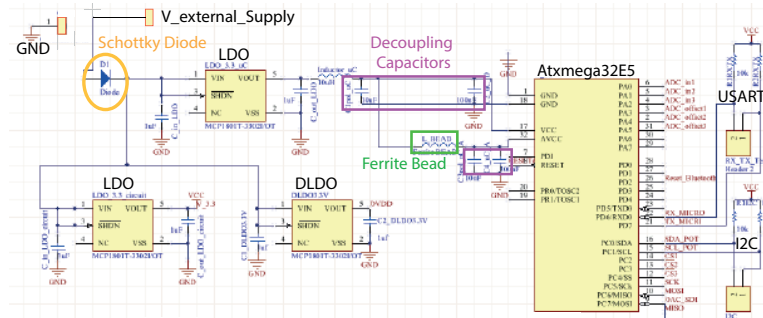


Figure 5.14 – Screen-shot from Altium with the schematic of the microcontroller. The main application notes were respected; e.g. Schottky diode, ferrite beads and decoupling capacitors were included.

suggested above for the co-design of mixed-signal circuits, the resulting layout of the second version of the custom-PCB potentiostat is depicted in Fig. 5.13. The electronic board measures  $10 \times 8$  cm and was included in a containing box ( $27 \times 21 \times 13$  cm) together with the RPi to ensure an easy system portability. As can be visible from the circuit schematic, we have separated the analog and digital components and protected the areas with *guard rings*, made of VIAs placed near to each other in order to obtain a shielding effect. The micro-controller and its related components have been separated in a further area, as well as the *Low-DropOuts* (LDOs) that are used to isolate sensitive loads from noisy power sources [197] since they offer good voltage ripple suppression and EMC performance [198]. The system *star ground* architecture is obtained by providing the ground (GND) signal to the different PCB parts through large non-overlapping tracks that radiate from the central GND pin of the power supply. Few localized lines interconnect the different areas of the board to allow the transmission of the signal in the

potentiostatic circuit. Furthermore, careful attention was paid in placing and connecting the central unit to the power supply; *i.e.* the micro-controller, by following the specific application notes described in *Atmel AT01080: XMEGA E Schematic Checklist*. In particular, as visible in the schematic detail in Fig. 5.14, we have placed a Schottky diode for power supply battery protection and low *Equivalent Series Resistance* (ESR) decoupling capacitors close to the device for each supply pin pair. Ferrite beads were also added between the external power and the  $V_{CC}$  for power filtering, since they give a better filtering performance than the common inductor at high frequency. Indeed, they employ high-frequency current dissipation in a ferrite ceramic to build high frequency noise suppression devices. We have chosen a bead with 10  $\mu\text{H}$  inductance [199].

### 5.1.3 Improved read-out signal by hardware filtering

We have redesigned the analog part of the PCB presented as “feasibility study” in the previous subsection by improving its performances with the aim of providing an even-more robust system for human serum detection. The main modification of the architecture relies on the readout circuit that now implements a first TIA stage with fixed gain followed in cascade by a 4<sup>th</sup>-order *Sallen Key* LPF to clean the signal directly in the PCB pipeline. The fixed gain of the first-stage TIA was chosen differently, so each channel could be tuned for its target drug: 10 K $\Omega$ , 30 K $\Omega$  and 500  $\Omega$  resistors selected for channel 0, 1 and 2 respectively. The rest of the circuit, as shown in Fig. 5.15, is still composed of the *ATxmega32E5* micro-controller driving the three independent actuation and sensing blocks for interfacing with three separated electrochemical cells. Each actuation block includes: a 10-bit DAC (MCP4911) and an operational amplifier (MAX4475ASA+, chosen for its low noise, low distortion and wide-band properties). Each sensing block consists of a 3-stage signal processing: (i) current-to-voltage conversion, (ii) filtering, (iii) voltage-level correction.

#### (i) *Current-to-voltage conversion*

This TIA stage (blue square in Figure 5.15) converts the current from the WE into a voltage signal. To minimize the noise, the MAX4475ASA+ operational amplifier was chosen for its low noise, low distortion and low input-bias current characteristics [200]. Besides that, a low noise feedback resistor with 0.1% tolerance is used.

#### (ii) *Filtering*

This stage (pink square in Figure 5.15) implements a 4<sup>th</sup> order Butterworth low-pass filter with unity-gain Sallen-Key topology. The Butterworth low-pass filter is selected as it gives the maximum passband flatness for the incoming signal [201] and it offers a higher roll off to the input signals beyond the cut-off frequency compared to lower order [202]. The smallest pulse period during measurement is 68 ms, as indicated in Table 5.2, which corresponds to a frequency of around 15 Hz. Therefore, by considering the stabilization time of the electrochemical signal when the potential is applied to the cell, the cut-off frequency  $f_c$  of the filter was set at 200 Hz.

## Chapter 5. Electronic platform

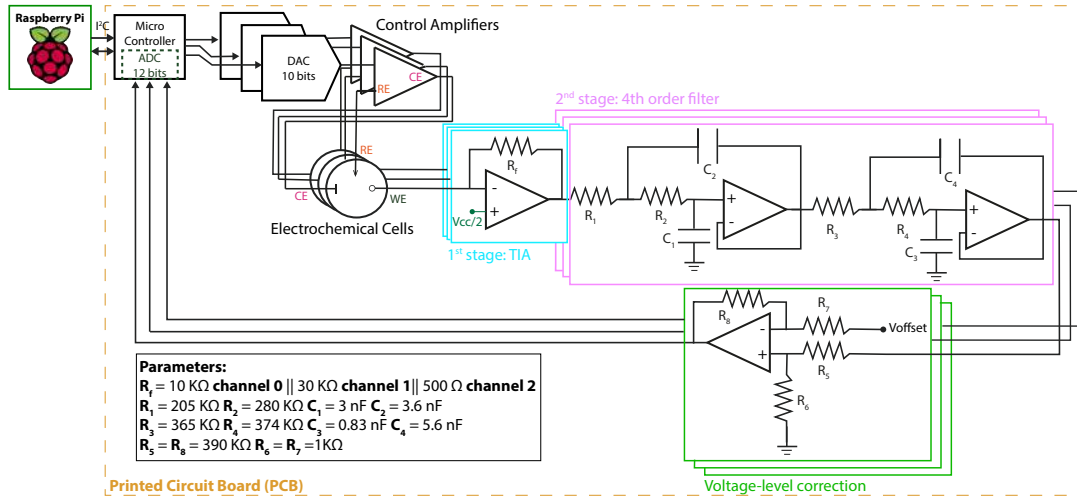


Figure 5.15 – Schematic of the final version of the portable electronic platform consisting of the RPi driving the custom-built PCB circuit through I2C serial communication.

Since the 4<sup>th</sup> order Butterworth filter is designed as 2-stage cascaded Sallen-Key 2<sup>nd</sup> order filters, we have derived the overall transfer function starting from the one of the second-order Sallen-Key filter:

$$H_{SK}(s) = \frac{V_{out}(s)}{V_{in}(s)} = \frac{1}{[1 + \omega_c C_1 (R_1 + R_2) s + \omega_c^2 C_1 C_2 R_1 R_2 s^2]} \quad (5.1)$$

Hence, the overall final transfer function is given by:

$$H_{BW}(s) = \frac{1}{[1 + \omega_c C_1 (R_1 + R_2) s + \omega_c^2 C_1 C_2 R_1 R_2 s^2]} \times \frac{1}{[1 + \omega_c C_3 (R_3 + R_4) s + \omega_c^2 C_3 C_4 R_3 R_4 s^2]} \quad (5.2)$$

Where  $\omega_c = 2\pi f_c$  and  $f_c$  is the cut-off frequency of the filter. By comparing the denominator with the 4<sup>th</sup> order normalized Butterworth polynomials:

$$B_4(s) = (s^2 + a_1 s + b_1)(s^2 + a_2 s + b_2) = (s^2 + 1.8478s + 1)(s^2 + 0.7654s + 1) \quad (5.3)$$

we have that  $a_1 = \omega_c C_1 (R_1 + R_2)$ ,  $b_1 = 1$ ,  $a_2 = \omega_c^2 C_1 C_2 R_1 R_2$ , therefore, by choosing appropriate values for  $C_1$ ,  $C_2$ ,  $C_3$  and  $C_4$  ( $C_2 \geq C_1 \frac{b_1}{a_1}$ , similarly for  $C_3$  and  $C_4$ ) the values of  $R_1$ ,  $R_2$ ,  $R_3$ ,  $R_4$  can be calculated accordingly ( $R_{1,2} = \frac{a_1 C_2 \pm \sqrt{(a_1 C_2)^2 - 4b_1 C_1 C_2}}{4\pi f_c C_1 C_2}$ , similarly for  $R_{3,4}$ ) [203]. The selected parameters are reported in the inset of Figure 5.15.

Knowing the transfer function  $H(s)$  and the cut-off frequency ( $f_c = 200\text{Hz}$ ), that for Butterworth filters is the same as the  $f_{-3dB}$  for all the orders [204], the *equivalent noise bandwidth* (ENBW) was evaluated to be:  $f_{eqnb} = 1.13 \times f_c$  ( $\alpha_{Butterworth} = 1.13$  [205]).

## 5.2. Measure of pH and temperature for calibrations

---

We obtained an  $f_{eqnb}$  of 226 Hz.

Also in this case simulations in *LTSpice XVIII*<sup>6</sup> were run to characterize the circuit noise. The *root mean square* (rms) voltage noise over the bandwidth is 3.6  $\mu\text{V}$  and the rms current noise is 437.22 pA. At 1 HZ the input referred current noise is 19.5  $\text{pA}/\text{Hz}^{1/2}$  and the output referred voltage noise is 195  $\text{nV}/\text{Hz}^{1/2}$ ; hence, the gain is estimated to be 10  $\text{K}\Omega$ .

Finally, at the 5V supply voltage, during the simultaneous measurements on the three channels, the total current consumption is 78 mA, so the power consumption of the electronic board is 390 mW.

### (iii) Voltage-level correction

The voltage signals at the output of the sensing blocks are measured by the 12-bit ADC inside the Micro-controller, furthermore, the reference voltage of the ADC is configured as 2V. So, the voltage-level correction stage (green box in Figure 5.17) is added after the filtering stage in order to guarantee that the voltage signal is in the input range of the ADC.

This final optimized front-end implementation will be adopted and tested in the overall IoT system solution in *Chapter 6*. The final complete system will integrate the electrochemical sensing part with the electronics part described here to validate and prove the overall system performance in on-line serum detection of two drugs under flow conditions.

## 5.2 Measure of pH and temperature for calibrations

Temperature and pH variations affect the electrochemical functions by influencing the reactivity of many chemical species [206]. Therefore, it is of vital importance to study their effects on point-of-care medical sensors due to their delicate use. *Temperature* (T) and pH can widely vary in patients' blood due to infectious diseases [207], acidosis or alkalosis [208]. Further, T variations may affect the pH [209]. These altered physical conditions often occur in hospitalized patients; hence, it is necessary to provide a constant monitoring of the pH levels in blood with respect to the T. As a result, the variable response of electrochemical sensors need to be characterized and parametrized to provide robust and reliable measurements over time [210]. Calibration processes for various T and pH conditions need to be performed. Different approaches have been investigated for pH and T monitoring, such as optical fiber [211], oxide-based thin-film transistors [212], graphenic materials [206], soluble polymeric dual sensors [213]. However, there are not yet complete systems that integrate the electrochemical monitoring of anesthetic drugs with pH and T control.

We have developed a ready-to-use, easy-to-reproduce system that interfaces with a commercial 1-wire temperature sensor and commercial potentiometric pH electrodes, for integration in the previously described custom-built potentiostatic board. A custom PCB-module sends

---

<sup>6</sup>The simulations were run by Abuduwaili Tuoheti, Politecnico di Torino, Italy



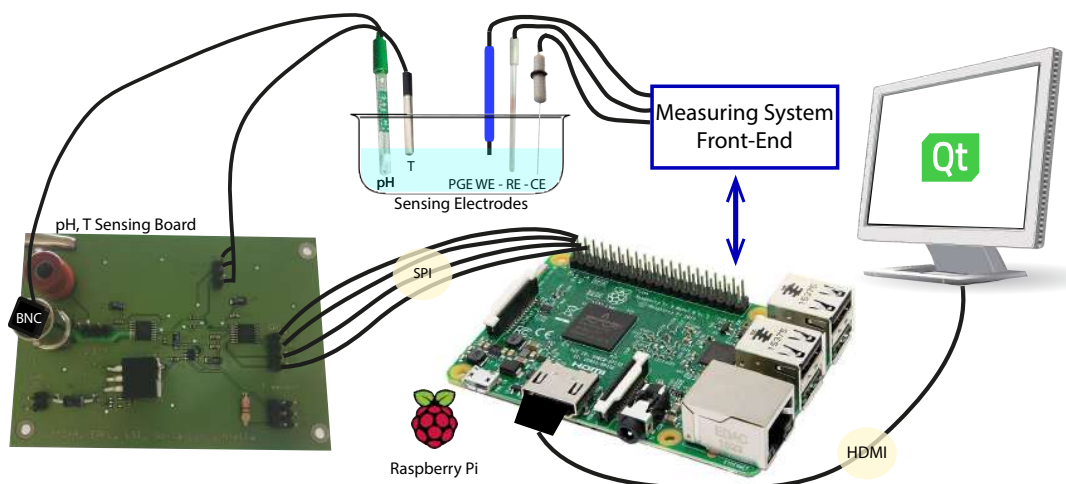


Figure 5.16 – System sketch for pH and T measurements: RPi is connected to the pH-T PCB circuit. A monitor, connected to RPi through HDMI visualizes the results. The pH and T monitoring run in parallel with electrochemical sensing driven by a dedicated front-end.

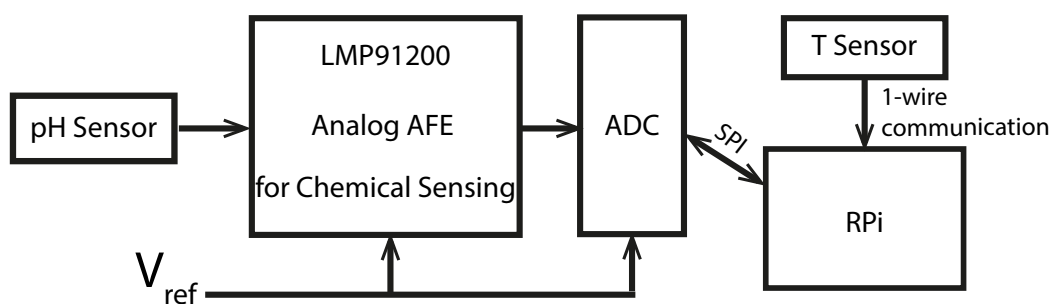


Figure 5.17 – Schematic of the portable mixed signal module for pH and T sensing.

the measured data from pH and T sensors in digital form through SPI and 1-wire serial port, respectively to the RPi computer, the core of the overall hardware system. These connections highlight our board as a module and not a standalone product proving its flexibility and ease of integration.

Fig. 5.16 shows the sketch of the entire monitoring system. The pH and T sensors are dipped into the same target solution in which the electrochemical cell is immersed. Therefore, while drug monitoring is performed by the dedicated front-end system, the pH and T of the analyzed solution are simultaneously controlled. The Qt GUI running on RPi drives the entire system.

The schematic of the realized pH-T sensing module is shown in Fig. 5.17. We can subdivide the architecture in two main blocks: (i) for pH and (ii) for T monitoring.

- (i) **pH sensing** is enabled by a potentiometry technique using an *Extech* standard polymer electrode ( $12 \times 160$  mm). We have designed the board so that it can be connected either to one electrode with built-in reference or to two separate electrodes, one as RE



## 5.2. Measure of pH and temperature for calibrations

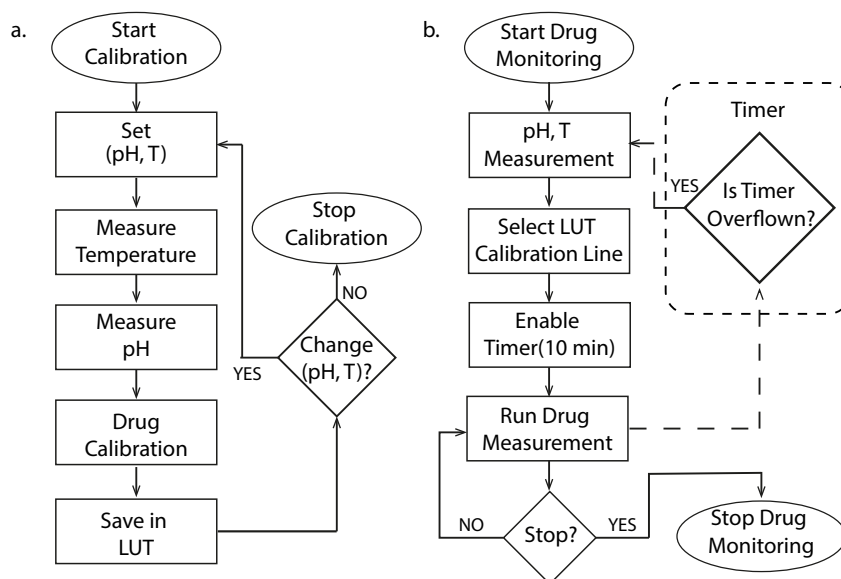


Figure 5.18 – Main processes for a) calibrating the pH-T system and for b) run drug measurements.

and one as WE. In this way, compatibility with other types of pH electrodes increases. A switch allows the user to set the preferred configuration. We chose an inner-built electrode connected to the PCB with BNC cable. Both the reference and the working electrodes of the pH sensing unit are connected to the LMP91200 *Analog Front End* (AFE) by Texas Instruments for low-power chemical sensing, as shown in Fig. 5.17. This chip detects input delta voltage from the sensor and returns a differential voltage that indicates the pH value in millivolts. In order to acquire a differential output, the common mode voltage pin of the chip is set to a certain voltage by being connected with the REF3220AIDBVR external voltage reference chip by Texas Instruments ( $V_{ref} = 2.048V$ ). The differential analog output of the AFE is afterwards converted to digital by the ADS1120 *Analog to Digital Converter* (ADC) by Texas Instruments. The ADC is connected to the same external voltage reference chip as the AFE that provides the suitable voltage for the conversion. Finally, the ADC SPI pins are connected through wires to the RPi dedicated module so that all the digitalized pH values are directly transferred to the micro-computer;

- (ii) **Temperature detection** was achieved by using a waterproof DS18B20 digital thermometer by Maxim-IC. The measured data are transferred to the micro-computer *via* 1-wire bus communication. By definition, this communication needs only one data line and the ground connection. So, the sensor is connected to the power supply of the PCB and to a GPIO pin on the RPi.

### 5.2.1 System calibration and drug measuring processes

The working principle of the developed system relies on two main processes: (i) preliminary calibration of the pH-T system-module, and (ii) continuous and simultaneous drugs monitoring, as shown in Fig. 5.18. The first process (Fig. 5.18.a) aims to create a *Look-Up-Table* (LUT) that describes the sensitivity of the drug measuring system, for example propofol, at different pH and T conditions. Indeed, it contains the slope and intercept values of the calibration line corresponding to the specific pair (pH, T). To realize the LUT the user sets up the specific (pH, T) conditions of the analyzed solution, the pH-T module measures these values to check them and then, a 3-point calibration process is run by the RPi. The calibration parameters for the respective pair (pH, T) are stored in the LUT in the RPi memory. This process continues by manually changing the (pH, T) parameters and by acquiring new calibration lines each time. Buffer solutions provided by *Certipur* with known pH values of 4.01, 7 and 10 were used for the preliminary calibration process. Once the LUT is completed, the process ends.

The second process (Fig. 5.18.b) describes the real application of the system in drug monitoring. As soon as the monitoring starts, pH and T are measured by the PCB and, according to the measured values, the respective LUT calibration line is chosen by RPi. At this point, a RPi *Timer* that overflows every 10 minutes is enabled. Further, the drug monitoring starts running in parallel. Every 10 minutes, the *Timer* enables a new pH-T measurement to check these conditions and a new calibration line is selected in case of variations. The continuous control over pH and T is stopped by the user through the GUI.

### 5.2.2 Preliminary calibration procedure

As mentioned above, the millivolt values sensed by the AFE chemical-sensing chip are sent to RPi to be converted into pH units according to the Nernst equation:  $E = E_0 - 2.3 \cdot \frac{RT}{nF} \cdot \log([H^+])$ , where  $E$  is the measured potential from the sensing electrode,  $E_0$  is related to the potential of the reference electrode,  $2.3 \cdot \frac{RT}{nF}$  is the Nernst factor and  $\log[H^+]$  is the pH ( $H^+$  is concentration of hydrogen ions) [214]. To characterize the behavior of our system a 3-point calibration was realized for known pH buffer solutions in values of 4.01, 7 and 10 at different T values ( $25^\circ - 50^\circ - 72^\circ - 95^\circ$ ). After having plotted the measured values upon each pH, we compared the obtained trend-line with the theoretical equation. As shown in Fig. 5.19, all the calibration lines cross the x-axis around pH 7 as predicted by theory. Only for T  $25^\circ\text{C}$  have we registered a small drift. For each different known pH, we continuously acquired pH measurements with the board for a period of 2 minutes and created each calibration point by calculating the average of these measurements.

### 5.2.3 Validation of the pH-T module with propofol calibrations

The reactivity of many chemical species is highly influenced by pH and T conditions. Therefore, it is necessary to continuously keep these parameters under control in a complete system for medical applications. We have validated the pH-T module by studying the pH and T

## 5.2. Measure of pH and temperature for calibrations

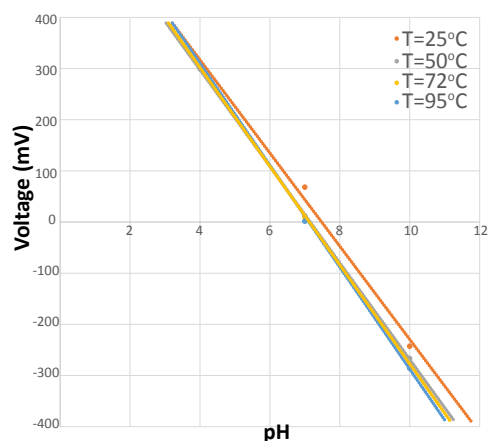


Figure 5.19 – pH calibrations line for different temperatures.

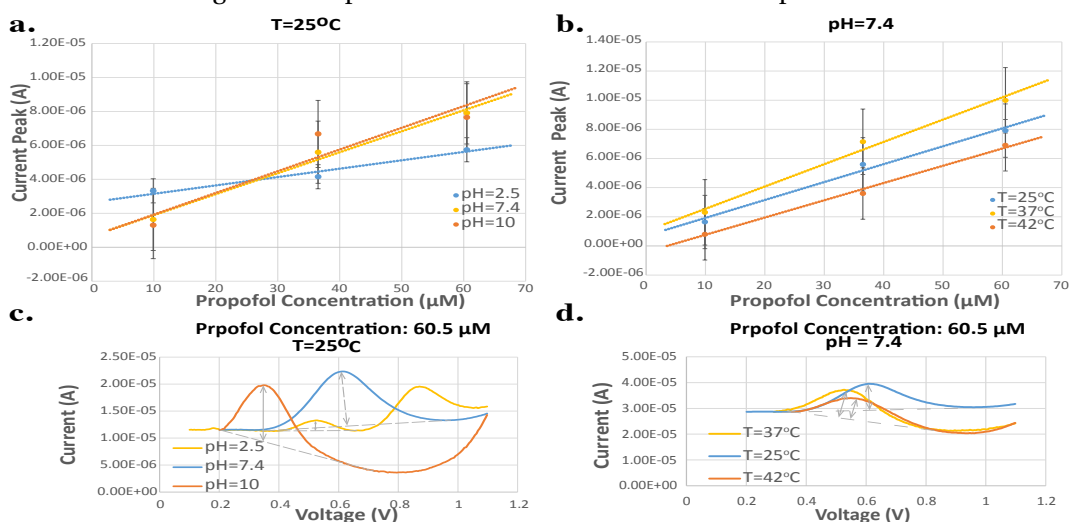


Figure 5.20 – Propofol calibration lines with: a) different pH at ambient T, b) different T at neutral pH. c) DPV peak at different pH and d) T at 60.5  $\mu\text{M}$  propofol.

dependencies in propofol RedOx reaction both in PBS and human serum solutions. Each 3-point calibration was repeated three times for each pH-T combination.

In PBS, we studied the DPV propofol oxidation process by calibrating the sensor (PGE 3H) for broad ranges of pH and T values: (i) pH values of 2.5 - 7.4 - 10 at ambient T and (ii) T of 25 $^{\circ}\text{C}$  - 37 $^{\circ}\text{C}$  - 42 $^{\circ}\text{C}$ ) at neutral pH where investigated. The obtained 3-point calibration lines for [9.9 - 36.5 - 60.5]  $\mu\text{M}$  propofol concentrations are shown in Fig. 5.20.a and .b. We can observe an increase in the sensitivity due to higher pH values (Fig. 5.20.a), while T variations lead to higher measured currents (Fig. 5.20.b). This is also confirmed by Fig. 5.20.c and .d where DPV trends are reported for fixed propofol concentration at 60.5  $\mu\text{M}$ . Two phenomena are visible in Fig. 5.20.c: (i) the increase of the height of the current peak while pH increases and (ii) the shift of the peak position due to change in pH. Fig. 5.20.d shows the similar peak heights obtained

Table 5.1 – Calibration LUT for propofol detection in human serum in different pH and T conditions.

Index	T	pH	slope	intercept
1	25	6.9	$5.3524 \times 10^{-9}$	$4.8168 \times 10^{-6}$
2	25	7.4	$2.8551 \times 10^{-9}$	$3.5729 \times 10^{-6}$
3	25	7.8	$3.8702 \times 10^{-9}$	$3.2325 \times 10^{-6}$
4	38	6.9	$2.1915 \times 10^{-8}$	$7.2571 \times 10^{-6}$
5	38	7.4	$8.4803 \times 10^{-9}$	$6.1782 \times 10^{-6}$
6	38	7.8	$1.2876 \times 10^{-8}$	$8.3445 \times 10^{-6}$
7	42	6.9	$4.1119 \times 10^{-8}$	$1.7582 \times 10^{-5}$
8	42	7.4	$1.0323 \times 10^{-8}$	$1.1561 \times 10^{-5}$
9	42	7.8	$1.2052 \times 10^{-8}$	$1.2869 \times 10^{-5}$

at different T values.

Afterwards, 3-point calibrations of propofol ( $[16.5 - 67.7 - 112] \mu\text{M}$ ) in various pH and T values were also conducted in diluted human serum (50% dilution). The pH and T conditions were chosen in order to simulate possible real cases of sick or healthy patients. Therefore, the temperature range was chosen between  $25^{\circ}\text{C} - 38^{\circ}\text{C} - 42^{\circ}\text{C}$  also to cover the case of patients with fever, while the pH values were ranged among 6.9, 7.4 and 7.8. This latter range was chosen considering that livable blood pH ranges are between 6.8 and 7.8. From these tests, we obtained the LUT in Table 5.1 where the slope and the intercept of the calibration lines are listed for each combination of T and pH.

Similar analysis should be provided for all the target drugs monitored by the RPi-based system, e.g. APAP and midazolam, in order to be able to run the procedure previously described in Fig. 5.18.b. LUTs for each anesthetic compound will be stored in the RPi memory so any drug concentration evaluation could be done according to the corresponding calibration curve.

### 5.3 Graphical User Interface on the RPi

A GUI in *Qt-Creator* environment (C++ code) was created to run on the RPi to let the user interact with the custom-built front-ends for drugs and pH-T monitoring. Since the electronic PCB implements three sensing channels in parallel, three electrochemical measurements can be carried out at the same time. Therefore, the user can: (i) enable up to three channels to use and (ii) set the desired parameters for each of these enabled sensing channels. The desired parameters include: (a) the information about the electrochemical procedure to run, such as applied potential for CA or start/end voltages and scan-rate for CV, and (b) the PCB hardware configurations to set, such as the gain of the PGA. Once these parameters have been set by the user, the measurements can be started and the acquired data from the sensors are plotted in real-time on separate graphs for each sensing channel. In addition to this, the user can also decide to enable pH and T monitoring in parallel with the simultaneous drug sensing. Fig. 5.21 represents all these details. In addition to that, the RPi has to send/receive wirelessly

### 5.3. Graphical User Interface on the RPi

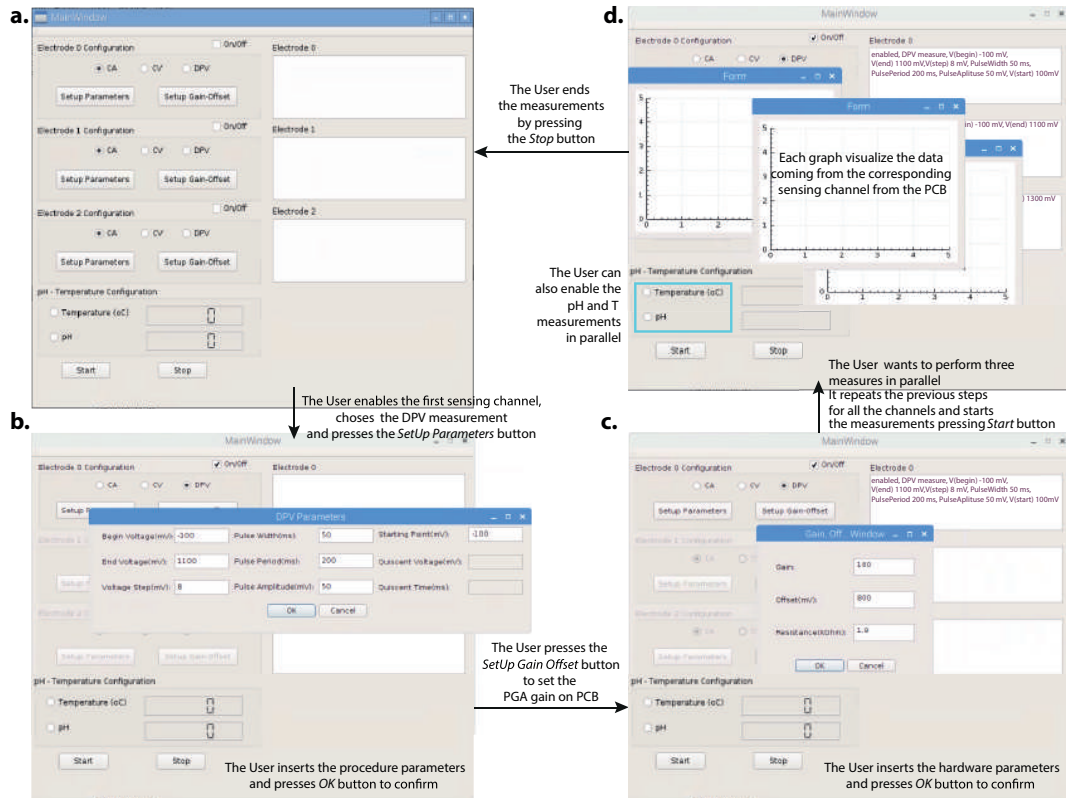


Figure 5.21 – *Graphical User Interface* (GUI) implemented on the RPi: a) main window where the user can enable the desired sensing channel and then b) set the electrochemical procedure parameters by pressing the *SetUp Parameters* and c) set the hardware parameters on the PCB by clicking the *SetUp Gain Offset* button. As soon as he has set all the desired technique/sensing channels, the measurements can be started by pressing the *Start* button. As many graphs as the enabled channels appear on the screen. The user can interrupt the measurements by clicking the *Stop* button while being able to perform simultaneous monitoring of pH and T.

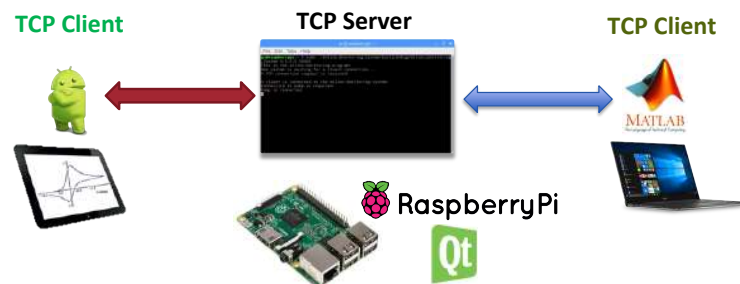


Figure 5.22 – *TCP Server* on RPi GUI that can be connected from a *TCP Client*, such as the *Matlab* or the *Android* app, via *TCP/IP* protocol.

the data *via* Wi-Fi to/from both Android apps and laptop, as shown in Fig. 5.1. To that aim, the GUI on the RPi also includes a *TCP Server* that can be connected from *TCP Clients*, such as from the Android app or from the *Matlab* code running on the laptop, *via* TCP/IP protocol. A schematic representation is shown in Fig. 5.22.

### 5.4 System validation

In this section the validation of the RPi-based potentiostatic circuit will be presented. Firstly, we validated the correct functioning of the electronic system and all its implemented electrochemical techniques by performing sensor calibration at C-SPE for APAP, considered as benchmark drug due to its well-known reaction. We then focused on propofol sensing at PGE WE with different electrochemical techniques, also in the presence of APAP interferent anesthetic. Finally, we executed scan-rate analysis to see how the system RedOx reactions change by making the experiments faster. Indeed, we would like to guarantee a fast detection, especially important in the case of drugs with rapid clearance.

#### 5.4.1 Materials and methods

APAP was purchased in powder from Sigma-Aldrich (Switzerland) while 2,6-Diisopropylphenol (propofol) by TCI chemicals. Propofol 5.4 mM stock solution was prepared by dissolving it in NaOH 0.1 M while APAP 30 mM stock solution was prepared by dissolving 5 mg of powder in 1 ml PBS (10 mM, pH: 7.4). Subsequent dilution has been done to obtain concentrations of: [9.9 - 19.6 - 38.5 - 56.6 - 80.5]  $\mu\text{M}$  and [50 - 100 - 150 - 200 - 250 - 300]  $\mu\text{M}$ , for propofol and APAP respectively. All the experiments were conducted in PBS (10 mM, pH:7.4) background solution and performed at room temperature. C-SPE with carbon WE (4 mm  $\varnothing$ ), silver RE and carbon CE were purchased by Dropsense (Spain). To perform electrochemical propofol detection a wood PGE (2 mm diameter) provided by *Staedtler Mars Lumograph*<sup>®</sup> was used as WE. Its specific lead composition is: 58% graphite, 36% clay and 5% wax, that corresponds to 3H notation. This composition of the PGE lead was selected in *Chapter 3* as optimum for propofol detection in terms of sensitivity and resistance to the fouling effect over time. The wood PGE was prepared by peeling out the two extremities. One extremity was used as electronic contact, while the other is cut to obtain a flat surface and is immersed in the analyte solution (electro active area, given by the sum of the flat surface and lateral dipped surface, is maintained at  $\sim 2.6 \text{ mm}^2$ ). To complete the electrochemical cell Ag/AgCl RE (K0265 - diameter 4 mm) and Pt wire from Princeton Applied Research - AMETEK was used.

A Metrohm Autolab system (PGSTAT 302N) was used as reference instrumentation to compare and validate our measurements. The Autolab is driven by *Nova 1.11* software.

A first validation was run to test the performance of the system with all the implemented electrochemical techniques; *i.e.* CV, DPV and CA. To do this, we performed APAP calibrations at commercially available C-SPE. APAP was chosen as a reference-drug due to its well-known

Table 5.2 – Electrochemical measurement parameters for APAP detection at C-SPE.

CV Measurements				
Start-V (mV)	End-V (mV)	V-Step (mV)	Step Width (ms)	Scan-Rate (V/s)
-100	1100	3.22	32	0.1

DPV Measurements			CA Measurements
Start-V (mV)	End-V (mV)	V-Step (mV)	
-100	1100	3.22 PCB - 5 Autolab	Applied-V (mV)
Pulse-Width (ms)	Pulse-Ampl. (mV)	Pulse Period (ms)	450
50	60	68	

Table 5.3 – “Feasibility study” PCB hardware parameters for APAP detection at C-SPE

Meas. Type	DPOT Gain	$R_f$ Gain (K $\Omega$ )	Offset (mV)	Channel
CV	236	2.42	966	0
DPV	216	0.86	300	1
CA	128	10	800	2

electro-activity properties. The CV DPV and CA parameters set for both Autolab and our custom PCB are reported in Tab.5.2. Moreover, in order to compare the output currents of our system with the commercial potentiostat, hardware parameters of the PCB have been set as in Tab.5.3. Afterwards, we investigated the propofol detection at PGE WE with different electrochemical techniques, also in the presence of APAP interferent anesthetic. DPV and CV electrochemical techniques were used to characterize the system for propofol measurements by plotting calibration lines (concentration versus oxidation peak current). The system parameters for these measurements were set through the dedicated Qt-GUI on the RPi as in Table 5.4.

The corresponding hardware parameters for the PCB were set from the GUI and are reported in Table 5.5. According to these values, the cut-off frequency ( $f_c$ ) of the first-order active LPF (first stage of the readout) is calculated from the capacitor ( $C = 1$  nF) and the resistor ( $R_f = 2.98$  K $\Omega$

Table 5.4 – Electrochemical measurement parameters for propofol and APAP detection at PGE WE with the “feasibility study” PCB version.

CV Measurements					
Start-V (mV)	End-V (mV)	V-Begin (mV)	V-Step (mV)	Step Width (ms)	Scan-Rate (V/s)
200	1350	210	3.22	32	0.1

DPV Measurements		
Start-V (mV)	End-V (mV)	V-Step (mV)
0	1100	3.22
Pulse Width (ms)	Pulse Ampl. (mV)	Pulse Period (ms)
50	60	68

## Chapter 5. Electronic platform

Table 5.5 – “Feasibility study” PCB hardware configuration for propofol and APAP detection at PGE WE.

Meas. Type	DPOT Gain	$R_f$ Gain (K $\Omega$ )	Offset (mV)	Channel
CV	186	2.98	285	2
DPV	186	9.28	333	1

Table 5.6 – Noise evaluation of the front-end circuit.  $SD_{@-3dB,output}$  is the SD for output referred voltage noise at the -3dB frequency,  $SD_{@-3dB,input}$  is the SD for input referred current noise at the -3dB frequency,  $V_{rms,noise}$  is the rms voltage noise and  $I_{rms,noise}$  is the rms current noise. These test parameters are obtained in the frequency range from 10 mHz to 10 kHz using *LTSpice*.

Channel	$SD_{@-3dB,output}$	$V_{rms,noise}$	$SD_{@-3dB,input}$	$I_{rms,noise}$	GAIN (@1Hz)
CV (2)	117.45 nV/Hz <sup>1/2</sup>	34 $\mu$ V	15pA/Hz <sup>1/2</sup>	4.34 nA	7.93 K $\Omega$
DPV (1)	120.5 nV/Hz <sup>1/2</sup>	19.51 $\mu$ V	4.8 pA/Hz <sup>1/2</sup>	1.06 nA	24.66 K $\Omega$

for CV and  $R_f = 9.28$  K $\Omega$  for DPV) as:  $f_c = \frac{1}{2\pi R_f \times C}$ . So, the cut-off frequencies are  $\sim 53.4$  KHz  $\sim 17.15$  KHz for CV and DPV, respectively. The -3 dB frequency and the cut-off frequencies are the same for 1<sup>st</sup>-order filters. Therefore, the *equivalent noise bandwidth* (ENBW)<sup>7</sup> can be calculated by the estimated cut-off frequencies as:  $f_{eqnb} = \alpha \times f_c$ , where  $\alpha$  is a factor scale that varies with the order of the filter and keeps in consideration the non-ideal behavior of the filter at the cut-off frequency. In case of first-order filters  $\alpha$  is equal to 1.57. Therefore, we obtained a  $f_{eqnb}$  of 83.85 KHz and 26.93 KHz for CV (Channel 2) and DPV (Channel 1), respectively.

Simulations in *LTSpice XVIII*<sup>8</sup> were run to characterize the circuit noise in order to prove the good performance of the custom-built potentiostat for the actual application. The *Spectra Density* (SD) functions for the output referred voltage noise at last op-amp stage of the circuit (output of the offset correction) and input referred current noise at first op-amp stage (input of the TIA) were simulated and from there we could evaluate the rms voltage and current noises through this approximation:

$$rms = SD_{@-3dB} \times \sqrt{f_{-3dB} \times \alpha} = SD_{@-3dB} \times \sqrt{f_{eqnb}} \quad (5.4)$$

Where  $SD_{@-3dB}$  is the value of the SD at the cut-off frequency (since in this case the -3dB frequency  $f_{-3dB}$  corresponds to the cut-off). Table 5.6 summarizes the value obtained for the two considered channels.

Finally we carried out scan-rate analysis for APAP and propofol to stress the performances of the system with faster measurements and to test the system response time in case of both CV and DPV. To that aim, CV and DPV measurements were performed by keeping the anesthetic concentration constant (at 36.5 $\mu$ M and at 300 $\mu$ M for propofol and APAP, respectively) and by

<sup>7</sup>The ENBW is defined as the bandwidth of a brick-wall filter, which produces the same integrated noise as the one of the actual filter [205].

<sup>8</sup>The simulations were run by Abuduwaili Tuoheti, Politecnico di Torino, Italy



setting different scan-rates: for CV [0.16 - 0.11 - 0.09 - 0.08 - 0.07 - 0.06] V/s while for DPV [0.08 - 0.06 - 0.05 - 0.04 - 0.03 - 0.02] V/s, keeping fixed 73.5% duty cycle. In this way, the required time to perform a measurement is [15 - 20 - 25 - 30 - 35 - 40] s for both techniques.

Data analysis and post-processing has been done in *Matlab R2016b* and *Igor Pro 6.22* software. A dedicated script in *Matlab* applies a Savitzky Golay digital filter (order 3) to smooth the signal data without distorting significantly [215], while data analysis consists of extrapolating the peak area and removing the baseline of each measurement to align them with respect to a common baseline and evaluating the height of the peaks with respect to the baseline. For interference study, an additional step in *Igor Pro 6.22* was introduced, to identify the peak position of the two drugs; propofol and APAP by performing Gaussian decomposition. After that peak position is identified, *Matlab* script is again used to evaluate the peak height to ensure consistency in the data.

The power consumption ( $P = V \times I$ ) of the electronic board was estimated to be 160 mW at 5V supply voltage, during simultaneous measurements on the three channels with total current consumption of 32mA.

### 5.4.2 Results

To evaluate the performances of the custom-built potentiostatic system with respect to all its implemented electrochemical techniques, we first decided to compare the APAP calibrations made with our system with those obtained, under the same conditions and drug concentrations, with the commercially-available Autolab instrumentation. Measurements are performed in neutral PBS background electrolyte by adding subsequent increasing concentrations of APAP: [50 - 100 - 150 - 200 - 250 - 300]  $\mu\text{M}$  for CV and DPV and [50 - 100 - 150 - 200]  $\mu\text{M}$  for CA. Referring to CV and DPV calibration curves, Fig. 5.23.a and .b, we can see that the performances of our system are highly comparable with the one of the Autolab. On the other hand, for CA measurements, Fig. 5.23.c, our system registers a faster stabilization of the current underlying a faster response of the circuit. This is probably due to the fact that Autolab integrates complex filtering options that slow its performances. Nevertheless, as shown in Fig. 5.24, the calibration lines obtained for all calibrations are almost equivalent for both our system and Autolab, even for CA. Moreover, the linearity of our system is confirmed by the  $r^2$  term that was evaluated to be 1 for CA and CV and 0.98 for DPV. Once the functionalities of the system have been validated with respect to the Autolab instrumentation, the electrochemical characterization of propofol and APAP. Fig. 5.25.a and .b shows the comparison of propofol sensing with CV and DPV techniques. We can deduce that both CV and DPV are suitable techniques for propofol sensing since they both obtain comparable sensitivities (S, evaluated as slope of the calibration line in Fig. 5.25.d and .e) of  $(30.2 \pm 5.2) \times 10^{-8} \text{ A}/\mu\text{M}$  and  $(11.0 \pm 1.4) \times 10^{-8} \text{ A}/\mu\text{M}$ , respectively. On the contrary, if we focus on the  $r^2$  and standard error parameters we can notice that DPV technique obtains more stable and linear results compared to CV. We also performed DPV calibration for APAP, as reported in Fig. 5.25.c and

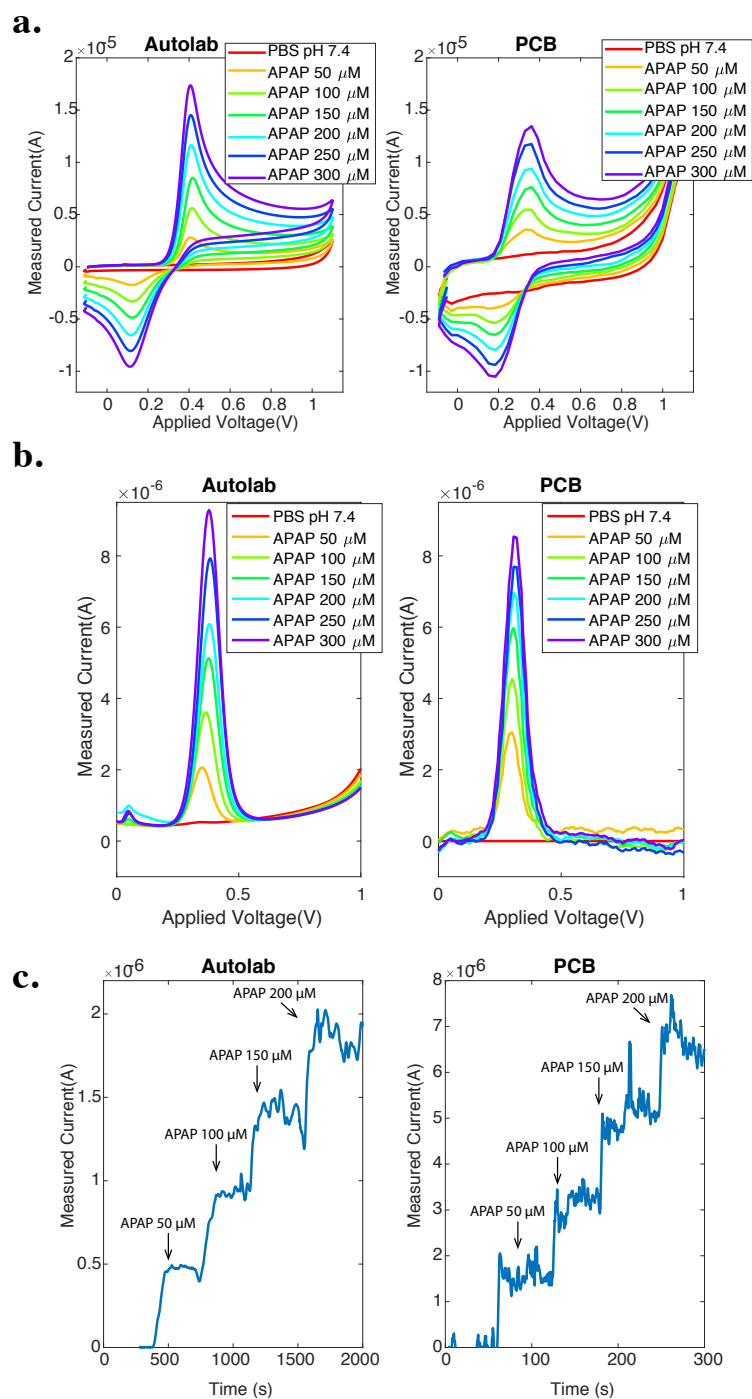


Figure 5.23 – System validation: APAP calibrations reported in comparison with the results from the commercial Autolab instrumentation for: a) CV, b) DPV and c) CA techniques.

## 5.4. System validation

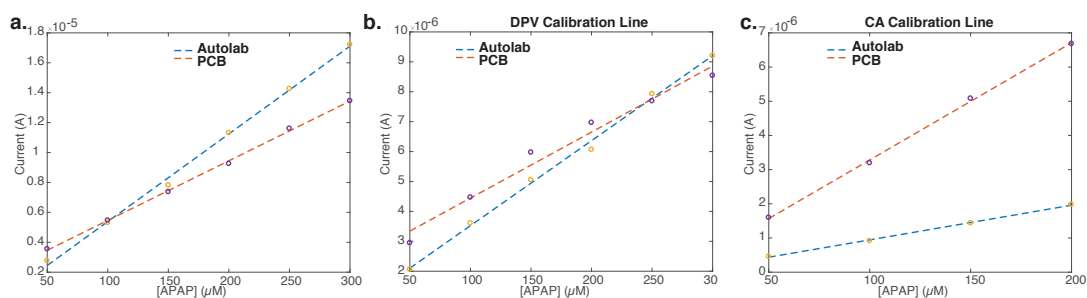


Figure 5.24 – Calibration curves comparison between our system and commercially available potentiostat: a.) CV, b.) DPV and c.) CA analysis.

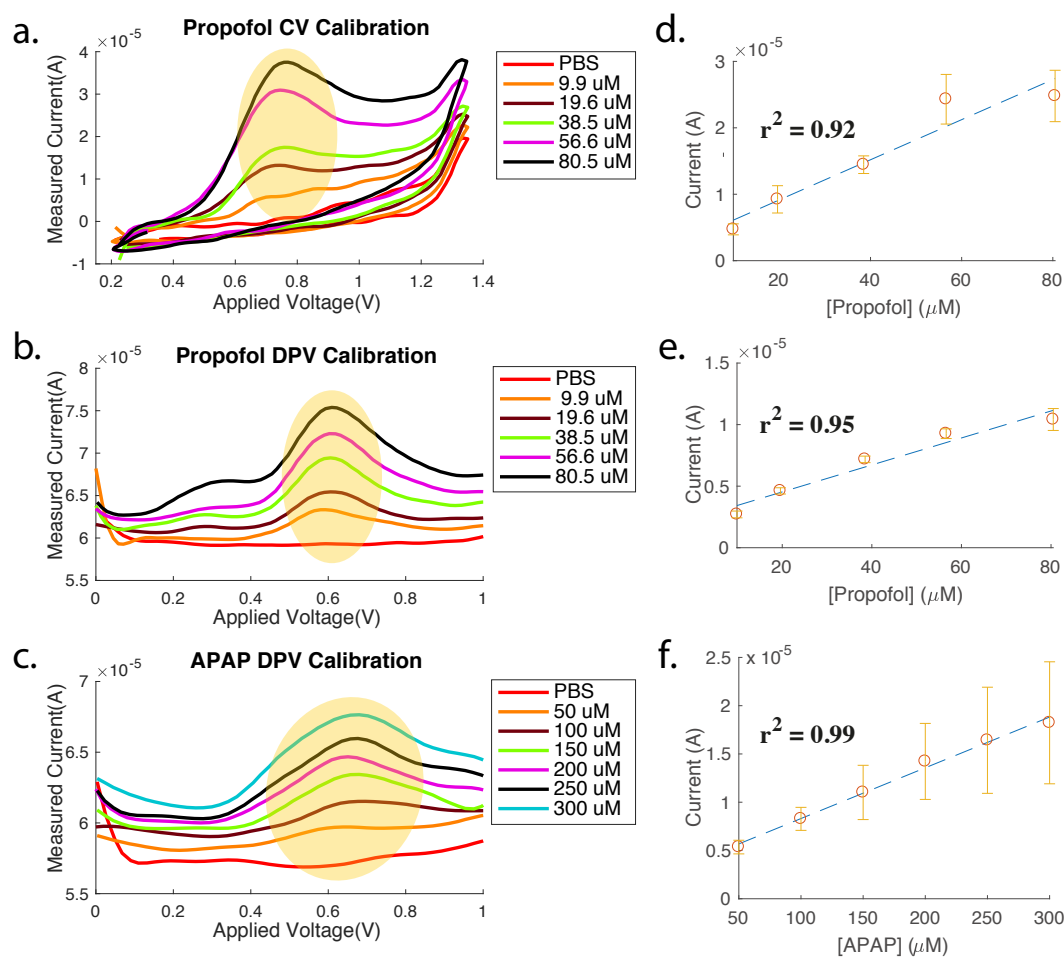


Figure 5.25 – Calibration curve studies: a) CV plots for propofol, b) DPV plots for propofol and c) DPV calibration for APAP. Calibration lines for propofol and APAP detection based on oxidation peak currents recorded by d) CV and e), f) DPV.

## Chapter 5. Electronic platform

5.25.f, to characterize its behavior at PGE so that to be able to analyze its interference with propofol. The system is able to sense the compound in the same voltage ranges of propofol measurements with a sensitivity of  $(52.6 \pm 2.3) \times 10^{-9} \text{ A}/\mu\text{M}$ , in Fig. 5.25.f. From the DPV characterization, an LOD of  $0.53 \mu\text{M}$  with a RSD% of 0.03 has been evaluated for propofol and of  $3.22 \mu\text{M}$  with a RSD% of 0.02 for APAP. LOD has been evaluated from the  $3\sigma_b$  rule, where  $\sigma_b$  is the standard deviation of the blank measurement ( $n = 3$ ), while the  $S$  is extracted as the slope of the calibration line. When measuring the solution containing a mixture of the two drugs, a complex voltammogram is measured and an additional step of Gaussian decomposition is required to identify the peak position of each drug. Fig. 5.26 shows the Gaussian

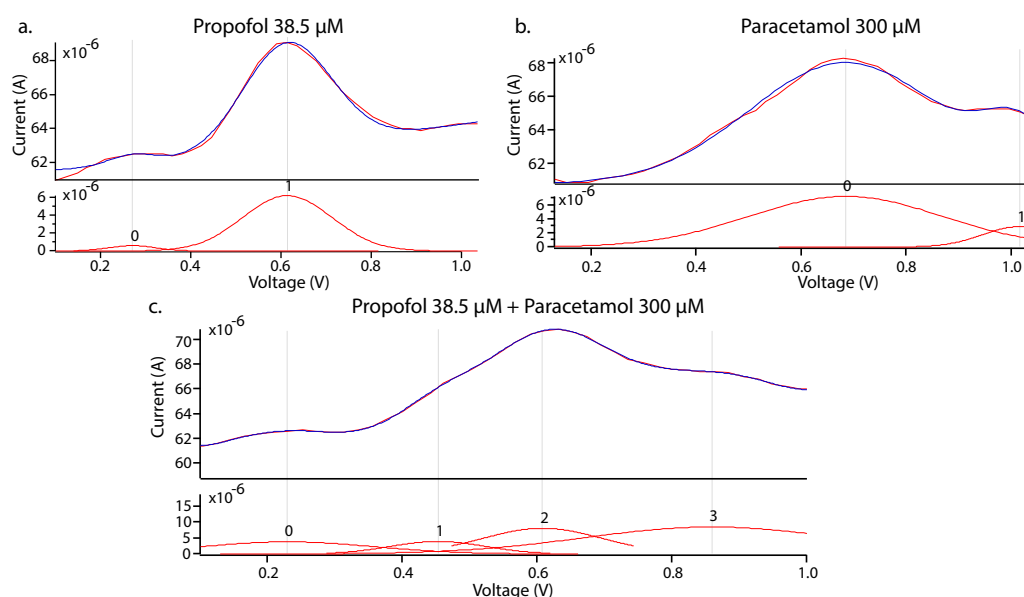


Figure 5.26 – Gaussian decomposition analysis on *Igor Pro 6.22* software for DPV curves of: a) Propofol  $38.5 \mu\text{M}$ , b) APAP  $300 \mu\text{M}$ , and c) a mixture of the two compounds (interference study).

decomposition step performed with *Igor Pro 6.22A* software. More specifically, Fig. 5.26.a and Fig. 5.26.b show the single contribution of propofol and APAP, respectively, when the two compounds are separately present in the analyzed solution. Fig. 5.26.c is the resulting voltammogram obtained with both compounds mixed in the analyzed solution. Thanks to Gaussian decomposition, it is possible to separate the two contributions from the obtained DPV measured curve. Therefore, after having identified the APAP and the propofol current peaks, the sensor calibration for both the compounds can be performed in *Matlab*, Fig. 5.27.a and .b. From calibration lines, the sensitivity values are calculated as  $28.0 \pm 1.1) \times 10^{-9} \text{ A}/\mu\text{M}$  and  $18.4 \pm 0.5 \times 10^{-9} \text{ A}/\mu\text{M}$  for propofol and APAP, respectively.

The measurement precision is assessed by evaluating the *Relative Standard Error* (RSE)%: 5.94% and 5.69% for propofol and APAP, respectively. These values are also largely acceptable for the U.S. National Center for Health Statistics ( $\epsilon \leq 30\%$ ) [216]. In addition, the accuracy and reliability of the measurements were evaluated by computing the *Relative Standard Deviation*

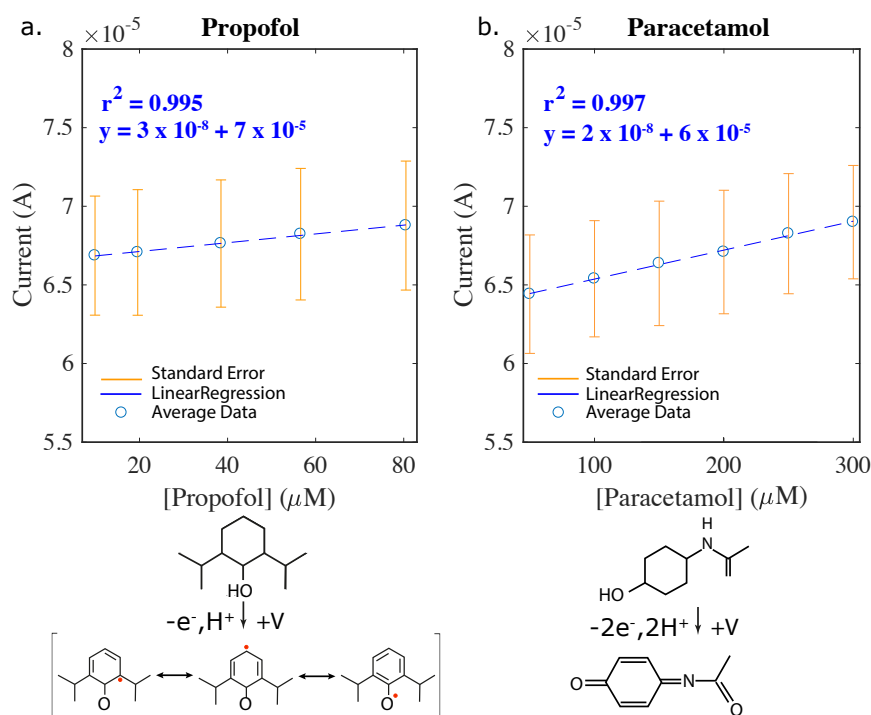


Figure 5.27 – Interference study: calibration lines for a) propofol (peak around 0.4 V) and b) APAP (peak around 0.85 V). On the bottom, general oxidation reaction mechanisms for the two drugs are reported.

RSD%. For propofol we obtained  $\leq 10.6$  RSD% and for paracetamol  $\leq 10.3$  RSD%, which are within the accuracy standards established by the *Food and Drug Administration* (FDA) guidance for commercial sensing-devices [217]. Therefore, we can conclude that, even if the sensitivity is decreased, a successful monitoring of propofol is possible and validated even in the presence of its APAP interference. The last system validation was about the speeding up of the measurements by changing the scan-rate. Indeed, normally the clearance of difficult-to-handle drugs, such as anesthetics, takes short-time and a rapid monitoring is requested. Figs. 5.28 and 5.29 show the results obtained by this analysis for  $36.5 \mu\text{M}$  propofol and  $300 \mu\text{M}$  APAP, respectively. CV and DPV measurements were tuned to complete one measurement in [15 - 20 - 25 - 30 - 35 - 40] s. The aim of this test was to see the time response of the system, including the occurrence of RedOx and its correct measurement. For both the drugs, it is evident that all the scan-rates allow RedOx to happen and the oxidative peaks tend to increase for increasing scan-rate values in CV plots (in case of APAP the reductive peak also decreases with increasing scan-rate values).

Furthermore, from CV scan-rate analysis, it is possible to plot the current peak upon the square-root of the scan-rate. This gives an indication of the kind of reaction happening for the target drug. For propofol, Fig. 5.28.c reports a linear trend that means that the oxidation is characterized by a diffusion-control process at PGE interface [218], therefore the fouling

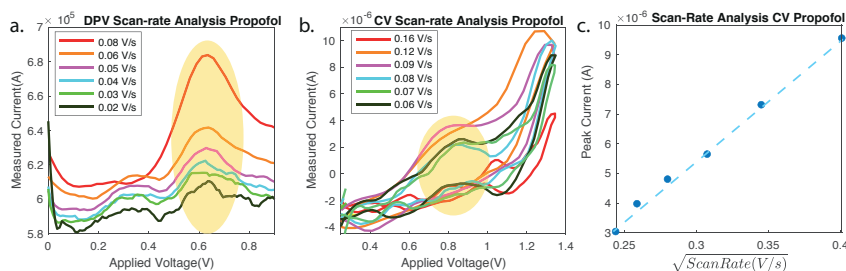


Figure 5.28 – Scan-rate study for 36.5 $\mu$ M propofol with: a) DPV and b) CV techniques. c) Reports the relationship between scan-rate and oxidation peak current from CV.

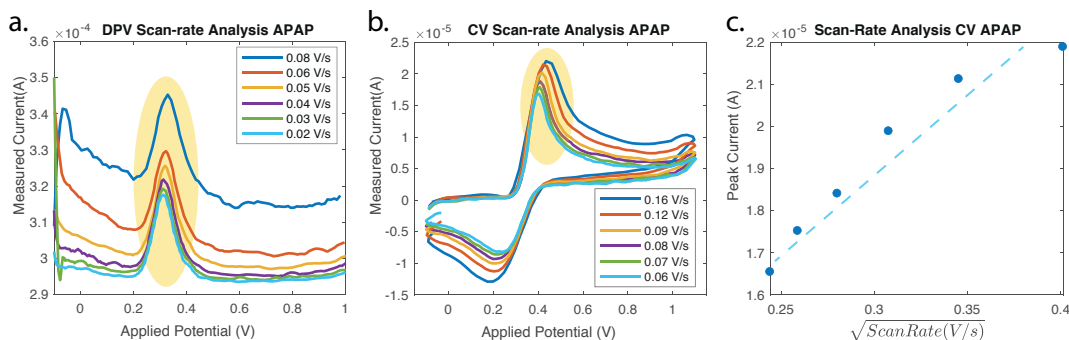


Figure 5.29 – Scan-rate analysis for 300 $\mu$ M APAP with: a) DPV and b) CV techniques. c) Reports the relationship between scan-rate and oxidation peak current from CV.

phenomenon is avoided.

Concerning APAP, the trend in Fig. 5.29.c can also be approximated by a linear relationship with the square root of the scan-rate meaning a diffusion-control process.

### 5.5 Summary and main original contributions

In this chapter we have designed and built a portable RPi-based potentiostat circuit for the simultaneous detection of several therapeutic compounds, as well as pH and T. Indeed, electrochemical activity of drugs is affected by these two parameters and, therefore, the drug concentration estimation has to be done according to their value. The main electronic details presented in this chapter are:

- The powerful single-board computer RPi has been used as the core of the electronic system to run simultaneous monitoring of multiple drugs plus pH and T through dedicated front-ends.
- We described the implementation process followed to obtain an optimized portable multi-channel potentiostat, capable of detecting up to three drugs with the same front-end. The drug monitoring front-end has been obtained by an optimization process

## 5.5. Summary and main original contributions

in terms of improved signal-to-noise ratio, flexibility (easy to interface with different sensors) and monitoring performances. To that aim, “star” ground (GND) configuration was implemented to keep the noisy digital parts well separated from the more silent and noise-sensible analog ones. Shielding guard rings were placed all around the different layout areas of the board design. The read-out circuit implements three independent actuation and sensing blocks for interfacing with three separated electrochemical cells to achieve a multi-target platform. The grounded working electrode configuration was used with a DDS architecture to apply the excitation potential waveform over the electrochemical cell and a three-stage read-out for collecting the RedOx signal. The three stages comprise a TIA with fixed gain, in cascade with a 4<sup>th</sup>-order Butterworth LPF for cleaning the signal from the high-noise components, and an offset corrector to exploit all the dynamic of the ADC.

- The custom-built potentiostat was interfaced with different kinds of electrodes, such as C-SPE and PGE (described in the *Chapters 3 and 4*). Therefore, we could test the system with two of the major anesthetic components, *e.g.* propofol and APAP, demonstrating the successful detection also in solutions containing both the drugs at the same time. Since propofol detection is the most challenging due to the undesired fouling effect resulting from its oxidative process, we made a comparison in Table 5.7 among different

Table 5.7 – Comparison table for propofol detection using various electrochemical approaches. *Full. Sys.* and *Simult. Det.* refer to the description of a full system with custom-built electronics integrated with sensors capable of performing simultaneous detection of APAP and propofol mixed in the solution, respectively. The *Linear Range* has to be referred to the therapeutic range for propofol that is [1 - 60]  $\mu\text{M}$ .

Work	WE	Full Sys.	Fast Scans	Fouling Effect	Simult. Det.	LOD $\mu\text{M}$	Linear Range $\mu\text{M}$
[132]	GC-PVC	no	5 min each measure	overcome by PVC membrane	no	$0.015 \pm 0.3$	0 - 19.6
[219]	GC-PVC	no	-	overcome by PVC membrane	no	<1	0 - 56.6
[220]	pre-anodized carbon	no	-	-	no	0.08	0.09 - 0.9
[134]	GC	no	-	-	no	$3.2 \pm 0.1$	0 - 30
This thesis	PGE 3H	yes	scan-rate analysis to provide measures in up to 15s	overcome by PGE composition	yes	$0.53 \pm 0.03$ (RSD%)	0 - 80.5

electrochemical approaches for propofol sensing compared to ours. From this table, we can clearly notice that our system is the only one providing a complete system consisting of custom-built electronics integrated with sensors able to perform simultaneous detection of APAP and propofol mixed in the solution. Further, the timing to perform a single measurement is often not discussed, and the ones we found turned out to be much slower compared to ours. Due to the rapid PK of propofol, fast measurements are needed to provide reliable values.

- We further presented the design and the validation of a hardware PCB module for providing the potentiostatic system with pH and T module. The pH-T module is interfaced with the RPi through SPI communication. Therefore, while measuring the anesthetics' concentration through the dedicated front-end, the RPi can also control pH and T measurements in parallel. It is of crucial importance to keep these two parameters under control since they affect the electrochemical behavior of chemical compounds. The pH-T module was preliminarily validated by running pH calibrations at different T and verifying the theoretical Nernst equation behavior. Afterwards, pH and T effects on propofol RedOx reaction were investigated and LUT were obtained by collecting intercept and slope values of calibration curves obtained for different (pH,T) human serum solutions. The drug concentration evaluation has to be done according to the corresponding solution's conditions.

In the following chapter, the results collected by the final complete system, including the custom-built RPi-based electronic board integrated with the electrochemical sensing platforms included in the fluidics system, will be presented. Furthermore, the overall system was enriched by an IoT network solution to provide an enhanced and powerful tool, ready to be adopted by specialist medical staff. A description of the IoT architecture will be given in the following chapter.



## 6 Overall IoT system architecture

The development process towards the final bio-electronic multi-panel system for anesthesia delivery monitoring was fueled on the one side by the creation of an optimized multi-sensing electrochemical platform as described in *Chapter 3* and *Chapter 4*, and on the other side by the design and the implementation of a custom-built electronic potentiostatic board driven by a RPi for the control of the sensors in *Chapter 5*. Considering the anesthesia-dedicated overall system presented in Fig. 6.1 (orange highlight), these parts correspond to *Sensing Platform*

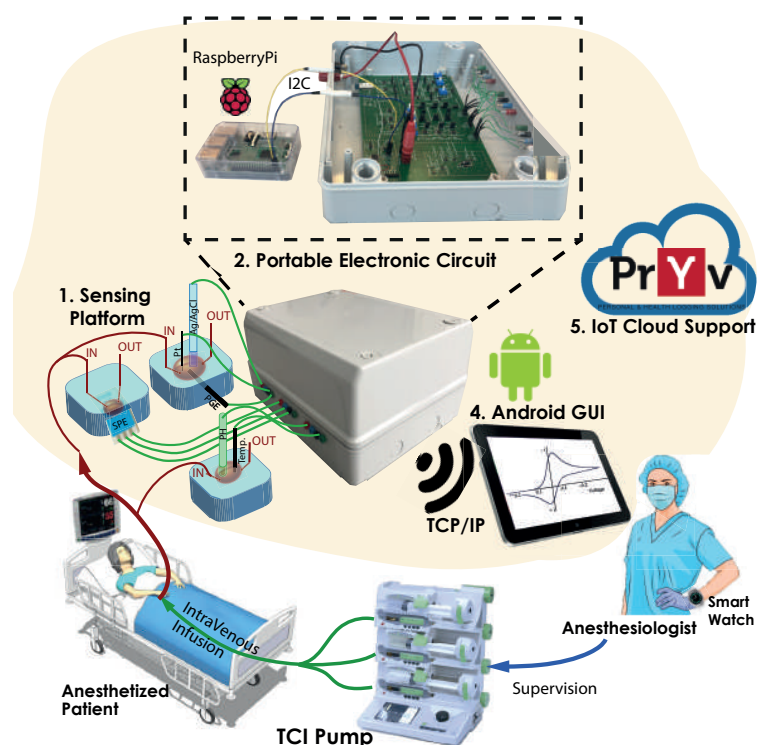


Figure 6.1 – Sketch of the IoT system (orange part) for the on-line continuous and simultaneous detection of anesthetics proposed to be a part of real hospital settings.

and *Portable Electronic Circuit* in the figure, respectively. To extend the technology, *Android GUI* and *IoT cloud support* were included as well.

The *sensing platform*, labeled as *nr. 1* in the figure, shows that the electrochemical sensors are incorporated in a fluidic device to drive the sample solutions directly on the sensing sites. The fabrication of the fluidics will be also discussed in this chapter. Furthermore, in this chapter, we will discuss the integration with the IoT cloud-based network developed in Android, and we will close with the validation of the system with the first-ever demonstration of simultaneous on-line monitoring of propofol and paracetamol concentrations over time in undiluted human serum under flow conditions.

*Section 6.2* will describe the IoT architecture developed in Android™ and based on the *PrYv* cloud middle-ware platform. *Section 6.3* will provide details about the development and integration of the fluidics with the sensors. Finally, *Section 6.4* will conclude with the successful validation of the overall system; and *Section 6.5* will further provide a solution for the integration of the infusion pump.

### 6.1 State-of-the-art

To the best of our knowledge, there is no complete system with a sensing module integrated with electronic circuit board that targets anesthesia monitoring for multiple sensing. Although Myers *et. al.* proposed a feedback controlled infusion of organic-based drugs for safer anesthesia monitoring [219], the simultaneous detection of different drugs, the development of a custom-built potentiostat and an IoT support were not provided. Moreover, other groups developed various costly and bulky strategies [122, 123] for monitoring anesthetics or even *via* electrochemical methods [132, 134, 139, 138], but without integration to an electronic board, or provided electronic platforms, for different applications [190].

The novelty of the system developed in this thesis, compared to the recent literature, relies on the fact that our system is complete and includes: (i) a low-noise, custom-built electronic potentiostatic PCB driven by a RPi, (ii) the multi-panel electrochemical sensing platform integrated into (iii) a fluidic system, which directs the sample on the sensing site, and (iv) an IoT network including a Cloud system that allows the doctor to control and share all the patient's data through a dedicated Android app.

### 6.2 IoT cloud-based network & Android development

The concept of *Smart Hospitals*, where all the medical equipment and devices are “smart” and able to interconnect and communicate with each other, is becoming a reality thanks to innovative IoT solutions. In the wake of this tendency, we wanted to provide our system with an IoT cloud-based network for anesthesia on-line monitoring. Our architecture allows the anesthesiologist to remain simultaneously connected to all the sedated patients through

## 6.2. IoT cloud-based network & Android development

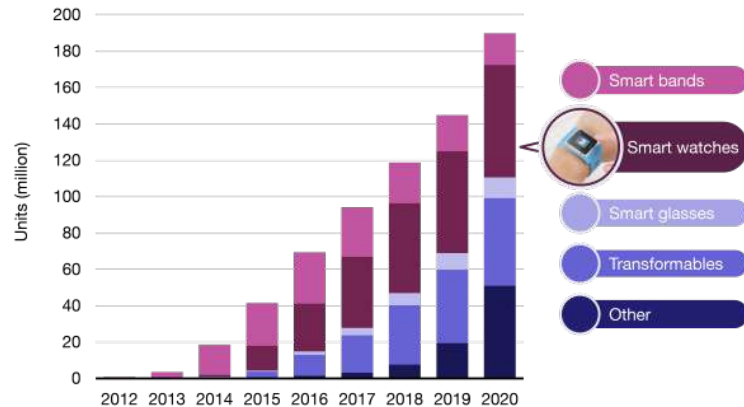


Figure 6.2 – Sales prospective of smart-wearables by device category (reprinted from [223]).

Android apps running on a mobile device, such as a tablet or a smart-phone, and/or on a wearable device, such as a smart-watch. Furthermore, through the Android app, the monitored medical data from the patients can be shared on the cloud to be accessible by geographically separated medical specialists, thereby enabling teleconsulting. Telehealth and telemedicine systems facilitate the exchange of electronic information and data for remote monitoring, diagnosis, telesurgery and other forms of medical services [221]. This would also be extremely beneficial in rural areas of under-developed Countries where there is a lack of health-care specialists [222].

The creation of the IoT solution passed through the implementation of two Android-based architectures. The first IoT network had a smart-watch, worn by the doctor, placed at the center of the network and able to interact *via* several Android applications with each of the monitored patient. The second network introduced the cloud support (provided by the PrYv middle-ware), which also makes the measured data available for remote monitoring and teleconsulting. Hereafter we will describe in detail the two architectures.

### 6.2.1 Smart-watch as paradigm-shifting player in medical IoT

Wearable technology, such as smart-watches, are considered revolutionary in the field of IoT since they satisfy the criteria of always-connected devices with the advantages of wearability, multiple functionality and low cost [224, 225, 226]. As can be seen from the sales trend by category reported in Fig 6.2, smart-watches are gaining popularity in the market. Their use has also been investigated for patient monitoring scenarios. The majority of wearable applications are developed for patients' smart-watches to detect body-motion, body temperature, physical exercises and sleep quality [227]. In addition to this, monitoring systems are also provided for specific applications, such as remote home monitoring in dementia care [228] or for patients with specific illnesses, such as autism, pulmonary disease or Alzheimer's [229, 230, 231]. However, the concept of "on-line monitoring" is also crucial in the hospital

environment, especially for critical medical scenarios, such as in *Intensive Care Units* (ICUs) [232] or in operating surgery rooms [233]. Up to now, only a few wearable solutions had been proposed for hospital use. An example is provided by the *Nurse-Watch* created by Bang *et. al.* featured with vital sign monitoring and checklist reminders to assist nurses during their daily responsibilities [234]. However, nurses were not allowed to move freely in the hospital areas without keeping both the smart-watch and the smart-phone. Indeed, the connection between these two devices was based on Bluetooth technology that can support only 10 m distances. To overcome this limitation, we developed a dedicated Android wearable application for the smart-watch, which becomes the central actor of our monitoring network for hospital environments (Fig. 6.3). The wearable device is worn by the medical doctor, responsible for the ward, and communicates *via* Wi-Fi with an independent bedside monitoring system connected to each patient. The bedside monitoring system consists of an Android application running on a tablet that continuously receives all the data measured by the sensing platform on the patient. In our case, the sensing platform coincides with the sensors that, integrated into the fluidics, are driven by the electronic system to simultaneously measure the level of multiple anesthetics in the patient.

In order to enable bidirectional communication between the smart-watch and the various Android bedside applications connected to the network, and an intermediary server is unavoidable since the smart-watch Android version Wear 1.0 enables the pairing of the wearable with only one device. Only by introducing this bridge between the smart-watch app and the patients' apps was it possible to enable the multi-patients monitoring feature. Therefore, by interacting with the smart-watch, the medical doctor or the caregiver (with different levels of responsibilities) can remotely monitor the patient's health status and can be alerted by a notification in case of anomalous recorded parameters.

All the Android app were developed in *Android Studio 2.1* using *Android* and *Android Wearable Software Developer Kit* (SDK) [235].

### Network architecture

The smartwatch-centered scenario, shown in Fig. 6.3, is based on three main building blocks:

- (a) **Client-Android app** running on a bedside tablet, that continuously receives all the data measured by the sensing system directly monitoring the patient. The concentrations of the most critical parameters measured by the sensors are immediately available for display on the bedside tablet's screen. The idea is to provide the same potentialities of the normally-used hospital monitors. Moreover, the acquired values are stored in files on the memory of the device to allow *a-posteriori* consulting. The connection between the sensing platform and the Android interface relies on *Bluetooth* (BT) technology since short-range radio frequency transmission is required. Fig 6.4 shows an example of monitored values displayed on the bedside Client app. This Android app was developed starting from an app that I previously developed and validated [237], and here it was updated to offer new functionalities based on a Wi-Fi protocol for Android intermediary-

### Smartwatches deliver alerts to intensive care doctors

Patients in intensive care must be constantly monitored. Their vital signs are recorded in real time by a series of biosensors. If an anomaly is detected, an alert is sent to the doctor on duty.

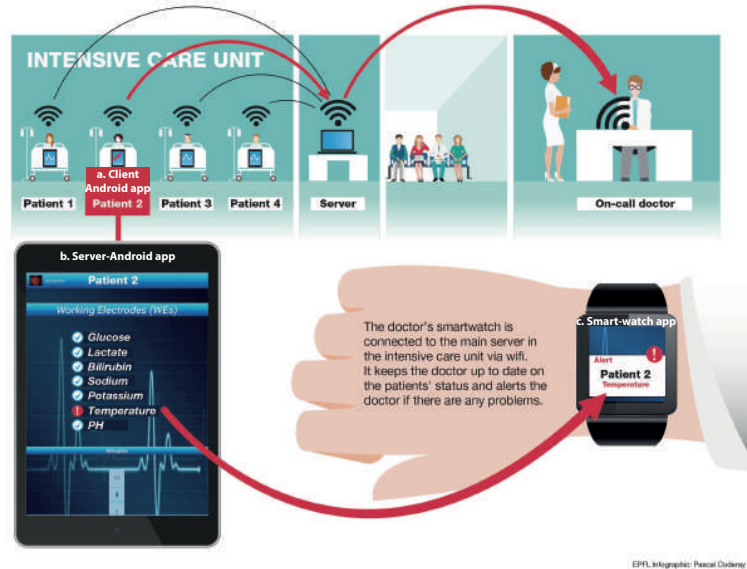


Figure 6.3 – IoT monitoring scenario: (a) Client-Android app gathers data from each patient's sensor, (b) Server-Android app redirects data to a (c) Watch-AndroidWear app to keep the medical doctor continuously connected (reprinted from [236]).

server communication.

- (b) **Server-Android app** runs on a tablet/smart-phone in a central workstation of the hospital ward. It collects the monitored data from all the patients/clients connected to the network enabling the bidirectional communication with the wearable device worn by the doctor, as visible in Fig. 6.5. Thanks to this server, it is possible to overcome the limitation of having the smart-watch connected to only one patient at time and one patient to a single doctor/caregiver, due to *Android Wear 1.0* restrictions. On the one side, we wanted to maintain a bedside tablet near each patient to show the real-time trend of all the measured parameters over time and for *a-posteriori* consulting of the data. On the other side, we wanted to receive *on-demand* the data on the smart-watch as well for alerts in case of emergencies without keeping track of the received values in order to lessen the load on the wearable app. Therefore, through the intermediate server the data are pushed to the smart-watch when requested by the doctor and an automatic message is promptly sent in case of anomalies in the recorded values. All these messages exchanged between the server and the smart-watch explicitly use the *patient identifier* and the *parameters-of-interest*. Both the server-to-clients and server-to-smartwatch connections adopt Wi-Fi communication. Indeed, if a BT piconet was implemented the distance restriction would be too limiting in the final application.
- (c) **Smart-watch app** for the doctor's watch device developed in *Android Wear 1.0*. It allows the doctor to freely move in other hospital areas and to perform different tasks in parallel

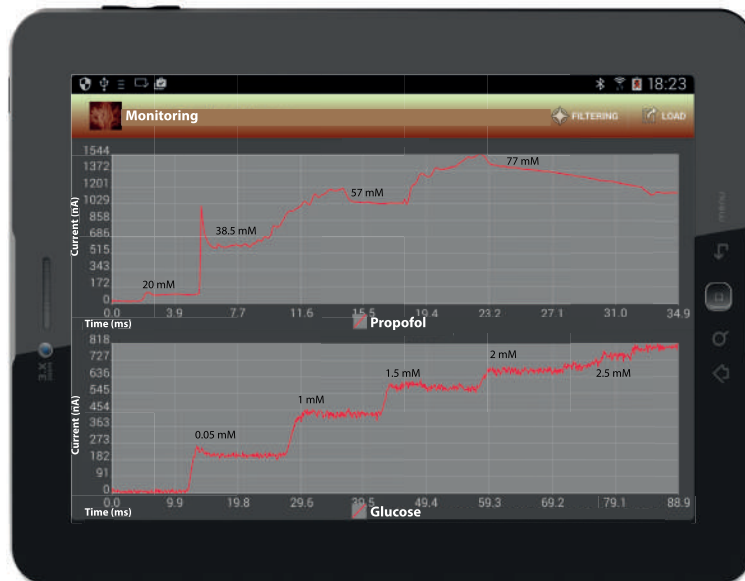


Figure 6.4 – Client Android application: the measured values from the sensing system are immediately displayed on the bedside tablet. An example of trend recorded for the endogenous glucose and for exogenous propofol anesthetic are reported.

without losing the control over the critical patients under his responsibility. Through the smart-watch the doctor, or the unit’s assistant, can query the system to receive some critical parameters from a specific patient connected to the network; he/she can also be alerted in case of emergency. The bidirectional communication between smart-watch and intermediate server exploits both the Wi-Fi or the BT technologies depending on the distance convenience. Indeed, normally the smart-watch prefers to communicate with the server tablet via BT to save battery enabling reliable data transmission, but in case of great distances Wi-Fi is necessary.

### Communication protocol

The protocol implemented to enable the bidirectional communication between the smart-watch and the multiple connected patients is shown in Fig. 6.6. The three peers that interact in the system are: (a) the patient/client Android app provided with the monitoring parameters, (b) the intermediary Android server running on a tablet that acts as a bridge to enable the multi-clients connection, and (c) the Smart-watch app for doctors/caregivers, considered as final users. Two main processes are handled by the communication protocol:

- **Query of parameters**, highlighted in blue in Fig. 6.6, when the doctor, through the smart-watch, requests from a client a specific measured parameter. The doctor has to choose the patient from among the connected ones and click the button corresponding to the parameter of interest. As soon as the button is pressed, a message, containing the infor-



Figure 6.5 – a) Server Android application: it keeps track of all the patients connected to the network and enables the bidirectional communication between them and the smart-watch. Smart-watch Android Wear application: b) the doctor can query for specific parameters from a connected patient, and c) is alerted in case of out-of-safe-range measured parameters.

mation about the selected patient and the requested parameter (On-demand (Patient #, Parameter \$)), is sent by the smart-watch to the central-server and from there the message is redirected to the target patient-client app (On-demand (Parameter §)). When the client # app receives the request, the mean of the last §samples is algorithmically evaluated and sent back to the server (Mean-§-samples), which redirects it back to the smart-watch.

- **Alerting** user in case of out-of-safe-range recorded values, displayed in purple in Fig. 6.6. As soon as, a critical measure is registered by the monitoring system, the client app sends a message to the server with an alert about the critical parameter (Alert (Parameter \$)). The server, on its side, pushes the warning to the smart-watch with information on the in-danger patient and the critical parameter (Alert (Patient #, Parameter \$)). The notification on the smart-watch occurs as a strong vibration and a pop-up that shows the involved client (Patient #) and the anomalous value (Parameter \$).

In order to face Internet unavailability, the alert/messages are sent several times until the smart-watch notifies the correct receiving through a broadcast message (Alert-Received). In this way no alert/message can be lost because as soon as the Internet connection is re-established the data transmission is successfully accomplished.

### Network validation

For the validation of the network we reproduced it by using a smart-watch for the final user (*Sony Smartwatch 3* with Android Wear 1.0) and three tablets: two tablets simulating two patients (a *Galaxy Note pro 12.2in* with Android 4.4.2 KitKat and a *Galaxy Tab 2* with Android 4.2.2 Jelly Bean) and connected as clients and a server tablet (*Nexus 7* with Android 5.0.2



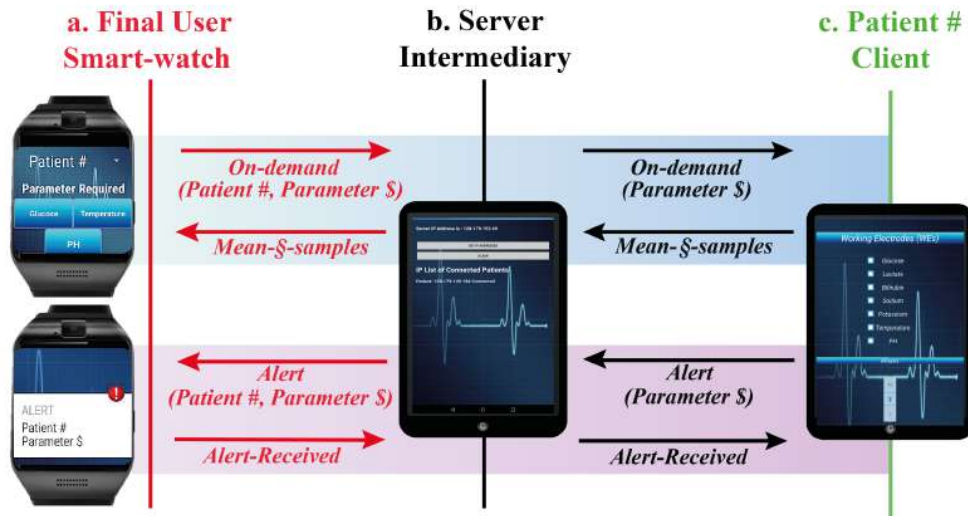


Figure 6.6 – Communication protocol, via Wi-Fi, adopted among: a) Client/Patient #, b) Intermediary Server and c) Smart-watch/Doctor.

Lollipop) as bridge. The pairing between smart-watch and server tablet is enabled by the dedicated Android Wear application from *Google Play Store*. The other connections (client-to-server and client-to-sensors) are handled by the developed Android applications.

Once we had established the network connections, we tested these following functionalities:

- The clients simultaneously connect to the server via Wi-Fi and to the monitoring sensing platform via BT.
- The server connects multiple clients and keeps track of all the IP addresses of the connected patients. Every time a new client is paired, a *Spinner List* on the smart-watch is automatically updated. The doctor handles/allows the client connection and disconnection.
- The smart-watch queries the server for receiving parameter  $S$  from client  $\#$ . In few seconds, the user receives the desired parameter from the correct patient. We tested the Internet transmission latencies by connecting to a personal hotspot obtaining less than 2 s for on-demand queries and less than 3 s for receiving alerts. Of course, these delays might vary accordingly to the available Internet connection.
- The alert message is sent to the smart-watch if  $n$  values received from the monitoring system exceed the physiological threshold. The threshold varies depending on the parameter and the number of acquired samples ( $n$ ) to be averaged for the comparison with the threshold. This  $n$  value changes depending upon the desired medical application.
- The correct reception of an alert notification on the smart-watch also in case of lack of Internet. The alarm is sent as soon as the connection is re-established and a notification is properly broadcast from the smart-watch.



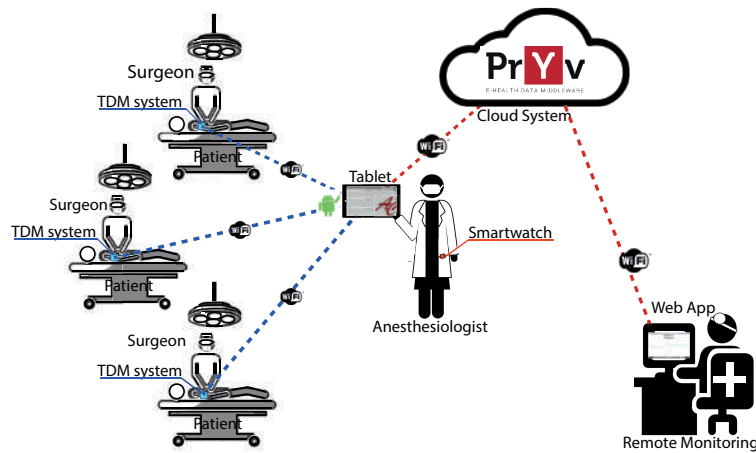


Figure 6.7 – Sketch of the cloud-based IoT network for the on-line monitoring of anesthesia delivery through dedicated app. The TDM systems directly measures the anesthesia levels in each patient and send the measurements to an Android app running on the tablet of the anesthesiologist. From here, the data are also shared through the cloud PrYv middle-ware, that is accessible through a Web app. This enables the possibility for telemedicine.

### 6.2.2 Cloud-based architecture for anesthesia monitoring

Connected and wearable medical devices are paving the way towards the realization of *Smart Hospitals* where patient care is enhanced and improved by IoT. Therefore, we wanted to include a cloud-based network in our network for anesthesia on-line monitoring. This architecture not only guarantees the anesthesiologist can remain simultaneously connected to all the sedated patients through an Android app, but also it enables a secure sharing of the patient's medical data on a cloud solution accessible by a web application. In this way, any medical specialist, even from a great distance, can consult the shared data from everywhere and at any time by accessing the cloud enabling the possibility for teleconsulting.

We have maintained the high flexibility and portability of the monitoring network to ensure the possibility of interfacing with any medical device sending the measured data wirelessly. In this cloud-supported network, sketched in Fig. 6.7, the central actor is still the anesthesiologist, but this time he was equipped with a tablet and the smart-watch was used as a feature to notify alerts. It receives alerts in case of out-of-safe-range parameters registered by the monitoring system. The incoming notification includes the name of the in-danger patient and the information about the critical parameter. Wi-Fi technology is used for all the communications: between the monitoring platforms, directly connected with the patient, and the dedicated Android app running on the doctor's mobile device, such as a tablet or a smart-phone. The Android app enables the secure data sharing on the cloud by enabling teleconsulting. The remote visualization and consulting was made possible by the development of a web application, from now on referred to as WebApp<sup>1</sup>.

Our architecture allows the anesthesiologist to monitor multiple patients in parallel so that

<sup>1</sup>The WebApp was realized by Thiebaud Modoux, Software Engineer at PrYv

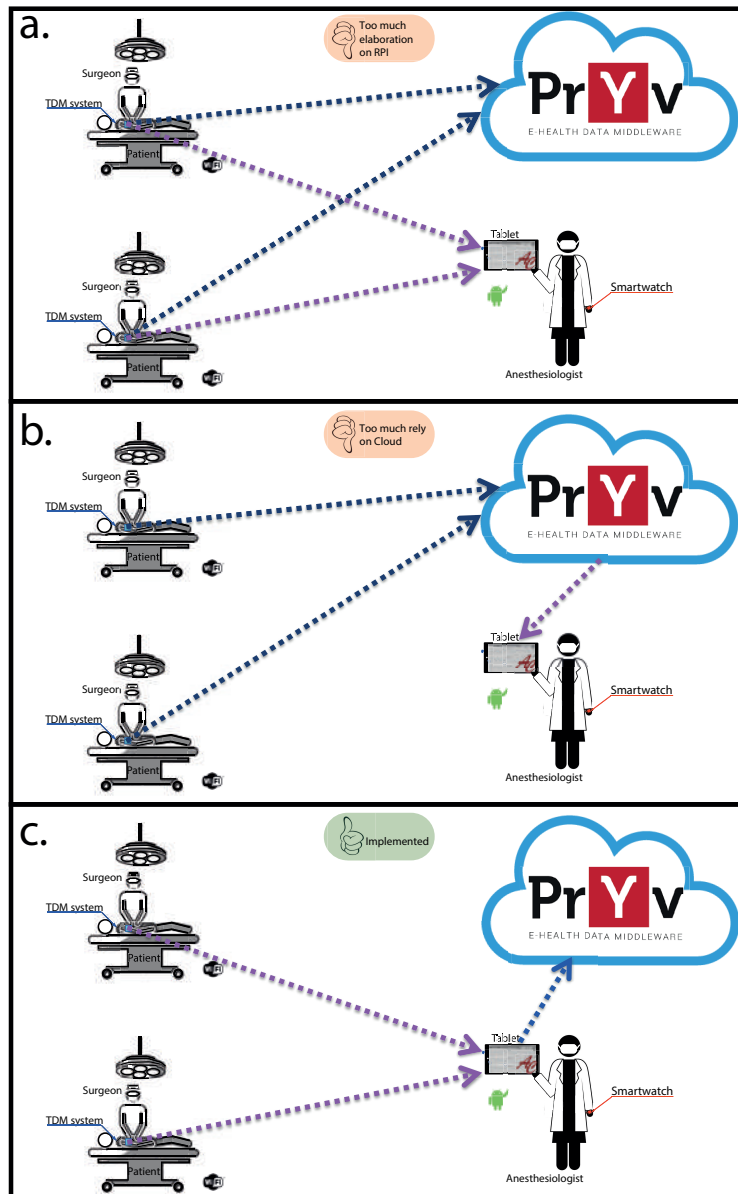


Figure 6.8 – Different architectures tested to optimize the cloud-based IoT network: a) the *Target Control Monitoring* (TDM) system simultaneously sends the data to the Android app and to the PrYv middle-ware, b) the TDM system sends data to the PrYv and the Android app takes the data from there and c) TDM sends the data to the Android app and from there the doctor can enable also the cloud sharing of PrYv.

the total process time is reduced while maintaining a high quality of medical performance.

With the aim of offering an optimized architecture, three different IoT network structures were considered as visible in Fig. 6.8. The first option was to let the TDM system simultaneously send the measured data both to the Android app and to the cloud solution, as shown in Fig. 6.8.a. This architecture was not implemented since there was no control over the data sent to the cloud storage by the medical specialist. Then, we evaluated the situation where the TDM system was sending data only to the cloud and the Android app was retrieving the data directly from PrYv, as shown in Fig. 6.8.b. This solution has also been discarded since too much reliance was placed on the cloud solution. Finally, we decided to implement a third solution, as shown in Fig. 6.8.c, where the TDM system sends the data to the Android app and from there also to the cloud, if the doctor and the patient previously agreed on this. In this way, the TDM is maintained lighter and the cloud sharing is enabled only according to the patient's permissions.

### Network architecture

The scenario depicted in Fig. 6.7 based on the optimized architecture shown in Fig. 6.8.c, relies on three main actors: (i) the anesthetized patient directly monitored by the TDM platform which continuously sends the measured data to (ii) the anesthesiologist's tablet where an Android application is running and from which the data can be redirected also to the PrYv cloud solution enabling teleconsulting from (iii) remote specialized and authorized users. A smart-watch, worn by the anesthesiologist on-duty and paired with his/her tablet where the Android app is running, enriches the network enabling fast alerting systems in case of out-of-safe-threshold parameter. The notifications sent by the Android app and received by the wearable is characterized by a strong vibration and a pop-up message displaying the name of the critical patient and the out-of-range parameter. In this way, faster interventions are ensured in case of emergencies. The Android app was developed in *Android Studio 3.0*, the WebApp in *Javascript*, HTML and CSS.

Hereafter, the main parts of the network are described in detail.

- (a) **TDM system** consists of the multi-panel electrochemical sensing platform driven by the RPi-based custom board. The measured values are sent by the RPi, communication master, to the Android app of the medical doctor exploiting the TCP/IP protocol. The data are sent following a specific protocol, as shown in Fig. 6.9, consisting of 6 bytes. The first byte (in green) contains the information about the measured drug and the electrochemical technique adopted. The following four bytes contain the data: the measured current value (in yellow) and the applied voltage (in blue). The last byte identifies the stop of the data packet (in red).
- (b) **Android App** allows the doctor to keep multiple monitored parameters under control from several patients. The app puts the doctor at the center of the architecture by establishing a bidirectional communication from one side with the TDM on the patient

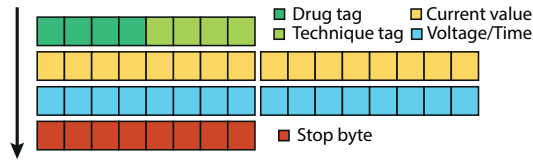


Figure 6.9 – Transmitted data packet between RPi-driven TDM system and Android app.

and from the other side with the cloud back-end. To guarantee an appropriate and safe recording of the measured parameters, the data are stored both in files on the memory of the smart-device and sent to the cloud. The main activities, reported in Fig. 6.10, are: (a) login activity that guarantees a secure access only to authorized doctors, (b) patient data activity where the doctor has to fill in the personal data of the patient and, if desired, cloud sharing is enabled, (c) Pryv login activity, that appears only if sharing has been previously selected, to sign in to the cloud environment and choose among the sharing links, (d) device list activity to establish communication with the TDM measuring the patient's parameters and (e) monitoring activity where the received data are visualized and different actions can be taken from the doctor, such as starting and stopping the measurements or adding new patients to the network. Furthermore, if an out-of-range value is measured during the monitoring from the TDM on the patient, an alert is sent to the doctor's smart-watch to ensure rapid intervention.

- (c) **Cloud Solution and WebApp** proposes user-friendly interfaces for patients and doctors who need to share health data while respecting of the medical regulations. This system is based on the Pryv e-health middle-ware solution exploiting the benefit from its data sharing features. Depending on who is accessing the sharing WebApp, two different interfaces are shown to the user, as shown in Fig. 6.11. For a patient, Fig. 6.11.a, the main window allows the sharing of a data-stream with the doctor, while for a doctor, Fig. 6.11.b, the shared patients' data-streams are listed. By selecting one of the shared subjects, the corresponding data are plotted on multiple graphs. Thanks to this visualization tool, the doctor can remotely monitor the patient status or access previous measurements. The cloud is fed with the measures received and processed by the Android app that sent them through the Pryv *RESTful API* (using HTTPS requests to get, update, post and delete data).

### Protocols and procedures

We have implemented some procedures to correctly set the IoT monitoring system through the cloud. Both the patient and the doctor have to complete some basic steps, that are summarized as work-flows in Fig. 6.12.

- **Patient-side Work-flow:** the patient gives prior consent to share his/her sensitive data on cloud during the monitoring. The patient has to access the WebApp (or create an

## 6.2. IoT cloud-based network & Android development

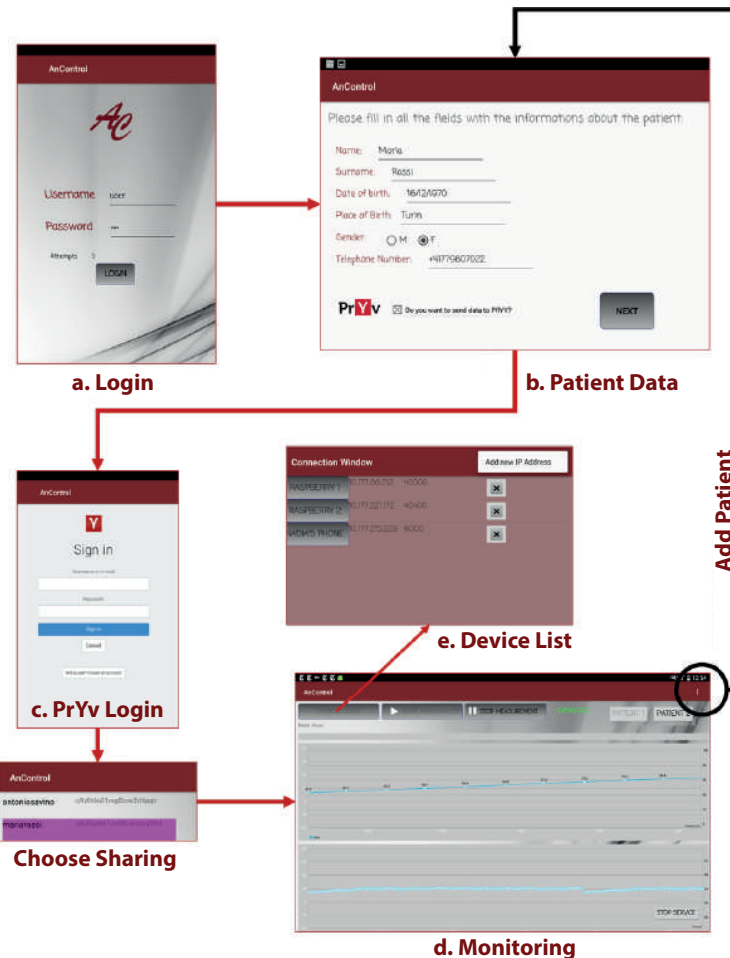


Figure 6.10 – Main activities of the *AnControl* Android app running on the anesthesiologist tablet or smart-phone. a) *Login* to guarantee secure access, b) *Patient Data* to fill with the patients information, c) *PrYv Login* if the doctor has enabled data sharing on the cloud, plus a *Choose Sharing* pop-up to select the correct patient’s sharing, d) *Monitoring* where the data are visualized on plot after having created the Wi-Fi connection with the specific monitoring device. To do that, the doctor has to select it in the e) *Device List*. From the *Monitoring* it is possible to *Add Patient* whenever necessary.

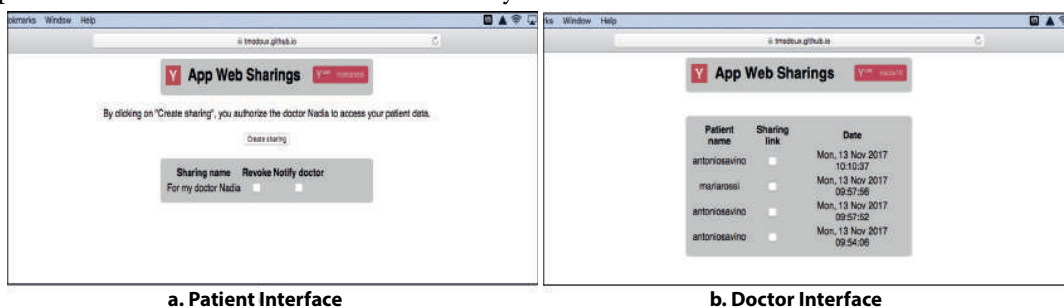


Figure 6.11 – WebApp user-friendly interfaces for: a) patient and b) doctor interaction with the PrYv e-health middle-wear.

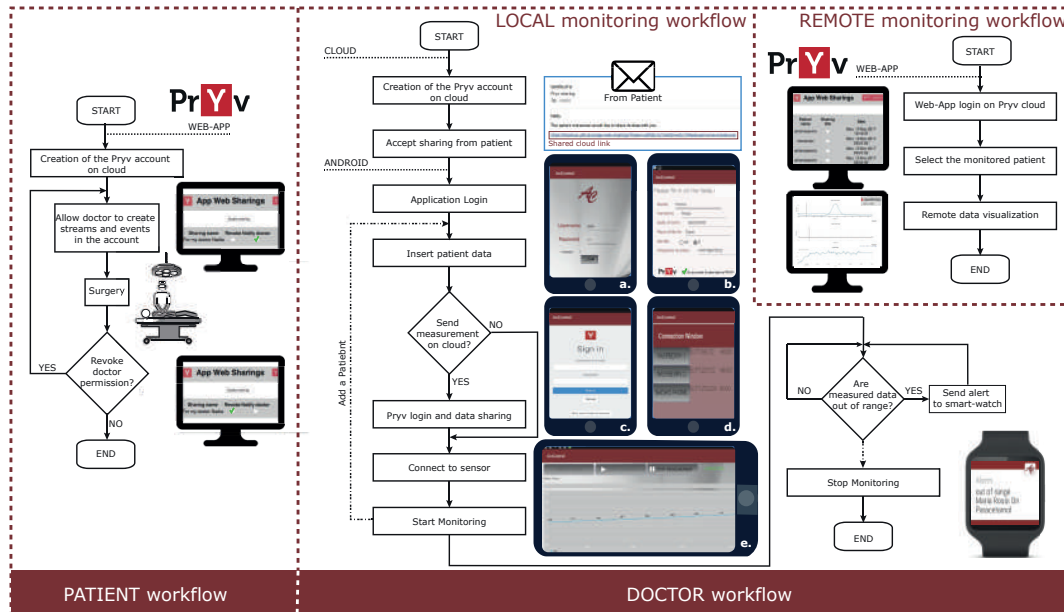


Figure 6.12 – Work-flow charts for patient-side and doctor side. In particular, doctor-side can be subdivided in *local* and *remote* monitoring.

account if first access), relying on PrYv shared access feature, to authorize the doctor to access a subset of data of his/her account. A consent form is presented to the patient and by clicking on a button, the patient can explicitly enable the doctor to access the data. This action results in the creation of a shared access between the patient and the doctor and in an automatic email that is sent to the doctor with a notification about the patient decision. From now on, the patient sees the new share in a list and can revoke it at any time.

- **Doctor-side Work-flow** is subdivided in two sub-flows depending on the role of the doctor:
  - *Local Monitoring Work-flow* for the in-charged anesthesiologist. After that new patient authorizes the sharing of a subset of data an email is received by the medical specialist containing a link to access the sharing. Through this link, the doctor is redirected to the WebApp where, after the login, the incoming request from the patient can be accepted. At this point, the doctor can use the Android app to keep control of all the patients under his/her responsibility and, if the patient's consent was set, to send the data on the cloud platform. The steps to use and navigate in the Android app were summarized in Fig. 6.12.
  - *Remote Monitoring Work-flow* for the medical doctor in teleconsulting. In addition to the Android app, any allowed medical specialists can remotely access patient's shared data through the WebApp. To do so, the doctor has to log on to the WebApp where a list of accepted patients sharing is available for remote consulting. The

### 6.3. Realization of the *sensing platform* with fluidics integration

---

shared links are listed according to the creation date and they access a visualization tool when clicked. The visualization tool is a simple web application where patients' data are plotted using *Plotly javascript library*.

#### Network validation

To simulate the scenario in Fig. 6.7 we used a Galaxy Note pro 12.2in with Android 5.1.1 Lollipop paired with a Sony Smartwatch 3 for the doctor monitoring, while two RPi-based TDMs were included to simulate two anesthetized patients. Finally, a laptop was used to access the WebApp on-cloud. We have validated the main features of the IoT architecture:

- The simultaneous communication of the Android app with the RPi and the cloud solution *via* Wi-Fi technology.
- The multiple patients connection to the doctor's Android app. Therefore, the anesthesiologist can easily follow different surgeries in parallel.
- The patient access in the WebApp and the possibility of sharing a subset of data with the doctor. An automatic email with the link to the shared data is sent to the doctor. Then, we also test the revoking of patient sharing.
- After receiving the email from the patient, the doctor uses the sharing link to access the WebApp and visualize the cloud data.
- The continuous receiving and the immediate visualization of the measured data received from the RPi-based TDM on the Android app.
- We have evaluated the latency time for an *event creation* call on Pryv API as under 100 ms, which is comparable to a standard HTTP request without any overhead. However, this parameter is influenced by the quality of the Internet connection, the server location and the size of the payload. In our case we tested the network with an Hotspot; the server was located in Switzerland and the events were data with double-precision floating-point.
- We proved the correct reception of the alert notification on the doctor's smart-watch when more than  $n$  measured values from one patient's monitored drug exceed the physiological threshold. The notification happens as a strong vibration and a pop-up displaying the name of the critical patient, and the out-of-range drug.

### 6.3 Realization of the *sensing platform* with fluidics integration

We finally realized a fluidic system to be integrated with the electrochemical sensors identified in the *Chapters* 3 and 4. In this way, through the fluidics, the sample solution is directly driven to the sites for detection. Considering that the infused anesthetic agents vary depending

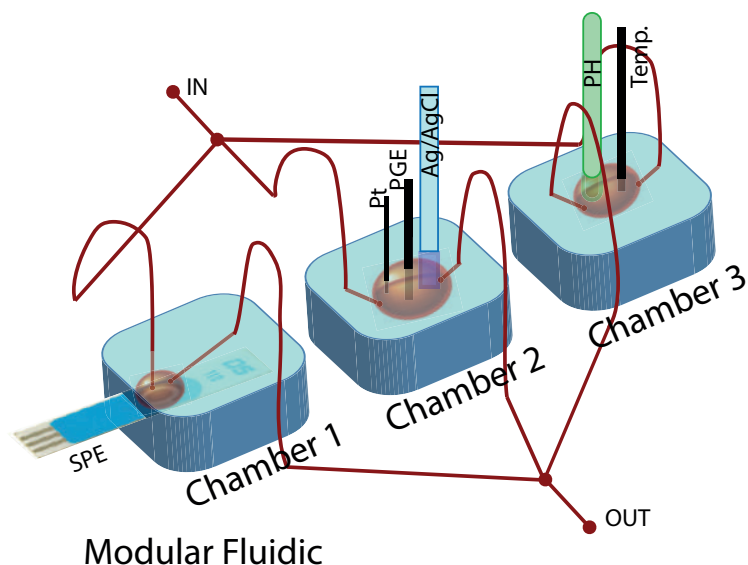


Figure 6.13 – Sketch of the *sensing platform* with the modular fluidic chambers for SPE, PGE plus T and pH monitoring.

on the kind of medical intervention and on the patient undergoing anesthesia, we wanted to create a modular fluidic device with different chambers, each for the specific drug to be analyzed plus one for monitoring the temperature and pH of the blood stream. In this way, the set up can be customized depending on the specific medical practices to be followed. Fig. 6.13 sketches the idea of the modular fluidic device.

Concerning the C-SPE used for midazolam monitoring (*Chamber 1* in the figure) a commercially available flow cell for standard format SPEs from Metrohm can be adopted (FLWCL), as seen in Fig. 6.14. The electrochemical cell is placed in the middle of the strip with inlet and outlet coming from the top. The closing system is based on powerful magnets included in the structure.

On the other hand, the passive electrochemical cell for propofol and APAP consists of a PGE WE (2.5 mm Ø) an Ag/AgCl RE (4 mm Ø) and Pt-wire CE (0.5 mm Ø). There is no commercial fluidics for this electrochemical cell; hence, we have designed and fabricated it in PDMS material.

### 6.3.1 Fabrication of fluidic chambers in PDMS (*Chambers nr.2 and nr.3*)

The development process of the fluidic devices started from fluidic simulations performed in *Comsol Multiphysics*<sup>2</sup> software to guarantee optimum mixing properties inside the chamber. Therefore, three different geometries have been investigated before the fabrication: (i) round, (ii) hexagonal and (iii) hexagonal with internal walls. *Laminar Flow Single Phase* mode simula-

<sup>2</sup>The Comsol simulations were run by Zijian Huang, internship master student at LSI, EPFL, Switzerland.



### 6.3. Realization of the *sensing platform* with fluidics integration



Figure 6.14 – Flow cell for standard format SPEs from Metrohm (*Chamber 1* in Fig. 6.13).

Table 6.1 – Fluid parameters set for *Comsol* simulations.

	<b>serum solution</b>
<b>density (g/mL)</b>	1.0242 [239]
<b>viscosity (mPa·s)</b>	1.27 [240]

tions in *Comsol Multiphysics* environment were run. In these simulations, laminar flow was ensured by adopting an appropriate Reynold value and by evaluating the inlet flow velocity  $\mu$  by the flow rate  $Q = 10.4\mu\text{L/s}$  as  $\mu = Q/A = 0.053\text{ m/s}$ , where  $A$  is the cross section area of the inlet (radius = 0.25 mm). Pressure at the inlet/outlet was set to zero and back flow at the outlet was suppressed. The domain equation in the model is incompressible Navier-Stokes equation, which is used for the main chamber to describe the fluid property [238]. The parameters to simulate serum solution flow as fluid were set as in the Table 6.1.

Fig. 6.15 reports the outputs obtained by the three simulations run for round, hexagonal and hexagonal with internal walls fluidic chambers. As we can deduce from the simulation results in Fig. 6.15, the internal soft-walls, which act as obstacles for the fluid flow, facilitate the internal mixing by causing turbulences. Therefore, the fluidic chamber was created in PDMS following this optimized geometry.

The fabrication of the chamber was carried out in the PDMS line (zone 12 in the cleanroom facilities) in the *Center of Micronanotechnology* (CMi) at EPFL following the process flow describe in Fig. 6.16.a. For the mold fabrication a 5<sup>th</sup> generation Desktop laser cutter from *Full Spectrum* emitting a very powerful beam of light (40W CO2) was used to print on PMMA layer (thickness of 3mm) the mold geometry previously designed in *Inkscape* software and exported in *scalable vector graphics* (svg) format. Top picture in Fig. 6.16.a shows the laser cutter and *Inkscape* logo used in this first process step. After the PMMA mold is ready, it is then immobilized at the base of a Petri dish (8 cm  $\varnothing$ ) thanks to double-side tape. The following

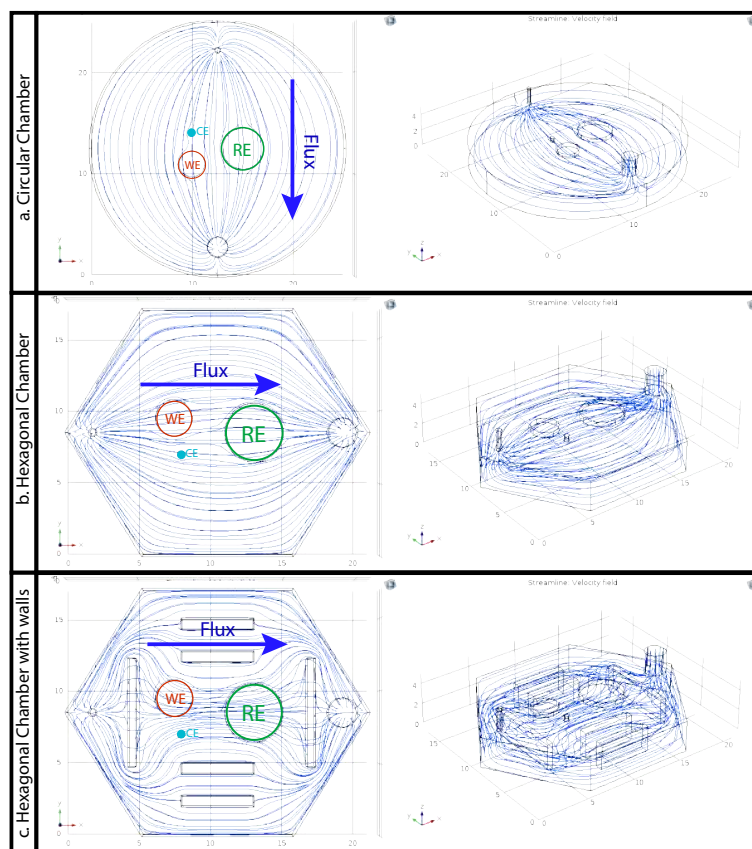


Figure 6.15 – *Comsol* simulation results for different geometries of the fluidic chamber: (a) circular, (b) hexagonal and (c) hexagonal with internal walls.

steps of the work-flow were carried out in CMI facilities. Fig. 6.16 shows the different steps and devices used for the PDMS creation. First, the mold's surface was conditioned to prevent PDMS sticking through a silanization passivation. This helps to release the PDMS from the mold at the end of the fabrication process. PDMS solution was obtained by dispensing PDMS (max 45 g) in a plastic cup, together with a catalyst (curing agent, max 4.5 g) in a proportion of 10 : 1 (Fig. 6.16.b). Then the plastic cup has to be placed in the mixing machine and, after having adjusted the revolution balance according to the total weight of the cup, the process to homogenize the mixture starts (1 min of mixing at 2000 rpm plus 2 min of defoaming at 2200 rpm, Fig. 6.16.c). Afterwards, the PDMS mixture is poured over the passivated mold placed in the Petri dish and removed all the bubbles removed by degassing in the desiccator (Fig. 6.16.d). Finally, PDMS was cured in the oven for at least 1 hour at  $sim 80^{\circ}C$  (Fig. 6.16.e). As soon as the PDMS is ready, it is detached from the mold (Petri dish) and it will constitute the main chamber. The top cover of the fluidic chamber has been created following the same process for the manufacture of the PDMS but using only a Petri dish as a mold to obtain a flat surface. To keep the two parts together, e.g. upper cover on the top of the hexagonal chamber, two PMMA discs, one with a central hole, were made with the laser cutter. We drilled four

### 6.3. Realization of the *sensing platform* with fluidics integration

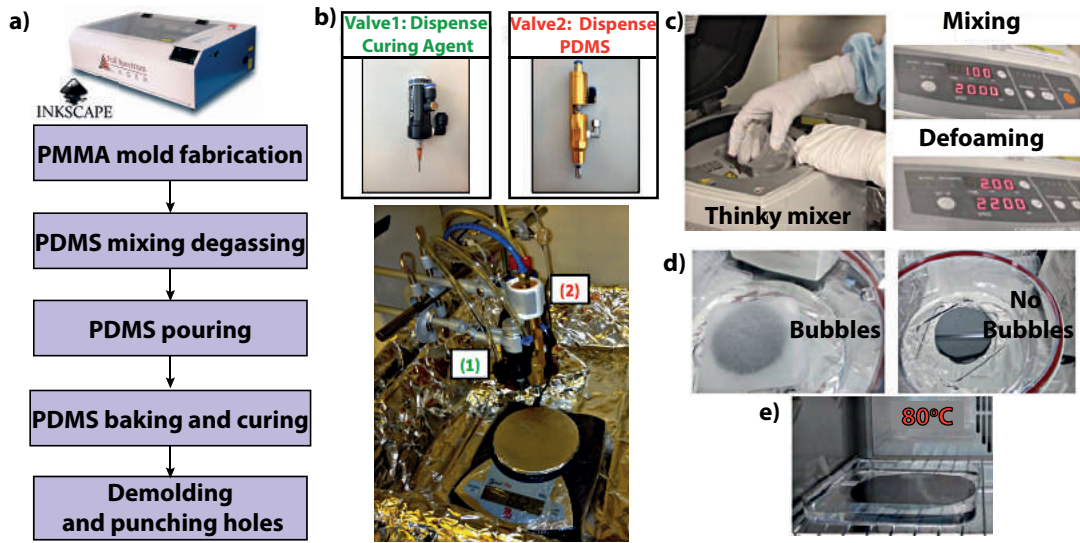


Figure 6.16 – Fluidic device fabrication: a) process flow to be followed that starts with the construction of the PMMA mold by laser cutter. b) PDMS solution obtained by mixing PDMS and curing agent (1:10), and c) mixing and defoaming the obtained composition. After having poured the PDMS in the mold, d) all the air bubbles have to be removed, and, finally, d) it has to be cured at 80°C overnight.

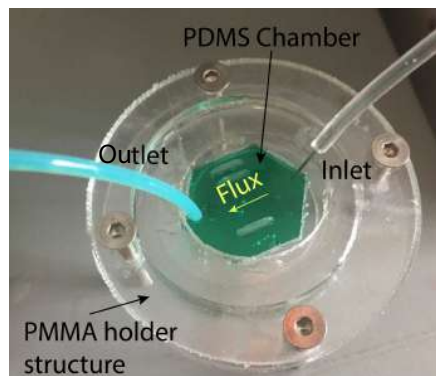


Figure 6.17 – Sandwich structure of the fluidic device: PMMA discs holding together the PDMS chamber.

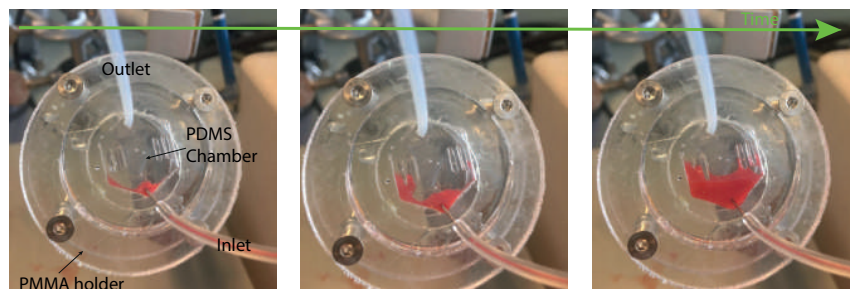


Figure 6.18 – Fluidic chamber tested with red dye flow.

## Chapter 6. Overall IoT system architecture

---

Table 6.2 – Flux velocities evaluation of the fluidics at different pump velocities (expressed in *revolutions per minute* (rpm)).

Pump Velocity (rpm)	Time to fill (s)	Velocity ( $\mu\text{L/s}$ )
48	5	10.4
47	5.8	8.9
46	6.4	8.1
45	6.7	7.7
44	7.3	7.1
43	7.5	6.9
42	9	5.7

symmetrical holes on the two disks to allow the passage of screws so as to obtain a sandwich structure with the fluidic device in between. The screws were tightened with bolts to prevent leaking. Fig. 6.17 shows the final fluidic device filled with green dye. The chamber flux in the chamber and leaking have been tested with dye, as shown in Fig. 6.18, before being used for anesthetic detection.

To complete the monitoring system, a dedicated module for temperature and pH control of the blood stream was also included in the final configuration. In fact, *Chamber 3* Fig. 6.13 shows the integration with the two sensors chosen for this monitoring, which are the DS18B20 waterproof digital thermometer by Maxim-IC, and the *Extech* standard polymer electrode ( $12 \times 160$  mm) for pH, as shown in *Chapter 5*.

### 6.3.2 Characterization of the fluidic device

We found the correspondence between the internal velocities of the *Minipuls 3* peristaltic pump provided by *Gilson Inc.* armed with a PVC tube (diameter = 0.38 mm, length = 460 mm and volume = 52  $\mu\text{l}$ ) and the effective fluid flux through the custom fluidics. Hereafter, we report the results in Tab. 6.2. Among these velocities (expressed in *revolutions per minute* (rpm)), 46 rpm or 48 rpm are the most suitable for reproducing the fast variability rate of the drug concentrations that characterize difficult-to-dose drugs, such as anesthetics. Therefore, for the final validation of the overall system in *Chapter 6 Section 6.4* the measures in flow conditions were performed at these velocities.

Further, the mixing parameters also have to be optimized. A preliminary qualitative evaluation was performed by using various dye solutions, as already shown by Fig. 6.18. After this empirical characterization, we evaluated the time required to ensure homogeneous drug concentration in the fluidic chamber. To that aim CA measurements in PBS solution for both APAP and propofol drugs were carried out.

For APAP CA detection, we applied a fixed potential of 0.9 V to the electrochemical chamber and we set the pump velocity at 46 rpm. For propofol CA procedure the applied potential was set at 1 V and the pump velocity at 48 rpm. Every 3 minutes, we replaced the input drug sample with another one having a higher drug concentration. Fig. 6.19 shows the two CA

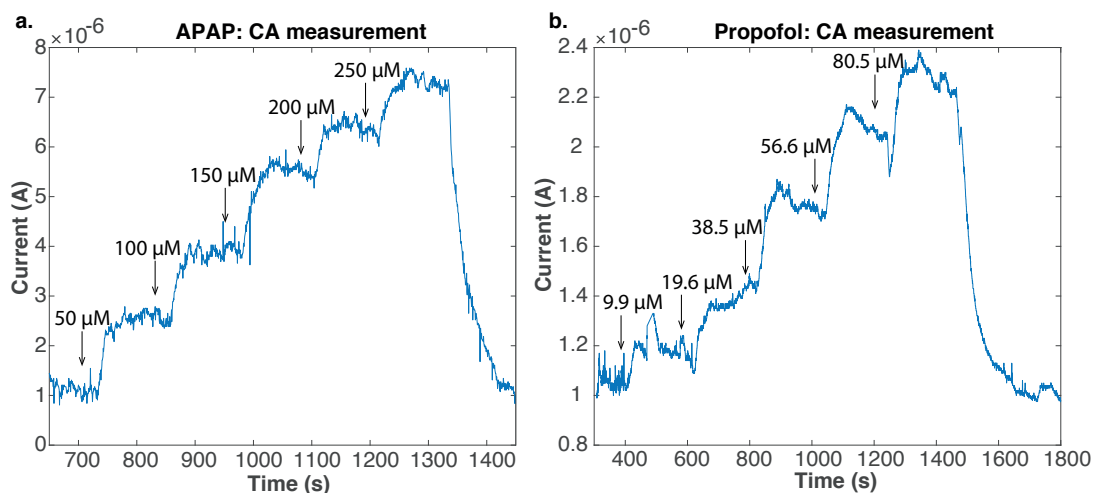


Figure 6.19 – CA measurements for: a) APAP and b) propofol drugs.

time-trends for APAP and propofol. From these graphs it is possible to deduce that the steady state was reached after around 50s by the increase of the drug concentration.

Based on this, 50s can be considered as the minimum waiting time to ensure that the drug concentration in the electrochemical chamber is the same as to the one in the input beaker.

## 6.4 Overall system validation

The present section focuses on the validation of the novel IoT monitoring system that has been proposed in the previous sections of this chapter. We have applied the realized IoT solution to a medical systems to offer an enhanced tool able to provide rapid and precise information on patients' sedation status at any time and from any place (within or outside the hospital). We finally assembled the whole system, shown in Fig. 6.1, to test its performances for drugs monitoring. It comprises: (i) the multi-panel electrochemical sensing platform integrated into (iii) a fluidic system, which directs the sample on the sensing site (**Sensing Platform**), (i) a low-noise, custom-built electronic potentiostatic PCB driven by a RPi (**Portable Electronic Circuit**), and (iv) an IoT network including a Cloud system (**IoT Cloud Support**) that allows the doctor to control and share all the patient's data through a dedicated Android app (**Android GUI**).

The electronic platform, consisting of the PCB and the RPi, was included in a containing box (27 × 21 × 13 cm) to guarantee its portability.

We validated the performance of our system by detecting the two complementary anesthetic compounds, *e.g.* propofol and APAP, under flow conditions in human serum. By these crucial experiments we demonstrate, for the first time, that our system has the potential to be used for multiple anesthetics monitoring in the future.

**Material and methods**

2,6-Diisopropylphenol (Propofol) was purchased from TCI chemical and dissolved in 0.1 M NaOH to prepare the stock solution of 5.4 mM. Subsequent dilutions of propofol stock solution were prepared in PBS (10 mM, pH:7.4) or in serum to obtain concentrations in the range [9.9 - 80.5]  $\mu$ M. The compounds APAP, NaOH and heat inactivated human male serum were purchased from Sigma Aldrich (Switzerland). APAP stock solution 30 mM was prepared by dissolving 5 mg of APAP powder in 1 ml PBS (10 mM, pH:7.4). Subsequent dilutions of APAP stock solution were made in PBS or serum in the range [50 - 300]  $\mu$ M. The propofol and APAP simultaneous detection was achieved by using a three-electrode electrochemical cell consisting of a PGE as WE, to overcome fouling effects due to propofol oxidation, a K0265 Ag/AgCl electrode from *Ametek Scientific Instruments* as RE and a Pt wire as CE. We chose the wood PGE 3H from *Staedtler Mars Lumograph* with composition: 58% graphite, 36% clay and 5% wax (binder).

A *Minipuls 3* peristaltic pump provided by *Gilson Inc.* and armed with a PVC tube (diameter = 0.38 mm, length = 460 mm and volume = 52  $\mu$ l) was used to simulate the flux in the fluidic chamber. Good mixing properties in the fluidic chamber are guaranteed in 50s from the exchange of the analyzed solution at the inlet. The validation of the fluidics was presented in *Section 6.3*.

CA and DPV electrochemical procedures were carried out to validate the system for propofol and APAP detection. The corresponding parameters were set through the RPi integrated GUI and are summarized in Tab. 6.3. Whenever a new data is read from the sensing platform, it is sent by the RPi to the Android app running on the anesthesiologist's tablet or smart-phone, exploiting Wi-Fi technology.

Table 6.3 – Electrochemical parameters for DPV, and CA measurements of APAP and Propofol.

<b>DPV Measurements APAP</b>		
Start-V (mV)	End-V (mV)	V-Step (mV)
-100	1100	5
Pulse-Width (ms)	Pulse-Ampl. (mV)	Pulse Period (ms)
50	90	68
<b>DPV Measurements Propofol</b>		
Start-V (mV)	End-V (mV)	V-Step (mV)
0	1100	5
Pulse-Width (ms)	Pulse-Ampl. (mV)	Pulse Period (ms)
75	90	102
<b>CA Measurements: APAP and Propofol</b>		
APAP Applied Voltage (mV)	Propfol Applied Voltage (mV)	
900	1000	

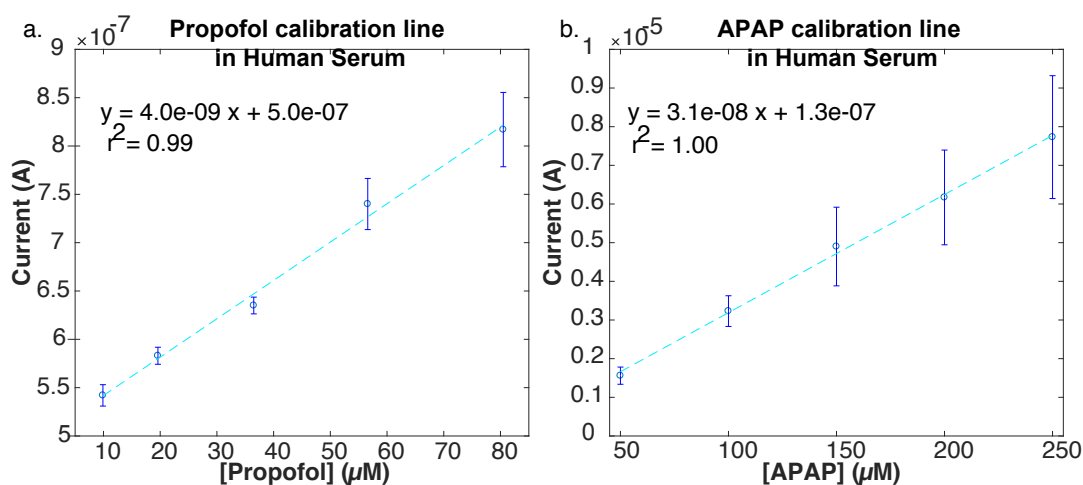


Figure 6.20 – DPV calibration lines with standard error bars ( $n = 3$ ) obtained under flow conditions in undiluted human serum for: a) propofol and b) paracetamol.

#### 6.4.1 Validation of the system in undiluted human serum

The conclusive and decisive validation of the system is based on the results obtained for the simultaneous detection of propofol and APAP in undiluted human serum under flow conditions.

To characterize the system we initially carried out DPV calibrations in flow conditions (pump velocity set at 48 rpm) for both propofol and APAP in human serum, as complex human fluid. We reported in Fig. 6.20 the calibration lines obtained. Sensitivity values were evaluated to be  $3.967 \times 10^{-09} \pm 1.9 \times 10^{-10}$  and  $3.056 \times 10^{-08} \pm 8.39 \times 10^{-10}$  for propofol and APAP, respectively. After having characterized the system, two main crucial experiments were carried out to assess the system performances:

- Mixing test:** serum solution containing three different APAP concentrations (50 - 150 - 300  $\mu\text{M}$ ) was fluxed from lower to higher concentration (pump velocity set at 48 rpm) in the chamber and measured by the system every 1 min 30s. Afterwards, while the APAP concentration was maintained at 300  $\mu\text{M}$ , various propofol concentrations (20, 50 and 80  $\mu\text{M}$ ) were added to the solution and measurements were taken every 1 min and 30s for each concentration. Fig. 6.21 displays the obtained DPV curves from this experiment. It is clear from the figure that any peak is evident in the blank control measurement, obtained when fluxing undiluted human serum without any drug. Thereafter, only one peak at  $\sim 0.7$  V (orange area) is visible when only APAP is present in the fluxed solution. The peak increases with the increase of the drug concentration. As soon as propofol is added in the solution (while APAP is kept constant) two other peaks at  $\sim 0.45$  V and  $\sim 0.6$  V (green areas) arise. The two peaks become higher when propofol concentration in the solution increases, while the APAP peak is not affected significantly. Therefore, we can conclude that these drugs do not interact with each other.



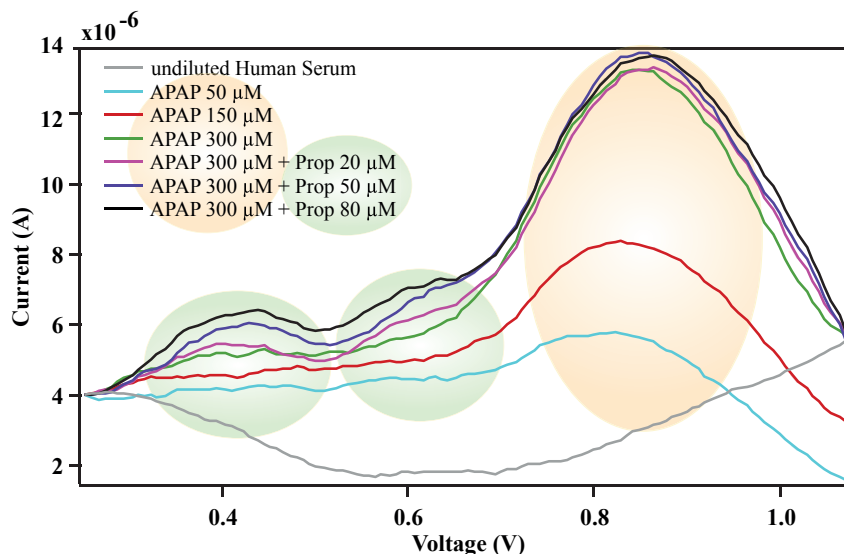


Figure 6.21 – *Mixing test*: DPV measurements in undiluted human serum fluxing (pump set at 48 rpm) a solution containing, first, three increasing concentrations of APAP (50 - 150 - 300  $\mu\text{M}$ ) and then three solutions with fixed APAP concentration (300  $\mu\text{M}$ ) and three increasing concentrations of propofol (20 - 50 - 80  $\mu\text{M}$ ). Blank measurement with no drug in fluxing serum solution is reported as control.

- *In-time monitoring test*: the chamber was filled with serum without any drug. Then, a serum solution containing 300  $\mu\text{M}$  of APAP was fluxed (pump velocity 48 rpm) to the system. We performed one DPV measurement (30s measurement time) every 10s of fluxing of the APAP solution. After 12 min we have changed the fluxing solution with serum containing only 60  $\mu\text{M}$  propofol. The same frequency of measurement was applied; a DPV every 10s during 12 min. The exchange of the fluxing solutions was done in the 10s of mixing in order to not interrupt the procedure. Fig. 6.22 reports the measured peak currents over time, which can be converted into drug concentration values according to the linear calibration equation expressed in Fig. 6.20. Therefore, to convert the current value in a concentration it is only necessary to substitute the  $x$  parameter in the corresponding equation and the corresponding concentration is provided by the  $y$  estimation. For the purposes of our analysis, we preferred to keep the data in current values to be able to visualize the two trends of APAP and propofol on the same plot.

The results of human serum detection, mixing test and in-time monitoring test show that with our system, we are capable of in-time monitoring of the change in concentration of two drugs, e.g. APAP and propofol, in undiluted human serum due to sample flux over a period of time.



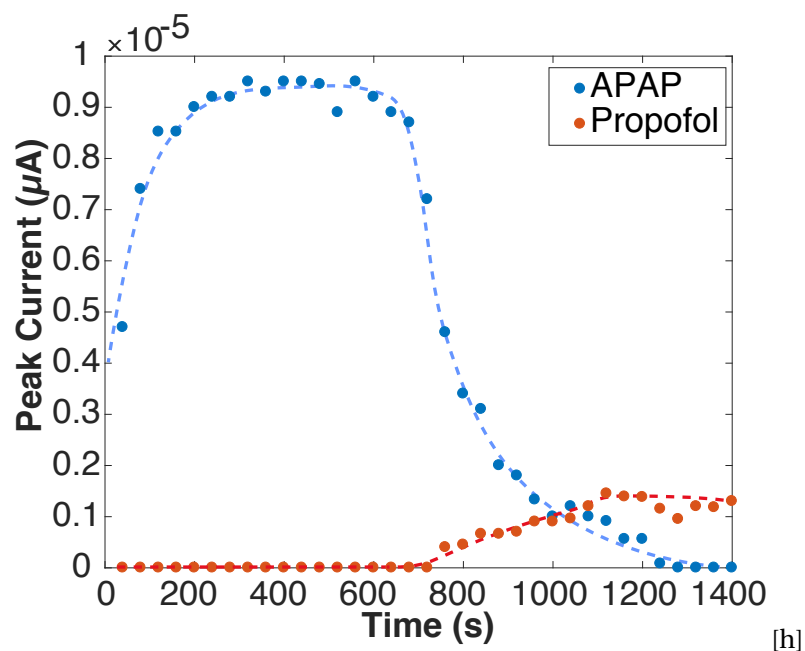


Figure 6.22 – *In-time monitoring test*: the concentration trends of APAP (300  $\mu\text{M}$ ) and propofol (60  $\mu\text{M}$ ) is monitored over time in undiluted human serum under fluxing conditions (pump set at 48 rpm).

## 6.5 Infusion pump integration: towards closed loop delivery

The introduction of an automatic control system, capable of delivering anesthesia according to the level of sedation of the patient, is extremely desirable and would lead to enormous benefits in terms of correct drug dosage and efficacy, by reducing over- or under- dosing malpractices [241]. The use of such an automatic controlled delivery system is fundamental to the realization of closed-loop anesthesia practices where the feedback controlled administration of drugs is tuned by the actual level of anesthesia measured by the *sensing platform*. By far the most largely used closed-loop controlling algorithm is the *Proportional-Integral-Derivative* (PID) algorithm. Basically, it automatically applies accurate and responsive corrections to a control function, which in the anesthesia delivery system is the PK/PD mathematical model of the injected drug implemented in the TCI pump. It does this by reading the measured value provided by the electrochemical sensor and by minimizing the error-difference between the actual measure and the desired level of anesthetic concentration [242].

Therefore, to facilitate the integration of the PID algorithm and the sensing platform as feedback in automatic and reliable drug delivery closed-loop systems, FIS systems are needed to ensure operation with very small sample volumes of samples, and to provide effective testing tools to evaluate sensor capabilities in real time [243]. Thanks to FIS it is possible to reproduce in an easier way the *in-vitro dissolution tests*, that are normally extremely laborious due to the large number of samples required, in an automated, precise and reproducible way. Up to now, various approaches have been presented in the literature to provide automatic testing

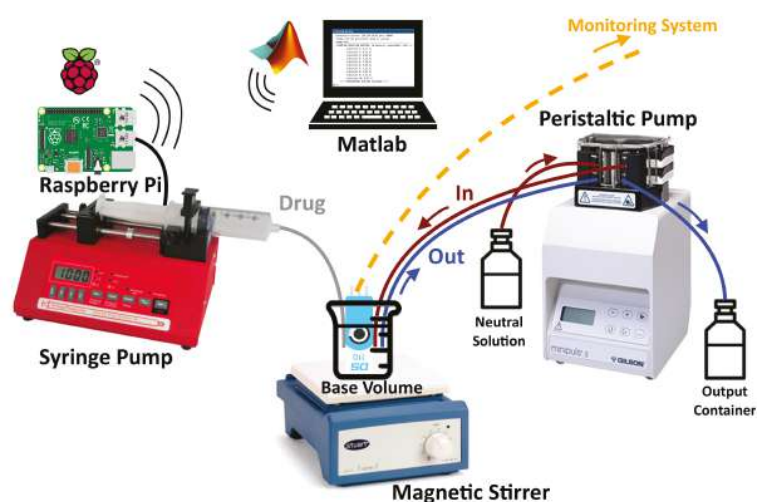


Figure 6.23 – Set-up of the realized FIS

tools [244, 245, 246]. However, these set-ups were not able to reproduce the in-time PK profile of the drug [247]. To this aim, we created an innovative solution for designing an automatic FIS driven by the RPi to assess the performance of our system in continuous monitoring over time.

### 6.5.1 Raspberry Pi-driven *Flow-Injection System* (FIS)

The FIS setup has been preliminarily validated by carrying out a qualitative test with a dye; we then successfully proved its ability in reproducing an in-time concentration trend for APAP drug.

### 6.5.2 FIS set-up

The set-up of the FIS is depicted in Fig. 6.23. The RPi has a central role in the FIS. On the one side, it activates an injection pump, Braintree Scientific Inc.<sup>TM</sup>NE-1000 Programmable Single Syringe Pump [248] completed by 1 ml or 0.5 ml plastic syringes with Polytetraflon@tubing from AWG (inner  $\varnothing$  0.41 mm) connected to the needle. The syringe is charged with the drug to reproduce the desired concentration trend in a given base-volume of buffer solution. The injection dose is regulated according to a PK mathematical model of the drug implemented in *Matlab*. Therefore, from the other side, the RPi receives from the *Matlab* script the instruction with the evaluated amount of the target concentration to achieve. This communication relies on Wi-Fi technology (TCP/IP protocol).

To accomplish the set-up, we used a Gilson<sup>TM</sup>Minipuls 3 peristaltic pump to dilute the base-volume with fresh buffer solution, a VWR magnetic stirrer to facilitate the mixing in the base-volume, and the PGSTAT101 Autolab and C-SPE from Metrohm to run the electrochemical

## 6.5. Infusion pump integration: towards closed loop delivery

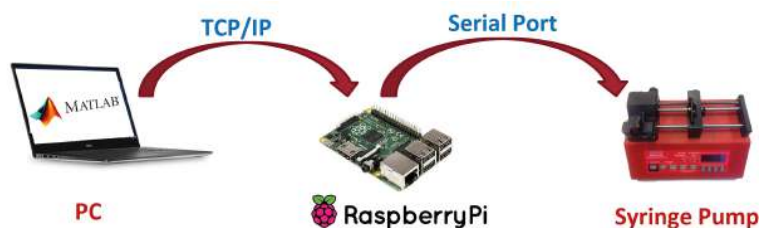


Figure 6.24 – Schematic representation of the communication protocols adopted between *Matlab* and RPi (TCP/IP) and between RPi and syringe pump (serial communication).

experiments for APAP detection (CV procedure applying voltages from -0.1 V to 1.1 V with 0.1 V/s scan-rate). We armed the peristaltic pump with Tygon™LMT-55 peristaltic pump tubing ( $\varnothing$  0.38 mm) for APAP, while PVC tubing ( $\varnothing$  1 mm) were used for dye tests.

As is evident from the figure, the system can be sub-divided into two parts according to their functionalities: (i) the “increasing concentration” part that relies on the syringe, and (ii) the “diluting concentration” driven by the peristaltic pump. On one side, the syringe pump is programmed to push the plunger of the syringe filled with the administered drug by means of a moving plate. On the other side, the peristaltic pump withdraws the solution from the base-volume beaker and fills it with fresh buffer solution. We have calibrated the in/out flows of the base-volume beaker to keep the volume constant. The two system parts are made running in a synchronized manner to reproduce the drug concentration trend in the base-volume. Therefore, while the peristaltic pump continuously dilutes the base-volume with buffer solution, the syringe pump injects the right amount of the drug to achieve the target concentration. We calibrated the peristaltic pump flux and we fixed it at a constant rate before starting each test. The RPi drives and communicates with the syringe pump through a physical serial connection RS-232. We realized a custom adapter to connect the RPi USB port with the syringe pump RJ-11 socket. Through the RPi we can configure the syringe pump. The main setup parameters to be configured are: (i) pumping rate, (ii) target volume, and (iii) syringe diameter. Knowing these parameters, the pump can automatically evaluate the injection time and regulate the plunger speed. As soon as the RPi receives a new calculated injection dose from the *Matlab* script, it sends the evaluated value to the syringe pump that confirms the correct reception of the command by sending back an acknowledgment message. Fig. 6.24 sketches the communication protocols adopted in the transmission of the next evaluated injection from the *Matlab* code to the RPi and then to the syringe pump.

We set the the pump to perform direct injection every time a new injection command is received. The injection is carried out by uniformly pushing the syringe plunger to constantly increase the amount of drug in the base-volume to reproduce a linear drug concentration trend.

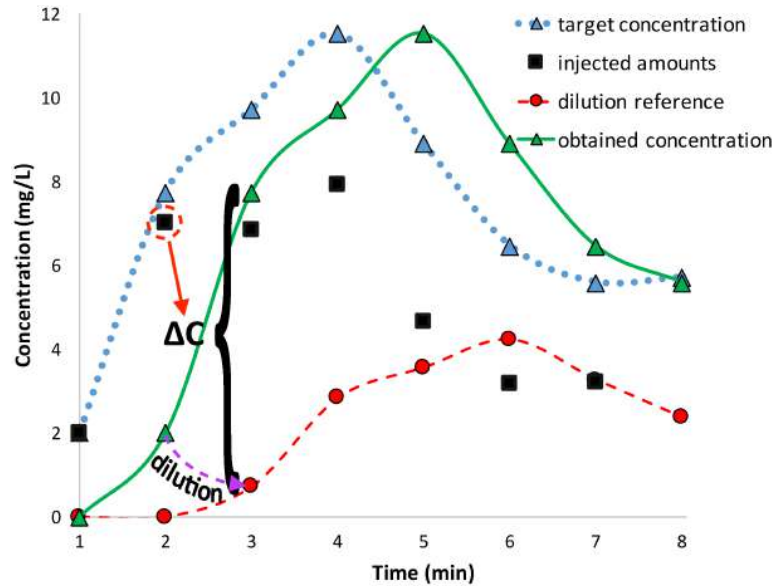


Figure 6.25 – An example of injection dose calculation for reproducing a sample target concentration trend. The *baseline dilution* is determined for a flow rate of 1 ml/min in a 1 ml base-volume. Differences among the plots have been exaggerated for readability.

### 6.5.3 Injection dose calculation

The *Matlab* process for estimating the next injection value to obtain a desired concentration trend in time has to keep in consideration the constant dilution effect due to the peristaltic flow fixed at a constant speed. The relation between dilution action and peristaltic flow is expressed in Eq. 6.1. This equation determines how an initial concentration  $[C_i]$  in a certain volume  $V$  decreases in time ( $t_{fi} = t_f - t_i$ ), if a dilution flow rate  $Q$  is maintained [249].

$$[C_f] = \frac{[C_i]}{e^{\frac{Q \cdot (t_f - t_i)}{V}}} \tag{6.1}$$

where  $[C_f]$  is the final concentration.

We can simplify Eq. 6.1 by expressing  $\frac{[C_f]}{[C_i]}$  as an unique coefficient  $\delta(t_{fi})$ . Moreover, under a continuous dilution, we can consider  $t_{fi}$  as an intermediate time  $t_m$  between two consecutive measurements ( $t_{n+1} - t_n$ ). Therefore, to reproduce a desired time-trend of the drug concentration ( $[C_t]$ ), we can evaluate the subsequent dose to be injected by using Eq. 6.2.

$$[C_{dose}] = \begin{cases} [C_t] - ([C_n] \cdot \delta(t_m)), & [C_t] \geq [C_n] \cdot \delta(t_m) \\ 0, & [C_t] < [C_n] \cdot \delta(t_m) \end{cases} \tag{6.2}$$

where  $[C_n]$  is the concentration at  $t = t_n$ ,  $t_m = t_{n+1} - t_n$ , and  $[C_{dose}]$  is the required concentration to be injected.

Fig. 6.25 represents the concept behind this injection evaluation method implemented in

## 6.5. Infusion pump integration: towards closed loop delivery

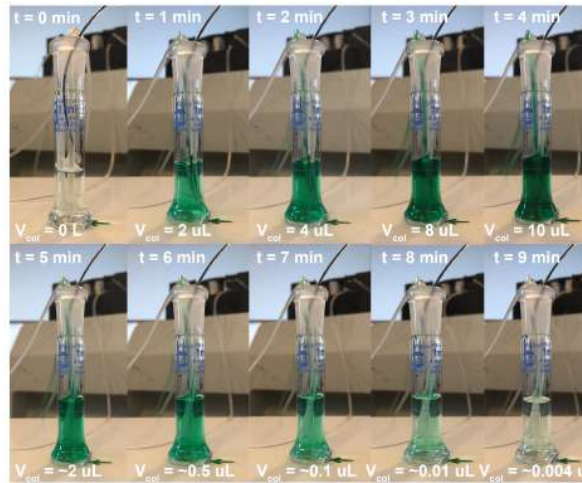


Figure 6.26 – Dye test:  $V_{col}$  is the dye volume in the base-volume beaker. In the upper part these values are the dye injections.

*Matlab.* The blue dotted line (*target concentration*) refers to the time-trend to reproduce according to Eq. 6.2, while the green line (*obtained concentration*) keeps track of the actual concentration in the base-volume. Considering the difference  $\Delta C$  between the diluted previous of the actual concentration  $C_{n1}$  and the target concentration  $C_{t1}$ , the new dose  $[C_{dose}]$  is evaluated and injected at the time  $t_n$ . The calculation of  $[C_{dose}]$ , as in Eq. 6.2, relies on the dynamic dilution continuously performed by the peristaltic pump. The algorithm predicts the drug concentration at the time  $t_{n+1}$  if no further drug is injected, red dashed line in the figure (*dilution prevision*). The black squares in the figure (*injected amounts*) show all the concentration values to be administered. Before sending these amounts to the syringe pump, a previous conversion in volume unit is needed. This conversion depends on the concentration of the drug stock solution. The converted values are sent to the RPi that notifies the pump. The pump continuously infuses each volume in a time  $t_m$  to ensure a smooth time-trend.

### 6.5.4 FIS validation

We validated the FIS by performing two different tests: (i) a qualitative test of the dilution ability with a green dye, and (ii) a quantitative test of reproducing a drug concentration time-trend for APAP. The time-trend to reproduce was characterized by a fast rising drug concentration followed by an exponential decrease of the concentration until the steady-state.

#### Qualitative test with dye

We injected green food dye in water, considered as the buffer solution (1 ml base-volume). The peristaltic flow rate was set at 1 ml/min. The injection dosage was programmed to obtain

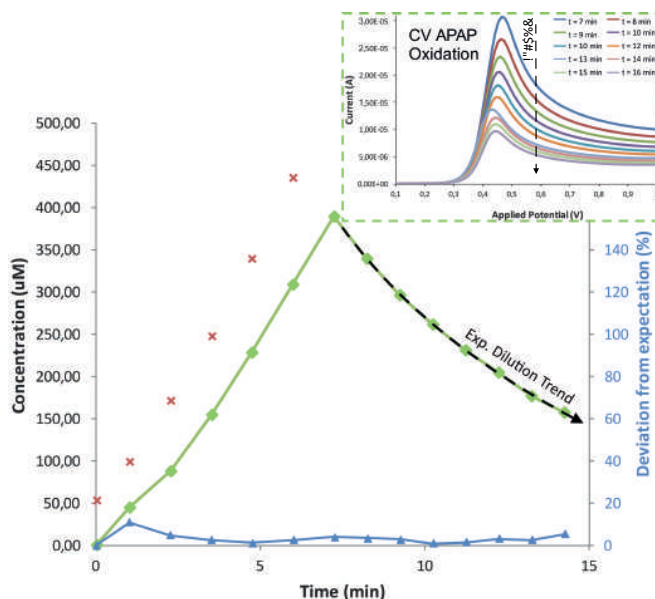


Figure 6.27 – APAP test: in the graph the sensed concentration for each measurement in time (green line), the evaluation in % of the variation between measured and expected concentrations (blue line) and the injected doses (red crosses). In the inset the CV oxidation peaks for the dilution are reported.

a linear increase in time of the dye concentration in the base-volume and then an exponential decrease caused only by dilution effect. The test was performed under stirring conditions to facilitate the mixing properties (level 9 of the magnetic stirrer). The visual results of the test are shown in Fig. 6.26. There is clearly a linear augmentation of the color tone intensity while the syringe is active, while an exponential reduction of the intensity is visible due to the dilution effect.

### Quantitative test with APAP

We challenged the FIS in reproducing a time-trend similar to a real drug administration by using APAP as a benchmark compound. We obtained the increasing trend by injecting APAP solution six times (one dose every 75 seconds) and then we monitored the dilution progress in the following 15 minutes. The results of this analysis are shown in Fig. 6.27. The base-volume was 6 mL and the peristaltic flow was set at 0.86 ml/min. PBS solution was used as buffer solution. The base-volume solution was stirred (200 rpm) between each measurement to ensure good mixing after drug injection. To quantify APAP concentration in the base-volume solution CV measurements were performed.

Thanks to this qualitative test, it was possible to find out the main trade-offs of the realized FIS: (i) the dimension of the base-volume with respect to the syringe injection speed (evaluated from syringe dimensions), (ii) the constant speed of the peristaltic flow, (iii) the stirring condition needed to obtain a well-mixed solution.

## 6.6 Summary and original contributions

In this chapter, we have finally completed our system of a fully functional and autonomous device for multi-sensing detection and delivery of anesthetic compounds over time. An *ad-hoc* fluidic device has been realized to automatically direct the human sample to the sensing spots. The developed system was also integrated with an Android-based IoT architecture to facilitate the doctor in monitoring multiple clients under his/her responsibility. Smart devices, such as tablets, smart-phones and smart-watches have been used in the network. Furthermore, we discussed a novel approach for implementing automatic delivery by the use of the RPi so that we have integrated also integrated the infusion pump within the system.

We concluded the chapter by demonstrating the successful simultaneous detection of the concentration trends of two anesthetic drugs in human serum over time.

Main research contributions from this chapter can be summarized as follows.

- **IoT network**

We have investigated and realized a novel approach to deal with intensive care monitoring scenarios by using an IoT solution. The developed IoT network keeps the anesthesiologist connected with all the patients under his/her responsibility at all times. Through this Android-based network, the monitored data are rapidly visualized on the mobile device of the anesthesiologist, such as a tablet or a smart-phone, and an alert notification is received on the doctor's smart-watch in case of an out-of-safe-range parameter registered from a connected patient. The short latencies for data/messages transmission ensure rapid medical interventions in case of emergency. In addition, the data can be shared and stored on the cloud enabling teleconsulting. This ensures a safer and continuous monitoring of the anesthesia delivery over time. These IoT features were achieved through two architectures: one based on a smart-watch app, the other supported by a cloud solution provided by PrYv e-health middle-ware. The first one relies on a smart-watch, through which the responsible doctors/caregivers can continuously keep the key parameters of several critical patients under control at the same time. The wearable device enables requests for measured parameters from a specific connected patient, and sends alerts in case of anomalies.

The latter includes a cloud-based network centered on a dedicated Android app running on the anesthesiologist's tablet/smartphone. The app bidirectionally communicates on the one side with the RPi-based TDM system measuring the anesthetic concentrations in the patient, and, on the other side, with the cloud back-end solution provided by PrYv and accessible by a WebApp. In case of any anomaly in measured data, the doctor is alerted with a notification pushed by the Android app to the smart-watch.

One further advantage of our IoT networks is that they can be considered as *on-the-top* monitoring solutions that can be interfaced with a variety of other medical applications requiring continuous patient monitoring. All that is needed is a medical device that is able to wirelessly send the measured data for the integration with this architecture.

If we compare the features of our network with the ones offered by previously presented

## Chapter 6. Overall IoT system architecture

Table 6.4 – Comparison among different IoT solutions in health-care for hospital (HS) or home (HM) monitoring.

Work	Medical Application	Architecture	Cloud	Full system	HS/HM
[250]	Elderly patients	Cloud provider, ECG sensor, mobile device app	✓	✓	HM
[251]	Medical imaging	Cloud, imaging device	✓	✗	HS
[252]	ECG health	Cloud system, ECG sensor, mobile device app, desktop software	✓	✓	HM
This thesis: wearable system	Anesthesia	TDM system, mobile device app, smart-watch	✗	✓	HS
This thesis: cloud system	Anesthesia	Pryv middle-ware, TDM system, mobile device app, smart-watch, WebApp	✓	✓	HS

IoT solutions in the literature, as summarized in Table 6.4, it is evident that the majority of them provide home monitoring for elderly people, but none are realized to provide an *ad-hoc* cloud-based solution for hospital practices. We have instead provided, with the second architecture, the first dedicated IoT cloud-based solution for anesthesia in medical practices.

- **Fluidics**

We designed a modular fluidic device which aims to interconnect different fluidic chambers, each for a target drug. We fabricated in PDMS the fluidic chamber for a PGE-based electrochemical chamber. We implemented an optimized geometry based on a hexagonal shape and internal walls that was guaranteeing the best mixing properties in proximity of the sensing site. Similarly, we created the fluidic chamber for pH and temperature sensors that was presented in *Chapter 5, Section 5.2*. Finally, the modular fluidic is completed by a commercially available fluidic chamber for the C-SPE.

- **Automatic anesthetics injection system with pump**

We have interfaced an infusion pump to be controlled by the RPi, using a novel approach for FIS. We tested the system by carrying out both qualitative and quantitative tests. As a consequence of the quantitative test we demonstrated that the system can reproduce the time-trend of any administered anesthetic compound, such as APAP. Furthermore, we could identify the main trade-offs of the system: (i) the dimension of the base-volume



with respect to the syringe injection speed (evaluated from syringe dimensions), (ii) the constant speed of the peristaltic flow, and (iii) the importance of a stirring action in obtaining a well-mixed solution for sensing. The system is potentially able to: (i) reproduce any concentration trend, just by adjusting its intrinsic characteristics (*e.g.* tubing dimensions, base-volume, and injection syringe volume) according to the target, and (ii) be used in any fluidic unit containing the sensors to be tested. An improved set-up of the system would include a programmable peristaltic pump so that it would be possible to interrupt the dilution effect whenever static conditions are required for measurement.

- **Validation of the overall system**

We finally validated the IoT overall system by performing some crucial experiments aiming at simultaneous anesthetics detection over time. We showed that it works efficiently for the simultaneous detection of propofol and APAP in human serum, considered as complex human bio-fluid. We have run two main experiments: one testing the mixing performances of the fluidic system and the other verifying the simultaneous detection of multiple anesthetic compounds over a period of time. We have thus demonstrated, for the first time, the successful detection of the concentration of the two drugs over 24 min.



## 7 Conclusions and future work

The objective of this thesis was the design, realization and characterization of a complete monitoring system to be used in intravenous anesthesia delivery, *e.g.* in surgeries or *Intensive Care Units* (ICUs). The anesthesia cocktail is made of a hypnotic, such as propofol; an analgesic, such as paracetamol; and a muscle relaxant, such as midazolam. A correct and personalized balance of this triad is crucial for inducing and maintaining a certain level of sedation over a determined period of time. Up to now, TCI pumps have been used to infuse the anesthetics in patient's veins under the control of the anesthesiologist. The software implemented in the TCI pump incorporates the PK models of the infused drugs to dose their administration accordingly. The anesthesiologist also keeps control of the BIS, evaluated by an EEG signal that is related with the patient's level of sedation. However, main limitations of the actual practices rely on these facts: (i) on the one hand the PK models in the TCI cannot reproduce the inter-patient variabilities in metabolism, and (ii) on the other the BIS is evaluated in an indirect manner, hence it can be affected by artifacts.

To overcome these limitations, a reliable technique for measuring drugs in plasma concentration during the anesthesia administration has been developed in this thesis.

Electrochemical sensors have been used for the on-line and simultaneous monitoring of multiple anesthetic compounds together with pH and temperature. Custom-built electronics that can actuate the sensing device, collect the data and transmit them wirelessly the data have been implemented. The main contributions and achievements obtained by this thesis are summarized below.

- **Fouling resistant electrode for Propofol long-term direct monitoring** Electrode fouling is a well-known undesired effect resulting from phenolic oxidation reaction. The oxidation of propofol, which is a phenolic compound, produces free radicals that lead to the formation of an electro-polymerized layer covering the sensor's surface. This causes a decrease of the electrode's sensitivity over subsequent measurements. A ready-to-use pencil graphite electrode (PGE) with a specific lead composition of 58% graphite, 36% clay and 5% wax has been identified as the best solid-state electrode for direct propofol monitoring in terms of (i) propofol sensitivity and (ii) fouling resistance properties over

time. Furthermore, electrochemical cleaning procedures were also implemented to guarantee an optimum sensing performance of the electrode for long-term propofol detection. This important and novel finding has been patented [253]. We achieved a monitoring of the propofol concentration of over 4 hours, as well as the drug detection in time in undiluted human serum under flux conditions.

- **Carbon-based electrodes for direct monitoring of paracetamol and midazolam** We have reported the electrochemical detection of midazolam in undiluted human serum by using MWCNTs-modified SPE for the first time. With MWCNT-nanostructured electrodes, not only midazolam, but also paracetamol (APAP) detection was achieved in the therapeutic range, under fluxed conditions and in complex solutions like human serum.
- **Interference study** We have also conducted an interference study among propofol, midazolam and APAP compounds to optimize and better characterize the sensing units. According to the results obtained by this analysis, we concluded that APAP and propofol can be detected simultaneously by the same PGE WE while midazolam does not have any interference action with the other target drugs. A Gaussian decomposition process has been used to discriminate the current contributions of APAP and paracetamol to the measured signal. Acid pH solutions may be preferred to improve the detection of these anesthetics.
- **Raspberry-pi based custom-built electronic potentiostat** In this thesis we investigated the use of the powerful RPi board as the central unit of the electronic system to drive the simultaneous monitoring of multiple drugs plus pH and T through dedicated front-ends. The potentiostatic circuit board constructed with COTS implements three parallel actuation and sensing blocks for interfacing with three separate electrochemical cells for enabling simultaneous monitoring. A 4<sup>th</sup>-order Butterworth low-pass filter has been included in each channel of the read-out circuit for cleaning the signal from the high-noise components. Wireless data transmission relies on WiFi technology. The electronic system showed great performances when compared to the commercially available Autolab potentiostat by Metrohm PGSTAT302N. The main advantages of our system are related with low costs, multi-detection of several drugs and pH and T at the same time, small dimensions (integrated in a containing box of 27 × 21 × 13 cm dimensions), and higher portability.
- **IoT Android-based network** IoT “smart” solutions in hospital environments are nowadays adopted to provide powerful tools for medical staff activities to guarantee improved and safer patient care. In the present work, we further investigated a medical IoT network to provide our system with a cloud-based solution for anesthesia on-line monitoring. We developed Android apps to allow the anesthesiologist to remain simultaneously connected to all the sedated patients in order to keep control over the monitored parameters. Alert notifications are sent to the medical doctor whenever an out-of-physiological-range parameter is measured on one of the monitored patients, to ensure fast intervention. The Android apps were developed to run on mobile devices,

---

such as a tablet or a smart-phone, or on wearable device, such as a smart-watch. Furthermore, the monitored medical data from the patients can be shared on the cloud to be accessible at any time and from any place, hence enabling teleconsulting.

- **System integration and validation tests** The present research was focused on the complete design and fabrication of the sensing and the electronic platforms and their integration in a complete IoT system for the on-line monitoring of anesthesia compounds. We also realized and characterized a fluidic device in which we have encapsulated the sensors. The fluidics drives the sample solution directly on the sensing sites. In the final chapter we showed the integration of the different components, the enrichment of the system by the IoT solution, and the in-vitro validation of the working prototype. We proved the excellent performance of the final overall prototype by running two crucial tests validating the multi-drug detection in undiluted human serum. With our system we were able to monitor the in-time variations of the concentration of two drugs, *e.g.* APAP and propofol, under flow conditions.

The results achieved in this thesis confirmed the promising performance of the prototype. However, further research could be dedicated to improve the system. Possible future works of this work are listed hereafter.

- **Blood-separation fluidics** An advanced microfluidic system could offer the possibility to: (i) perform on-chip separation of plasma from the whole blood [254] and (ii) vary the sample pH to more acid contents to optimize the detection. The sketch of this fluidics structure, which includes blood-separation and mixing modules, is shown in Fig. 7.1.
- **Miniaturization of the sensing electrodes** Miniaturized electrodes would be highly attractive, reducing the volume of the sample and facilitating its integration in catheter-like tools. This would lead to an easier use of the device and to the possibility of measuring the concentration of the drug directly in the patient's veins without adding further delay due to the blood sampling system.
- **Optimized electronics** Further optimization of the electronic platform would be beneficial on the one hand in reducing the power consumption and on the other by improving the S/N ratio. In particular, the front-end for midazolam detection should be revised. Due to the high midazolam concentrations (mM) that are normally administered, a high current comes from the electrochemical cell leading to a saturation of the electronic front-end. Alternative architectures could be investigated to overcome this saturation issue. In the light of an optimized electronics, switched capacitors architectures could offer a suitable solution since they require less power and less area respect to traditional op amp configurations and, moreover, they offer a wider range of voltage gains [255, 256].

With this thesis, we successfully created a first multi-panel prototype for the simultaneous monitoring of several anesthetic compounds over time, contributing a great step forward

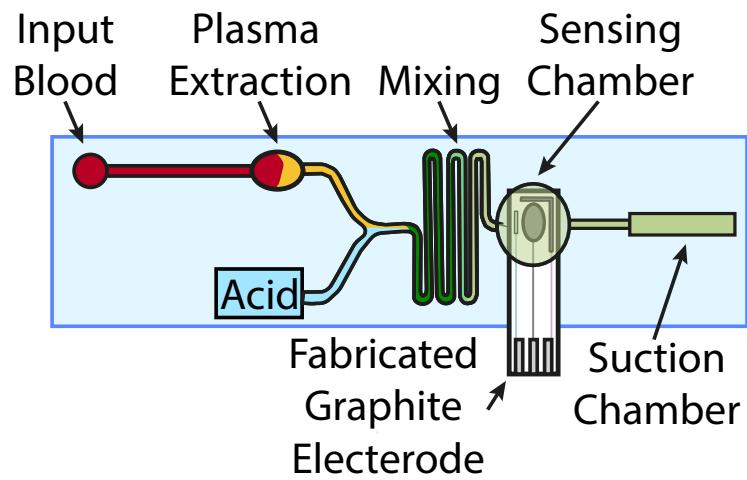


Figure 7.1 – Sketch of the advanced micro-fluidic device able to provide on-chip serum separation from blood and mixing properties (inspired by [254]).

for the state-of-the-art. The research presented in this thesis is the foundation for further developments in clinical applications.

# A Micro-controller firmware

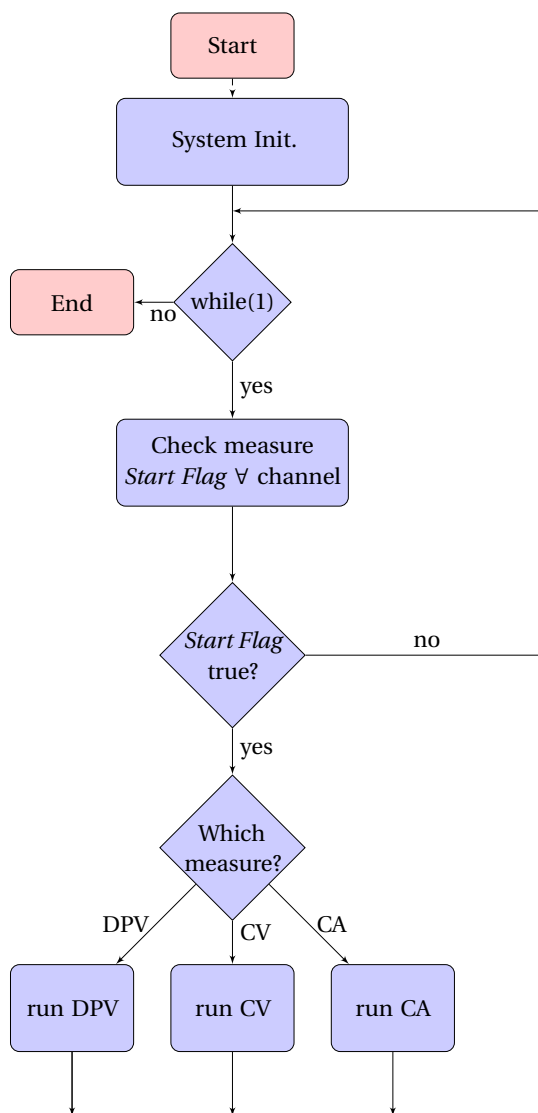


Figure A.1 – Micro-controller firmware work-flow.

## Appendix A. Micro-controller firmware

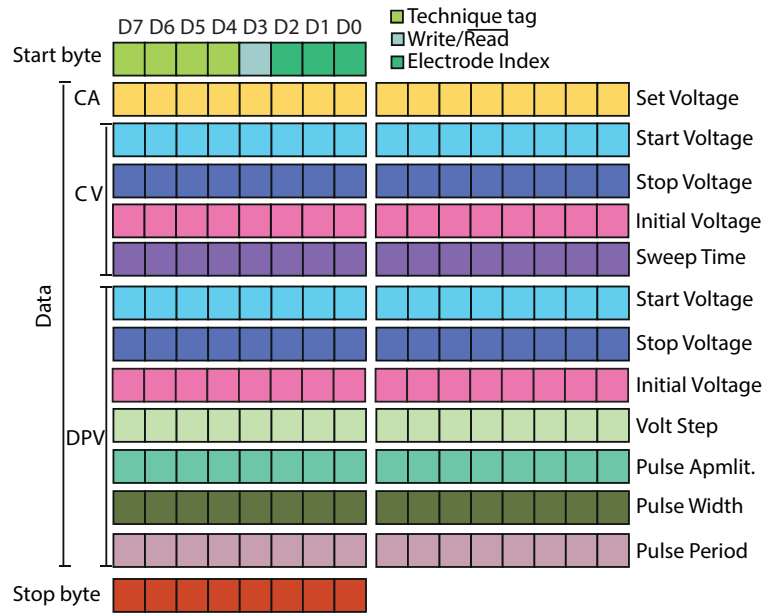


Figure A.2 – Data packet adopted in the communication protocol from RPi to PCB: *start byte*, *data* and *stop byte*.

### A.1 main.c

The **main.c** file contains the entrance of the whole firmware and the `while(1)` loop that runs continuously. The flow-chart in Fig. A.1 shows the firmware architecture of the micro-controller. Inside the loop, there are the individual states for each of the three electrochemical channels to control if any measurement has been started by the user (`Start Flag` for each channel). If a measurement is started/running then the corresponding technique is performed according to the user's request.

### A.2 Twi\_protocol.h

The **Twi\_protocol.h** file defines the protocol for I<sup>2</sup>C communication as reported in Fig. A.2. Namely, we can further identify:

- the *stop tag* as 1-byte set to 0×BB.
- In *start byte* the *Technique tag* as 4 bits [D7-D4] indicating the measurement type according to Table A.1.
- If D3 in *start byte* is 1: the master (RPi) writes to the slave (micro-controller), *viceversa* if it is 0.
- In *start byte* the *Electrode index* is indicated in [D2-D0] according to Table A.2.



Table A.1 – Measurement type extracted from the *Technique tag* bits.

D7	D6	D5	D4	Hex	Type
1	0	1	0	A	CA
1	1	1	1	F	CV
1	1	0	1	D	DPV
1	1	0	0	C	Stop Measurement

Table A.2 – Sensing channel extracted from the *Electrode index* bits.

D2	D1	D0	Electrode index
0	0	0	0
0	0	1	1
0	1	0	2

### A.3 Setup\_twi.c

The **Setup\_twi.c** file is responsible for configuring the *Two Wire Interface* (TWI) ports for I<sup>2</sup>C. This communication is adopted to set up the digital potentiometers and to interface with the RPi. Some fundamental functions are:

- `Setup_twi_master()` configures the TWI port of the micro-controller as master in the communication with the digital potentiometers for their configuration.
- `Setup_digitalPot()` is called as soon as the TWI master configuration is accomplished. This function sends the configuration data to the potentiometers from the micro-controller.
- `Reset_twi_master()` disables the *master-mode* for the TWI port of the micro-controller so that it can be configured again as TWI slave or master in the next communication.
- `Setup_twi_slave()` configures the TWI port of the micro-controller as a slave in the communication with the RPi.
- `Slave_process()` is assigned whenever the TWI port of the micro-controller is set as slave. It handles the process data interrupt. It is the most crucial function since it is responsible for processing the data and commands during the I<sup>2</sup>C communication with the RPi.

During the data processing, the master reads/sends data from/to the slave. The procedure for read and write operations are different.

- *Master read operation:* the RPi (master) wants to read data from the micro-controller (slave). Before reading the data, the RPi sends a 1-byte data that contains: (i) the index of the sensor electrodes from which to read the data, (ii) the *read indication flag* and

(iii) the type of measurement. As soon as the data is received from the TWI slave, the slave parses the 1-byte data to extract the index and the measurement type so that it can put the required data to the *send buffer*. After that the RPi has sent the 1-byte data, it executes *read operation* and waits TWI slave to send the data back. The data packet from the micro-controller to the RPi consists in a *start byte*, 2-byte of data containing the applied voltage for the measure, 2-byte data with the value of the measured current signal from the RedOx, and a *stop byte*. This data packet is the same indistinctly from the electrochemical technique is running.

- *Master write operation*: the RPi (master) will send to the micro-controller (slave) the configuration parameters for running a certain type of measurement chosen by the user. The master sends a 1-byte data, named as *start byte*, containing: (i) the configuration parameters for running a certain type of measurement, (ii) the specific sensing channel, which is identified by an index, and (iii) the *write operation flag*. When the micro-controller receives the *start tag* from the RPi, it extracts the measurement type, the read/write operation type and the electrode index. Knowing the measurement type, the slave assigns to the receive data counter the maximum expected data bytes (4-byte received for CA, 8-byte received for CV and 14-byte for DPV) to receive and sets the *start receiving flag* as *true*. When the consequent data arrives, the slave continues to save them in the *receive buffer array* until the expected data bytes are received. Once completed the receiving of the data packet, the slave assigns the received data to the corresponding sensing channel and updates the *start measurement flag* of the corresponding channel. For CA measurement, any timer is required since the excitation waveform is a fixed potential. On the contrary, for CV and DPV measurements, that requires more complex excitation waveform to be applied on the electrochemical cell, there are three timers TCC4, TCC5 and TCD5, one for each sensing channel. The data packet received from the RPi ends with a *stop byte*.

Finally, when the user decides to finish a measurements, the RPi sends a *stop measurement* command containing: (i) the electrode index and (ii) the *stop measurement tag*. As soon as this command is received, the output of the corresponding DAC is reset, and, in case of CV or DPV measurements running, also the timers are disabled.

### A.4 Setup\_timer.c

The **Setup\_timer.c** file is responsible for updating the counts and timing for given types of electro-chemical techniques, such as CV and DPV. Since there are three electrodes (indexes: 0-2), three timers are dedicated to each of them. TCC4 for electrode 0, TCC5 for electrode 1, TCD5 for electrode 2. Each timer can operate independently, hence enabling the possibility of running different measurements in parallel. For running CA measurements, any timer is needed since a fixed potential is applied over the electrochemical cell. For performing CV measurements, the excitation waveform consists of linear sweep potential ramp between  $V_{start}$  and  $V_{end}$ . To realize the ramp, a voltage value is applied for a given amount of time

( $\delta t$ ), then it is increased by a given voltage step ( $\delta V = V_{step}$ ) and then, the new voltage value is apply for another  $\delta t$  of time, and so on until the end of the ramp. The scan rate is given by  $\delta V/\delta t$ . The total number of increment ( $N_{ofSteps}$ ) starting from the start voltage ( $V_{start}$ ) is calculated by:

$$N_{ofSteps} = (V_{end} - V_{start})/V_{step} \quad (A.1)$$

While the applied potential ( $V_{applied}$ ) at each step ( $N_{stepindex}$ ) is calculated as:

$$V_{applied} = V_{start} + V_{step} \times N_{stepindex} \quad (A.2)$$

Each time the timer overflows, the step counter  $N_{stepindex}$  is increased by 1 until it reaches the  $N_{ofSteps}$ . When it reaches the maximum value of steps, the step counter  $N_{stepindex}$  starts to decrease by 1 at each timer overflow until it reaches the 0. When step counter  $N_{stepindex}$  is 0, it is again increased and so on until the measurement is stopped by the user.

Finally, for running DPV measurement, two different periods (*first period* and *second period*) has to be evaluated considering the pulse width and the pulse period. Initially, the timer period is set to the *first period*. In the *first period*, a voltage that is the sum of start voltage ( $V_{start}$ ), pulse amplitude ( $V_{pulseAmplitude}$ ) and voltage steps ( $V_{step}$ ) is applied, as shown in Eq. A.3. When the timer overflows, the timer period is set to the *second period*. In the *second period*, a different voltage value is applied, which is one pulse amplitude ( $V_{pulseAmplitude}$ ) smaller than the previous one, as calculated in Eq. A.4. When the timer overflows after the *second period*, then it is set again to the *first period* and the process is repeated. Similarly as CV measurement, the number of steps ( $N_{ofSteps}$ ) for DPV can be calculated as in Eq. A.1. The step counter ( $N_{stepindex}$ ) can increase until it reaches the maximum number of steps and, after that, it can decrease until it reaches the 0, then the process is repeated until the measurement is stopped by the user.

$$V_{FirstPeriod} = V_{start} + V_{pulseAmplitude} + V_{step} \times N_{stepindex} \quad (A.3)$$

$$V_{SecondPeriod} = V_{start} + V_{step} \times N_{stepindex} \quad (A.4)$$



## Bibliography

- [1] J. Cranshaw, K. Gupta, and T. Cook, "Litigation related to drug errors in anaesthesia: an analysis of claims against the nhs in england 1995–2007," *Anaesthesia*, vol. 64, no. 12, pp. 1317–1323, 2009.
- [2] F. R. Vogenberg, C. I. Barash, and M. Pursel, "Personalized medicine: part 1: evolution and development into theranostics," *Pharmacy and Therapeutics*, vol. 35, no. 10, p. 560, 2010.
- [3] S. Mathur and J. Sutton, "Personalized medicine could transform healthcare," *Biomedical reports*, vol. 7, no. 1, pp. 3–5, 2017.
- [4] W. Sadée and Z. Dai, "Pharmacogenetics/genomics and personalized medicine," *Human molecular genetics*, vol. 14, no. suppl\_2, pp. R207–R214, 2005.
- [5] A. Dubovitskaya, T. Buclin, M. Schumacher, K. Aberer, and Y. Thoma, "Tucuxi: An intelligent system for personalized medicine from individualization of treatments to research databases and back," in *Proceedings of the 8th ACM International Conference on Bioinformatics, Computational Biology, and Health Informatics*. ACM, 2017, pp. 223–232.
- [6] G. Schreier, "The internet of things for personalized health," *Stud Health Technol Inform*, vol. 200, pp. 22–31, 2014.
- [7] S. R. Islam, D. Kwak, M. H. Kabir, M. Hossain, and K.-S. Kwak, "The internet of things for health care: a comprehensive survey," *IEEE Access*, vol. 3, pp. 678–708, 2015.
- [8] F. . Sullivan, "Future of smart hospitals, concept definition, application, and growth opportunities," 2017. [Online]. Available: <https://store.frost.com/future-of-smart-hospitals.html#section1>
- [9] C. Donohue, B. Hobson, and R. C. Stephens, "An introduction to anaesthesia," *British Journal of Hospital Medicine*, vol. 74, no. 5, pp. C71–C75, 2013.
- [10] M. Sarwar, A. Nadeem, J. Nadeem, B. Mirza, M. Sarwar, M. Khalid, and M. Sarwar, "Fundamental practices of anesthesia that physician can do to permit surgery of a patient," *Journal of Anesthetics and Anesthesiology*, vol. 1, no. 1, 2017.

## Bibliography

---

- [11] H. AlBattikhi, "General physiology - action potential," 2015. [Online]. Available: <https://www.slideshare.net/hamzehbattikhi/general-physiology-action-potential>
- [12] F. Hossain, "Propofol (techno drugs ltd)," 2015. [Online]. Available: <https://www.slideshare.net/FarukHossain11/propofol-techno-drugs-ltd-49398876>
- [13] Y. Ishizawa, "Mechanisms of anesthetic actions and the brain," *Journal of anesthesia*, vol. 21, no. 2, pp. 187–199, 2007.
- [14] P. Tonner, "Balanced anaesthesia today," *Best Practice & Research Clinical Anaesthesiology*, vol. 19, no. 3, pp. 475–484, 2005.
- [15] P. S. Garcia, S. E. Kolesky, and A. Jenkins, "General anesthetic actions on gabaa receptors," *Current neuropharmacology*, vol. 8, no. 1, p. 2, 2010.
- [16] I. Vasileiou, T. Xanthos, E. Koudouna, D. Perrea, C. Klonaris, A. Katsargyris, and L. Papadimitriou, "Propofol: a review of its non-anaesthetic effects," *European journal of pharmacology*, vol. 605, no. 1-3, pp. 1–8, 2009.
- [17] J. Kanto and E. Gepts, "Pharmacokinetic implications for the clinical use of propofol," *Clinical pharmacokinetics*, vol. 17, no. 5, pp. 308–326, 1989.
- [18] A. Shah, S. S. Jhawar, and A. Goel, "Analysis of the anatomy of the papez circuit and adjoining limbic system by fiber dissection techniques," *Journal of Clinical Neuroscience*, vol. 19, no. 2, pp. 289–298, 2012.
- [19] H. Zhang, W. Wang, Z. Zhao, Y. Ge, J. Zhang, D. Yu, W. Chai, S. Wu, and L. Xu, "The action sites of propofol in the normal human brain revealed by functional magnetic resonance imaging," *The Anatomical Record*, vol. 293, no. 12, pp. 1985–1990, 2010.
- [20] J. M. Tepper, T. Koós, and C. J. Wilson, "Gabaergic microcircuits in the neostriatum," *Trends in neurosciences*, vol. 27, no. 11, pp. 662–669, 2004.
- [21] J. d. Reves, R. J. Fragen, H. R. Vinik, and D. J. Greenblatt, "Midazolam: pharmacology and uses." *Anesthesiology*, vol. 62, no. 3, pp. 310–324, 1985.
- [22] D. Information, "Midazolam hydrochloride syrup," 2017-2018. [Online]. Available: <http://www.druginformation.com/RxDrugs/M/Midazolam%20HCl%20Syrup.html>
- [23] F. Scholz, "Midazolam," *DrugBank*, March 2018. [Online]. Available: <https://www.drugbank.ca/drugs/DB00683>
- [24] G. G. Graham and K. F. Scott, "Mechanism of action of paracetamol," *American journal of therapeutics*, vol. 12, no. 1, pp. 46–55, 2005.
- [25] D. Memis, M. T. Inal, G. Kavalci, A. Sezer, and N. Sut, "Intravenous paracetamol reduced the use of opioids, extubation time, and opioid-related adverse effects after major surgery in intensive care unit," *Journal of critical care*, vol. 25, no. 3, pp. 458–462, 2010.

- [26] H. Borazan, T. B. Erdem, M. Kececioglu, and S. Otelcioglu, "Prevention of pain on injection of propofol: a comparison of lidocaine with different doses of paracetamol," *European Journal of Anaesthesiology (EJA)*, vol. 27, no. 3, pp. 253–257, 2010.
- [27] S. Chavan and V. Roy, "Designer drugs: A review," *World Journal of Pharmacy and Pharmaceutical Sciences*, vol. 4, no. 8, pp. 297–336, 2015.
- [28] R. Al-Hasani and M. R. Bruchas, "Molecular mechanisms of opioid receptor-dependent signaling and behavior," *Anesthesiology: The Journal of the American Society of Anesthesiologists*, vol. 115, no. 6, pp. 1363–1381, 2011.
- [29] P. W. Peng and A. N. Sandler, "A review of the use of fentanyl analgesia in the management of acute pain in adults," *Anesthesiology: The Journal of the American Society of Anesthesiologists*, vol. 90, no. 2, pp. 576–599, 1999.
- [30] N. Mehrotra, M. Gupta, A. Kovar, and B. Meibohm, "The role of pharmacokinetics and pharmacodynamics in phosphodiesterase-5 inhibitor therapy," *International journal of impotence research*, vol. 19, no. 3, p. 253, 2007.
- [31] T. N. Tozer and M. Rowland, *Introduction to pharmacokinetics and pharmacodynamics: the quantitative basis of drug therapy*. Lippincott Williams & Wilkins, 2006.
- [32] J. Wagner, "Kinetics of pharmacologic response i. proposed relationships between response and drug concentration in the intact animal and man," *Journal of Theoretical Biology*, vol. 20, no. 2, pp. 173–201, 1968.
- [33] M. A. Felmler, M. E. Morris, and D. E. Mager, "Mechanism-based pharmacodynamic modeling," in *Computational Toxicology*. Springer, 2012, pp. 583–600.
- [34] D. A. Smith, K. Beaumont, T. S. Maurer, and L. Di, "Volume of distribution in drug design: Miniperspective," *Journal of medicinal chemistry*, vol. 58, no. 15, pp. 5691–5698, 2015.
- [35] P. R. Smith, I. K. Moppett, and J. G. Hardman, "Pharmacokinetic analysis," *Anaesthesia & Intensive Care Medicine*, vol. 9, no. 8, pp. 366–368, 2008.
- [36] Z. Al-Rifai and D. Mulvey, "Principles of total intravenous anaesthesia: basic pharmacokinetics and model descriptions," *Bja Education*, vol. 16, no. 3, pp. 92–97, 2015.
- [37] S. Hill, "Pharmacokinetics of drug infusions," *Continuing education in anaesthesia, critical care & Pain*, vol. 4, no. 3, pp. 76–80, 2004.
- [38] A. Dubois, J. Bertrand, and F. Mentré, "Mathematical expressions of the pharmacokinetic and pharmacodynamic models implemented in the pfim software," *UMR738, INSERM, Paris Diderot University*, 2011.
- [39] S. Norn, P. Kruse, and E. Kruse, "On the history of injection," *Dansk medicinhistorisk arbog*, vol. 34, pp. 104–113, 2006.

## Bibliography

---

- [40] L. Campbell, F. H. Engbers, and G. N. Kenny, "Total intravenous anaesthesia," *CPD ANAESTHESIA*, vol. 3, no. 3, pp. 109–119, 2001.
- [41] J. Hendrickx and A. De Wolf, "Special aspects of pharmacokinetics of inhalation anaesthesia," in *Modern Anesthetics*. Springer, 2008, pp. 159–186.
- [42] S. Sivasubramaniam, "Target controlled infusion [tci] in anaesthetic practice," 2007.
- [43] A. Absalom, V. Mani, T. De Smet, and M. Struys, "Pharmacokinetic models for propofol—defining and illuminating the devil in the detail," *British journal of anaesthesia*, vol. 103, no. 1, pp. 26–37, 2009.
- [44] R. Eyres, "Update on tiva," *Pediatric Anesthesia*, vol. 14, no. 5, pp. 374–379, 2004.
- [45] S. Kelley, "Monitoring consciousness using the bispectral index (BIS) during anaesthesia: a pocket guide for clinicians. covidien," 2010.
- [46] G. Schneider and S. PS., "Monitoring depth of anaesthesia," *European Journal of Anaesthesiology Supplement*, vol. 15, pp. 21–28, 1997.
- [47] B. Musizza and S. Ribaric, "Monitoring the depth of anaesthesia," *Sensors*, vol. 10, no. 12, pp. 10 896–10 935, 2010.
- [48] J. Bruhn, P. Myles, R. Sneyd, and M. Struys, "Depth of anaesthesia monitoring: what's available, what's validated and what's next?" *British journal of anaesthesia*, vol. 97, no. 1, pp. 85–94, 2006.
- [49] J. Liu, H. Singh, and P. F. White, "Electroencephalographic bispectral index correlates with intraoperative recall and depth of propofol-induced sedation," *Anesthesia & Analgesia*, vol. 84, no. 1, pp. 185–189, 1997.
- [50] L. T. D. Duarte and R. Â. Saraiva, "When the bispectral index (BIS) can give false results," *Revista brasileira de anesthesiologia*, vol. 59, no. 1, pp. 99–109, 2009.
- [51] H. Q. Ontario, "Bispectral index monitor: An evidence-based analysis," *Ontario Health Technology Assessment Series*, vol. 4, no. 9, pp. 1–70, 2004.
- [52] U. Ha, J. Lee, M. Kim, T. Roh, S. Choi, and H.-J. Yoo, "An eeg-nirs multimodal soc for accurate anaesthesia depth monitoring," *IEEE Journal of Solid-State Circuits*, vol. 53, no. 6, pp. 1830–1843, 2018.
- [53] U. Ha, Y. Lee, H. Kim, T. Roh, J. Bae, C. Kim, and H.-J. Yoo, "A wearable eeg-heg-hrv multimodal system with simultaneous monitoring of tes for mental health management," *IEEE transactions on biomedical circuits and systems*, vol. 9, no. 6, pp. 758–766, 2015.
- [54] A. R. Absalom and K. P. Mason, *Total intravenous anaesthesia and target controlled infusions*. Springer, 2017.



- [55] K. Leslie, "Awareness and dreaming during tiva," in *Total Intravenous Anesthesia and Target Controlled Infusions*. Springer, 2017, pp. 783–796.
- [56] P. Samuelsson, L. Brudin, and R. H. Sandin, "Late psychological symptoms after awareness among consecutively included surgical patients," *The Journal of the American Society of Anesthesiologists*, vol. 106, no. 1, pp. 26–32, 2007.
- [57] S. A. K. Craig and R. Kitson, "Risks associated with anaesthesia," *Anaesthesia & Intensive Care Medicine*, vol. 11, no. 11, pp. 464–468, 2010.
- [58] D. J. Eleveld, J. H. Proost, L. I. Cortínez, A. R. Absalom, and M. M. Struys, "A general purpose pharmacokinetic model for propofol," *Anesthesia & Analgesia*, vol. 118, no. 6, pp. 1221–1237, 2014.
- [59] L. O. Boréus, "The role of therapeutic drug monitoring in children," *Clinical pharmacokinetics*, vol. 17, no. 1, pp. 4–12, 1989.
- [60] S. Layne, G. Mayer-Kress, and J. Holzfuss, "Problems associated with dimensional analysis of electroencephalogram data," in *Dimensions and entropies in chaotic systems*. Springer, 1986, pp. 246–256.
- [61] I. Kissin, "Depth of anesthesia and bispectral index monitoring," *Anesthesia & Analgesia*, vol. 90, no. 5, pp. 1114–1117, 2000.
- [62] F. Stradolini, T. Kilic, I. Taurino, G. De Micheli, and S. Carrara, "Cleaning strategy for carbon-based electrodes: Long-term propofol monitoring in human serum," *Sensors and Actuators B: Chemical*, 2018.
- [63] F. Stradolini, T. Kilic, A. Di Consiglio, M. Ozsoz, G. De Micheli, and S. Carrara, "Long-term monitoring of propofol and fouling effect on pencil graphite electrodes," *Electroanalysis*.
- [64] N. Aliakbarinodehi, F. Stradolini, S. A. Nakhjavani, I. Tzouvadaki, I. Taurino, G. De Micheli, and S. Carrara, "Performance of carbon nano-scale allotropes in detecting midazolam and paracetamol in undiluted human serum," *IEEE Sensors Journal*, 2018.
- [65] F. Stradolini, A. Tuoheti, P. Motto Ros, D. Demarchi, and S. Carrara, "Raspberry pi based system for portable and simultaneous monitoring of anesthetics and therapeutic compounds," in *CAS (NGCAS), 2017 New Generation of*. IEEE, 2017, pp. 101–104.
- [66] F. Stradolini, A. Tuoheti, T. Kilic, D. Demarchi, and S. Carrara, "Raspberry-pi based system for propofol monitoring," 2018.
- [67] S. L. Ntella, F. Stradolini, A. Tuoheti, D. Demarchi, A. A. Hatzopoulos, and S. Carrara, "Architecture and procedures for ph and temperature monitoring in medical applications," in *SENSORS, 2017 IEEE*. IEEE, 2017, pp. 1–3.

## Bibliography

---

- [68] F. Stradolini, E. Lavalle, G. De Micheli, P. Motto Ros, D. Demarchi, and S. Carrara, "Paradigm-shifting players for IoT: Smart-watches for intensive care monitoring," in *International Conference on Wireless Mobile Communication and Healthcare*. Springer, 2016, pp. 71–78.
- [69] F. Stradolini, N. Tamburrano, T. Modoux, A. Tuoheti, D. Demarchi, and S. Carrara, "IoT for telemedicine practices enabled by an android™ application with cloud system integration," in *Circuits and Systems (ISCAS), 2018 IEEE International Symposium on*. IEEE, 2018, pp. 1–5.
- [70] F. Stradolini, A. Tuoheti, T. Kilic, S. L. Ntella, N. Tamburrano, Z. Huang, G. De Micheli, D. Demarchi, and S. Carrara, "An IoT solution for on-line monitoring of anesthetics in human serum based on an integrated fluidic bio-electronic system," *Transaction of Biomedical Circuits and Systems Journal*, 2018.
- [71] B. Donato, F. Stradolini, A. Tuoheti, F. Angiolini, D. Demarchi, G. De Micheli, and S. Carrara, "Raspberry pi driven flow-injection system for electrochemical continuous monitoring platforms," in *Proceedings of the IEEE Biomedical Circuits and Systems Conference (BioCAS)*, no. EPFL-CONF-233771. IEEE, 2017.
- [72] S. Basalingappa, A. Sharma, and S. Amarnath, "Basic concepts of therapeutic drug monitoring," *Int. J. Current Pharm. Rev. Res*, vol. 5, no. 4, pp. 70–75, 2014.
- [73] D. J. Birkett, *Pharmacokinetics made easy*. McGraw Hill Professional, 2002.
- [74] J. Wang, "Electrochemical biosensors: towards point-of-care cancer diagnostics," *Biosensors and Bioelectronics*, vol. 21, no. 10, pp. 1887–1892, 2006.
- [75] A. J. Bard and L. R. Faulkner, "Electrochemical methods: principles and applications," *Electrochemical Methods: Principles and Applications*, pp. 386–428, 2001.
- [76] J. Colomer-Farrarons, P. L. Miribel-Català, A. I. Rodríguez-Villarreal, and J. Samitier, "Portable bio-devices: design of electrochemical instruments from miniaturized to implantable devices," in *New Perspectives in Biosensors Technology and Applications*. InTech, 2011.
- [77] P. T. Kissinger and W. R. Heineman, "Cyclic voltammetry," *Journal of Chemical Education*, vol. 60, no. 9, p. 702, 1983.
- [78] C. A. Schroll and S. M. Cohen, *Introduction to Experimental Electrochemistry*. Gamry Instruments Inc, 2017.
- [79] D. Harvey, *Modern analytical chemistry*. McGraw-Hill New York, 2000, vol. 381.
- [80] K. Aoki, J. Osteryoung, and R. A. Osteryoung, "Differential normal pulse voltammetry-theory," *Journal of Electroanalytical Chemistry and Interfacial Electrochemistry*, vol. 110, no. 1-3, pp. 1–18, 1980.

- [81] F. Scholz, "Voltammetric techniques of analysis: the essentials," *ChemTexts*, vol. 1, no. 4, p. 17, Sep 2015. [Online]. Available: <https://doi.org/10.1007/s40828-015-0016-y>
- [82] O. B. da Silva and S. A. Machado, "Evaluation of the detection and quantification limits in electroanalysis using two popular methods: application in the case study of paraquat determination," *Analytical Methods*, vol. 4, no. 8, pp. 2348–2354, 2012.
- [83] S. Carrara, *Bio/CMOS Interfaces in Constant Bias*. New York, NY: Springer New York, 2013, pp. 207–224. [Online]. Available: [https://doi.org/10.1007/978-1-4614-4690-3\\_8](https://doi.org/10.1007/978-1-4614-4690-3_8)
- [84] Q.-L. Yan, M. Gozin, F.-Q. Zhao, A. Cohen, and S.-P. Pang, "Highly energetic compositions based on functionalized carbon nanomaterials," *Nanoscale*, vol. 8, no. 9, pp. 4799–4851, 2016.
- [85] C. Zhu, G. Yang, H. Li, D. Du, and Y. Lin, "Electrochemical sensors and biosensors based on nanomaterials and nanostructures," *Analytical chemistry*, vol. 87, no. 1, pp. 230–249, 2014.
- [86] P. Araujo, *Carbon Nanostructures*. Springer, 2018.
- [87] A. Hirsch, "The era of carbon allotropes," *Nature materials*, vol. 9, no. 11, p. 868, 2010.
- [88] M. Peter, "The material that came out of a pencil," 2014. [Online]. Available: [https://www.empa.ch/documents/56164/256666/1red-2014-12-22-EmpaNews-47-en\\_Graphen.pdf/aa6b2257-df97-435c-b956-01871f6b50cc?version=1.0](https://www.empa.ch/documents/56164/256666/1red-2014-12-22-EmpaNews-47-en_Graphen.pdf/aa6b2257-df97-435c-b956-01871f6b50cc?version=1.0)
- [89] J. H. Luong, K. B. Male, and J. D. Glennon, "Boron-doped diamond electrode: synthesis, characterization, functionalization and analytical applications," *Analyst*, vol. 134, no. 10, pp. 1965–1979, 2009.
- [90] R. Trouillon and D. O'Hare, "Comparison of glassy carbon and boron doped diamond electrodes: Resistance to biofouling," *Electrochimica Acta*, vol. 55, no. 22, pp. 6586–6595, 2010.
- [91] S. Stankovich, D. A. Dikin, G. H. Dommett, K. M. Kohlhaas, E. J. Zimney, E. A. Stach, R. D. Piner, S. T. Nguyen, and R. S. Ruoff, "Graphene-based composite materials," *nature*, vol. 442, no. 7100, p. 282, 2006.
- [92] F. Criscuolo, I. Taurino, S. Francesca, S. Carrara, and G. De Micheli, "Highly-stable li+ ion-selective electrodes based on noble metal nanostructured layers as solid-contacts," *Analytica Chimica Acta*, 2018.
- [93] W. Feng and P. Ji, "Enzymes immobilized on carbon nanotubes," *Biotechnology advances*, vol. 29, no. 6, pp. 889–895, 2011.
- [94] C. Baj-Rossi, "Implantable multi-panel platform for continuous monitoring of exogenous and endogenous metabolites for applications in personalized medicine," 2015.

## Bibliography

---

- [95] J. P. Villagrasa, J. Colomer-Farrarons, and P. L. Miribel, "Bioelectronics for amperometric biosensors," in *State of the Art in Biosensors-General Aspects*. Intech, 2013.
- [96] L. T. C. SINE, "Fundamentals of direct digital synthesis (dds)."
- [97] W.-S. Wang, H.-Y. Huang, S.-C. Chen, K.-C. Ho, C.-Y. Lin, T.-C. Chou, C.-H. Hu, W.-F. Wang, C.-F. Wu, and C.-H. Luo, "Real-time telemetry system for amperometric and potentiometric electrochemical sensors," *Sensors*, vol. 11, no. 9, pp. 8593–8610, 2011.
- [98] S. Carrara, *Bio/CMOS Interfaces in Constant Bias*. New York, NY: Springer New York, 2013, pp. 185–205. [Online]. Available: [https://doi.org/10.1007/978-1-4614-4690-3\\_8](https://doi.org/10.1007/978-1-4614-4690-3_8)
- [99] L. Atzori, A. Iera, and G. Morabito, "The internet of things: A survey," *Computer networks*, vol. 54, no. 15, pp. 2787–2805, 2010.
- [100] T. Kurakova, "Overview of the internet of things," *Proceedings of the Internet of things and its enablers (INTHITEN)*, pp. 82–94, 2013.
- [101] C. Ryu and C.-W. Hur, "A monitoring system for integrated management of IoT-based home network," *International Journal of Electrical and Computer Engineering*, vol. 6, no. 1, p. 375, 2016.
- [102] A. Al-Fuqaha, M. Guizani, M. Mohammadi, M. Aledhari, and M. Ayyash, "Internet of things: A survey on enabling technologies, protocols, and applications," *IEEE Communications Surveys & Tutorials*, vol. 17, no. 4, pp. 2347–2376, 2015.
- [103] J. Manyika, M. Chui, J. Bughin, R. Dobbs, P. Bisson, and A. Marrs, *Disruptive technologies: Advances that will transform life, business, and the global economy*. McKinsey Global Institute San Francisco, CA, 2013, vol. 180.
- [104] L. Yu, Y. Lu, and X. Zhu, "Smart hospital based on internet of things." *JNW*, vol. 7, no. 10, pp. 1654–1661, 2012.
- [105] C. O. Rolim, F. L. Koch, C. B. Westphall, J. Werner, A. Fracalossi, and G. S. Salvador, "A cloud computing solution for patient's data collection in health care institutions," in *eHealth, Telemedicine, and Social Medicine, 2010. ETELEMED'10. Second International Conference on*. IEEE, 2010, pp. 95–99.
- [106] A. Gluhak, S. Krco, M. Nati, D. Pfisterer, N. Mitton, and T. Razafindralambo, "A survey on facilities for experimental internet of things research," *IEEE Communications Magazine*, vol. 49, no. 11, 2011.
- [107] A. B. Pawar and S. Ghumbre, "A survey on IoT applications, security challenges and counter measures," in *Computing, Analytics and Security Trends (CAST), International Conference on*. IEEE, 2016, pp. 294–299.
- [108] S. Marston, Z. Li, S. Bandyopadhyay, J. Zhang, and A. Ghalsasi, "Cloud computing—the business perspective," *Decision support systems*, vol. 51, no. 1, pp. 176–189, 2011.

- [109] P. SA, "PrYv," 2018. [Online]. Available: <https://pryv.com/product/>
- [110] A. Farahzadi, P. Shams, J. Reza zadeh, and R. Farahbakhsh, "Middleware technologies for cloud of things-a survey," *Digital Communications and Networks*, 2017.
- [111] P. SA, "Api concepts," 2018. [Online]. Available: <https://api.pryv.com/concepts/>
- [112] Magiva, "Android os versions and its features (2008 - 20017)," 2017. [Online]. Available: <http://magivatech.com/blog/info/android-versions>
- [113] N. Smyth, *Android 4.2 App Development Essentials*. eBookFrenzy, 2013.
- [114] F. Forcolin, "Sviluppo di app per sistema operativo android: aspetti generali," 2013.
- [115] M. Udantha, "Android software stack and terminology (tutorial 01)," 2014. [Online]. Available: <https://dzone.com/articles/android-software-stack-and>
- [116] Techopedia, "Dalvik," 2018. [Online]. Available: <https://www.techopedia.com/definition/4262/dalvik>
- [117] A. Developers, "Android architecture components," 2018. [Online]. Available: <https://developer.android.com/topic/libraries/architecture/>
- [118] C. Hock-Chuan, "Android programming more basics, activity's life cycle," 2015. [Online]. Available: [https://www.ntu.edu.sg/home/ehchua/programming/android/Android\\_BasicsMore.html](https://www.ntu.edu.sg/home/ehchua/programming/android/Android_BasicsMore.html)
- [119] A. Developers, "Meet android studio," 2018. [Online]. Available: <https://developer.android.com/studio/intro/>
- [120] E. Chaum, E. Lindner, and J. Guo, "Method and device for detection of bioavailable drug concentration," Apr. 30 2015, uS Patent App. 14/404,674.
- [121] V. Fodale and E. La Monaca, "Propofol infusion syndrome," *Drug safety*, vol. 31, no. 4, pp. 293–303, 2008.
- [122] J. Yarbrough, R. Harvey, and S. Cox, "Determination of propofol using high performance liquid chromatography in whole blood with fluorescence detection," *Journal of chromatographic science*, vol. 50, no. 3, pp. 162–166, 2012.
- [123] F. Vaiano, G. Serpelloni, M. Focardi, A. Fioravanti, F. Mari, and E. Bertol, "Lc–ms/ms and gc–ms methods in propofol detection: Evaluation of the two analytical procedures," *Forensic science international*, vol. 256, pp. 1–6, 2015.
- [124] C. Smith, "Disadvantages & advantages of an hplc," 2018. [Online]. Available: <https://sciencing.com/disadvantages-advantages-hplc-5911530.html>

## Bibliography

---

- [125] G. Brandhorst, M. Oellerich, G. Maine, P. Taylor, G. Veen, and P. Wallemacq, "Liquid chromatography–tandem mass spectrometry or automated immunoassays: what are the future trends in therapeutic drug monitoring?" *Clinical chemistry*, vol. 58, no. 5, pp. 821–825, 2012.
- [126] T. Perl, E. Carstens, A. Hirn, M. Quintel, W. Vautz, J. Nolte, and M. Jünger, "Determination of serum propofol concentrations by breath analysis using ion mobility spectrometry," *British journal of anaesthesia*, vol. 103, no. 6, pp. 822–827, 2009.
- [127] G. Harrison, A. Critchley, C. Mayhew, and J. Thompson, "Real-time breath monitoring of propofol and its volatile metabolites during surgery using a novel mass spectrometric technique: a feasibility study," *British journal of anaesthesia*, vol. 91, no. 6, pp. 797–799, 2003.
- [128] W. Miekisch, P. Fuchs, S. Kamysek, C. Neumann, and J. K. Schubert, "Assessment of propofol concentrations in human breath and blood by means of hs-spme–gc–ms," *Clinica chimica acta*, vol. 395, no. 1-2, pp. 32–37, 2008.
- [129] S. Kamysek, P. Fuchs, H. Schwoebel, J. P. Roesner, S. Kischkel, K. Wolter, C. Loeseken, J. K. Schubert, and W. Miekisch, "Drug detection in breath: effects of pulmonary blood flow and cardiac output on propofol exhalation," *Analytical and bioanalytical chemistry*, vol. 401, no. 7, p. 2093, 2011.
- [130] S.-Z. Fan, H.-Y. Yu, Y.-L. Chen, and C.-C. Liu, "Propofol concentration monitoring in plasma or whole blood by gas chromatography and high-performance liquid chromatography," *Anesthesia & Analgesia*, vol. 81, no. 1, pp. 175–178, 1995.
- [131] J. Wang, "Portable electrochemical systems," *TrAC Trends in Analytical Chemistry*, vol. 21, no. 4, pp. 226–232, 2002.
- [132] F. Kivlehan, E. Chaum, and E. Lindner, "Propofol detection and quantification in human blood: the promise of feedback controlled, closed-loop anesthesia," *Analyst*, vol. 140, no. 1, pp. 98–106, 2015.
- [133] F. Kivlehan, F. Garay, J. Guo, E. Chaum, and E. Lindner, "Toward feedback-controlled anesthesia: voltammetric measurement of propofol (2, 6-diisopropylphenol) in serum-like electrolyte solutions," *Analytical chemistry*, vol. 84, no. 18, pp. 7670–7676, 2012.
- [134] J. Langmaier, F. Garay, F. Kivlehan, E. Chaum, and E. Lindner, "Electrochemical quantification of 2, 6-diisopropylphenol (propofol)," *Analytica chimica acta*, vol. 704, no. 1-2, pp. 63–67, 2011.
- [135] X. Yang, J. Kirsch, J. Fergus, and A. Simonian, "Modeling analysis of electrode fouling during electrolysis of phenolic compounds," *Electrochimica Acta*, vol. 94, pp. 259–268, 2013.

- [136] M. Ferreira, H. Varela, R. M. Torresi, and G. Tremiliosi-Filho, "Electrode passivation caused by polymerization of different phenolic compounds," *Electrochimica Acta*, vol. 52, no. 2, pp. 434–442, 2006.
- [137] E. Chaum, E. Lindner, and J. Guo, "Method and device for detection of bioavailable drug concentration," May 29 2018, uS Patent 9,983,162.
- [138] M. R. Ganjali, B. Larijani, and P. Norouzi, "Determination of midazolam by potentiometric pvc membrane and mwcnts based carbon paste sensors," *Int. J. Electrochem. Sci*, vol. 7, pp. 4822–4833, 2012.
- [139] C.-C. Hong, C.-C. Lin, C.-L. Hong, Z.-X. Lin, M.-H. Chung, and P.-W. Hsieh, "Handheld analyzer with on-chip molecularly-imprinted biosensors for electrical detection of propofol in plasma samples," *Biosensors and Bioelectronics*, vol. 86, pp. 623–629, 2016.
- [140] W.-C. Lee, C.-H. Cheng, H.-H. Pan, T.-H. Chung, and C.-C. Hwang, "Chromatographic characterization of molecularly imprinted polymers," *Analytical and bioanalytical chemistry*, vol. 390, no. 4, pp. 1101–1109, 2008.
- [141] K. Haupt, "Peer reviewed: molecularly imprinted polymers: the next generation," 2003.
- [142] H. B. Martin, A. Argoitia, U. Landau, A. B. Anderson, and J. C. Angus, "Hydrogen and oxygen evolution on boron-doped diamond electrodes," *Journal of the Electrochemical Society*, vol. 143, no. 6, pp. L133–L136, 1996.
- [143] M. N. Latta, D. J. Riley, and P. W. May, "Impedance studies of boron-doped cvd diamond electrodes," *Diamond and Related Materials*, vol. 9, no. 3-6, pp. 1181–1183, 2000.
- [144] L. Özcan, M. Sahin, and Y. Sahin, "Electrochemical preparation of a molecularly imprinted polypyrrole-modified pencil graphite electrode for determination of ascorbic acid," *Sensors*, vol. 8, no. 9, pp. 5792–5805, 2008.
- [145] M. M. Walczak, D. A. Dryer, D. D. Jacobson, M. G. Foss, and N. T. Flynn, "ph dependent redox couple: An illustration of the nernst equation," *Journal of chemical education*, vol. 74, no. 10, p. 1195, 1997.
- [146] R. Vittal and K.-C. Ho, "Cobalt oxide electrodes-problem and a solution through a novel approach using cetyltrimethylammonium bromide (ctab)," *Catalysis Reviews*, vol. 57, no. 2, pp. 145–191, 2015.
- [147] Z. Tasic, V. Gupta, and M. Antonijevic, "The mechanism and kinetics of degradation of phenolics in wastewaters using electrochemical oxidation," *Int. J. Electrochem. Sci*, vol. 9, pp. 3473–3490, 2014.
- [148] I. Taurino, A. Magrez, F. Matteini, A. Cavallini, L. Forró, G. De Micheli, and S. Carrara, "High-performance multipanel biosensors based on a selective integration of nanographite petals," *Nano letters*, vol. 14, no. 6, pp. 3180–3184, 2014.

## Bibliography

---

- [149] J. Li and N. Wu, *Biosensors based on nanomaterials and nanodevices*. CRC Press, 2013.
- [150] J. X. Mazoit and K. Samii, "Binding of propofol to blood components: implications for pharmacokinetics and for pharmacodynamics," *British journal of clinical pharmacology*, vol. 47, no. 1, pp. 35–42, 1999.
- [151] J. S. Krouwer and G. S. Cembrowski, "A review of standards and statistics used to describe blood glucose monitor performance," 2010.
- [152] B. L. Hanssen, S. Siraj, and D. K. Wong, "Recent strategies to minimise fouling in electrochemical detection systems," *Reviews in Analytical Chemistry*, vol. 35, no. 1, pp. 1–28, 2016.
- [153] K. A. Desousa, "Pain on propofol injection: Causes and remedies," *Indian journal of pharmacology*, vol. 48, no. 6, p. 617, 2016.
- [154] F. Shihana, D. Dissanayake, P. Dargan, and A. Dawson, "A modified low-cost colorimetric method for paracetamol (acetaminophen) measurement in plasma," *Clinical toxicology*, vol. 48, no. 1, pp. 42–46, 2010.
- [155] R. Baselt and R. Cravey, "Methadone," *Disposition of Toxic Drugs and Chemicals in Man*, 9th ed. Seal Beach, CA: Biomedical Publications, pp. 1021–1025, 2011.
- [156] G. Burgot, F. Auffret, and J.-L. Burgot, "Determination of acetaminophen by thermometric titrimetry," *Analytica chimica acta*, vol. 343, no. 1-2, pp. 125–128, 1997.
- [157] J. Hanaee, "Simultaneous determination of acetaminophen and codeine in pharmaceutical preparations by derivative spectrophotometry," *Pharmaceutica Acta Helvetiae*, vol. 72, no. 4, pp. 239–241, 1997.
- [158] M. Knochen, J. Giglio, and B. F. Reis, "Flow-injection spectrophotometric determination of paracetamol in tablets and oral solutions," *Journal of pharmaceutical and biomedical analysis*, vol. 33, no. 2, pp. 191–197, 2003.
- [159] R. M. Riggin, A. L. Schmidt, and P. T. Kissinger, "Determination of acetaminophen in pharmaceutical preparations and body fluids by high-performance liquid chromatography with electrochemical detection," *Journal of pharmaceutical sciences*, vol. 64, no. 4, pp. 680–683, 1975.
- [160] E. R. Lepper, J. K. Hicks, J. Verweij, S. Zhai, W. D. Figg, and A. Sparreboom, "Determination of midazolam in human plasma by liquid chromatography with mass-spectrometric detection," *Journal of Chromatography B*, vol. 806, no. 2, pp. 305–310, 2004.
- [161] F. Rubio, B. Miwa, and W. Garland, "Determination of midazolam and two metabolites of midazolam in human plasma by gas chromatography—negative chemical-ionization mass spectrometry," *Journal of Chromatography B: Biomedical Sciences and Applications*, vol. 233, no. 1, pp. 157–165, 1982.



- [162] D. J. Greenblatt, A. Locniskar, H. R. Ochs, and P. M. Lauven, "Automated gas chromatography for studies of midazolam pharmacokinetics." *Anesthesiology*, vol. 55, no. 2, pp. 176–179, 1981.
- [163] R. Dixon, R. Lucek, D. Todd, and A. Walser, "Midazolam: radioimmunoassay for pharmacokinetic studies in man." *Research communications in chemical pathology and pharmacology*, vol. 37, no. 1, pp. 11–20, 1982.
- [164] E. Bakker and M. Telting-Diaz, "Electrochemical sensors," *Analytical chemistry*, vol. 74, no. 12, pp. 2781–2800, 2002.
- [165] A. Chen and S. Chatterjee, "Nanomaterials based electrochemical sensors for biomedical applications," *Chemical Society Reviews*, vol. 42, no. 12, pp. 5425–5438, 2013.
- [166] H. S. Blix, K. K. Viktil, T. A. Moger, and A. Reikvam, "Drugs with narrow therapeutic index as indicators in the risk management of hospitalised patients," *Pharmacy practice*, vol. 8, no. 1, p. 50, 2010.
- [167] P. Fanjul-Bolado, P. J. Lamas-Ardisana, D. Hernández-Santos, and A. Costa-García, "Electrochemical study and flow injection analysis of paracetamol in pharmaceutical formulations based on screen-printed electrodes and carbon nanotubes," *Analytica chimica acta*, vol. 638, no. 2, pp. 133–138, 2009.
- [168] O.-W. Lau, S.-F. Luk, and Y.-M. Cheung, "Simultaneous determination of ascorbic acid, caffeine and paracetamol in drug formulations by differential-pulse voltammetry using a glassy carbon electrode," *Analyst*, vol. 114, no. 9, pp. 1047–1051, 1989.
- [169] R. Jain and R. K. Yadav, "Voltammetric behavior of sedative drug midazolam at glassy carbon electrode in solubilized systems," *Journal of Pharmaceutical Analysis*, vol. 2, no. 2, pp. 123–129, 2012.
- [170] N. Aliakbarinodehi, I. Taurino, J. Pravin, A. Tagliaferro, G. Piccinini, G. De Micheli, and S. Carrara, "Electrochemical nanostructured biosensors: carbon nanotubes versus conductive and semi-conductive nanoparticles," *Chemical Papers*, vol. 69, no. 1, pp. 134–142, 2015.
- [171] M. Rawlins, D. Henderson, and A. Hijab, "Pharmacokinetics of paracetamol (acetaminophen) after intravenous and oral administration," *European journal of clinical pharmacology*, vol. 11, no. 4, pp. 283–286, 1977.
- [172] A. Peigney, C. Laurent, E. Flahaut, R. Bacsa, and A. Rousset, "Specific surface area of carbon nanotubes and bundles of carbon nanotubes," *Carbon*, vol. 39, no. 4, pp. 507–514, 2001.
- [173] N. Aliakbarinodehi, G. De Micheli, and S. Carrara, "Optimized electrochemical detection of anti-cancer drug by carbon nanotubes or gold nanoparticles," in *Ph. D. Research in Microelectronics and Electronics (PRIME), 2015 11th Conference on*. IEEE, 2015, pp. 25–28.

## Bibliography

---

- [174] Y. Li and S.-M. Chen, "The electrochemical properties of acetaminophen on bare glassy carbon electrode," *Int. J. Electrochem. Sci*, vol. 7, no. 3, 2012.
- [175] N. Ramalakshmi, S. Muthukumar, and B. Marichamy, "Preparation and characterization of 4-hydroxybenzylidencarbamide-ctab modified glassy carbon electrode by using [Fe(CN)<sub>6</sub>]<sup>4-</sup>/[Fe(CN)<sub>6</sub>]<sup>3-</sup>-redox system," *Sciences*, vol. 2, pp. 16–24, 2013.
- [176] S. Carrara, C. Baj-Rossi, C. Boero, and G. De Micheli, "Do carbon nanotubes contribute to electrochemical biosensing?" *Electrochimica Acta*, vol. 128, pp. 102–112, 2014.
- [177] E. Alipour, M. R. Majidi, A. Saadatirad, S. mahdi Golabi, and A. M. Alizadeh, "Simultaneous determination of dopamine and uric acid in biological samples on the pretreated pencil graphite electrode," *Electrochimica Acta*, vol. 91, pp. 36–42, 2013.
- [178] J. H. Zagal and P. Herrera, "Electrochemistry of cysteine and cystine on metal-phthalocyanines adsorbed on a graphite electrode," *Electrochimica Acta*, vol. 30, no. 4, pp. 449–454, 1985.
- [179] Z. A. Alothman, N. Bukhari, S. M. Wabaidur, and S. Haider, "Simultaneous electrochemical determination of dopamine and acetaminophen using multiwall carbon nanotubes modified glassy carbon electrode," *Sensors and Actuators B: Chemical*, vol. 146, no. 1, pp. 314–320, 2010.
- [180] X. Chen, J. Zhu, Q. Xi, and W. Yang, "A high performance electrochemical sensor for acetaminophen based on single-walled carbon nanotube-graphene nanosheet hybrid films," *Sensors and Actuators B: Chemical*, vol. 161, no. 1, pp. 648–654, 2012.
- [181] N. Ghorbani, S. Hosseinzadeh, S. Pashaei, A. Hosseinzadeh, and H. A. Hamidi, "The effect of produce conditions for preparation of potentiometric carbon paste sensor for determination of midazolam in pharmaceutical," *Int. J. Electrochem. Sci*, vol. 9, pp. 3772–3783, 2014.
- [182] R. N. Goyal and S. P. Singh, "Voltammetric determination of paracetamol at C<sub>60</sub>-modified glassy carbon electrode," *Electrochimica Acta*, vol. 51, no. 15, pp. 3008–3012, 2006.
- [183] A. Aliabadi, G. H. Rounaghi, and M. H. A. Zavar, "A new droplet-based polymeric banana electrochemical biosensor for analysis of one microliter solution of paracetamol," *Sensors and Actuators B: Chemical*, vol. 241, pp. 182–189, 2017.
- [184] R. N. Goyal, V. K. Gupta, and S. Chatterjee, "Voltammetric biosensors for the determination of paracetamol at carbon nanotube modified pyrolytic graphite electrode," *Sensors and Actuators B: Chemical*, vol. 149, no. 1, pp. 252–258, 2010.
- [185] R. components, "Raspberry Pi 3 model B," 2018. [Online]. Available: <http://docs-europe.electrocomponents.com/webdocs/14ba/0900766b814ba5fd.pdf>
- [186] DMetrohm, "Autolab pgstat128n - entry level modularity," 2018. [Online]. Available: <http://www.ecochemie.nl/Products/Echem/NSeriesFolder/PGSTAT128N>

- [187] A. S. Gross, "Best practice in therapeutic drug monitoring," *British journal of clinical pharmacology*, vol. 52, no. S1, pp. 5–9, 2001.
- [188] E. Ghodsevali, S. Morneau-Gamache, J. Mathault, H. Landari, É. Boisselier, M. Boukadoum, B. Gosselin, and A. Miled, "Miniaturized fdda and cmos based potentiostat for bio-applications," *Sensors*, vol. 17, no. 4, p. 810, 2017.
- [189] P. Bezuidenhout, K. Land, and T. Joubert, "A low-power cmos operational amplifier ic for a heterogeneous paper-based potentiostat," in *Fourth Conference on Sensors, MEMS, and Electro-Optic Systems*, vol. 10036. International Society for Optics and Photonics, 2017, p. 100360P.
- [190] S. S. Ghoreishizadeh, I. Taurino, S. Carrara, and G. De Micheli, "A current-mode potentiostat for multi-target detection tested with different lactate biosensors," in *Biomedical Circuits and Systems Conference (BioCAS), 2012 IEEE*. IEEE, 2012, pp. 128–131.
- [191] S. Ghoreishizadeh, E. G. Kilinc, C. Baj-Rossi, C. Dehollain, S. Carrara, and G. De Micheli, "An implantable bio-micro-system for drug monitoring," in *Biomedical Circuits and Systems Conference (BioCAS), 2013 IEEE*. IEEE, 2013, pp. 218–221.
- [192] F. Basilotta, S. Riario, F. Stradolini, I. Taurino, D. Demarchi, G. De Micheli, and S. Carrara, "Wireless monitoring in intensive care units by a 3d-printed system with embedded electronic," in *Biomedical Circuits and Systems Conference (BioCAS), 2015 IEEE*. IEEE, 2015, pp. 1–4.
- [193] S. Pithadia and S. More, "Grounding in mixed-signal systems demystified, part 2," *Analog Applications*, 2013.
- [194] W. Kester, J. Bryant, and M. Byrne, "Grounding data converters and solving the mystery of " agnd" and " dgnd," *Analog Devices Tutorial*, 2006.
- [195] J. Ardizzoni, "A practical guide to high-speed printed-circuit-board layout," *Analog Dialogue*, vol. 39, no. 9, pp. 1–6, 2005.
- [196] A. D. T. (MT-101), "Decoupling techniques, what is proper decoupling and why is it necessary?" 2009.
- [197] R. E. Corporation, "Understanding linear regulators and their key performance parameters," 2008. [Online]. Available: <https://www.intersil.com/content/dam/Intersil/whitepapers/linear-regulator/understanding-ldos.pdf>
- [198] D. Xu, "Fundamentals of designing with ldos in automative battery direct connect applications," 2017. [Online]. Available: <http://www.ti.com/lit/ml/slyb232/slyb232.pdf>
- [199] Atmel, "Application note, atmel at01080: Xmega e schematic checklist, atmel avr xmega e," 2013. [Online]. Available: [http://ww1.microchip.com/downloads/en/appnotes/atmel-42087-xmega-e-schematic-checklist\\_application-note\\_at01080.pdf](http://ww1.microchip.com/downloads/en/appnotes/atmel-42087-xmega-e-schematic-checklist_application-note_at01080.pdf)

## Bibliography

---

- [200] M. Integrated, "Max4475-max4478/max4488/max4489 sot23, low-noise, low-distortion, wide-band, rail-to-rail op amps," 2012. [Online]. Available: <http://www.mouser.com/ds/2/256/MAX4475-MAX4489-64486.pdf>
- [201] E. Hub, *Butterworth Filter*, 2015. [Online]. Available: <https://www.electronicshub.org/butterworth-filter/>
- [202] H. L. Fernandez-Canque, *Analog Electronics Applications: Fundamentals of Design and Analysis*. CRC Press, 2016.
- [203] R. filter Chapter, "Active filter design techniques literature number sloa088 thomas kugelstadt," 16.
- [204] J. Karki, "Active low-pass filter design," *Texas Instruments Application Report*, 2000.
- [205] R. Geek, "Equivalent noise bandwidth," 2014. [Online]. Available: <http://analog.intgckts.com/equivalent-noise-bandwidth/>
- [206] P. Salvo, N. Calisi, B. Melai, B. Cortigiani, M. Mannini, A. Caneschi, G. Lorenzetti, C. Paoletti, T. Lomonaco, A. Paolicchi *et al.*, "Temperature and ph sensors based on graphenic materials," *Biosensors and Bioelectronics*, vol. 91, pp. 870–877, 2017.
- [207] D. I. Sessler, "Mild perioperative hypothermia," *New England Journal of Medicine*, vol. 336, no. 24, pp. 1730–1737, 1997.
- [208] J. A. Kellum, "Determinants of blood ph in health and disease," *Critical Care*, vol. 4, no. 1, p. 6, 2000.
- [209] J. J. B. C. Ashton and L. Geary, "The effects of temperature on ph measurement," *TSP*, vol. 1, no. 2.
- [210] S. Patel, H. Park, P. Bonato, L. Chan, and M. Rodgers, "A review of wearable sensors and systems with application in rehabilitation," *J. of neuroengineering and rehabilitation*, vol. 9, no. 1, p. 21, 2012.
- [211] P. Zubiate, C. Zamarreño, I. Del Villar, I. Matias, and F. Arregui, "Tunable optical fiber ph sensors based on te and tm lossy mode resonances (lmrs)," *Sensors and Actuators B: Chemical*, vol. 231, pp. 484–490, 2016.
- [212] N. Liu, Y. Liu, L. Zhu, Y. Shi, and Q. Wan, "Low-cost ph sensors based on low-voltage oxide-based electric-double-layer thin film transistors," *IEEE Electron Device Letters*, vol. 35, no. 4, pp. 482–484, 2014.
- [213] C. Pietsch, R. Hoogenboom, and U. S. Schubert, "Soluble polymeric dual sensor for temperature and ph value," *Angewandte Chemie International Edition*, vol. 48, no. 31, pp. 5653–5656, 2009.

- [214] J. Janata and M. Josowicz, "Peer reviewed: A fresh look at some old principles: The kelvin probe and the nernst equation," *Analytical Chemistry*, vol. 69, no. 9, pp. 293A–296A, 1997.
- [215] J. Luo, K. Ying, P. He, and J. Bai, "Properties of savitzky–golay digital differentiators," *Digital Signal Processing*, vol. 15, no. 2, pp. 122–136, 2005.
- [216] R. J. Klein, M. P. H. Suzanne, E. Proctor, M. S. P. H. Manon, A. Boudreault, and K. M. Turczyn, "Healthy people 2010 criteria for data suppression," 2002.
- [217] D. GUIDANCE, "Self-monitoring blood glucose test systems for over-the-counter use draft guidance for industry and food and drug administration," 2014.
- [218] N. Ding, J. Xu, Y. Yao, G. Wegner, X. Fang, C. Chen, and I. Lieberwirth, "Determination of the diffusion coefficient of lithium ions in nano-si," *Solid State Ionics*, vol. 180, no. 2, pp. 222–225, 2009.
- [219] M. H. Myers, Y. Li, F. Kivlehan, E. Lindner, and E. Chaum, "A feedback control approach to organic drug infusions using electrochemical measurement," *IEEE Transactions on Biomedical Engineering*, vol. 63, no. 3, pp. 506–511, 2016.
- [220] S. Thiagarajan, C.-Y. Cheng, S.-M. Chen, and T.-H. Tsai, "Electrochemical detection of propofol at the preanodized carbon electrode," *Journal of Solid State Electrochemistry*, vol. 15, no. 4, pp. 781–786, 2011.
- [221] A. Alamri, "Cloud-based e-health multimedia framework for heterogeneous network," in *Multimedia and Expo Workshops (ICMEW), 2012 IEEE International Conference on*. IEEE, 2012, pp. 447–452.
- [222] P. Matlani and N. D. Londhe, "A cloud computing based telemedicine service," in *Point-of-Care Healthcare Technologies (PHT), 2013 IEEE*. IEEE, 2013, pp. 326–330.
- [223] E. VELASCO-CASTILLO, "The smart wearables market will be worth usd22.9 billion worldwide by 2020," 2014. [Online]. Available: <http://www.analysismason.com/About-Us/News/Insight/smart-wearables-forecast-Sep2014/>
- [224] D. C. Ruiz and A. Goransson, *Professional Android Wearables*. John Wiley & Sons, 2015.
- [225] M. Murar and S. Brad, "Monitoring and controlling of smart equipments using android compatible devices towards IoT applications and services in manufacturing industry," in *Automation, Quality and Testing, Robotics, 2014 IEEE International Conference on*. IEEE, 2014, pp. 1–5.
- [226] R. Rawassizadeh, B. A. Price, and M. Petre, "Wearables: Has the age of smartwatches finally arrived?" *Communications of the ACM*, vol. 58, no. 1, pp. 45–47, 2015.
- [227] S. Subramaniam, "Smartwatch with a multi-purpose sensor for remote monitoring of a patent," Aug. 27 2015, uS Patent App. 14/189,877.

## Bibliography

---

- [228] C. Boletsis, S. McCallum, and B. F. Landmark, "The use of smartwatches for health monitoring in home-based dementia care," in *International Conference on Human Aspects of IT for the Aged Population*. Springer, 2015, pp. 15–26.
- [229] A. M. Amiri, N. Peltier, C. Goldberg, Y. Sun, A. Nathan, S. V. Hiremath, and K. Mankodiya, "Wearsense: detecting autism stereotypic behaviors through smartwatches," in *Health-care*, vol. 5, no. 1. Multidisciplinary Digital Publishing Institute, 2017, p. 11.
- [230] R. Wu, E. De Lara, D. Liaqat, I. Thukral, and A. S. Gershon, "Feasibility of using smartwatches and smartphones to monitor patients with copd," in *A49. COPD: CARE DELIVERY*. American Thoracic Society, 2016, pp. A1695–A1695.
- [231] M. Al-Holaibah and N. Al-Saleh, "A smartwatch centric social networking application for alzheimer people."
- [232] M. Moore, "Telemedicine in the icu: reduction in mortality, cost, and average length of stay," Ph.D. dissertation, University of Pittsburgh, 2015.
- [233] M. J. Brown, A. Subramanian, T. B. Curry, D. J. Kor, S. L. Moran, and T. R. Rohleder, "Improving operating room productivity via parallel anesthesia processing," *International journal of health care quality assurance*, vol. 27, no. 8, pp. 697–706, 2014.
- [234] M. Bang, K. Solnevik, and H. Eriksson, "The nurse watch: design and evaluation of a smart watch application with vital sign monitoring and checklist reminders," in *AMIA Annual Symposium Proceedings*, vol. 2015. American Medical Informatics Association, 2015, p. 314.
- [235] A. Developers, "Android studio," 2018. [Online]. Available: <https://developer.android.com/studio/>
- [236] S. Evangelista, "Smartwatches connect intensive care doctors and their patients," 2016. [Online]. Available: <https://actu.epfl.ch/news/smartwatches-connect-intensive-care-doctors-and-th/>
- [237] F. Stradolini, S. Riario, C. Boero, C. Baj-Rossi, I. Taurino, G. Surrel, G. De Micheli, and S. Carrara, "Wireless monitoring of endogenous and exogenous biomolecules on an android interface," *IEEE Sensors Journal*, vol. 16, no. 9, pp. 3163–3170, 2015.
- [238] C. INC., "What are the navier-stokes equations?" 2018. [Online]. Available: <https://www.comsol.com/multiphysics/navier-stokes-equations>
- [239] L. T. Sniegowski and J. R. Moody, "Determination of serum and blood densities," *Analytical chemistry*, vol. 51, no. 9, pp. 1577–1578, 1979.
- [240] M. L. Eginton, "Evaluation of the effectiveness of a commercial cooling collar in reducing body temperature during heat stress: theoretical modeling of body temperature distribution," Ph.D. dissertation, University of Maryland, Baltimore County, 2007.

- [241] F. Padula, C. Ionescu, N. Latronico, M. Paltenghi, A. Visioli, and G. Vivacqua, "Optimized pid control of depth of hypnosis in anesthesia," *Computer methods and programs in biomedicine*, vol. 144, pp. 21–35, 2017.
- [242] A. Simalatsar, M. Guidi, and T. Buclin, "Cascaded pid controller for anaesthesia delivery," in *Engineering in Medicine and Biology Society (EMBC), 2016 IEEE 38th Annual International Conference of the*. IEEE, 2016, pp. 533–536.
- [243] M. Trojanowicz and P. Alexander, "Portable flow-injection systems for field testing," in *Biosensors for Direct Monitoring of Environmental Pollutants in Field*. Springer, 1998, pp. 173–184.
- [244] F. Ortega, E. Dominguez, G. Jönsson-Pettersson, and L. Gorton, "Amperometric biosensor for the determination of phenolic compounds using a tyrosinase graphite electrode in a flow injection system," *Journal of biotechnology*, vol. 31, no. 3, pp. 289–300, 1993.
- [245] X.-Z. Liu and Z.-L. Fang, "Sequential-injection system for drug-dissolution studies of ibuprofen tablets and sustained-release formulations," *Analytica chimica acta*, vol. 358, no. 2, pp. 103–110, 1998.
- [246] N. Wangfuengkanagul and O. Chailapakul, "Electrochemical analysis of acetaminophen using a boron-doped diamond thin film electrode applied to flow injection system," *Journal of pharmaceutical and biomedical analysis*, vol. 28, no. 5, pp. 841–847, 2002.
- [247] B. Li, Z. Zhang, and W. Liu, "Flow-injection system for automated dissolution testing of isoniazid tablets with chemiluminescence detection," *Talanta*, vol. 54, no. 4, pp. 697–702, 2001.
- [248] B. S. Inc.<sup>TM</sup>, *BS-8000/9000 Multi-Phaser Programmable Syringe Pump Manual*.
- [249] E. W. Finucane, *Definitions, Conversions, and Calculations for Occupational Safety and Health Professionals, Third Edition*. CRC Press, 2017.
- [250] D. Thilakanathan, S. Chen, S. Nepal, R. Calvo, and L. Alem, "A platform for secure monitoring and sharing of generic health data in the cloud," *Future Generation Computer Systems*, vol. 35, pp. 102–113, 2014.
- [251] S. Shini, T. Thomas, and K. Chithraranjan, "Cloud based medical image exchange-security challenges," *Procedia Engineering*, vol. 38, pp. 3454–3461, 2012.
- [252] M. S. Hossain and G. Muhammad, "Cloud-assisted industrial internet of things (IIoT)-enabled framework for health monitoring," *Computer Networks*, vol. 101, pp. 192–202, 2016.
- [253] S. Carrara, F. Stradolini, and T. Kilic, "Fouling-resistant pencil graphite electrode," Patent PCT/IB2017/053 175, 2017.

## Bibliography

---

- [254] M. Kersaudy-Kerhoas and E. Sollier, "Micro-scale blood plasma separation: from acoustophoresis to egg-beaters," *Lab on a Chip*, vol. 13, no. 17, pp. 3323–3346, 2013.
- [255] W. R. Grise, "Applications of switched-capacitor circuits in active filters and instrumentation amplifiers," *Technology Interface*, vol. 3, no. 3, 1999.
- [256] P. Vinella, *Switched Capacitor: working principles and real IC-device application*, 2014.



# Francesca Stradolini

Ph.D. at École Polytechnique Fédérale de Lausanne (EPFL)

## details

address:  
Avenue de Préfaully 21  
Chavannes-Renens  
1022, Switzerland

birth date:  
19.12.1990

email:  
francesca.stradolini  
@gmail.com

## languages

**italian** mother-tongue  
**english** C1  
**french** B1/B2

## programs

Java & Android  
Matlab, C/C++,  
Python, LabVIEW  
L<sup>A</sup>T<sub>E</sub>X, Office, Adobe  
Illustrator CC

## driving licence

A and B

## summary

Biomedical engineer with more than 3 years' experience in R&D for clinical medical devices. Expert in developing electro-chemical sensors for drug monitoring in humans and of IoT networks. At ease in working in multicultural and multidisciplinary team.

## main expertise

- Analytic and synthetic mindset developed during 3+ years engineering R&D activities in life-science international environment: solution oriented.
- Thorough biomedical engineering background in biotechnology, medical devices, chemistry, electronics, medical informatics, hospital processes *etc.*
- Detailed qualification in electro-chemistry for realization of sensors; specifically for clinical devices in hospital environments.
- Excellent time management skills, ensuring the respect of deadlines with high quality results.
- Strong team player attitude guaranteeing an easily integration both in existing teams and the management leading of newly formed ones to success.

## professional experiences

04/15 - 07/18 **Ph.D. Assistant** EPFL, Laboratory of Integrated Circuit (LSI), Lausanne

*Design, realization and in-vitro testing of medical clinical device*

- Project Management: management of multi-disciplinary anesthesia monitoring system project. Plan and management of tasks in bio-engineering, chemistry, electronics, medical devices, IoT and software.
- Platform Design: research process towards the definition of methodologies to develop a complete in-vitro diagnostic tool with IoT cloud support for anesthesia monitoring.
- Trainings: accomplishment of several trainings on fluidics, microscopy, electronics (MEAD), technology transfer (Mintt) and software (LabView, Illustrator *etc.*) subjects.
- Technology Transfer: identification of optimal material for propofol (hypnotic) detection to arrive at *Fouling-resistant Pencil Graphite electrode* patent (PCT/IB2017/053175)
- Teaching Support: courses of analog bio-nano chip design.
- Leadership: Extensive student supervision along 8 complex biotech projects. Main topics: Android programming and IoT cloud integration; security analysis of wireless communications; realization of rehabilitative tools (Bitalino); realization of different flexible and solid bio-electronic platforms.
- Communication skills: speaker in several international conferences.

09/14 - 3/15 **Research Assistant** EPFL, LSI, Lausanne

*Android developing for biomedical applications*

- Software Design: developing of customized software solution (Android) for direct interfacing with implantable biosensors.
- Process: validation of wireless communication, data communication protocols, data plotting and sensors calibrations activities.

- 04/13 - 12/13 **Teaching Assistant part-time (150 h)** DIBRIS - University of Genoa  
*Fundamentals of biomedical instrumentation laboratory:*
- Teaching: design, realization and testing of hardware components for biomedical data acquisition and processing.
  - Software: LabVIEW developing.
  - Practical Activities: use of laboratory instrumentation for circuit characterization (oscilloscope, function generator, multimeter, *etc.*).
- 5/12 - 10/12 **Research Assistant** DIBE - University of Genoa  
*Image processing*
- Software Design: C++ develop and optimization of image processing method (fuzzy segmentation).
  - Software Validation: software testing on Magnetic Resonance 3D-images for automatic detection of Multiple Sclerosis plaques.

## education

- 04/15 - 07/18 **Ph.D. in Electrical Engineering** EPFL  
 Electrical Engineering School (EDEE).  
*Continuous Monitoring of Anesthetics, CoMofA project supported by Swiss National Science Foundation (SNF)*
- 09/12 - 03/15 **Master in Biomedical Engineering, Neuroscience** University of Genoa  
score: 110/110 cum laude
- 09/09 - 10/12 **Bachelor in Bio-Engineering** University of Genoa  
score: 110/110
- 09/09 - 09/12 **ISICT - High Institute of Information and Communication Technologies** University of Genoa  
ICT excellence degree on: marketing, communication, technologies, data science and soft skills.

## Additional Courses

MEAD Course - EPFL - Practical aspects in mixed-signals circuits;  
Mintt - Technology Transfer Office, EPFL - Management of innovation and technology;  
IEEE Sensors Council Summer School - EPFL - Multidisciplinary view in medical wearable sensors design and fabrication towards distributed diagnostic.

## honors and awards

- Apr. 17 and 18 **Invited speaker** Droidcon, Turin  
 International Android Conference  
*Talks on*: Smart-watches and Cloud-based architectures for IoT monitoring systems towards Smart-Hospitals.
- 7-9 Sept. 2017 **Gold Leaf Award** IEEE NGCAS, Genoa  
*Raspberry Pi Based System for Portable and Simultaneous Monitoring of Anesthetics and Therapeutic Compounds*
- 14-16 Nov. 2016 **Best Paper Award** EAI Mobihealth, Milan  
*Paradigm-Shifting Players for IoT: Smart-Watches for Intensive Care Monitoring*

## publications and presentations

### Patent

- Fouling Resistant Pencil Graphite Electrode, **F. Stradolini**, T. Kilic, S. Carrara, PCT/IB2017/053175, Réf.: 6.1721 - PCT, 2017

### Journals

- Cleaning Strategy for Carbon-based Electrodes: Long-Term Propofol Monitoring in Human Serum, **F. Stradolini**, T. Kilic, I. Taurino, G. De Micheli, S. Carrara, *Sensors and Actuators B: Chemicals Journal*, 2018
- Long-Term Monitoring of Propofol and Fouling Effect on Pencil Graphite Electrodes, **F. Stradolini**, T. Kilic, Alberto Di Consiglio, Giovanni De Micheli, Mehmet Ozsoz, S. Carrara, *Electroanalysis Journal*, 30(7), 1363-1369, 2018
- An IoT Solution for On-line Monitoring of Anesthetics in Human Serum Based on an Integrated Fluidic Bio-Electronic System, **F. Stradolini**, A. Tuoheti, T. Kilic, S. L. Ntella, N. Tamburrano, Z. Huang, G. De Micheli, D. Demarchi, S. Carrara, *accepted in IEEE Transactions on Biomedical Circuits and Systems*, 2018
- Raspberry-Pi Based System for Propofol Monitoring, **F. Stradolini**, A. Tuoheti, T. Kilic, D. Demarchi, S. Carrara, *Integration Journal*, <https://doi.org/10.1016/j.vlsi.2018.04.004>, 2018
- Highly-stable Li<sup>+</sup> ion-selective electrodes based on noble metal nanostructured layers as solid-contacts, F. Criscuolo, I. Taurino, **F. Stradolini**, S. Carrara, G. De Micheli, *Journal of Analytica Chimica Acta*, 2018
- Performance of Carbon Nano-Scale Allotropes in Detecting Midazolam and Paracetamol in Undiluted Human Serum, N. Aliakbarinodahi\*, **F. Stradolini**\*, S. A. Nakhjavani\*, I. Tzouvadaki, I. Taurino, G. De Micheli, S. Carrara, \*equally contribution, *IEEE Sensors Journal*, 2018
- Organs-on-chip monitoring: sensors and other strategies (review), T. Kilic, F. Navaee, **F. Stradolini**, P. Renaud, S. Carrara, *accepted in Microphysiological Systems Journal*, 2018
- Wireless Monitoring of Endogenous and Exogenous Biomolecules on an Android™ Interface, **F. Stradolini**, S. Riaro, C. Boero, C. Baj-Rossi, G. Surrel, G. De Micheli and S. Carrara, *IEEE Sensors Journal*, DOI 10.1109/JSEN.2016.2524631, 2016
- In-Vivo Validation of Fully Implantable Multi-Panel Devices for Remote Monitoring of Metabolism, C. Baj-Rossi, A. Cavallini, E. G. Kilinc, **F. Stradolini**, T. Rezzonico Jost, M. Proietti, G. De Micheli, F. Grassi, C. Dehollain, and S. Carrara, *BioCAS 2015 Special Issue in the IEEE Transactions on Biomedical Circuits and Systems*, 2016
- A System for Wireless Power Transfer and Data Communication of Implantable Bio-Sensors in Freely Moving Animals, E. G. Kilinc, C. Baj-Rossi, S. Ghoreishizadeh, S. Riaro, **F. Stradolini**, C. Boero, G. De Micheli, F. Maloberti, S. Carrara, and C. Dehollain, *IEEE Sensors Journal*, Vol. 15, No. 11, 2015

### Conferences

- IoT for Telemedicine Practices Enabled by an Android Application with Cloud System Integration, **F. Stradolini** and N. Tamburrano, T. Moudox, A. Tuoheti, D. Demarchi and S. Carrara, *IEEE ISCAS*, Florence, 2018
- A Flexible Front-End for Wearable Electrochemical Sensing, I. Ny Hanitra, L. Lobello, **F. Stradolini**, A. Tuoheti, F. Criscuolo, T. Kilic, D. Demarchi, S. Carrara, G. De Micheli, *MeMeA*, Rome, 2018

- Generating Safety Guidance for Medical Injection with Three-Compartment Pharmacokinetics Model, C. Yu, H. Riener, **F. Stradolini** and G. De Micheli, ISVLSI Symposium, 2018
- Portable Mixed Signal Circuit for pH and Temperature On-line Monitoring in Biomedical Applications, S. L. Ntella and **F. Stradolini**, A. Tuoheti, D. Demarchi, A. A. Hatzopoulos and S. Carrara, IEEE Sensors, Glasgow, 2017
- Raspberry Pi Driven Flow-Injection System for Electrochemical Continuous Monitoring Platforms, B. Donato, **F. Stradolini**, A. Tuoheti, F. Angiolini, D. Demarchi, G. De Micheli and S. Carrara, IEEE BioCAS, Torino, 2017
- Raspberry Pi Based System for Portable and Simultaneous Monitoring of Anesthetics and Therapeutic Compounds, **F. Stradolini** and A. Tuoheti, P. Motto Ros, D. Demarchi and S. Carrara, IEEE NGCAS, Genova, 2017 Gold Leaf Award
- Paradigm-Shifting Players for IoT: Smart-Watches for Intensive Care Monitoring, **F. Stradolini** and E. Lavalle, G. De Micheli, P. Motto Ros, D. Demarchi, S. Carrara, MOBIHEALTH, Milan, 2016 Best Paper Award
- FPGA-based Approach for Automatic Peak Detection in Cyclic Voltammetry, M. Schirmer and **F. Stradolini**, S. Carrara and E. Chicca, 23rd IEEE ICECS, Monte Carlo, Monaco, December 11-14, 2016.
- Simultaneous Monitoring of Anesthetics and Therapeutic Compounds with a Portable Multichannel Potentiostat, **F. Stradolini** and T. Elboshra, A. Biscontini, G. De Micheli, S. Carrara, IEEE ISCAS, Montreal, Canada, 2016
- Wireless Monitoring in Intensive Care Units by a 3D-Printed System with Embedded Electronic, F. Basilotta, S. Riario, **F. Stradolini**, I. Taurino, D. Demarchi, G. De Micheli, S. Carrara, IEEE BioCAS, Atlanta, USA, 2015
- Full System for Translational Studies of Personalized Medicine with Free-Moving Mice, S. Carrara, C. Baj-Rossi, S. Ghoreishizadeh, S. Riario, G. Surrel, **F. Stradolini**, C. Boero, G. De Micheli, E. G. Kiliç, C. Dehollain, ISCAS, Lisbon, Portugal, 2015

### Live Demonstration

- Live Demonstration: an IoT Cloud-Based Architecture for Anesthesia Monitoring, **F. Stradolini** and N. Tamburrano, T. Moudox, A. Tuoheti, D. Demarchi and S. Carrara, Demo in IEEE ISCAS, Florence, 2018
- Live Demonstration: An IoT SmartWatch-based System for Intensive Care Monitoring, **F. Stradolini** and E. Lavalle, P. Motto Ros, G. De Micheli, D. Demarchi and S. Carrara, Demo in IEEE BioCAS, Torino, 2017

